

Signal processing-enhanced laser-based infrared spectroscopy



University of
Strathclyde
Glasgow

A thesis presented in fulfilment
of the requirements for the degree of
Doctor of Engineering

by

Adam Polak

Department of Electronic & Electrical Engineering,
University of Strathclyde

2018

This thesis is the result of the author's original research. It has been composed by the author and has not been previously submitted for examination which has led to the award of a degree.

The copyright of this thesis belongs to the author under the terms of the United Kingdom Copyright Acts as qualified by University of Strathclyde Regulation 3.50. Due acknowledgement must always be made of the use of any material contained in, or derived from, this thesis.

Signed:

Date:

Acknowledgements

I would like to begin by expressing my gratitude to my supervisors, Prof Stephen Marshall and Dr David Stothard, for the leap of faith they undertook by accepting me for the doctoral position, followed by continuous support, guidance and masterminding all the projects I was involved with over the years of the course. Thank you very much!

During this programme, I have also been fortunate to work and study simultaneously in two institutions, giving me a great opportunity to work with two teams of wonderful people. I would like to thank to literally everyone in the Fraunhofer team for being always available for discussions and patiently providing support, whenever asked. Especially, I would like to thank to Dr John-Mark Hopkins and Dr Simon Andrews for granting me a post-doctoral place in the Fraunhofer team, even before first pages of this thesis were drawn.

I am sincerely grateful to the colleagues in the Centre for Signal & Image Processing and Hyperspectral Imaging Centre, especially to Dr Jinchang Ren, Dr Paul Murray and Dr Timothy Kelman for support in all the image processing, programming and paper writing challenges I struggled with.

I would like to thank to everyone in the office of the EPSRC Centre for Doctoral Training in Applied Photonics for keeping the formal part of the programme so well organised and allowing me to focus on my studies.

I am truly thankful to the Royal Commission of the Exhibition 1851 for awarding me the engineering fellowship and inviting to their family. It has been an honour and privilege to hold this fellowship.

Finally, I want to express my deepest appreciations to my family. Thank you for all your love and support. There are no words that could express my gratitude and this doctorate would not be possible without you!

Abstract

In this dissertation, a portfolio of three projects is presented where intracavity embodiment of optical parametric oscillators (OPO) and various signal processing tools applied to the data they produced are the common factors in all the work done during this programme. Two demonstrated projects were based on a study of new potential applications for commercialised OPO based imaging system, while in the last one the unmatched characteristics of such a system were exploited, in order to develop new embodiment of a spectroscopic technique.

The INHERIt project explored the use of hyperspectral imaging technologies, combined with advanced signal processing techniques, for the purpose of automatically recognising counterfeit paintings. Various challenges associated with laser based imaging are discussed as well as hardware based solutions to resolve some of these issues are proposed. The application of classification techniques was demonstrated based on the data acquired from both bespoke and actual forged paintings.

The Rosdam project aimed to evaluate two types of hyperspectral imaging systems, as well as their capability and applicability for the detection of oil spillages in ice-affected waters. This work lead to the conclusion that the employed technology was not suitable for oil under ice detection. The undertaken experimental approach is explained, the treatment of oil and ice is discussed and the findings and lessons learned during this work are presented.

The IC-OPO-PAS project aimed to develop an optical molecular gas sensor exhibiting high levels of selectivity and sensitivity. The outstanding sensitivity demonstrated by this technology is rooted in a novel combination of photoacoustic spectroscopy (PAS) operated within the cavity of a continuous-wave, Intracavity OPO. In this work detection at the level of single parts-per-billion (ppb) is shown and a discussion on how this technology could be readily refined to potentially demonstrate a sensitivity of 10's parts-per-quadrillion (ppq) is presented.

This thesis revealed a successful combination of seemingly two independent fields of science which, when utilised together, can provide superior results. Moreover, it demonstrated the need for broadly tuneable laser sources operating in infrared spectral region. Overall conclusions are given in this portfolio of presented above projects and possible future research opportunities are discussed in the context of the results obtained over the course of this programme.

Table of Contents

Acknowledgements.....	iii
Abstract.....	iv
Table of Contents	v
List of Figures.....	xi
List of Tables.....	xxii
Nomenclature	xxv
Roman Symbols.....	xxv
Greek Symbols.....	xxviii
Acronyms / Abbreviations	xxix
Chapter 1: Introduction	- 1 -
1.1. Introduction.....	- 1 -
1.2. Hyperspectral Imaging.....	- 2 -
1.3. Mid-infrared tuneable lasers.....	- 5 -
1.4. Thesis overview.....	- 7 -
References.....	- 9 -
Chapter 2: Theoretical Background	- 13 -
2.1. Introduction.....	- 13 -
2.2. Signal Processing.....	- 13 -
2.2.1. Classification process	- 14 -
2.2.2. Survey of classification methods.....	- 17 -
2.2.3. Support Vector Machine	- 21 -
2.2.3.1. Feature extraction	- 21 -
2.2.3.2. Classification.....	- 23 -
2.2.3.3. Performance assessment.....	- 26 -
2.2.4. Partial Least Squares regression	- 27 -
2.2.4.1. Partial Least Squares model.....	- 28 -
2.2.4.2. Simulation data.....	- 34 -
2.2.4.3. Model validation results	- 36 -
2.2.4.4. Data size reduction.....	- 40 -
2.3. Optical Parametric Oscillators.....	- 42 -

2.3.1.	Parametric process.....	- 42 -
2.3.2.	Cavity configurations	- 47 -
2.3.3.	IC-OPO	- 50 -
2.3.3.1.	Threshold, power and efficiency	- 52 -
2.3.3.2.	Relaxation oscillations.....	- 55 -
2.4.	Laser scanning.....	- 58 -
2.5.	Conclusions.....	- 60 -
	References.....	- 61 -
Chapter 3: INHERIt project.....		- 70 -
3.1	Project background.....	- 70 -
3.2	Hyperspectral equipment.....	- 73 -
3.2.1	Image acquisition with Red Eye 1.7	- 75 -
3.2.2	Image acquisition with Firefly IR Imager	- 76 -
3.2.2.1	2D Galvanometer scan – full field of view.....	- 78 -
3.2.2.2	Normalisation with the calibration image	- 81 -
3.2.2.3	1D Galvanometer scan (line scan)	- 82 -
3.2.2.3.1	Fast translation	- 83 -
3.2.2.3.2	Gradual translation	- 85 -
3.2.2.4	Segmental 2D Galvanometer scan	- 88 -
3.3	Hardware improvement techniques for imaging artefacts.....	- 90 -
3.3.1	Noise.....	- 91 -
3.3.1.1	Per-pulse jitter.....	- 93 -
3.3.1.1.1	Optical Pulsed Source	- 93 -
3.3.1.1.2	Boxcar integrator and normalisation electronics	- 98 -
3.3.1.1.3	Results.....	- 102 -
3.3.1.2	Speckle effect.....	- 105 -
3.3.2	Specular reflection	- 109 -
3.3.3	Integration with the mid-infrared illumination source	- 113 -
3.4	Development of algorithms for artwork classification.....	- 118 -
3.4.1	Building and validating a spectral library using bespoke paintings.....	- 118 -

3.4.2	Algorithm development and feature extraction.....	- 120 -
3.5	Results.....	- 124 -
3.5.1	Candidate paint selection.....	- 124 -
3.5.2	Spectral classification of the test painting.....	- 124 -
3.5.3	Analysis of forged paintings.....	- 127 -
3.6	Conclusions.....	- 129 -
3.7	Acknowledgments	- 131 -
	References.....	- 131 -
Chapter 4:	ROSDAM.....	- 137 -
4.1.	Project background.....	- 137 -
4.2.	HIDE – the initial proof of concept study.....	- 138 -
4.2.1.	Passive system setup	- 138 -
4.2.2.	Active system setup.....	- 139 -
4.2.3.	Results	- 140 -
4.3.	ROSDAM project - Experimental setup	- 142 -
4.3.1.	Imaging hardware arrangement.....	- 142 -
4.3.1.1.	Passive system	- 142 -
4.3.1.2.	Active system.....	- 143 -
4.3.2.	Ice growth and control	- 143 -
4.3.3.	Oil injection and monitoring	- 145 -
4.4.	Background tests.....	- 147 -
4.4.1.	Spectral response of water	- 147 -
4.4.2.	Spectral response of crude oil.....	- 150 -
4.4.3.	Refractive index considerations.....	- 150 -
4.5.	Imaging challenges and data extraction.....	- 151 -
4.6.	Experimental work	- 153 -
4.6.1.	First full scale test.....	- 153 -
4.6.1.1.	Test schedule	- 153 -
4.6.1.2.	Passive system results - first imaging run.....	- 155 -
4.6.1.3.	Passive system results - Second imaging run.....	- 156 -
4.6.1.4.	Active system results – first imaging run	- 158 -

4.6.1.5.	Active system results – second imaging run.....	- 160 -
4.6.1.6.	Automatic detection of oil beneath ice	- 162 -
4.6.2.	First small sample test - repeatability of the ice spectra	- 164 -
4.6.2.1.	Experimental procedure	- 165 -
4.6.2.2.	Ice spectra repeatability results	- 166 -
4.6.2.3.	Impact of the ice surface condition	- 167 -
4.6.2.4.	Impact of the oil injection.....	- 169 -
4.6.2.5.	Summary of the experiment.....	- 170 -
4.6.3.	Second full scale test	- 171 -
4.6.3.1.	Experimental setup.....	- 171 -
4.6.3.2.	Test plan.....	- 171 -
4.6.3.3.	Results.....	- 172 -
4.6.3.4.	Other oil and ice conditions.....	- 176 -
4.6.3.5.	The notion of the visible range illumination for the oil detection.....	- 178 -
4.6.3.6.	Summary of the experiment.....	- 179 -
4.6.4.	Verification of the ice transmission in the infrared region	- 179 -
4.6.4.1.	Design of the experiment	- 179 -
4.6.4.2.	Results.....	- 180 -
4.6.5.	Measurement of the ice transmission in the visible region.....	- 181 -
4.6.6.	Verification of the influence of mechanical impact on the ice spectra.....	- 183 -
4.6.6.1.	Spectral measurements.....	- 184 -
4.6.6.2.	Visual inspection.....	- 185 -
4.7.	Conclusions.....	- 187 -
4.8.	Acknowledgments	- 188 -
	References.....	- 188 -
Chapter 5:	IC-OPO-PAS.....	- 191 -
5.1.	Project background.....	- 191 -
5.2.	Optical Parametric Oscillator	- 194 -
5.2.1.	Design.....	- 194 -
5.2.2.	Power performance.....	- 199 -

5.2.3.	Wavelength, linewidth and tuning properties of the IC-OPO.....	- 202 -
5.3.	Photoacoustic spectrophone.....	- 206 -
5.3.1.	Microphone-based spectrophone	- 206 -
5.3.1.1.	Design.....	- 206 -
5.3.1.2.	Characterisation.....	- 209 -
5.3.2.	Quartz tuning fork-based spectrophone.....	- 212 -
5.3.2.1.	Commercial spectrophone from CDP Systems.....	- 213 -
5.3.2.2.	In-house fabricated spectrophone	- 215 -
5.3.2.3.	Bare QTF spectrophone.....	- 217 -
5.4.	Results.....	- 220 -
5.4.1.	Microphone-based PAS cell results	- 220 -
5.4.1.1.	Spectroscopy and sensitivity	- 220 -
5.4.1.2.	Comparison with extra-cavity photoacoustic configuration.....	- 228 -
5.4.2.	QE-PAS results.....	- 230 -
5.5.	Conclusions.....	- 235 -
5.6.	Improvements & future work.....	- 236 -
5.6.1.	Sensitivity improvements	- 237 -
5.6.2.	Tuning	- 239 -
5.6.3.	Modulation.....	- 242 -
5.6.4.	Excitation in deeper IR.....	- 242 -
5.6.5.	Preparations for deployment	- 243 -
5.7.	Acknowledgments	- 244 -
	References.....	- 244 -
Chapter 6:	Conclusions	- 249 -
6.1.	Introduction.....	- 249 -
6.2.	Summary of the portfolio and conclusions	- 249 -
6.3.	Future work	- 253 -
6.4.	Summary.....	- 255 -
	References.....	- 256 -
Appendix A.....		- 258 -
I.	The full description of all paints contained by the ‘grid canvas’	- 258 -

II. The average spectra from all paints contained by the ‘grid canvas’, imaged by the passive system.....	- 262 -
III. The average spectra from all paints contained by the ‘grid canvas’, imaged by the active system.....	- 265 -
IV. The PCA scores plots for first three principal components obtained from all paints contained by the ‘grid canvas’, imaged by the passive system.....	- 268 -
V. The PCA scores plots for first three principal components obtained from all paints contained by the ‘grid canvas’, imaged by the active system.....	- 271 -
Appendix B.....	- 274 -
I. Journal Publications.....	- 274 -
II. Conference Proceedings.....	- 274 -

List of Figures

1.1.	Typical spectral imaging approaches: (a) Whiskbroom; (b) Pushbroom; (c) Staring; (d) Snapshot; PGP stands for Prism-Grating-Prism arrangement.....	4
2.1.	Steps for supervised image classification.....	14
2.2.	2D representation of two class data represented by full and empty circles; a) different correct linear classifications of the data set; b) the optimal hyperplane with circles around support vectors and γ indicating the margin between them and the hyperplane.	25
2.3.	Illustration of mapping the data points into new feature space; a) data set in their original 2D space (with indication of separating hyperplane); b) data set from graph (a) mapped into an additional feature dimension where classification with a linear hyperplane is possible.....	26
2.4.	Representation of data arrangements and its projection to latent structures.....	30
2.5.	Geometric interpretation of the PLS regression model.....	31
2.6.	Example of the graph representing proportion of the total predictors (a) and responses (b) variance explained by the model as a function of number of PLS components.....	32
2.7.	Example plots of the model validation: a) MSE for prediction with external validation set; b) PRESS based on cross-validation.....	33
2.8.	Single intensity image from the hyperspectral data used in this example. Image represents 4 different types of tea leaves (rows) with 4 snapshots per each type (columns) combined in one picture.	35
2.9.	Four selected spectra used in this example as the endmembers.	35
2.10.	Scatter plot of fitted vs. observed response value per each endmember; a) $g=2$, b) $g=4$.	37
2.11.	Cumulative percentage of the variance in X and Y explained by the model; a) $g=2$, b) $g=4$	37
2.12.	Estimated Mean Squared Prediction Error graph as a function of PLS components; a) $g=2$, b) $g=4$	38
2.13.	Comparison of the spectrum, generated based on the observed (simulated) fractions with the one based on the prediction with number of PLS components: a) $g=2$, b) $g=4$.	38
2.14.	Normal probability plot for Y-residuals; a) $g=2$, b) $g=4$	40
2.15.	Distance to the model in X-space (DModX) per observation for X-residuals; a) $g=2$, b) $g=4$	40
2.16.	Surface graph of MSE variation as a function of spectrum window size and position.....	41
2.17.	Schematic of the parametric frequency down-conversion where high energy pump photon is split into lower energy signal and idler photons.....	42

2.18.	The dependence of parametric gain on the phase matching parameter $\Delta k l/2$	43
2.19.	Periodically poled nonlinear crystal structure with a) single, b) fan-out and c) slanted fan-out grating periods.....	45
2.20.	Spectral (up to mid-infrared) and temporal coverage of OPOs based on selection of nonlinear crystals.....	45
2.21.	Wavelength tuning with a) single grating PPLN crystal with the temperature and grating tuning [82] and b) fanned grating PPLN crystal with the crystal position tuning.....	46
2.22.	Cavity configurations for CW OPOs: (a) singly resonant; (b) doubly resonant; (c) pump enhanced; (d) intracavity; (e) dual cavity, doubly resonant; (f) doubly resonant, with pump tuning; and (g) dual cavity, pump enhanced. Black, grey, and striped arrows indicate the pump, signal and idler waves, respectively. Nonlinear media and gain media are shown by darker and lighter shading, respectively.....	49
2.23.	Basic diagram of an IC-OPO.....	51
2.24.	Down-conversion parameters of an IC-OPO.....	53
2.25.	(a) Linear output power of OPO once above threshold and (b) clamping effect of the IC-OPO upon the circulating field.....	54
2.26.	Typical measured traces of the transient behaviour of the ICOPO with (a) down-conversion suppressed (i.e. laser operation only), (b) down-conversion permitted (with no SHG) and (c) both down-conversion and SHG enabled.....	56
2.27.	Recovery transient dynamics after perturbation of the steady state of an IC-OPO pumped internal to (a) an Nd:YVO ₄ and (b) VECSEL laser.....	57
2.28.	Sketch of the imaging set-up from: HeNe – helium neon laser, TD – triggering detector, PS – polygon scanner, TM – tilting mirror, G – galvanometer, m – micro-mirror, LC – illumination focusing lens, L – collection lens, F – band pass filter, D – MCT detector.	60
3.1.	Illustration of the scanning set-up for Red Eye 1.7 camera (a) and Firefly IR Imager (b), along with the two targets: grid canvas (c) and test painting (d).....	75
3.2.	Graphical User interface of the software for decoding and pre-processing images acquired with the Firefly IR Imager.....	77
3.3.	Example of the SURF registration algorithm, where single band image at 3050.1nm with overlaid circles indicating location of features used for registration is shown in panel a), single band image at 3053.6nm with overlaid circles indicating features location is shown in panel b) and graph in panel c) demonstrates a comparison between the two; Note that the axes of c) are not in scale to better illustrate the phenomenon....	78
3.4.	Single band image (at 3000nm) of the two grid canvases placed next to each other, with indicated regions of interest (a) and graphical representation of the classification algorithm based on this data set (b).....	79
3.5.	Simplified diagram of the minimum and maximum beam positions at one horizontal plane during the image scan.....	80

3.6.	Results of the test for the impact of painting position on the intensity variation across the image. Colours of the lines in the graphs correspond to regions selected on the single band image.....	81
3.7.	Single band image (at 3000nm) of the shotblasted aluminium sheet used as the calibration tile (a), normalised image of two grid canvases placed next to each other, with indicated regions of interest (b) and graphical representation of the classification algorithm based on this data set (c).....	82
3.8.	Subsequent steps of line scan imaging approach with fast painting translation (based on single band image at 1550nm), where (a) to (d) represent initial data, (e) rearranged and stitched composition, (f) cropped and (g) subsampled image.....	84
3.9.	Single band image at 1710nm with four regions of interest indicated by coloured ellipses (a) and average spectral profiles extracted from these regions (b).....	85
3.10.	Single band image at 1710nm with regions of interest indicating selected training data (a) and graphical representation of the classification result (b). Note: classification of the paint samples is valid only for the paints selected in the training data, classification of other paints was not the purpose of this exercise and the result demonstrate the best match from the algorithm.	85
3.11.	Data acquisition sequence with gradual increase of the spectral resolution, where blue line indicates the data collection sequence and red circles mark the images that were actually acquired within available time.	86
3.12.	Single band image at 3200nm with four regions of interest indicated by coloured ellipses (a) and average spectral profiles extracted from these regions (b).....	87
3.13.	Single band image at 3200nm with regions of interest indicating selected training data (a) and graphical representation of the classification result (b). Note: classification of the paint samples is valid only for the paints selected in the training data, classification of other paints was not the purpose of this exercise and the result demonstrate the best match from the algorithm.....	87
3.14.	Illustration of the segmentation procedure for the two target paintings with examples of the stitched single band images in near- and mid-IR regions. Note: the black colour at the bottom right corner of the grid canvas HSI data represent lack of data.....	89
3.15.	Single band image at 3400nm with regions of interest indicating selected training data (a) and graphical representation of the classification result (b). Note: classification of the paint samples is valid only for the paints selected in the training data, classification of other paints was not the purpose of this exercise and the result demonstrate the best match from the algorithm.....	89
3.16.	Image examples demonstrating salt-and-pepper type of noise as well as the impact of the specular reflection on the spectral signature of the area affected by this phenomenon.	90
3.17.	A diagram (a) and a photograph (b) of the EC-OPO developed in this test.	94

3.18.	Pump laser characteristic of average power and peak energy as function of Q-switching repetition rate.....	95
3.19.	Pulse energy of the idler as a function of pump pulse energy.....	96
3.20.	Tuning range of the EC-OPO through its phase matching range.....	97
3.21.	Test bed of the EC-OPO based imaging setup for the normalisation experiment.....	98
3.22.	The Boxcar Integrator electronics: PCB layout (a), photograph of ready board (b) and the electronic circuit of the integrator part (c).....	99
3.23.	Oscilloscope screens (a) - (f) demonstrating the operation of the boxcar integrator electronics where trace 1 illustrates TTL trigger signal, subsequent traces constitute as follow: 2 - the laser pulse, 3 - the boxcar timing, 4 - the reset signal, 5 - the integrated signal, 6 - the “sample and hold” timing, 7 - the quasi-continuous integrated signal of one channel, 8 - the normalised signal, 9 - the averaged normalised signal.	100
3.24.	Tests of the boxcar integrator performance: linearity check (a) and test of any residual noise (b) where the traces represent the measured signal on both channels of the normalisation circuitry with laser being switched off.....	102
3.25.	Time series (a) and signal voltage level distribution (b) in the channels A (reflected), B (reference) and A/B (normalised) of the boxcar electronics in the Channel A = Channel B case.	102
3.26.	Oscilloscope traces for Channel A = Channel B (a) and Channel A \neq Channel B (b) cases. Yellow and cyan traces represent signals in channels A and B while magenta trace is the normalised A/B signal.....	103
3.27.	Time series (a) and signal voltage level distribution (b) in the channels A (reflected), B (reference) and A/B (normalised) of the boxcar electronics for the single point in time test.	103
3.28.	Time series (a) and signal voltage level distribution (b) in the channels A (reflected), B (reference) and A/B (normalised) of the boxcar electronics for the spatial scan test.	104
3.29.	Speckle formation in (a) free space and (b) an imaging system.....	106
3.30.	Composite of two images showing varying granulation of speckle pattern when observed via larger (left) and smaller (right) size of the aperture placed in the optical path.....	107
3.31.	Signal-to-noise ratio derived for the single point in time data from the directly reflected and normalised signals, as a function of the aperture diameter.	108
3.32.	Illustration of selected aperture diameters and corresponding acquired images with the data represented in a form of histogram and derived SNR for the reflected and normalised signals.	109
3.33.	Signal-to-noise ratio derived for the 2D imaging scan data from the directly reflected and normalised signals, as a function of the aperture diameter.	109

3.34.	Intensity of reflected light from highly specular (a) and highly diffusive (b) objects, as a function of beam deflection angle, with varying angle of the polariser analysing the reflected beam.....	111
3.35.	Series of images of the same highly specular object with varying angle of the polariser analysing the reflected beam. The pixel intensity range on all pictures was fixed to the one from 0° polariser alignment.	112
3.36.	Series of images of the same highly diffuse object with varying angle of the polariser analysing the reflected beam. The pixel intensity range on all pictures was fixed to the one from 0° polariser alignment.	112
3.37.	Series of images of cardboard box with highly glossy surface with varying angle of the polariser analysing the reflected beam. The pixel intensity range on all pictures was fixed to the one from 90° polariser alignment.	113
3.38.	Single band intensity images of the grid painting recorded by slow analogue channels with default FPGA code of Red Pitaya (a) and by fast analogue channels with updated FPGA code (b); polariser setting - 90°.....	114
3.39.	Single band intensity images of the grid painting reconstructed from directly reflected (a) and normalised (b) signal, with inserts demonstrating the low-amplitude, long-term intensity fluctuations in reflected signal (marked by arrows and curly brackets), removed from the image by the normalisation process; polariser setting - 0°.....	115
3.40.	Single band intensity images of the grid painting reconstructed from normalised signal, captured with the polariser set to 0° (a), 60° (b) and 90° (c).....	116
3.41.	Single band intensity images of highly specular and highly diffusive surfaces, reconstructed from normalised signal, captured with the polariser set to 0° and 90°.....	117
3.42.	Illustration of paintings used during the lab stage of the project and their ground truth description: a) the pigment grid canvas serving as a training data; b) description of the pigments used in the grid canvas; c) Pastiche of "Untitled (Suprematist Composition)," by Kazimir Malevich as testing painting; d) ground truth data of pigments used for creation of the Kazimir Malevich pastiche.....	119
3.43.	Average spectral response of all the green coloured pigments acquired by passive (a) and active (b) system.....	120
3.44.	PCA scores plot of first three principal components for the group of green paints imaged with passive (a) and active (b) system.	121
3.45.	Illustration of the classification algorithm validation based on Red Eye 1.7 data: a) intensity image on one wavelength for two grid canvas; b) single row with assigned colour labels to each paint c) classification result of the training data set (on the left side) and validation data set (on the right).	123
3.46.	Illustration of the analysis software developed for painting analysis with demonstration of ROI's implemented on the training and mask on the testing image.....	123

3.47.	Illustration of the analysis approach for pigment classification on tested painting. For each colour on the painting, a subset of training paints was chosen (first column – Training data) and classification was performed on the masked area of the painting corresponding to this colour (second column – Masked regions). It resulted in per-pixel classification of the selected area (third column – Classification result) and majority vote was drawn for these regions effecting in selection of one pigment corresponding to one colour (fourth column – majority vote result). Three examples of this approach are shown in here, for the regions of brown (a), green (b) and white (c) paint (demonstration based on Firefly IR Imager data).....	125
3.48.	Graphical illustration of class labelling for all the regions of the test painting: a) the colour coding of the result demonstration; b) ground truth data illustration; c) the result based on data from Firefly IR Imager; d) the result based on data from Red Eye 1.7 system.....	126
3.49.	Example of receiver operating characteristic (ROC) curves for both tested HSI sensors.	127
3.50.	Illustration of two forged paintings with indication of analysis region and classification result of selected colours: a) intensity image of grid canvas with selection of paints used for training and the legend identifying the colour coded pigments; b) painting described as Sevrancx with white/cream colour classification result; c) painting referred as HM501 and white colour classification.....	128
4.1.	Small container with ice (a) and oil introduced beneath the ice layer (b).	138
4.2.	Scanning setup with the Firefly IR Imager above the container with ice (a); the ice block of approximately 80 mm thickness cut after the imaging (b).	140
4.3.	Firefly IR Imager in thermal enclosure (on left) and Red Eye 1.7 camera mounted on the translation stage with halogen illumination (on right) in the testing setup.....	143
4.4.	Insulated containers: used as ice tanks during the experiment (a), with underwater camera thickness indicators and oil injection piping (b), filled with sea water (c).....	144
4.5.	Ice formations: fully filling the container and attached to its wall (a), with thinner edges and thick middle part prepared for free floating ice (b).	145
4.6.	Underwater view images of one of the oil introduction cases (the case of 11cm tick ice) illustrating a situation with no oil (a) and the oil distribution in three oil thickness cases: 0.5cm (b), 1cm (c) and 2cm (d).....	146
4.7.	Background verification setup for imaging with (a) passive and (b) active HSI system...	147
4.8.	Absorption coefficient of water and matching penetration depth in the infrared region...	149
4.9.	Spectral response of crude oil measured in Near-IR with: (a) passive system (950nm – 1700nm), (b) active system (1490nm – 1850nm), (c) Mid-IR with active system only (2500nm – 3750nm). The spectral response in Mid-IR represents only the hardware baseline demonstrating full absorption of the radiation in this range.....	150

4.10.	Single band intensity picture of ice imaged with passive system (a) and with active system (b) and their respective regions for spectral data extraction (red frame).	152
4.11.	Single band intensity image (at 3000nm) of ice (a) and colour coding for 5 regions of this image (b), average spectra extracted from illustrated regions in Near-IR band (c) and Mid-IR band (d).	153
4.12.	Ice formation stuck to the bottom surface of the main ice layer – view of the bottom of the ice block cut out from the contained after imaging.	154
4.13.	Colour coding (a) and averaged spectral response (b) of 4cm pure ice layer, extracted from the data acquired with passive system.	156
4.14.	Colour coding (a) and averaged spectral response (b) of 4cm ice layer without and with oil injections underneath, extracted from the data acquired with passive system.	156
4.15.	Colour coding (a) and averaged spectral response (b) of 3cm, 7cm and 11cm pure ice layers, extracted from the data acquired with passive system.	157
4.16.	Colour coding (a) and averaged spectral response of 3cm (b), 7cm (c) and 11cm (d) ice layers without and with oil injections underneath, extracted from the data acquired with passive system.	158
4.17.	Colour coding (a) and averaged spectral response of 4cm pure ice layer in Near-IR (b) and Mid-IR (c) spectral region, extracted from the data acquired with active system.	159
4.18.	Colour coding (a) and averaged spectral response of 4cm ice layer without and with oil injections underneath, in Near-IR (b) and Mid-IR (c) spectral region, extracted from the data acquired with active system.	159
4.19.	Colour coding (a) and averaged spectral response of 3cm, 7cm and 11cm pure ice layers, in Near-IR (b) and Mid-IR (c) spectral region, extracted from the data acquired with active system.	160
4.20.	Plot of the average reflected signal, reduced to first four bands, as used for training of the classifier. These average spectra are computed based on the data extracted from no-oil (red) and 2cm oil (green) cases of 3cm ice thickness. The training area is illustrated by the circles on the intensity images in Table 4.6 (b).	162
4.21.	Experimental setup for the small sample runs of ice imaging. The two photographs depict the Firefly IR Imager next to the Labcold freezer imaging the ice sample located inside the freezer.	164
4.22.	Photograph of the ice block partially overflowed with water during placement for the floating ice condition. Water rapidly froze down changing the ice surface into a smooth, mirror-like structure.	168
4.23.	Photographs of the ice preparation for the oil introduction: a) drilling the bores b) ice block with oil introduced through the two bores, with oil spilled around the wholes during injection.	169
4.24.	Oil distribution underneath the ice block viewed from below of ice in the tank 1 (a), tank 2 (b) and tank 3 (c).	172

4.25.	Intensity image at 3200nm of the pure ice sample in different moments of the its handling: uncut ice, stationary condition (a), pressure on ice from the drill bit, just before first drilling (b) situation just after the first hole was drilled (c), free floating ice, stationary condition (d).....	176
4.26.	Top view of the ice tank with more versatile oil spill simulation: the oil stain on top of the floating ice block, the oil sample mixed with water and slush at the edge of ice with oil spilled underneath. The subset of this view captured by the Firefly IR Imager is presented and a single band intensity image (at 3200nm) of this test setup is also demonstrated, with all the different areas identified.	177
4.27.	Frames of the underwater camera footage, where highly scattered visible laser radiation can be observed passing through 10cm of the ice specimen. Both the orange coloured radiation (a) and green radiation (b) are barely visible in the still form and can be better observed only when the scanning process moves this radiation with respect to background. The place where this highly broadened light line is present at these given images is marked by red rectangle.	178
4.28.	Photograph of the three aluminium blocks (before surface roughening) used in this experiment (a) and comparison of the top view on the ice sample with encapsulated aluminium targets made with standard digital camera (b) and with a single band image (at 3200nm) captured with Firefly IR Imager (c). The tallest block is visible through ice on the image (b).....	180
4.29.	Setup of the ice transmission measurement in the visible spectral region with the selection of three laser diodes a) red (630nm) b) green (532nm) and c) blue (405nm). ..	182
4.30.	Graphical representation of the ice transmission data for the three laser diodes (red, green and blue) and three ice path lengths (2.5cm, 5.0cm and 13.0cm).	183
5.1.	An illustration of a photoacoustic setup.....	192
5.2.	An intracavity OPO exciting an extra-cavity photoacoustic spectrophone.....	193
5.3.	Intracavity OPO with intracavity quartz enhanced photoacoustic spectrophone.....	194
5.4.	Schematic representation of the signal resonant IC-OPO as developed during this project.	195
5.5.	Parametric gain lineshape simulated for utilised PPLN crystal with full-width at half-maximum gain bandwidth centred around 6529 cm^{-1}	196
5.6.	Frequency selectivity of the air-spaced (red) and solid silicon (green) etalons used in this study, projected onto the parametric gain lineshape of utilised PPLN crystal (as will be derived below, the FSR of the corresponding cavity is $\sim 430\text{MHz}$).....	197
5.7.	Intracavity OPO with extended signal arm to accommodate etalons and spectrophone (not shown).....	198

5.8.	Power characteristics of constructed OPO where blue triangles represent intracavity pump field with OPO not working, blue circles depict the same with OPO working and black squares represent extracted idler power, total down-converted power and intracavity signal field on their respective axes.	200
5.9.	Impact of three different AOM modulation levels on the pump and signal fields. Green trace: modulation drive signal; yellow trace: circulating signal power; purple trace: circulating pump field. The three regions are described in the text.....	201
5.10.	Oscilloscope traces of the scanning Fabry-Perot Interferometers for a) the modulation working zones (a) and (b) (see Figure 5.9) where pump wave is not affected and b) the modulation working zone (c) where the loss created by AOM affects the pup wave, which subsequently induces the relaxation oscillations and high frequency noise in the pump and signal lineshapes. The trace 1 is the ramp signal of the interferometer; the trace 2 is the lineshape of the oscillating pump wave and trace 3 of the oscillating signal wave.	201
5.11.	Coarse tuning of the OPO by varying the grating period.....	202
5.12.	High precision tuning of the signal wave with air-spaced etalon.....	203
5.13.	Folded signal cavity containing both air-spaced and solid silicon etalons. Note, silicon etalon is mounted on a galvanometer for precise angular control and the PAS cell is located at the second focal point.....	204
5.14.	High precision signal tuning with both ASE and solid silicon etalon.....	205
5.15.	3D printed spectrophone (basis of adopted design) in cross section.....	206
5.16.	PAS spectrophone designed for this project.....	207
5.17.	Reflectivity curves for Calcium Fluoride at 1.5 μ m and 3.3 μ m radiation wavelength with an insert plot showing an offset between the two respective Brewster angles.	207
5.18.	Typical (measured) frequency response of the INMP504 microphone.	208
5.19.	3D-printed spectrophones as used in this project: (a) before integration with microphone, featuring the PCB for microphone connection and (b) fully integrated and installed in the optical setup.	209
5.20.	Characteristic of the PAS spectrophone in the extra-cavity position as a function of the modulation frequency.	210
5.21.	Characteristic of the PAS spectrophone in the intracavity position as a function of the modulation frequency.	211
5.22.	QE-PAS spectrophone geometries. (a) bare QTF, (b) in-line, and (c) off-axis.....	212
5.23.	Commercial CDP Systems QE-PAS system purchased for use in this project.....	213

5.24.	Graphical interface of the software controlling the CDP Systems QE-PAS system.....	214
5.25.	Acoustic detection module received from CDP Systems.....	214
5.26.	Close up of the CDP Systems ADM. (a) resonance tube surrounding QTF, (b) poor finish on tube end, (c) tube end after de-burr.....	215
5.27.	Preliminary material evaluation with PEEK [(a) & (b)] and brass [(c) & (d)].....	216
5.28.	Off-axis QE-PAS spectrophones. (a) Literature design (8mm long, 150 μ m slot width), (b) in-house design (dimensions same as in (a)).....	217
5.29.	A QTF removed from its packaging (a) and a close-up with the measurement of the gap between the prongs (b).....	217
5.30.	Comparison of QTF performance under different conditions.....	218
5.31.	Bare QTF spectrophone mounted in the signal cavity. The yellow tracer indicated the path and waist positions of the signal excitation mode.....	218
5.32.	QTF within its plenum cell. Note here the cover has been removed. The pound coin is provided for scale.....	219
5.33.	Noise spectral density at the output of the preamplifier under various conditions.....	220
5.34.	Absorption spectrum of NH ₃ . Shaded area shows tuning range of OPO under ASE control	221
5.35.	First intracavity PAS result. Upper trace: measured; lower trace: library.....	222
5.36.	Higher resolution spectrum enabled by silicon etalon. Upper trace: measured; lower trace: library.....	223
5.37.	Initial sensitivity measurement.....	223
5.38.	Identification of alternative, stronger absorption feature in the ammonia spectrum.....	224
5.39.	Photoacoustic response centered at the 6605.6cm ⁻¹ line with coarse (a) and fine (b) etalon tuning.....	224
5.40.	Sensitivity of the system when tuned to 6605.6cm ⁻¹	225
5.41.	Photoacoustic and library spectra of water vapour alone (a) and compared with 100ppm of NH ₃ (b).....	225
5.42.	System response with its improvements implemented.....	227
5.43.	Amplitude stability of the system: time series (a) and Allan variance plot based on this data (b).....	228
5.44.	Extra-cavity photoacoustic spectroscopy configuration.....	229
5.45.	Resonance response of the spectrophone with the excitation from the DFB laser.....	229
5.46.	Signal cavity model with approximately 100 μ m waist diameter at QTF position.....	231

5.47.	Spectrum of signal produced by QTF (and preamplifier): full frequency sweep (a) and a close up in the region of the QTF resonance (b); In the legend S stands for Signal generator and ML for Modulated laser; note the logarithmic y-axis.....	231
5.48.	Bare QTF with laser on. The green light visible on the prongs of the QTF results from the parasitic doubling of the 1064nm pump.....	232
5.49.	Multiple beam paths upon radiation transmission through the etalon (a) (Image source: https://en.wikipedia.org/wiki/Fabry-Perot_interferometer); Magnitude of the QTF signal as a function of acquired samples during translation of the fork across the laser beam with solid etalon and ASE included in the cavity (b), with only solid etalon tilted off-axis (c) and with only solid etalon in near perpendicular alignment (d); Shaded area shows 8mm travel range of the translation and the arrows indicate where the clipping of the beams (main and satellite) occurred; note that there is a dip in the centre of each graph, as obscuring the main beam with the QTF switches off the OPO	233
5.50.	Modified signal cavity model with tighter focus - approximately 50 μ m waist diameter at QTF position.....	234
5.51.	Off-axis QE-PAS spectrophone designed during this project. The slot (highlighted) is only 150 μ m wide.....	238
5.52.	QE-PAS spectrophone based upon inscribed glass, as developed at FCAP. Here, the glass has been 'written' but not etched (indicated with an arrow); (a): acoustic bore; (b) anti-nodal pipe for QTF excitation	239
5.53.	Simulated ammonia absorption spectrum at the selected spectral range with ambient pressure of 1atm (continuous line) and with ambient pressure decreased ten times (dotted line); note the increased selectivity of the spectral features, with the dominating triplet peak at the centre of the plot now being resolved as actually 7 distinct peaks....	240
5.54.	Simulated transmission plots for two 333GHz FSR etalons with 20%R (a) and 70%R (b). Both plots illustrate 3 FSR's of respective etalons, centred on 1530nm; adapted from.....	241
5.55.	Example diagram of an IC-OPO in the ring configuration with QE-PAS module located intracavity to the ring with circulating down-converted field.....	241
5.56.	Infrared transmission spectrum of acetone. The purple, green and red zones roughly correspond to the near-, mid- and deep infrared regions. Note the strong and very characteristic features in the latter.....	243

List of Tables

2.1.	Observed and predicted fractions of all 4 endmembers with $g=2$ and $g=4$, coefficient of determination R^2 for each component and MSE of these predictions.	39
3.1.	Calculated performance indicators for the Channel A = Channel B case.	102
3.2.	Calculated performance indicators for the single point in time test.....	103
3.3.	Calculated performance indicators for the spatial scan test.....	104
4.1.	HIDE experiment results based on the data acquired with passive and active systems. The left column illustrates the average spectra of pure ice and ice with oil underneath. The right column illustrates the two sizes of training data and colour representation of the Support Vector Machine classification result.....	141
4.2.	Spectral response of highly reflective object (ceramic tile - region and graphs in red) and highly absorbing object (polyethylene bucket - region and graphs in green) imaged directly through 25 mm and 110 mm water layer.....	148
4.3.	Spectral response of highly reflective object (ceramic tile – red region and graphs) and highly absorbing object (polyethylene bucket – green region and graphs) imaged directly and through 40 mm water layer. The spectra presented here are not corrected by any reference response. The seemingly significant spectral signatures acquired through the water layer are, in fact, only graphs of hardware determined baseline.....	149
4.4.	Test schedule of two data acquisition runs of first full scale test.....	155
4.5.	Colour coding and averaged spectral response of 3cm, 7cm and 11cm ice layers without and with oil injections underneath, in Near-IR and Mid-IR spectral region, extracted from the data acquired with active system. Dotted ellipses highlight spectral features of interest for oil under ice identification.	161
4.6.	Data acquired from the 3cm ice layer test for all the oil injection conditions: (a) the underwater images of the oil distribution, (b) single band intensity images (at 1500nm) of all the test cases with indication of the regions used for training data, (c) graphical representation of the SVM based classification results.....	163
4.7.	Experimental procedure of small sample test.....	165
4.8.	Average spectra of the ice samples imaged in two conditions (as grown and floating on water) in both available spectral bands – Near-IR and Mid-IR. The legend of each graph demonstrates the relation between the colour coding and the freezing time of each ice block.....	167

4.9.	Average spectra of the ice sample floating on water with the data extracted from the original surface (red line) as well as the one changed upon overflowing and freezing of water (blue line).....	168
4.10.	Comparison of the Near-IR and Mid-IR average spectra of the ice block fixed in the bucket “as grown” (blue line), “floating on water” (red line) and the one after oil injection (yellow line).....	170
4.11.	Test plan of the second full scale imaging session. The numbers in the table indicate the sequence of data acquisition per each condition.....	171
4.12.	Average spectra in the Near-IR and Mid-IR range comparing all the ice handling cases for each ambient temperature range. The spectra in red colour represent the pure ice in “as grown” condition, the spectra in green are extracted from free floating ice and the ones in blue represent oil under ice condition.....	173
4.13.	Average spectra in the Near-IR and Mid-IR range comparing all the different ambient temperature variations for each ice condition. The spectra in red colour represent the -10°C to -7°C range, in green represent the -7°C to -4°C range and the ones in blue represent the -3°C to +1°C range.....	174
4.14.	Comparison of the Near-IR and Mid-IR average spectra of the three conditions: oil mixed with water and slush (blue line), oil on top of ice (green line) and oil underneath ice (red line).....	177
4.15.	Comparison of the Near-IR and Mid-IR average spectra of the four targets located under the ice: the three aluminium blocks with the ice column between them and the surface being 15mm - represented by yellow line, 65mm - blue line, 90mm - red line and the bottom of the bucket with 120mm ice column - green line.....	181
4.16.	Average spectra in the Near-IR and Mid-IR range comparing all spectral responses of the three ice growths in three different conditions: ice before the impact, as grown (blue line), just after the impact (red line) and after re-freezing (yellow line). The re-freezing condition was not acquired for the first ice growth.....	185
4.17.	Microscopic images of the ice surface from two ice samples before and after the mechanical impact taken.....	186
5.1.	Designs of the pump (upper) and signal (lower) cavities. In the latter, the waist between lens L2 and the end mirror M2 is to place the spectrophone. The collimated area in between L1 and L2 is evident. Main parameters of used components are indicated in the description, where: λ – resonant wavelength; M1, M2, M3 - end mirrors of created cavities; QS – Q-Switch (Acousto-optic modulator); IC-L, L1, L2 – intracavity lenses; BS – beam splitter; PPLN – nonlinear PPLN crystal.	198
5.2.	Changed design of the signal cavity allowing sufficient space in the collimated section for multiple etalons.....	204

5.3.	Summary of the predicted improvements, along with quantification of their magnitude; the sensitivity developed in this project is used as a base line to these projections (* - selected NH ₃ absorption lines).....	238
6.1.	Summary of the predicted improvements, along with quantification of their magnitude; the sensitivity demonstrated during described project is used as a base line to these projections (* - selected NH ₃ absorption lines).....	255

Nomenclature

Roman Symbols

b	scalar used for defining a line in 2-dimensional space
\mathbf{B}	PLS-regression coefficient
BS	beam splitter
c	speed of light
C	instrumental constant of PAS spectrophone
C_p	heat capacity
\mathbf{C}	matrix of weights computed by PLS algorithm for matrix of responses
\mathbf{C}'	transposed matrix of weights \mathbf{C}
d	diameter
D	data set
\mathbf{E}	matrix of residuals computed by PLS algorithm for matrix of predictors
f	frequency
f_c	characteristic resonance frequency
\mathbf{F}	matrix of residuals representing deviations between observed and modelled responses
g	number of latent structures derived by the PLS model
\mathbf{G}	matrix of residuals computed by PLS algorithm for matrix of responses
h	Planck's constant
I_D	dark reference image
I_N	improvement in the noise level
I_R	relative reflectance image
I_{SNR}	improvement in the signal-to-noise ratio
I_W	white reference image
I_0	raw reflectance image
k_p	wave vector magnitude of pump wave
k_s	wave vector magnitude of signal wave
k_i	wave vector magnitude of idler wave
K	dimension of a space

l	length
L	lens
M	number of components in response matrix
$M1, M2, M3$	mirrors
n	refractive index
n_1	refractive index of medium 1
n_2	refractive index of medium 2
n_p	refractive index of pump wave within the nonlinear medium
n_s	refractive index of signal wave within the nonlinear medium
n_i	refractive index of idler wave within the nonlinear medium
N	number of components / observations
N_L	noise level
N_{orig}	noise level of original image
N_{norm}	noise level of normalised image
P	power
P_{DC}	power of down-converted field
$P_{DC_{max}}$	maximum total down-converted power
$P_{idler_{ex}}$	power of idler field extracted outside of the OPO cavity
P_{in}	primary input power
$P_{out_{max}}^L$	maximum obtainable output power from the pump laser
P_{th}^L	pump power at laser threshold
P_{th}^{OPO}	pump power at OPO threshold
P_s	power of signal field
\mathbf{P}	matrix of loadings computed by PLS algorithm for matrix of predictors
\mathbf{P}'	transposed matrix of loadings \mathbf{P}
Q	quality factor
r	radius
R	reflectance
R^K	Real number in K-dimensional space
R^2	Coefficient of determination
s_m	scale of mother wavelet function
S	signal from photoacoustic spectrophone

SNR_{orig}	signal-to-noise ratio of original image
SNR_{norm}	signal-to-noise ratio of normalised image
t	time
T	temperature
\mathbf{T}	matrix of X-scores computed by PLS algorithm
\mathbf{U}	matrix of Y-scores computed by PLS algorithm
\vec{w}	weight vector used for defining a line in 2-dimensional space
$\ \vec{w}\ $	the norm of the weight vector \vec{w}
\mathbf{W}	matrix of weights computed by PLS algorithm for matrix of predictors
\mathbf{W}^*	matrix of weights \mathbf{W} transformed to be independent between components
$w(t)$	window function
\vec{x}	Vector in 2-dimensional space
\mathbf{X}	matrix of predictors
\mathbf{X}_2	matrix of predictors after first deflation
\mathbf{X}_g	matrix of predictors residuals after g deflation
$x(t)$	signal in time domain.
$X(f)$	signal in frequency domain
\mathbf{Y}	matrix of responses
\mathbf{Y}_2	matrix of responses after first deflation
\mathbf{Y}_g	matrix of responses residuals after g deflation
z	distance

Greek Symbols

α	molecular absorption coefficient
β_s	signal cavity round-trip loss
γ	margin between support vectors and a hyperplane
γ_h	specific heat ratio
Δk	wave vector mismatch
Δf	full width at half maximum bandwidth of the damped resonator
$\Delta\lambda_s$	phase matching range for signal wave
$\Delta\lambda_i$	phase matching range for idler wave
A	polling period
η_{abs}	amount of this pump power that is absorbed by parent laser gain medium
η_{in}	optical coupling efficiency of the primary pump laser at λ_{p-in} to the parent laser gain medium
κ	thermal conductivity
λ	wavelength
λ_s	wavelength of the signal wave
λ_p	wavelength of the parent pump laser
λ_{p-in}	wavelength of the primary pump source
λ_i	wavelength of the idler wave
μ	dynamic viscosity
ν_i	energy of idler photon
ν_p	energy of pump photon
ν_s	energy of signal photon
ρ	gas density
σ	standard deviation
σ_{max}	output slope efficiency of the pump laser
σ_s	speckle size
τ	translation of mother wavelet function
$\psi(t)$	mother wavelet function,

Acronyms / Abbreviations

ADM	Acoustic Detection Module
AM	Amplitude Modulation
ANN	Artificial Neural Networks
AOM	Acousto-Optic Modulator
AR	Anti-Reflective
ASE	Air Spaced Etalon
CNN	Convolutional Neural Networks
COTS	Commercial Off-The-Shelf
CPU	Central Processing Unit
CW	Continuous Wave
DFB	Distributed Feedback
DFG	Difference-Frequency Generation
DFT	Discrete Fourier Transform
DModX	Distance to the model in X-space
DRO	Doubly Resonant Oscillator
DTC	Decision Tree Classifier
EC	Extra-cavity
EC-OPO	Extra-Cavity Optical Parametric Oscillator
EC-SRO	Extra-Cavity Singly Resonant Oscillator
FCAP	Fraunhofer Centre of Applied Photonics
FFT	Fast Fourier Transform
FM	Frequency Modulation
FoV	Field of View
FPA	Focal-Plane Array
FPGA	Field-Programmable Gate Array
FSR	Free Spectral Range
FTIR	Fourier Transform Infrared
FWHM	Full Width at Half Maximum
GHz	giga Hertz
GIS	Geographical Information Systems
GRIN	Graded-Index

GUI	Graphical User Interface
HeNe	Helium-Neon
HSI	Hyperspectral Imaging
HR	Highly-Reflecting
IC	Intracavity
ICA	Independent Component Analysis
ICL	Interband Cascade Laser
IC-OPO	Intracavity Optical Parametric Oscillators
IC-SRO	Intracavity Singly Resonant Oscillator
IR	Infrared
ITOPF	International Tanker Owners Pollution Federation Limited
JSON	JavaScript Object Notation
kHz	kilo Hertz
LED	Light-Emitting Diode
LIA	Lock-in Amplifier
MEMS	Micro-Electrical-Mechanical Systems
MHz	Mega Hertz
MKL	Multiple Kernel Learning
MLA	Maximum Likelihood Algorithm
MLR	Multiple Linear Regression
MNF	Maximum Noise Fraction
MS	Mega Sample
MSE	Means Square Error
mW	Milliwatt
MWR	Microwave Radiometers
NesCOPO	Nested Cavity Optical Parametric Oscillator
NIR	Near Infrared
nm	Nanometer
OPA	Optical Parametric Amplifier
OPG	Optical Parametric Generator
OPO	Optical Parametric Oscillators
PAS	Photoacoustic Spectroscopy

PCA	Principal Component Analysis
PCB	Printed Circuit Board
PCR	Principal Component Regression
PEEK	Polyether Ether Ketone
PE-SRO	Pump Enhanced Singly Resonant Oscillator
PLS	Partial Least Squares
PLS-R	Partial Least Squares Regression
PPLN	Periodically-Polled Lithium Niobate
ppm	parts-per-million
ppq	parts-per-quadrillion
PRESS	Predictive REsidual Sum of Squares or PRediction Error Sum of Squares
psu	Practical Salinity Unit
QCL	Quantum Cascade Laser
QE-PAS	Quartz-Enhanced Photoacoustic Spectroscopy
QTF	Quartz Tuning Fork
R&D	Research and Development
RF	Radio Frequency
ROC	Receiver Operating Characteristic
ROI	Regions of Interest
s	Second
SAMS	Scottish Association for Marine Science
SAR	Synthetic Aperture Radar
SEM-EDX	Scanning Electron Microscopy-Energy Dispersive X-ray Spectrometry
SHG	Second Harmonic Generation
SNR	Signal-to-Noise Ratio
SRO	Singly Resonant Oscillator
STFT	Short-time Fourier transform
SURF	Speeded-Up Robust Features
SVM	Support Vector Machine
TDLS	Tunable Diode Laser Spectroscopy
TTL	Transistor-Transistor Logic
Vis	Visible spectral range

VOC	Volatile Organic Compounds
W	Watt
WBC	Wavelength Beam Combining
WM	Wavelength Modulation
WT	Wavelets Transform

Chapter 1: Introduction

1.1. Introduction

Technological progress undertaken in recent years has enabled access to vast amounts of information, about virtually any aspect of human life. From exploration of space and testing mega-objects like stars and planets to identification of micro-organisms and nano-particles within humans' bodies – people seek the answers for new questions every day. Among such fields of science, spectroscopy is a very potent one that provides information-rich data sets. With variety of its modalities, spectroscopic tools can be classified into many categories and one of these is based on the location of the detector and operator. The main two groups that can be distinguished are point (or in-situ) and standoff (or remote) spectroscopy [1]. Although remote and standoff are often considered interchangeably, additional differentiation can be also made between these two. In remote sensing the operator is always in a distance from tested object, however the detector may be close to the inspected scene. On the other hand, standoff type of testing describes situation where operator and detector are both at certain distance from the object of interest [2]. Over years, the broad interest in remote sensing technology is facilitating the rapid development of various sensing equipment.

Whenever it is required to identify the existence of an object, define its composition or quality, spectroscopic devices are often the first to be chosen. However, rarely can problems be solved directly by acquisition of a spectrum. Very extensive data sets produced by these tools often require complex analyses to answer even the very basic questions. Until recently, only skilled scientists could perform analyses of spectral profiles, making the techniques very expensive and not easily accessible. This problem is dealt with by another extensively developing technological field – signal processing – which enables unprecedented access to the information stored in spectra. A synergy between the powerful data acquisition and automated algorithms transforming it into a problem-solving fact, enormously increase the potential applications for these techniques. The profusion of signal processing tools, beyond the pre-treatment of the raw data and dimensionality reduction, allows predicting a trend or composition of an object, tracking it and classifying among others. There are countless numbers of algorithms that are used in order to perform ever more complex operations. However, the effectiveness of these methods relies on the quality of the data they analyse and exactly the symbiosis between these, supported by the demand from extensive market of applications, drives the researchers in both these technology

fields to deliver innovative techniques and continuously expand their capabilities for various applications.

During the programme of this Engineering Doctorate this synergy was explored and the undertaken research focused on the development, improvement and use of spectroscopic techniques along with processing of the data they produce, including preparation of bespoke fit-for-purpose algorithms, satisfying the needs of specific applications.

1.2. Hyperspectral Imaging

Next to spectral data, spatial information about the observed scene is often extremely important factor in spectroscopy. Since the invention of practical photography in 1839 [3], the imaging techniques have undergone significant advance, that from daguerreotype through digital photography lead to the introduction of imaging spectroscopy. Development of hyperspectral sensors and software for analysis of the image data can be considered as the significant breakthrough in remote sensing [4].

The prefix 'hyper' in hyperspectral image stands for a large number of detected wavelength bands. To place hyperspectral technology in the range of imaging methods, one should consider different modes of data collection. Standard digital camera is able to capture brightness and single colour value per pixel. It carries no spectral information, and spectral resolution (if one tends to describe any for this type of camera) depends on the spectral response of the detector used in that camera [5]. Multispectral technology carries much more information than standard imaging. It contains a few to dozens of spectral bands, but is still characterised by low spectral resolution only. Although this technology is able to serve for object detection, its ability for material identification is very poor. At this point hyperspectral imaging (HSI) provides the next level of capabilities. With ability to capture hundreds up to thousands spectral bands, usually with high spectral resolution, it opens a new range of sensing and detection possibilities. Ultraspectral or even full spectrum imaging technologies are the topic of discussions and development. Although, as long as hyperspectral imaging cameras are commercially available, anything beyond that is currently available only on laboratory scale and full spectrum imaging is rather a theoretical consideration [6].

Historically, developed from the study of visible light dispersed by the prism across all its wavelengths (400-700nm) [5], spectroscopy has now expanded to any interaction of the electromagnetic radiation as a function of its frequency. Each material reacts differently with electromagnetic radiation on different wavelengths, which means that a portion of the radiation

at certain wavelength may be reflected by one object, while it may be absorbed by another. These patterns of reflectance and absorption across wavelengths can uniquely identify certain materials [4]. Combining the fact that reflectance spectrum can help exclusively recognise different objects with the ability of hyperspectral imaging collecting spatial data containing reflectance values over vast range of wavelengths, one can easily understand the goals of this imaging method. The main objective of hyperspectral imaging is the identification of materials or phenomena from their reflectance or emissivity spectra that leads to three major categories of its application: anomaly detection, target detection and material identification [7]. In order to achieve these goals one can distinguish a two-part process where the first step is the collection and possible correction of hyperspectral data followed by an application-dependant quantitative and qualitative analysis [6, 8, 9]. This second step allows providing specific information tailored to the particular application and instead of a huge amount of raw data, provides the potential go/no-go answers sought by the non-specialist users. Different image processing classification techniques facilitate these analyses and are discussed in Chapter 2.

Although the data produced by hyperspectral systems have always the same generic structure (three-dimensional record of spatial and spectral information), the devices capable of collecting them can have various forms. There are four common methods of the acquisition of a hyperspectral image: point scanning (whiskbroom), line scanning (pushbroom), area scanning (staring) and single shot (snapshot) [10, 11, 12, 13]. With the typical whiskbroom method, a single point of spatial data with the full spectral signature is recorded on a linear detector and full spatial information is obtained by a form of scanning across the observed scene. The pushbroom method utilises a focal-plane array (FPA) type of detector to record one line of spatial domain with full spectral signature for each pixel on an acquired line. For this method full hyperspectral data cube is obtained by introduction of relative movement between the object and detector, along the second spatial dimension. Staring method usually provides full 2D spatial information recorded on FPA and tuning across available frequencies of electromagnetic spectrum is necessary to reproduce spectral profile of the imaged scene. The snapshot technique does not require any scanning and both, full spectral and spatial information are recorded with single shot of the imaging system. Figure 1.1 provides illustration of these techniques and the data they produce. Although these four approaches capture the operation principle of most of the systems available on the market, there are also other sets that combine aspects of individual methods where, for example, the whiskbroom one can acquire single point at the time in both, spatial and spectral domain, then scanning across the observed scene and the wavelengths of electromagnetic spectrum are required to acquire full hyperspectral cube [14]. Although novel and unconventional hyperspectral imaging techniques are being constantly developed (examples in [15, 16, 17]), the data acquisition approaches always fall under these four presented or their combinations.

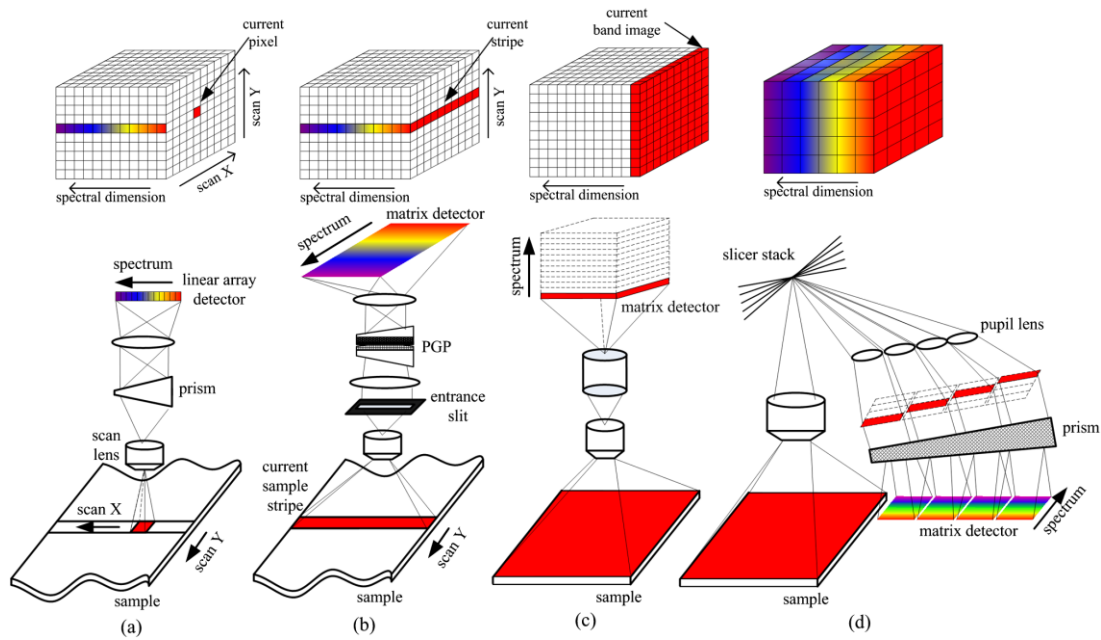


Figure 1.1. Typical spectral imaging approaches: (a) Whiskbroom; (b) Pushbroom; (c) Staring; (d) Snapshot; PGP stands for Prism-Grating-Prism arrangement. [11]

Another possible classification of hyperspectral devices can be created from distinguishing the source of the reflected radiation, dividing sensors into active and passive ones. This classification can have a twofold meaning. From one perspective the term active can indicate that the scene of interest has been actively illuminated by an artificial radiation source, while for passive systems the primary source of illumination is the Sun [9, 18]. The other way of approaching this classification, and that is the one taken in this dissertation, is the consideration whether the source of illuminating radiation is embedded in the imaging setup. In this understanding, active devices are only these that illuminate and image the scene of interest at the same time, while all the other systems (performing only data acquisition) are considered passive, despite the fact that the scene of interest may be illuminated from an artificial source.

Due to the fact that HSI is based on reflectance spectroscopy, the electromagnetic radiation (light, when operating in visible range of spectrum) is a key factor of an imaging system as it carries the information from the observed object to the detector [12]. As a result of the broadband nature of this imaging technology, an adequate illumination source is required and a number of most common sources, adequate for the HSI are available. The omnipresent broadband source is the Sun and although there is significant number of applications where solar illumination is exploited for HSI, it is difficult to accept in low visibility conditions or for indoor applications [19]. Incandescent lamps emit the radiation closest to the one of the Sun and are the most frequently used artificial illuminators for hyperspectral imaging. Within the group of

incandescent, the halogen lamps are mainly used, providing sufficient intensity and continuous spectrum over the visible and near-infrared bands [20, 12]. The spectral quality of light irradiated from light-emitting diodes (LEDs) is being improved with the progressing technology and these are becoming viable competitors for halogen lamps (especially in the visible range) [21, 12].

Alternative to the broadband are the narrow bandwidth tuneable sources. There are examples of work done on moving the dispersive elements from the imaging to the illumination path of the optical system [22, 12] however, in a background this still uses a broadband illuminator. Genuinely narrow bandwidth sources applicable for HSI are tuneable lasers. Laser absorption spectroscopy has gained already strong appreciation and enabled many new applications for spectroscopic testing [23, 24]. There is a selection of tuneable laser sources available on the market, covering the visible and near-infrared bands of the electromagnetic spectrum. Nevertheless, there is only a moderate number of spectroscopic sources with emission beyond the near-infrared range. From the point of view of spectroscopy, mid-infrared (mid-IR) is a very valuable range of electromagnetic spectrum but is poorly served by “classic” laser sources. It contains the key absorption features of the majority of hydrocarbons, which by their extensive applications are very significant group of materials. In line with broad applications of hydrocarbons there is a high interest in the detection and identification of these materials. Applications of hyperspectral imaging in mid-infrared range include chemical agent detection, explosives detection, biomedical imaging and forensics [18]. An introduction to tuneable lasers, with a focus on their operation in mid-IR regime is presented in Section 1.3.

1.3. Mid-infrared tuneable lasers

Radiation emitted by lasers has a set of very specific characteristics, differentiating them from other radiation sources. The key features that define all lasers are high spectral purity, directionality with minimal divergence, potentially immense coherence length and very high brightness [25]. Some types of laser systems provide also tunability of emitted radiation and this, together with the aforementioned proprieties, make them an excellent choice for spectroscopic applications. The first developed broadly tuneable sources of coherent radiation were dye lasers, with tuning range reaching from near ultraviolet to near-infrared (320–1200nm) [26]. Later developments brought transition metal solid-state lasers, such as very popular arrangements of titanium-sapphire laser ($\text{Ti}^{3+}:\text{Al}_2\text{O}_3$) with spectral coverage ranging from red end of visible spectrum to the near-infrared (660-986nm) [27] and alexandrite laser ($\text{Cr}^{3+}:\text{BeAl}_2\text{O}_4$) with less extensive, however still impressive tuning range in near-IR (701-818nm) [28]. Over the years, scientists developed a selection of tunable lasers, spectrally ranging from UV to near-IR. These include more examples of transition metal solid-state lasers, tuneable excimer lasers, laser

oscillators with intracavity dispersion and semiconductor lasers in external-cavity configuration [29, 23]. Nevertheless, there is only a modest selection of laser sources working in the mid-infrared bandwidth.

Among few available technologies, historically very important are the carbon dioxide (CO₂) isotope lasers. These, over the configurations of various isotopes, sparsely cover very important spectral regime between 9 and 12 μ m [29, 30]. Other significant line tuneable gas lasers are carbon monoxide (CO) with lines in the region of 5.1-5.6 μ m, hydrogen fluoride (HF) and deuterium fluoride (DF) lasers with lines ranging from 2.8 μ m up to 4 μ m [23]. Although these lasers can produce very high powers and have found a multitude of applications, their form factor of bulky gas laser limits their spectroscopic applications to lab-based systems. Other technologies that could be considered as potential spectroscopic laser sources in this spectral regime are Lead Salt Diode Lasers, Quantum and Interband Cascade Lasers as well as Optical Parametric Oscillators.

Lead Salt Diode lasers offer mid-infrared radiation in impressive 3-30 μ m regime. Although lead salt diode-based mid-infrared spectrometers have been demonstrated [31, 23], these lasers require cryogenic cooling to achieve population inversion. Additionally, they exhibit very poor spatial mode quality along with low output powers (typically 100-500 μ W). Additionally, the tuning range of lead salt diodes is dictated by the band-gap within the semiconductor material and is therefore restricted to tens of nanometres. All these properties counterweight the extensive tuning range and limit the applications of the above-mentioned sources [24, 23].

Quantum Cascade Lasers (QCLs) and Interband Cascade Lasers (ICLs) have undergone by far the greatest research effort in the pursuit for a mid-infrared spectroscopic radiation source. In recent years rapid progress has been made in this area [32]. External-cavity QCLs and ICLs are nowadays commercially available and cover the entire mid-infrared region, and are able to tune across a range greater than 100 cm⁻¹ of optical bandwidth within tens of milliseconds. Due to the fact that some applications require even faster tuning, further research led to the development of multi-wavelength QCL arrays [33, 18, 34, 35]. Although these arrangements usually cannot compete with external-cavity configuration with respect to spectral resolution, they possess a set of other advantages which include: (1) extremely high-speed electronic tuning, (2) higher average power by driving multiple lasers either simultaneously or in an interleaved fashion as well as (3) compact and rugged designs with no moving parts. Additionally, the application of wavelength beam combining (WBC) methods to QCL arrays, allows the beams from each laser in the array to be spatially overlapped to interrogate a common target [18, 33]. These sources have been demonstrated in use for hyperspectral imaging [18, 36] and are gaining more and more interest, but this text does not focus on them.

Optical parametric oscillators (OPO) provide a flexible source of tuneable coherent radiation, particularly in the mid-infrared spectral region [14, 29]. Next to the difference-frequency generation (DFG), OPOs belong to the group of techniques based on nonlinear optical frequency conversion, expanding the frequency range of robust visible and near-infrared lasers to the mid-IR [23, 24]. After its development over the last few decades, Optical Parametric Oscillators have gained recognition as very powerful tool for spectral data acquisition [24]. Among several types of OPOs, the intracavity configuration (IC-OPO) enabled significant miniaturisation of these systems and allowed their exploitation outside of the research labs. Since the IC-OPO is the heart of the optical systems in all the projects presented in this portfolio, the technology is described in greater detail in Chapter 2.

1.4. Thesis overview

This EngD doctoral thesis introduces investigations done during three projects: the first two (described in Chapter 3 and 4) were focused on exploring potential applications for an active hyperspectral imager and the third one (presented in Chapter 5) on the development of a novel spectroscopic solution. The common factor for all these studies was the use of an Intracavity Optical Parametric Oscillator (IC-OPO) at the heart of the hardware setups and (especially for first two projects) various signal processing algorithms applied to the data produced by these systems. Due to the fact that all the projects from this portfolio are associated with different applications and technologies, the literature review for each of them is provided in project background sections at the beginning of each experimental chapter – sections 3.1, 4.1 and 5.1 respectively. All of the work done during this programme was executed under commercial projects with well-defined scope and timeline. On account of this approach, some of the presented results may be inconclusive or the work may appear unfinished, however the presented outcomes reflect the work performed under the structure of these projects and when appropriate, follow up activities were recommended.

A theoretical background of the two crucial aspects of this programme, signal processing and OPO's, is presented in Chapter 2. Out of the vast suite of signal processing tools, the classification algorithms were selected as the most relevant to the work described. Initially the generalised structure of the classification process is presented, introducing all the steps necessary for successful implementation of the algorithms. Subsequently, a survey of available techniques is described, followed by a detailed introduction to two algorithms – Support Vector Machine (SVM) and Partial Least Squares (PLS) – along with an example application of these tools demonstrating data analysis and information extraction. The second part of Chapter 2 provides an introduction to the Optical Parametric Oscillators. The main focus of this section is directed on the intracavity

configuration of OPOs and properties of this specific formation are detailed. This chapter is finished by introduction of OPO as an illumination source in the imaging arrangement creating an active, laser-based, mid-infrared hyperspectral imager.

The following part, Chapter 3, introduces the work performed during the project INHERIt: Intelligent Hyperspectral Imaging. This is the first, out of the two projects, exploring use of an active, mid-IR HSI for an application never attempted before with such a system. This work studied the use of hyperspectral imaging technologies, combined with advanced signal processing techniques, for the automatic recognition of counterfeit paintings. Since this was the first time when data collected by this system was a subject of automatic statistical analysis, new image acquisition mode had to be developed to deliver sufficient quality data sets. All the artefacts induced by the physical properties of the laser-based imaging arrangement were carefully considered and, where possible, mitigation techniques provided. The performance of this device for paint recognition is demonstrated and compared with a conventional, commercial off-the-shelf (COTS) HSI imaging system operating in the near-infrared spectral region (900nm – 1700nm). Both, bespoke paintings created for this work as well as actual forged paintings were analysed with these tools and, by successful identification of an anachronistic paint used in the examined artwork, they demonstrated the potency of the HSI empowered by the algorithms developed for the pigment classification.

The second project investigated a new area of application for the active, mid-IR imager - the Rosdam (Remote Oil Spill Detection And Monitoring on ice-covered waters) project – is presented in Chapter 4. As indicated in its name, this study was focused on the verification whether infrared hyperspectral technology is able to detect oil spilt underneath the analysed ice. During this project the mid-IR imager was again used in parallel with a conventional NIR hyperspectral camera to test and compare the performance of both techniques. This work was initiated upon completion of a short study that demonstrated promising results for both devices used in this application. These preliminary findings were based on data from a single sample and acquired in non-optimal testing conditions. Therefore, this research project was dedicated to execute a detailed test matrix, exploring various thickness of ice and oil layers, with special attention to the test conditions. Within this chapter all the experiments and their findings are presented in chronological order, revealing the final conclusion that none of the tested devices could inform on the presence of oil beneath ice. This chapter presents a series of challenges that were overcome in order to execute this project. It also highlights the pitfalls and lessons learned, providing thorough documentation of the work.

The final experimental part – Chapter 5 – diverges from the exploration of HSI applications to the presentation of a project focused on the development of new spectroscopic

system. Although initiated with a specific application in mind – explosives detection – this technique could be used for any task requiring ultra-sensitive gas detection. This performance was achieved by successful combination of the Photoacoustic Spectroscopy (PAS) functioning inside the resonating cavity of the intracavity OPO. Exploitation of the very high circulating field, present in the down-converted cavity of the OPO setup, as an excitation source for the photoacoustic effect leads to a significant improvement in optical excitation power, when compared with the conventional extra-cavity approach. This chapter presents the development and characterisation of the optical system as well as the miniature photoacoustic spectrophone. It describes the process of integration of these two technologies and the steps undertaken to demonstrate the sensitivity of single parts-per-billion of ammonia (NH_3) as a target molecule. Additionally, the wide selectivity given by the inherent broad tunability and narrow optical linewidth of an OPO was demonstrated by acquisition of molecular spectral profiles of ammonia and water vapour. This successful proof-of-concept project helped to verify the impact of excitation power on the sensitivity of photoacoustic signal. This chapter presents a discussion on how this technology could be readily refined to potentially demonstrate a sensitivity of 10's parts-per-quadrillion (ppq). Improvement of the most prominent factor affecting the signal – quality factor of the PAS spectrophone - was also attempted during this study by exploration of the quartz enhanced realisation of PAS, however this was not finalised within the timeframe of the project.

The last chapter of this dissertation – Chapter 6 – provides overall conclusions on the programme as well as all the projects from presented portfolio. Additionally, possible future research opportunities are discussed in the context of the results obtained over the course of this study.

References

- [1] National Research Council, *Sensor Systems for Biological Agent Attacks: Protecting Buildings and Military Bases.*, Washington, DC: The National Academies Press., 2005.
- [2] C. W. V. Neste, L. R. Senesac and T. Thundat, “Standoff photoacoustic spectroscopy,” *Applied Physics Letters*, vol. 92, pp. 1-3, 2008.
- [3] R. Hirsch, *Seizing the Light: A History of Photography*, New York: McGraw-Hill, 2000.
- [4] P. Shippert, “Introduction to Hyperspectral Image Analysis,” *Online Journal of Space Communication*, no. 3, pp. 1-13, 2003.

- [5] G. ElMasry and D.-W. Sun, "Principles of Hyperspectral Imaging Technology," in *Hyperspectral Imaging for Food Quality Analysis and Control*, London, Elsevier Inc., 2010, pp. 32-36.
- [6] J. R. Gilchrist, "Hyperspectral Imaging across the spectrum," in *UKIVA Vision in Action*, 2013.
- [7] D. Manolakis, R. Lockwood and T. Cooley, *Hyperspectral Imaging Remote Sensing: Physics, Sensors, and Algorithms*, University Cambridge Press, 2016.
- [8] H. Yao and D. Lewis, "Spectral Preprocessing and Calibration Techniques," in *Hyperspectral Imaging for Food Quality Analysis and Control*, London, Elsevier, 2010, pp. 45-78.
- [9] D. Manolakis, D. Marden and G. A. Shaw, "Hyperspectral Image Processing for Automatic Target Detection Applications," *Lincoln Laboratory Journal*, vol. 14, no. 1, pp. 79-116, 2003.
- [10] H. F. Grahn and P. Geladi, *Techniques and Applications of Hyperspectral Image Analysis*, John Wiley & Sons Ltd, 2007.
- [11] Q. Li, X. He, Y. Wang, H. Liu, D. Xu and F. Guo, "Review of spectral imaging technology in biomedical engineering: achievements and challenges," *Journal of Biomedical Optics*, vol. 18, no. 10, pp. 1-28, 2013.
- [12] J. Qin, "Hyperspectral Imaging Instruments," in *Hyperspectral Imaging for Food Quality Analysis and Control*, London, Elsevier, 2010, pp. 129-172.
- [13] National Center For Geospatial Intelligence Standards, "Pushbroom/Whiskbroom Sensor Model, Metadata Profile Supporting Precise Geopositioning," National Geospatial Intelligence Agency, 2009.
- [14] D. J. M. Stothard, M. H. Dunn and C. F. Rae, "Hyperspectral imaging of gases with a continuous-wave pump-enhanced optical parametric oscillator," *Optics Express*, vol. 12, no. 5, pp. 947-955, 2004.
- [15] R. French, S. Gigan and O. L. Muskens, "Speckle-based hyperspectral imaging combining multiple scattering and compressive sensing in nanowire mats," *Optics Letters*, vol. 42, no. 9, pp. 1820-1823, 2017.
- [16] B. W. Smith and J. M. Harlander, "Imaging spatial heterodyne spectroscopy: theory and practice," in *Proc. SPIE 3698, Infrared Technology and Applications XXV*, Orlando, 199.
- [17] R. Braun, J. Eichmann, S. Sabbah, R. Harig and C. R. Howle, "Remote Detection of Liquid Surface Contamination by Imaging Infrared Spectroscopy: Measurements and Modelling," in *Proceedings of SPIE - The International Society for Optical Engineering*, 2011.
- [18] A. Goyal, T. Myers, C. A. Wang, M. Kelly, B. Tyrrell, B. Gokden, A. Sanchez, G. Turner and F. Capasso, "Active hyperspectral imaging using a quantum cascade laser (QCL) array and digital-pixel focal plane array (DFPA) camera," *OPTICS EXPRESS*, vol. 22, no. 12, pp. 1-10, 2014.

- [19] M. Nischan, R. Joseph, J. Libby and J. Kerekes, "Active Spectral Imaging," *LINCOLN LABORATORY JOURNAL*, vol. 14, no. 1, pp. 131-144, 2003.
- [20] M. W. Davidson, "Tungsten-Halogen Incandescent Lamps," ZEISS, [Online]. Available: <http://zeiss-campus.magnet.fsu.edu/articles/lightsources/tungstenhalogen.html>. [Accessed 15 January 2016].
- [21] M. W. Davidson, "Fundamentals of LightEmitting Diodes (LEDs)," ZEISS, [Online]. Available: <http://zeiss-campus.magnet.fsu.edu/articles/lightsources/leds.html>. [Accessed 03 06 2018].
- [22] M. E. Klein, B. J. Aalderink, R. Padoan, G. de Bruin and T. A. G. & Steemers, "Quantitative hyperspectral reflectance imaging," *Sensors*, vol. 8, no. 9, p. 5576–5618, 2008.
- [23] R. F. Curl and F. K. Tittel, "Tunable infrared laser spectroscopy," *Annu. Rep. Prog. Chem., Sect. C: Phys. Chem.*, vol. 98, pp. 219-272, 2002.
- [24] F. Tittel, D. Richter and A. Fried, "Mid-Infrared Laser Applications in Spectroscopy," in *Solid-State Mid-Infrared Laser Sources. Topics in Applied Physics*, Berlin, Heidelberg, Springer, 2003, pp. 458-529.
- [25] S. M. Naidu, *Engineering Physics*, Pearson India, 2009.
- [26] F. Duarte and L. Hillman, *Dye Laser Principles*, Academic Press, 1990.
- [27] P. F. Moulton, "Spectroscopic and laser characteristics of Ti:Al₂O₃," *Journal of the Optical Society of America B*, vol. 3, no. 1, pp. 125-133, 1986.
- [28] J. Walling, O. Peterson, H. Jenssen, R. Morris and E. O'Dell, "Tunable alexandrite lasers," *IEEE Journal of Quantum Electronics*, vol. 16, no. 12, pp. 1302 - 1315, 1980.
- [29] F. Duarte, *Tunable Lasers Handbook*, Academic Press, 1995.
- [30] O. Pfister, F. Guernet, G. Charton, C. Chardonnet, F. Herlemont and J. Legrand, "CO₂-laser sideband spectroscopy at ultrahigh resolution," *Journal of the Optical Society of America B*, vol. 10, no. 9, pp. 1521-1525, 1993.
- [31] H. Preier, Z. Feit, J. Fuchs, D. Kostyk, W. Jalenak and J. Sproul, "Status of lead-salt diode laser development at spectra-physics," in *Monitoring of Gaseous Pollutants by Tunable Diode Lasers*, Freiburg, 1988.
- [32] M. S. Vitiello, G. Scalari, B. Williams and P. D. Natale, "Quantum cascade lasers: 20 years of challenges," *Optics Express*, vol. 23, no. 4, pp. 5167-5182, 2015.
- [33] M. F. Witinski, "Standoff detection of explosives, CWAs, and industrial chemicals using quantum cascade laser arrays (Conference Presentation)," in *Proc. SPIE 10639, Micro- and Nanotechnology Sensors, Systems, and Applications X*, Orlando, 2018.
- [34] B. G. Lee, M. A. Belkin, C. Pflugl, L. Diehl, H. A. Zhang, R. M. Audet, J. MacArthur, D. P. Bour, S. W. Corzine, G. E. Hufner and F. Capasso, "DFB quantum cascade laser arrays," *IEEE Journal of Quantum Electronics*, vol. 45, no. 5, p. 554–565, 2009.

- [35] P. Rauter, S. Menzel, B. Gokden, A. K. Goyal, C. A. Wang, A. Sanchez, G. Turner and F. Capasso, "Single-mode tapered quantum cascade lasers," *Applied Physics Letters*, vol. 102, p. 181102, 2013.
- [36] C. Carson, J. Macarthur, M. Warden, D. Stothard, L. Butschek, S. Hugger, J.-P. Jarvis, M. Haertelt, R. Ostendorf, A. Merten, M. Schwarzenberg, J. Grahmann and M. Ratajczyk, "Towards a compact, portable, handheld device for contactless real-time standoff detection of hazardous substances," in *Proc. SPIE 10624, Infrared Technology and Applications XLIV*, Orlando, 2018.

Chapter 2: Theoretical Background

2.1. Introduction

In this chapter, the discussion on the two scientific topics that constitute the common factor among the projects from the dissertation is presented. The first described aspect is the signal processing techniques applicable for spectroscopic data, with special focus placed on the tools for classification. Initially the generic process of data treatment and algorithm implementation is introduced, followed by the survey of classification techniques, introducing various groups under which these algorithms can be categorised. Subsequently, two signal processing tools are presented in detail, demonstrating the underlying concept, the process of algorithm implementation and finally, the results analysis and demonstration. The first one is the Support Vector Machine (SVM) applied as a texture classification tool of intensity (grayscale) images. The second introduced algorithm is the Partial Least Squares (PLS) in the regression configuration (PLS-R) performing spectral unmixing (decomposition of a mixed spectra into individual components – endmembers) on the simulated data from various types of tea leaves.

The second aspect introduced in this chapter reveals a photonic arrangement called Optical Parametric Oscillator (OPO). This section expands on the information provided in Chapter 1, where tuneable laser sources were introduced. In this section the principle of operation is described. The debate on various configurations of OPOs is shown, with a focus on the intracavity configuration (IC-OPO). Lastly, the concept of a laser-based imaging arrangement is described, with the example of IC-OPO as the illumination source. This last part provides a link between pure laser physics and signal processing, demonstrating an arrangement of active, laser-based, mid-infrared hyperspectral imager.

2.2. Signal Processing

Signal processing is a very wide technological field that includes data acquisition and pre-treatment, but predominantly its analysis and extraction of user sought results. It may be targeted for data captured in time, frequency or spatial domain. Without preference for any type of data-recording sensor, similar algorithms can be applied to various technologies. In the case of imaging, analogous tools can be applied for analysis of images from digital photography, biological imaging,

remote sensing and many others. In this section the focus will be placed on the tools for classification techniques.

2.2.1. Classification process

Classification of the data represented by the image is used to assign equivalent levels with respect to groups with similar characteristics, aiming to discern different objects presented within this image from each other. Classification is usually based on spectral or spatial features, as for instance density or texture, within their space. One can say that classification divides the feature space into a certain number of classes - mentioned levels of groups with similar characteristics – based on certain decision rule [1].

A classification between two objects is often an easy task for the human brain, but it is a complex problem for machines. The computational classification process typically consists of few steps as presented in Figure 2.1.

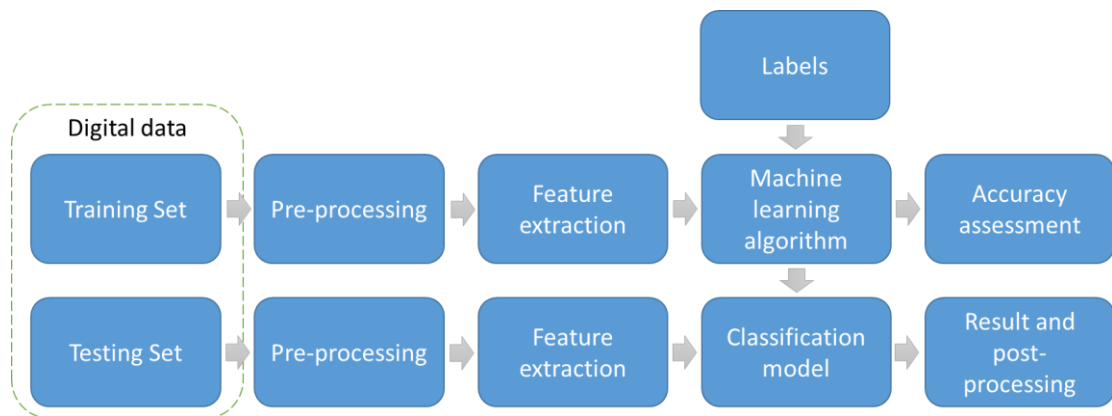


Figure 2.1. Steps for supervised image classification.

In subsequent sections a more detail introduction to this process will be provided based on the example of specific classification methods, but first the generic principles of each individual step are discussed.

A. Digital data – training and testing sets – and labels

An image can be processed by optical, photographic or electronic means, but the most common and at the same time the fastest and most flexible method is processing with the use of digital computers [2], therefore this text will focus only on digitally collected data.

When certain information is sought based on remotely sensed data, it should be considered that different sensors can vary in spatial, radiometric, spectral and temporal resolutions as well as various other parameters. Understanding the characteristics of different types of sensors

is critical for the selection of suitable remotely sensed data for image classification. In some cases, it may be appropriate to consider the use of supplementary sensors to compensate for the lack of some data provided by the main source. For example, consideration of the use of thermal imaging as a supplementing technology for visible cameras while analysing heat emitting objects may be required, or in different example, use of Radar technology should be complementing the optical detectors, when cloudy weather or other atmospheric conditions are an obstacle for good quality data [3].

A substantial part of this thesis consists of the discussion on hyperspectral imaging. For each potential application it is necessary to know if the use of hyperspectral equipment is beneficial for a specific task. Furthermore, it is still required to identify which spectral bandwidth should be useful to provide expected information, what kind of data collection technique is suitable for specific application or what spatial resolution of resulting image will provide sufficient detail of the scene. Acquisition of adequate data is essential for further analysis.

While the testing set is the data captured for study of specific problem, training set is required to build the classification model. A suitable classification system and a sufficient number of representative training samples are fundamental for a successful process [4]. Training data should be sampled in order to determine proper decision rules. When the study area captured on the image is complex and heterogeneous, selecting sufficient training samples becomes difficult. This task becomes even more complicated when medium or coarse spatial resolution data are used for classification. It is caused by large volume of mixed pixels which may occur on the image, making it difficult to assign one specific class (label) to this area. Due to this reason, while selecting training set, it is necessary to consider the spatial resolution of the remote sensed data of interest, availability of ground truth reference data and the complexity of the scene in the studied area [1, 3]. Labels are known or user-defined categories, assigned to every observation in the training set, used to build the classification model.

B. Pre-processing

Methods of data pre-processing depend highly on the type of sensors used for the acquisition, imaged scene and type of tools employed in further steps of classification. The typical examples of pre-processing operations may include the detection and restoration of bad (poor quality) lines (or pixels – depending on the acquisition mode), wavelength and radiometric calibration as well as atmospheric correction. Within pre-processing of the image, various noise reduction techniques or filters eliminating intensity gradients caused by uneven illumination can be applied. For a variety of data processing tools, it is vital to normalise acquired figures, especially when various packages of data come from different sensors and may be expressed with numerous units [2, 3, 5].

C. Feature extraction

Selection of suitable variables is a critical step for successful classification. Many potential values may be used for this task, including spectral signatures, transformed images, textural and contextual information and many others [6]. It is important to select only the features that are most useful for specific classes, especially when hyperspectral or multisource data are employed, because use of too many variables in a classification procedure may decrease classification accuracy [3, 7]. In order to reduce data redundancy, many approaches, such as principal component analysis, minimum noise fraction transform, discriminant analysis, decision boundary feature extraction, non-parametric weighted feature extraction, wavelet transform and spectral mixture analysis may be used for data dimensionality reduction, prior to feature extraction [3, 8]. In practice the combination of few techniques can be applied for effective classification of specific data.

D. Machine learning algorithm

Selection of a classifier most suitable for specific study is often difficult and depends on the application and data type. Different techniques applied to the same task may result in varying performance [3] therefore it is crucial to choose suitable technique for the algorithm development. The subsequent paragraphs of this document provide a review of some classification methods as well as detailed introduction to the two chosen techniques used in our concept of spatial and spectral classifications. Selected algorithm will serve to build a set of decision rules – model - to classify the testing data.

E. Accuracy assessment

After successful creation of classification model, the results should be checked for their accuracy and reliability. Although the classification process is already complete, it is considered that evaluation of classification performance is an essential step of the whole procedure [9, 10, 11]. Various assessment approaches may be used, ranging from a qualitative evaluation based on expert knowledge to a quantitative accuracy assessment [3]. Different methods are proposed in literature for accuracy evaluation. At one place a set of six criteria is presented: accuracy, reproducibility, robustness, ability to fully use the information content of the data, uniform applicability and objectiveness [12]. Although the performance of the classifier can be described by these criteria, no classification algorithm can fulfil all these requirements. Due to different data sets and classification objectives it is also possible that at some cases certain criteria will not be applicable [12]. R.S Defries et al. [13] suggest application of multiple criteria to assess correctness of the algorithm. These standards include classification accuracy, computational resources, stability of the algorithm and robustness to noise in the training data. Classification accuracy

evaluation is the most common approach among all the classification performance evaluation methods [13].

F. Classification model

Based on the training sets a decision rules are defined, all pixels of the testing image are assigned to a class [1]. Depending on the feature extraction approach and classification technique, each pixel is considered individually or as a part of a field, within which all pixels belong to the same category. Spatial representation of this result creates a map of classification output. It may be considered as the final outcome of the task but often additional data treatment is required to de-noise the result.

G. Result and post-processing

The classification of the testing set and assignment of a class to each observation may be the last step and final result of the classification process. However, as indicated by previous research [14, 15, 16] post-classification processing is an important step in the overall process and can significantly improve the quality of classification result. Traditional pixel-by-pixel method of classification tends to end in so called “salt and pepper” effect in classification maps. For instance, in airborne imaging an automatic classification may run into some misperception between different green areas. The recreational grass is often found in residential areas, while pasture and crops are largely located away from residential areas, with sparse houses and a low population density. Therefore, supplementary classification input can be developed based on the relationships between housing or population densities and urban land-use classes to help separate recreational grass from pasture and crops [3]. One method for combination of results from multiple classifiers is the majority voting technique [17, 18]. As an alternative to combination of classifiers, the use of majority voting process was also proposed, where the final class is assigned to a field based on the number of representatives for given category. The result is that the whole field is labelled as the class that had the largest number of occurrences [16].

The list presented above provides very brief and generic overview of the classification process. Each of these steps can be performed in various ways, applying tools from very rich and constantly growing portfolio of algorithms. In the following Section, a survey of most common classification techniques, with segregation for different approaches for this task, is presented.

2.2.2. Survey of classification methods

As indicated in previous section, various classification problems may require different approaches to obtain the best performance. Depending on the detector type determining recorded

data, availability and content of the training set and expected outputs, the available classifiers can be segregated into different categories. The overview below provides seven main groups [19], categorising various practices of classification algorithms. It is important to point out that different approaches may be executed by the same algorithm but build on different data set or feature extraction method.

- A. On the basis of characteristic type
 - a. Shape-based: This technique relies on the extraction of features based on the spatial characteristics of objects in the observed scene. In this approach, often morphological tools are employed to extract the attributes, like centroid, perimeter and eccentricity. In other cases, features can be based on primitive shapes (like ellipse or rectangle) or edges and contours of objects [20, 21, 22, 23].
 - b. Motion-based: In this method the temporal characteristics of objects are extracted and used as critical features for classification purposes. Algorithms like: Support Vector Machine, Multiple Kernel Learning (MKL) and Convolutional Neural Networks (CNN) can perform motion-based classification [24, 25, 26, 27].
- B. On the basis of the training sample
 - a. Supervised classification: The classification process with use of data set of known informational classes (training sets) to categorise pixels of unknown identity is called supervised classification [19]. In order to identify the decision rule for classification, it is necessary to know spectral information or spatial features of each class from training set. It is critical to provide unbiased sampling of training sets to deliver representative information of the total population. Examples of algorithms utilising this approach are: Maximum Likelihood Algorithm (MLA) [28], Support Vector Machine [29, 16] and Partial Least Squares Regression [30].
 - b. Unsupervised classification: This method examines large number of unknown pixels and splits them into a number of classes based on natural grouping of features that are present in the image. It determines spectrally homogenous classes and estimates the population statistics. No prior extensive knowledge about imaged scene is required. Exemplary tools used for this technique are: K-means Clustering Algorithm [31], Complex Wishart Distribution [32] and Principal Component Analysis (PCA) [33].

- C. On the basis of assumption of a parameter on the data
- a. Parametric classifiers: The main characteristic of these classifiers is the fact that a Gaussian distribution is assumed for the collected data. The parameters like mean vector or covariance matrix are usually generated based on training data. Use of these techniques have several well-known drawbacks. When the scene captured on the image is complex, these classifiers often produce ‘noisy’ results. Additionally, integrating the auxiliary data, like spatial or contextual attributes, into the classification procedure is problematic [19, 3]. Maximum Likelihood Algorithm [34], Linear Discriminant Analysis [35] can serve as the examples of this approach.
 - b. Non-parametric classifiers: While using this type of classifiers no assumption about the data is required. Moreover, no statistical parameters are necessary in order to compute class separation. Non-parametric classifiers are especially suitable for incorporation of non-remote-sensing data into a classification procedure. Examples of tools used in this technique are: Artificial Neural Networks (ANN) [36], Support Vector Machine [37] and Decision Tree Classifier (DTC) [38].
- D. On the basis of pixel information taken
- a. Per-pixel classifiers: Conventional per-pixel classifier produce a signature by using the combination of the spectra of all training-set pixels from a given feature. The contributions of all materials existing in the training-set pixels are presented in the resulting signature, while the problems of mixed pixels are ignored. Examples of algorithms using this method are Maximum Likelihood Algorithm [34] and Support Vector Machine [16].
 - b. Subpixel classifiers: It is assumed that the spectral value of each pixel is a linear or non-linear combination of defined pure materials called endmembers that provide proportional membership of each pixel to each defined endmember. Subpixel classifiers are able to handle the mixed pixel problems, suitable for medium and coarse spatial resolution images. The representative algorithm: Partial Least Squares Regression [39].
 - c. Object-oriented classifiers: Pixels of the image are merged into objects and then classification process is executed on the basis of these objects. This procedure involves 2 stages: image segmentation and image classification. Image segmentation unites pixels into objects and subsequently a classification is

- implemented based on these objects. Examples of implementation are: Support Vector Machine, Artificial Neural Network and Maximum Likelihood [40, 41].
- d. Per-field classifiers: The per-field classifier is meant to handle the problem of environmental heterogeneity, as well as improve the classification accuracy. Geographical Information Systems (GIS) play an important role in per-field classification, integrating raster and vector data in a classification. The vector data are often used to subdivide an image into parcels, and classification is based on the parcels, avoiding the spectral variation inherent in the same class [3]. This method is typically used in GIS-based classification procedures [42, 43, 44].
- E. On the basis of number of outputs for each spatial element
- a. Hard classification: When this technique is applied, a definitive decision is made for all the pixels of the image and each pixel is allocated to a single class. The area estimation achieved by hard classification may result in large errors, especially from coarse spatial resolution data caused by the mixed pixel problem [3]. Most of classifiers follow this approach, with examples of applications in Artificial Neural Network [45] and Support Vector Machine [37].
 - b. Soft (fuzzy) classification: This method provides a measure of the degree of similarity for each pixel of every class. Soft classification usually provides more information and potentially more accurate results, especially for classification of coarse spatial resolution data [46, 47].
- F. On the basis of spatial information
- a. Spectral classifiers: Pure spectral information is used to perform the classification of an image. This type of classification often produces a ‘noisy’ result caused by a large variation in the spatial distribution of the same class pixels. Examples: Maximum Likelihood Algorithm [34] and Artificial Neural Network [48].
 - b. Contextual classifiers: Image classification is executed based on the information from spatially neighbouring pixels. The Markov random field-based contextual classifiers are the most frequently used methods in contextual classification [49].
 - c. Spectral-contextual classifiers: This method applies both spectral and spatial information. Initial classification is performed based on parametric or non-parametric classifiers and then contextual classifiers are used in initially classified images. Example: combination of parametric or non-parametric and contextual algorithms [3].

G. Combination of multiple classifiers

Various classifiers have their strengths and drawbacks thus, combination of two or more techniques may be beneficial for the overall result increasing the accuracy when compared to single classifier [50, 51].

The above presented overview demonstrates a typical division of classification techniques. It is apparent that many of them can fall under different categories, depending on the segregation basis as well as the application and data provided. In subsequent sections, the fundamentals of two from abovementioned algorithms are introduced and the performance and data representation are demonstrated on specific examples of spatial classification of a texture image and unmixing of hyperspectral data.

2.2.3. Support Vector Machine

Texture image can be described as an area containing repeating pattern of pixel intensities arranged in a particular way. It is often used to analyse certain properties of observed objects, such as granularity, smoothness, roughness and periodicity [52]. Due to extensive number of various textures, there is no single and precise definition for this property and each of them must be considered separately [53]. In order to facilitate texture recognition, various classification techniques have been introduced in the literature. They usually fall into the contextual group of classifiers with per field or per pixel approach. The main objective of classification based on textures is to categorise the scene into different clusters, based on specific characteristics for each region [54]. In this text the application of SVM for this task is demonstrated. As a classification algorithm, it requires all the steps described in Section 2.2.1, however in this section the focus is placed on the feature extraction, classification method and performance assessment.

2.2.3.1. Feature extraction

Based on recent trends in texture classification the feature extraction process can be grouped into five main tactics: (1) structural; (2) statistical; (3) signal processing; (4) model-based stochastic and (5) morphology-based methods [55, 53, 56, 57]. Out of these five, statistical and signal processing are the most widely used techniques, because they can be applied onto any type of texture. This text will focus only on these two approaches with application only to grayscale images.

Statistical methods of texture analysis use mathematical procedures and models to analyse the spatial distribution of the grey values in a texture image and use this as a source of information

[53, 56]. Usually the statistical approach computes all features of each point in the texture and subsequently derives sets of statistics based on the distribution of these structures. Since texture is a spatial property that characterises groups of pixels, these features are computed locally over selected area of the image. It is done by application of the mentioned mathematical procedures to the point (pixel) of interest and predefined total amount of neighbouring pixels. The local characteristics are then derived based on this neighbourhood and assigned to the point of interest. This way one can obtain various texture features, based on very basic calculations as standard deviation, sum or mean value out of selected pixels (which in case of grayscale image represents the intensity), as well as other calculations, such as contrast between chosen pixel and neighbouring ones, variance or uniformity in the chosen neighbourhood range [58].

Signal processing methods are characterised by analysis of the image in frequency space. Fourier transform, and especially Fast Fourier Transform (FFT), introduced half century ago as an effective algorithm of Discrete Fourier Transform (DFT) [59] is used to calculate frequency content of a time-domain signal. Fourier transform decomposes a time domain signal into complex exponential values of different frequencies. The technique used in this transform is defined by the following equation [60]:

$$X(f) = \int_{-\infty}^{\infty} x(t) \cdot e^{-2j\pi ft} dt \quad [2.1]$$

where t stands for time, f for frequency, j is the imaginary unit (representing square root of -1), $X(f)$ denotes the signal in frequency domain and $x(t)$ the original signal in time domain. However, Fourier transform have one significant drawback. As can be observed in the Equation 2.1, for each chosen frequency the transform integrates the signal $x(t)$ at all times what means that it can describe only global frequency content of the original signal, without any localisation in temporal domain and therefore it does not work for non-stationary signals. Further developments brought a tool called Short-time Fourier transform (STFT) [60]. This tool is based on the use of window functions $w(t)$ aiming in fragmenting the signal to receive small portions of original signal, where frequency domain will be almost stationary. It is defined by the equation [60]:

$$STFT_x^w(t', f) = \int_{-\infty}^{\infty} x(t) \cdot w^*(t - t') \cdot e^{-2j\pi ft} dt \quad [2.2]$$

where $x(t)$ is the original signal, $w(t)$ is the window function, and $*$ denotes the complex conjugate. The fixed window function, and therefore also constant time-frequency resolution over the whole time-frequency plane, is still a significant disadvantage of this tool. This was successfully mitigated two decades ago by introduction of a new method called Wavelets Transform (WT) [61]. The main motivation behind the development of wavelet transform was to overcome the constant resolution disadvantage of STFT. The basic concept of wavelet transform is very similar to the

one of STFT. Both of them use windowing process to segment the original signal, however the wavelet transform has the advantage by providing capability for multiresolution analysis. Continuous Wavelet Transform is defined by the equation [60]:

$$CWT_X^\Psi(\tau, s_m) = \frac{1}{\sqrt{s}} \int x(t) \cdot \psi^*\left(\frac{t-\tau}{s_m}\right) dt \quad [2.3]$$

where variables τ and s_m are translation and scale respectively. The window functions are called wavelets and the main transforming wavelet function, $\psi(t)$, chosen for specific analysis is called the mother wavelet. The mother wavelet carries that name as it is a prototype for generating other window functions by being scaled and translated over the whole signal to capture both frequency temporal information in the frequency domain. Scaling of the wavelet is the property of creating different lengths of wavelet function by compressing or dilating the mother wavelet. Translation is the movement of every created wavelet function over the entire data set in order to capture temporal localisation of the information [61, 60, 53]. The techniques presented above are also applicable to a spatial data where in result, an image can be represented in frequency space. Since the development of the Wavelet Transform, it become a very popular algorithm for image processing as it can be successfully applied to the image for feature extraction.

To reiterate the point made in Section 2.2.1, regardless of the method used for feature extraction, it is recommended to consider if normalisation of extracted features is necessary. This process standardises the features, so that each of these used for signal description will have similar value range, to prevent classification bias towards specific features [56].

2.2.3.2. Classification

Described above feature extraction process is an inherent part of classification and can be understood as preparation of the input data for subsequent steps. Before the classifier is trained, the set of features describing the signal (image) must be properly prepared. One can visualise this training data as a matrix, where each column represents all extracted features, and each row corresponds to an observation of these characteristics. Additionally, to provide full training information, one more column is added to this matrix, containing labels of trained classes. With such training set, the classifier is taught (trained) to assign class labels to specified feature values as given in the training set. When building the classification algorithm, the data pre-treatment as well as selection and parameters of selected features have to be fixed and kept identical for the training process as well as all the classification problems solved with this algorithm. When the classifier is built based on the training set and the matrix of features extracted from studied image is also ready, the algorithm can start the classification execution. The result of this process is a label assigned to every spatial area of the image subjected to this operation. As discussed in the

Section 2.2.2, several approaches can be taken with respect to the pixel information. Therefore, depending if per-pixel or per-field technique was selected, in result of this classification, each pixel or each field of the image will have an assigned label informing one about the predicted class for this unit of the image.

The Support Vector Machine in its original form is a binary classifier, which means that it can solve segregation problem when the input data has only two classes. Although various objects can be classified with the use of SVM, in this text only one particular type of object will be considered – finite dimensional real vectors. As an example, a set of vectors in 2-dimensional space can be selected where each object can be described as $\vec{x} = (x_1, x_2)$. Graphically such an element could be represented as a point on a surface. A line in such a dimension can be characterised by an equation [62]:

$$\vec{w} \cdot \vec{x} + b = 0 \quad [2.4]$$

where \vec{w} is a weight vector, b is a scalar and $\vec{w} \cdot \vec{x}$ is a dot product between vectors \vec{w} and \vec{x} . Such a line defines an algorithm known as linear classifier. It divides the whole space into two areas and separates each vector \vec{x} depending on its position with respect to this line: vectors \vec{x} for which $\vec{w} \cdot \vec{x} + b > 0$ is true are classified as +1 and these for which $\vec{w} \cdot \vec{x} + b < 0$ is true are assigned to class -1. If a vector \vec{x} falls precisely on the line described with Equation 2.4 then there is indeterminacy [62]. Set of N training vectors for such a classification problem in K -dimensional space can therefore be described as [62]:

$$D = \{(\vec{x}_1, y_1) \dots (\vec{x}_N, y_N)\}, \quad \vec{x}_i \in R^K, y_i \in \{-1, +1\} \quad [2.5]$$

For any vector \vec{w} and scalar b in given space the set of points \vec{x} which satisfies the Equation 2.4 is called a hyperplane. The hyperplane is a subspace of one dimension less than its ambient space (e.g. for 2D space it is a line and for 3D space it is a surface). A training set D is said to be linearly separable if there is at least one such a hyperplane (line in this example) that correctly classifies data set D . That means all the N observations must comply with:

$$\begin{cases} \vec{w} \cdot \vec{x}_i + b > 0 & \text{if } y_i = +1 \\ \vec{w} \cdot \vec{x}_i + b < 0 & \text{if } y_i = -1 \end{cases} \quad \text{for } i = 1, \dots, N$$

If a data set is linearly separable, one is often able to draw many lines separating these two groups (see Figure 2.2 (a)). An SVM classifies data by finding the best hyperplane that separates all data points of one class from those of another class [53, 55]. The hyperplane (in this example shown as the line) determined by an SVM is always the one with the largest margin between representatives of both classes [63]. This is called the optimal hyperplane and it is defined by a pair (\vec{w}, b) which satisfied the condition [62, 64]:

$$\begin{cases} \vec{w} \cdot \vec{x}_i + b \geq 1 & \text{if } y_1 = +1 \\ \vec{w} \cdot \vec{x}_i + b \leq -1 & \text{if } y_1 = -1 \end{cases}$$

and for which $\|\vec{w}\|$ – the norm of vector \vec{w} – is minimum. This denotes constrained optimisation problem, whose solution is the optimal hyperplane.

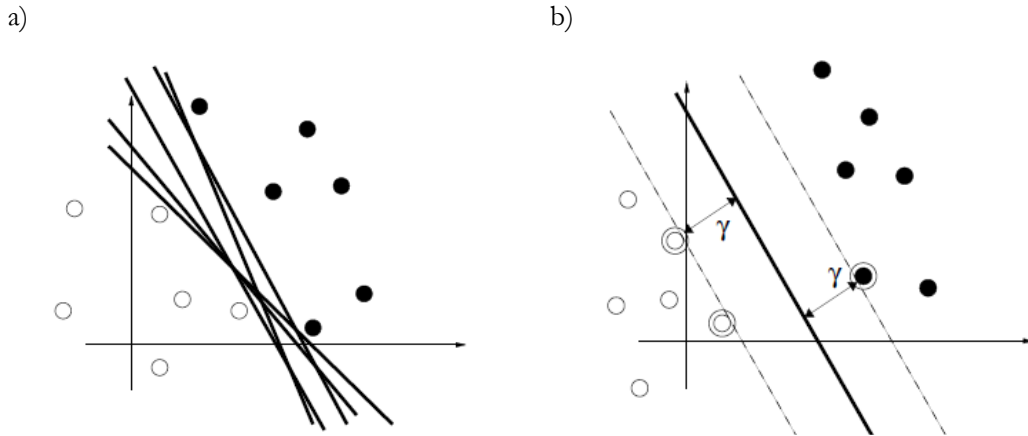


Figure 2.2. 2D representation of two class data represented by full and empty circles; a) different correct linear classifications of the data set; b) the optimal hyperplane with circles around support vectors and γ indicating the margin between them and the hyperplane [62].

The mentioned margin (noted by γ in Figure 2.2 (b)) is a space parallel to the determined hyperplane that has no data points of any of classes. This space is bounded by the points which are the closest to the separating hyperplane. These vectors are called the support vectors and they also explain the name of this classifier [62]. The support vectors and optimal hyperplane are illustrated in Figure 2.2 (b). For some data sets separation of the classes with linear hyperplane may not be possible. In these cases, some hyperplanes can divide the data better than others, but none of them can perfectly provide the classification. When this happens, SVM can use a “soft margin” – approach allowing the hyperplane to separate many, but not all data points. In this case the optimal hyperplane is called soft margin hyperplane that is able to separate the training set with minimal number of errors. The importance of misclassification can be set during the tuning process of the classifier [64].

It is often impossible to find linear hyperplane to separate two classes of data. The SVM overcomes this by the use of so called “kernel tricks”. Kernel is a function enabling mapping of the data into other dimensions - for any point in the input space, the same point can be represented in other geometry, called feature space. Using other words, in n-dimensional data set space, the SVM is able to find an additional dimension of feature space where linear hyperplane classification will be possible [53, 54]. Figure 2.3 visualises this concept, considering again a 2D problem, where 2 class data set (illustrated as red and blue dots) is inseparable by linear hyperplane

in this data space (see Figure 2.3 (a)) however, it can be easily divided when the kernel function is applied to map the data into additional feature space (see Figure 2.3 (b)).

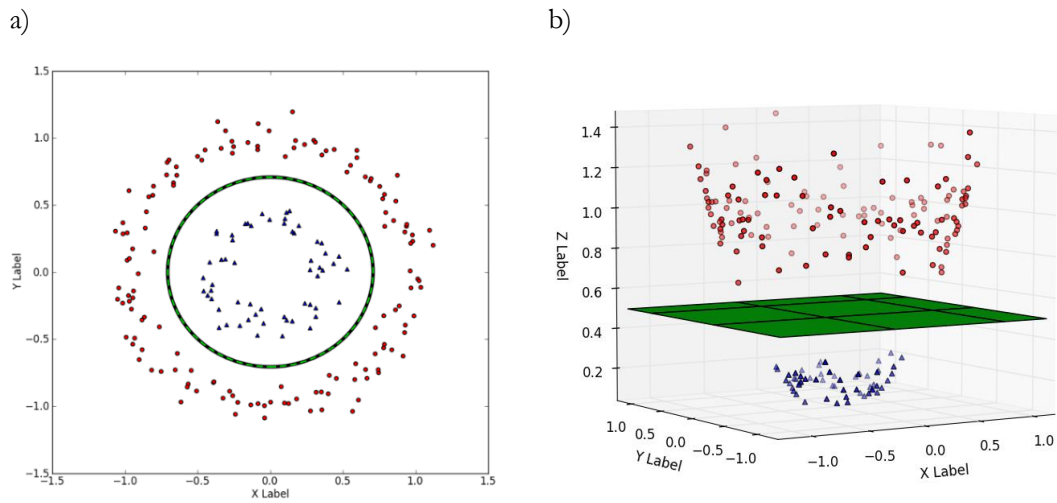


Figure 2.3. Illustration of mapping the data points into new feature space; a) data set in their original 2D space (with indication of separating hyperplane); b) data set from graph (a) mapped into an additional feature dimension where classification with a linear hyperplane is possible [65].

As mentioned above, the SVM can be used for classification when the input data consist of two classes only. Nevertheless, there are several approaches to adapt SVMs to solve classification problems of three or more classes. The most common ones are one-versus-one (or all-pairs) and one-versus-all (or one-versus-rest) methods [66]. One-versus-one is a method which has one binary SVM for each pair of classes to separate members of one class from the other. Consequently, the results of these tests are combined. The simplest approach involves the majority vote, which means that each data set is assigned to the class into which it is the most frequently classified. In case of a tie, the sample is considered equivocal. One-versus-all classification takes place when one binary SVM is used to separate members of one class from members of all the other classes. Usually, classification of an unknown pattern is done according to the maximum output among all SVMs [66].

2.2.3.3. Performance assessment

As indicated in Section 2.2.1, the accuracy assessment is the last part of the algorithm building process. However, the classification accuracy is not the only parameter informing about the overall performance of the tool. Operation of the classifier can be assessed on a few different levels. The direct measure is given by the ratio of the correctly grouped samples versus all the data

points subjected to this process. Similarly, the error rate could be tested by using incorrectly classified samples in this equation. Although this method is very intuitive, it has a significant drawback – requirement of the ground truth data to perform this assessment. Ground truth is the information set providing true labelling of the test data. When this kind of data is input to the classification assessment, it is easy to check if the labelling done by classifier was correct or not. However, this kind of information is not always available for real data sets and therefore, application of this technique is limited only to very well-known and defined data sets [54].

Other parameters often used for classification assessment are the computing power needed for a classification and the process execution time. Each part of the classification procedure requires some time for its execution. Different methods of feature extraction, various sizes of their matrices and different settings of the classifier itself can significantly influence execution time of the process as well as the required computing power [53]. In many cases optimisation of the classifier requires compromise between different aspects of the classifier implementation. The classification accuracy and execution time may significantly vary depending on the selected settings in feature extraction and classification process. Often improved accuracy is obtained only at the cost of longer computation time and trade-off between these parameters is required to provide optimal performance for a specific task.

2.2.4. Partial Least Squares regression

Use of classification techniques is not restricted to the labelling of different groups in a data set. In some cases, data describing specific property of an object may be difficult to obtain. This may be because it is technologically complicated, very expensive or time consuming. Some characteristics may require contact, invasive or even destructive testing, which is not always possible. Due to this reason, alternative methods are sought, capable to model and predict these properties based on a set of easily obtainable measurements of features correlated with the characteristic under examination. Multivariate analysis techniques can be helpful to deal with this task [67]. Methods like Multiple Linear Regression (MLR) and Principal Component Regression (PCR) can be applied (with certain restrictions) to solve these problems, but Partial Least Squares Regression (PLS-R) is another technique that qualifies and it is considered in this chapter.

The PLS method exists in various implementations but the two-block predictive version is the most popular form of this algorithm used in science and technology [68]. It models relationship between two data matrices \mathbf{X} and \mathbf{Y} , and can analyse strongly correlated and noisy data of matrix \mathbf{X} and simultaneously model several variables of matrix \mathbf{Y} . The name of this technique indicates the core of this modelling, where each model parameter is iteratively estimated

at the slope of a simple bivariate regression between the data of y and x variables [69]. Similar to simple regression, the two data blocks – \mathbf{X} and \mathbf{Y} – are respectively called predictors and responses. The nomenclature calls them independent (although, as mentioned above, these data often tend to be highly correlated and therefore the name “independent” is not always appropriate) and dependent variables. These names clearly illustrate the purpose of this process where the variation in one set of variables is explained or predicted, based on another data set. The PLS algorithm minimises error scores across all individual observations in order to enhance the prediction. It uses the principle of least squares where among many possible lines, the one that best fits the data is selected. This is done by minimising the sum of squared vertical distances from the observed data points to the fitted line [70]. To give the PLS algorithm more descriptive meaning, this abbreviation is also interpreted as Projection to Latent Structures [71]. The following sections explain this projection and the fundamentals of the PLS model.

2.2.4.1. Partial Least Squares model

Modelling methods applied in the science and technology often consists of two steps. The aim of the first step is to find a representation which will describe the relationship $\mathbf{Y}=f(\mathbf{X})$ between predictors and dependent variables. Similar to the generic process described in Section 2.2.1, this is called calibration or training step and the data used at this point - training set. The model parameters are named regression coefficients. In the second part, the predictors are obtained for one or more samples, and together with regression coefficients they are used to predict the values of dependent variables. This is the prediction step and the data used in this step is called prediction or test set [72].

For illustrative description of this algorithm, the whole introduction is based on an example. For this purpose, application of the PLS-R model for unmixing of the hyperspectral data was proposed. In this application, the model aims to predict the composition of a target object or extraction of sub-pixel components (so called end-members) in imaged scene. In this example, the technique is used to predict composition of $M=4$ different constituents based on mixed reflectance spectra of the target object. In order to build the training set of the algorithm, the spectral fingerprint of N observations (in this example $N=20$) was created, where each observation has a known combination of all four components of interest. Therefore, the input data to the training set consists of a spectrum of selected wavelength range K (in this example range of 170nm, with data point every 1 nm resulting in $K=170$ data points per observation) and given composition of tested materials. This data is grouped in two blocks – matrix of predictors \mathbf{X} with dimensions $(N*K)$ - 20 observations in rows and 170 columns of spectral data - as well as

matrix of dependant variables \mathbf{Y} with dimensions (N*M) - the same number of rows and 4 columns corresponding to the known composition of four components of tested material.

As mentioned in Section 2.2.1, normalisation of the data set is often crucial for the successful implementation of the algorithm. Although scaling is not essential when the matrix of predictors consist of spectral data only and every data point is with the same scale, it can be of high significance when the matrix of predictors is built from various parameters of different weight. Usually each variable can be scaled to unit variance through dividing it by their standard deviation and centring the data by subtracting their averages.

There is a specific case in the PLS technique, where only one response per observation occurs (Y has only one column). Here, the algorithm of the model is simplified and it is also distinguished by separate name as PLS1 (in contrary for the PLS2 when the response matrix is two dimensional). Although the PLS1 model can be used to evaluate the multi-response problem simply by analysing each column of its response matrix separately, this calculation method is advised only when the Y values measure truly different things and therefore they are relatively independent. In such a circumstance, the PLS1 model would have fewer dimensions and would be much easier to interpret [68]. When responses are correlated, they should be analysed together and, in this case, the PLS2 model gives one overall picture of all the variables. In this text only the outline of the PLS2 algorithm is presented.

The basic principle of the PLS model is that it finds new variables that are the estimations of the latent ones. These new variables are called the X-scores and are denoted as matrix \mathbf{T} . They are found from linear combinations of original \mathbf{X} values with the coefficients, so called weights, stored in matrix \mathbf{W} . The X-scores are the actual predictors of \mathbf{Y} values. The relationship between these matrices is given in Equation 2.6 presented in matrix form [69]:

$$\mathbf{T} = \mathbf{XW}^* \quad [2.6]$$

where \mathbf{W}^* stands for matrix of weights transformed to be independent between components. The basic property of X-scores is that the set of scores \mathbf{T} multiplied by adequate loadings \mathbf{P} add up well to the original \mathbf{X} . As a consequence, after this regression process, the X-residuals \mathbf{E} are relatively small [69]:

$$\mathbf{X} = \mathbf{TP}' + \mathbf{E} \quad [2.7]$$

The magnitude of values in \mathbf{T} depends on the relationship found by the first score values, however this property assures that the scores vector derived during the regression presented in formula 2.7 will lead to the smallest residuals possible with the given data set. Similar to the matrix \mathbf{X} , for the

\mathbf{Y} one, the \mathbf{Y} -scores matrix, denoted as matrix \mathbf{U} , multiplied by the weights \mathbf{C} summarise well to the matrix \mathbf{Y} , so that the residuals \mathbf{G} are small [69]:

$$\mathbf{Y} = \mathbf{U}\mathbf{C}' + \mathbf{G} \quad [2.8]$$

As shown in Equation 2.7, the \mathbf{X} -scores matrix \mathbf{T} model the original \mathbf{X} values, however they are also good predictors of \mathbf{Y} values [69]:

$$\mathbf{Y} = \mathbf{T}\mathbf{C}' + \mathbf{F} \quad [2.9]$$

where \mathbf{F} – matrix of residuals – represents the deviations between observed and modelled responses. Based on the given above equations it can be seen that the relationship established by the model holds rather between these latent variables than the observed ones. The Equations 2.6 and 2.9 can be rewritten in a form [69]:

$$\mathbf{Y} = \mathbf{X}\mathbf{W}^*\mathbf{C}' + \mathbf{F} = \mathbf{X}\mathbf{B} + \mathbf{F} \quad [2.10]$$

where \mathbf{B} is the PLS-regression coefficient and can be expressed as [69]:

$$\mathbf{B} = \mathbf{W}^*\mathbf{C}' \quad [2.11]$$

Figure 2.4 illustrates the datasets used in this technique.

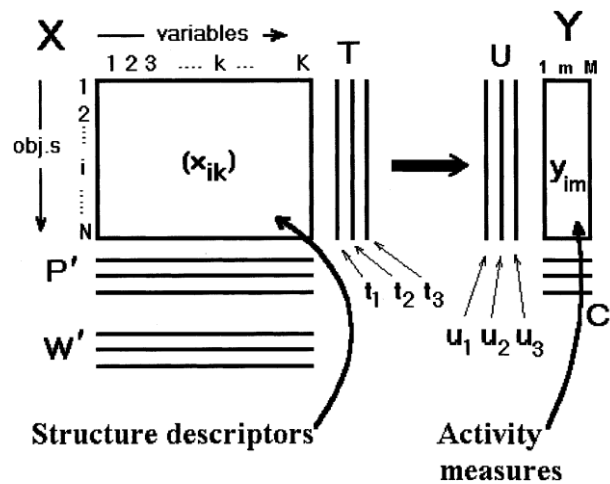


Figure 2.4. Representation of data arrangements and its projection to latent structures [68].

Since the PLS model is a projection method, it can be also presented as a geometric interpretation of predictors' projection into the latent structures. This interpretation shows N points (the same N number as the amount of observations) in the K dimensional space (where K is the number of variables – in this example, it is the number of wavelengths), projected down on a g -dimensional hyperplane (where g is the number of latent structures derived by the model) in a way that the coordinates of this projection are good predictors of matrix \mathbf{Y} [68]. For the purpose

of this geometric interpretation, an example simplified to three variables will produce a 3-dimensional space, easy to demonstrate as the Euclidean geometry. In this approach, the \mathbf{X} matrix (of N observations and $K=3$ variables per observation) can be represented as N points in K dimensional space, where each column of this matrix defines one coordinate axis. Therefore, with three variables per observation, N points is located in 3-dimensional space. The PLS model characterises a g -dimensional hyperplane. The example presented in Figure 2.5 illustrates this hyperplane as a two-dimensional surface, therefore the amount of PLS components g for this case equals 2. This plane is defined by one direction per each component, where coefficients of these directions are expressed by the loadings matrix. The coordinates of all N points projected on this plane are expressed by the values in the scores matrix. These positions are related to the values of the response matrix \mathbf{Y} .

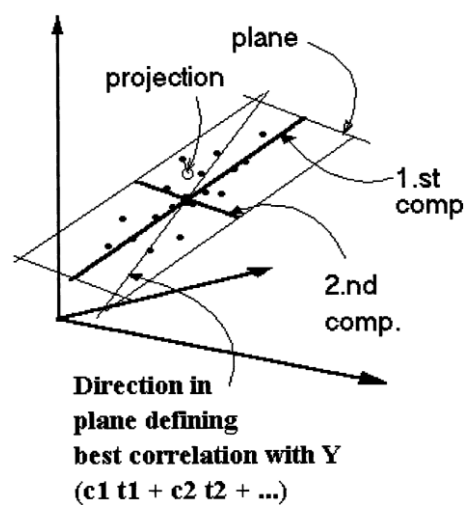


Figure 2.5. Geometric interpretation of the PLS regression model [68].

After the first iteration of creating the latent variables, the new \mathbf{X} and \mathbf{Y} matrices are created from residuals left after first projection (that can be described as \mathbf{X}_2 and \mathbf{Y}_2). This process can be found in the literature under the names: deflation or peeling off [71, 73]. Next, the algorithm finds the best linear combination of the columns of \mathbf{X}_2 for the purpose of predicting \mathbf{Y}_2 , consequently picking up any further structure in the connection between \mathbf{X} and \mathbf{Y} not described by first vector of scores. This is done recurrently, which explains the iterative manner of this model. Therefore, each run of the algorithm in principle reveals more and more information about the connection between \mathbf{X} and \mathbf{Y} [74].

In principle, the number of scores – g – should be chosen in such a way that residuals of \mathbf{X}_g regression would contain no further information about residuals of \mathbf{Y}_g . In other words, both these residual matrices should be nearly uncorrelated with each other [74]. Therefore, the amount of these latent variables is a few in number and only as many, as it is significant for the prediction

power of the model. Moreover, it is important for it to apply the correct number of components g since, when too few are used, the model is under-fitting, which means that the entire signal has not been explained by it and prediction quality can still be improved by increasing the value of g . When the g is chosen too large, the model is over-fitting which indicates that it explains not only the signal but also partially the noise. In this case the predictive ability of the model can be improved by decreasing the amount of g , as there is no value of fitting the model to the noise [74].

There are two most common ways to identify the number of components suitable for a specific model. The first one is to observe the proportion of the total \mathbf{X} and \mathbf{Y} variance explained by the model. A quick way to choose the number of components is to plot the percent of variance explained in the response variable as a function of the components number (see Figure 2.6).

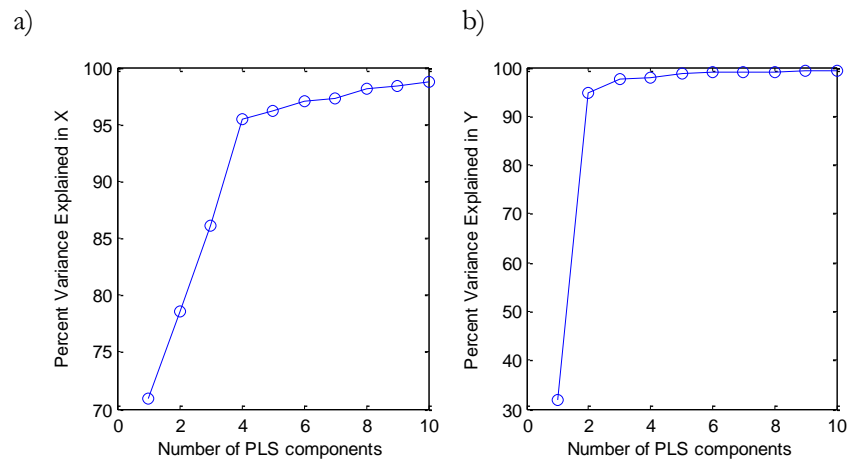


Figure 2.6. Example of the graph representing proportion of the total predictors (a) and responses (b) variance explained by the model as a function of number of PLS components.

The example presented above illustrates the variance of both predictors and responses calculated for the models containing a number of components g from one up to ten. Taking into account that it should be chosen in such a way that the percentage of variation explained would be large for both \mathbf{X} and \mathbf{Y} , it can be observed in the Fig 2.6 that the model with 4 components explains most of the variance in both matrices and would be recommended for this specific example.

Before discussing the second method of defining the number of components, it is necessary to introduce the model validation method. Using the Means Square Error (MSE) is a good way to validate the PLS models. The MSE expresses the overall quality of the value predicted by the model because it contains information about both the accuracy and the precision of predicted value [74]. To calculate the MSE, both the predicted as well as the actual values of this response variable are required. Two types of validation can be distinguished: the external one, where an additional independent data set is provided and the cross-validation, where the calibration data is used for validation. The MSE of external validation set is usually the best

measure of the model quality. Applying the calibration set may give very good results, but in practice, a model may fit the calibration data without being valid for any new data. Independent validation set (from different batch, production date or based on other adequate differentiator) can give the best information on the predictive power quality of the model. [74]

The independent data set is not always available and therefore the cross-validation method is commonly applied for the validation. Basically, cross-validation is performed by dividing the data in a number of groups and then developing a number of parallel models from reduced data with one of the groups deleted. After developing a model, differences between actual and predicted Y-values are calculated for the deleted data. The sum of squares of these differences is computed and collected from all the parallel models to form PRESS ('Predictive REsidual Sum of Squares' or 'PRediction Error Sum of Squares') [72], which estimates the predictive ability of the model. There is a very simple mathematic relation between MSE and PRESS, that is cross-validation based $MSE = PRESS/M$ [74], where M is the number of components in response matrix, as indicated earlier in this Section.

Presented validation methods can serve as a second way to identify required amount of PLS components. Figure 2.7 represents two examples that can be used to decide how many components should be used in the model.

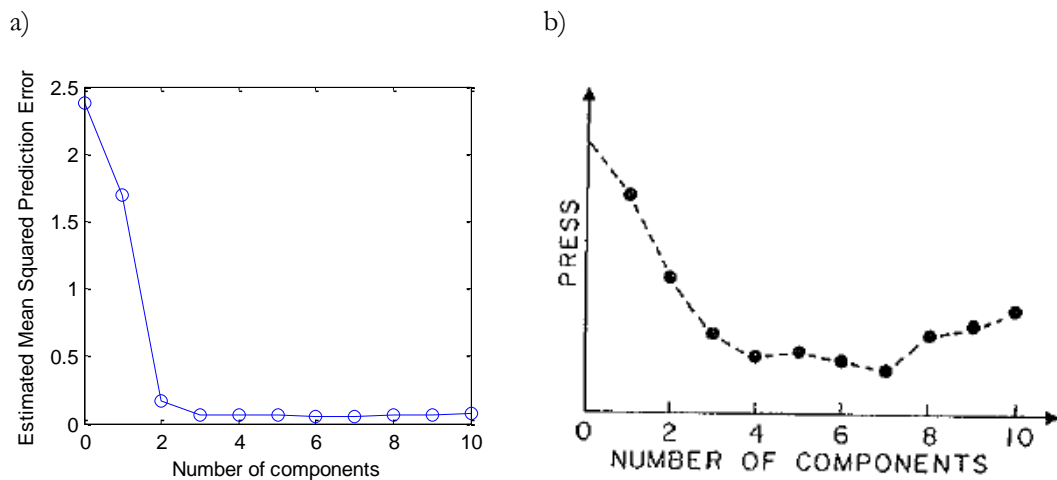


Figure 2.7. Example plots of the model validation: a) MSE for prediction with external validation set; b) PRESS based on cross-validation [72].

In the example presented in Figure 2.7 (a), three PLS components should be selected for optimal performance of the algorithm. The graph depicted in this figure represents analysis of the same data set as used in plotting graphs from Figure 2.6. While the former figure was indicating that 3 components explain the percentage of variance in **Y** matrix, only the number 4 would be satisfactory, explaining variance **X**. The graph in Figure 2.7 (a) clearly indicates that 3 components

are sufficient for good prediction ability of the model and it does not benefit from any additional ones. Using the MSE/PRESS method is an advised tool to derive the amount of PLS components g for optimal model performance [68].

In some cases, the plot of MSE or PRESS as a function of the number of PLS components g tends to be U-shaped (see Figure 2.7 (b)). As explained above, increasing amount of PLS components initially produces better fit to the calibration data and therefore, a better prediction can be observed by lowering its error. However, in some cases, when the optimal value g is exceeded, the fitting of the model into the noise instead of the meaningful signal may occur, bringing in consequence the secondary raise of MSE. Therefore, the number of components resulting in minimum MSE/PRESS is the optimal choice for the best prediction performance of the model. In case of the example shown in Figure 2.7 (b) it would be between the components 4 and 7 [72].

There are also other techniques of judging the model quality. Among these, the most common are:

- a) Coefficient of determination (also known as R^2) – it is a statistical tool that indicates how well the data point fits the model used for prediction.
- b) Scatterplots of values fitted (predicted) versus observed. This can be done for both predictors and responses.
- c) Plots of residuals for \mathbf{X} and \mathbf{Y} matrices. It is expected that generating the normal probability plot for Y-residuals will result in the fitting of it to the normal distribution line. The observation should be classified as an outlier, where the point representing it on the graph clearly deviates from the line and is outside of ± 4 standard deviation. For X-residuals it is advised to calculate the standard deviation for each observation (for each row of residuals matrix of predictors). It should be done so because this standard deviation value is proportional to the distance between the data point and the model plane in X-space. This value is often called DModX (distance to the model in X-space). When DModX is greater around 2.5 times than the overall standard deviation of X-residuals, then the observation is an outlier [68].

Examples of these validation tools will be presented in the following section.

2.2.4.2. Simulation data

As indicated in previous section, the implementation of the PLS model is demonstrated by the prediction example where concentration of different components is derived based on observation of the sample's reflectance spectrum. The spectral signature represented by each pixel

of the hyperspectral data can be expressed as a linear combination of spectrally pure constituents, weighted by fractions (quantity) that indicate the proportion of each endmember appearing in the scene indicated by that pixel. The data for this example was sourced from a collage of hyperspectral images with 170 spectral bands, representing four different tea leaves (see Figure 2.8). The simulation set was created by sampling and mixing four reflectance spectra (one per each tea type) obtained from this image. These spectra are illustrated in Figure 2.9 and are further assumed as pure constituents and as such were used for the development of this model.



Figure 2.8. Single intensity image from the hyperspectral data used in this example. Image represents 4 different types of tea leaves (rows) with 4 snapshots per each type (columns) combined in one picture.

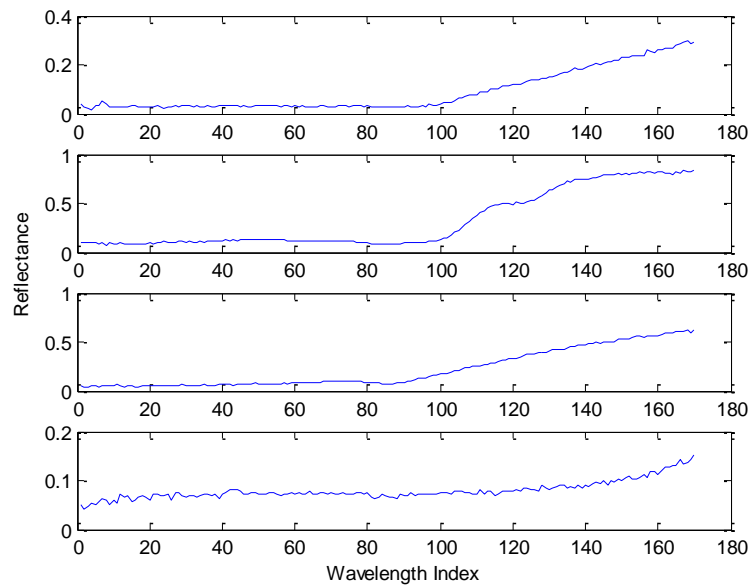


Figure 2.9. Four selected spectra used in this example as the endmembers.

Based on these constituents, a set of 80 different spectra were randomly created. Out of these, the 60 signatures were used for calibration and the remaining 20 for validation of the model. Additional single mixed spectra were also created for testing the prediction performance on unseen data. Each of these simulated spectra were created by summation of the endmembers spectra multiplied by their weight (fraction within the mixed profile). To account for natural occurrence of the noise in the measured signals, this factor was also included in the simulated data. The formula for the spectra creation could be mathematically described as:

$$y = B_1 \times \alpha_1 + B_2 \times \alpha_2 + B_3 \times \alpha_3 + B_4 \times \alpha_4 + \text{noise} \quad [2.12]$$

where B_i represents the spectra of four endmembers and α_i their fractions. In this simulation it is assumed that quantities of all endmembers sum up to the value of 1. The values of simulated reflectance spectra created the matrix of predictors and respective fractions per each observation formed the matrix of responses. After data creation, both predictors and response matrices were zero-mean standardised (the mean of each column was subtracted from the matrix, leaving all the data with the mean equal zero) and in this form they were used as input data for the model.

In this experiment the set, of artificial data was created to build the demonstration model, however in real situation, obtaining a suitable data set is an important and often very difficult step. When applying this model to some specific task, it is required to provide reliable sets of data that can be used for calibration as well as for validation. Additionally, the composition of tested samples (or any other property that will be predicted by the model) has to be measured by some other testing techniques that will serve as the response matrix for the model calibration.

2.2.4.3. Model validation results

In this section all the model validation techniques introduced in Section 2.2.4.1 are demonstrated. For this purpose, the results of the described simulation are always provided for computation of the model with $g=2$ and $g=4$ components. This illustrates the performance of under-fitted and properly trained prediction algorithm.

Figure 2.10 presents scatter plots of fitted (predicted) response values as a function of the observed (measured) ones. It is noticeable that the model with only 2 PLS components does not predict all the variables and although some linearity can be observed for all of them, the second and the third response show poor fit of the predicted vs. observed values. The model with 4 components gives the perfect prediction for all variables.

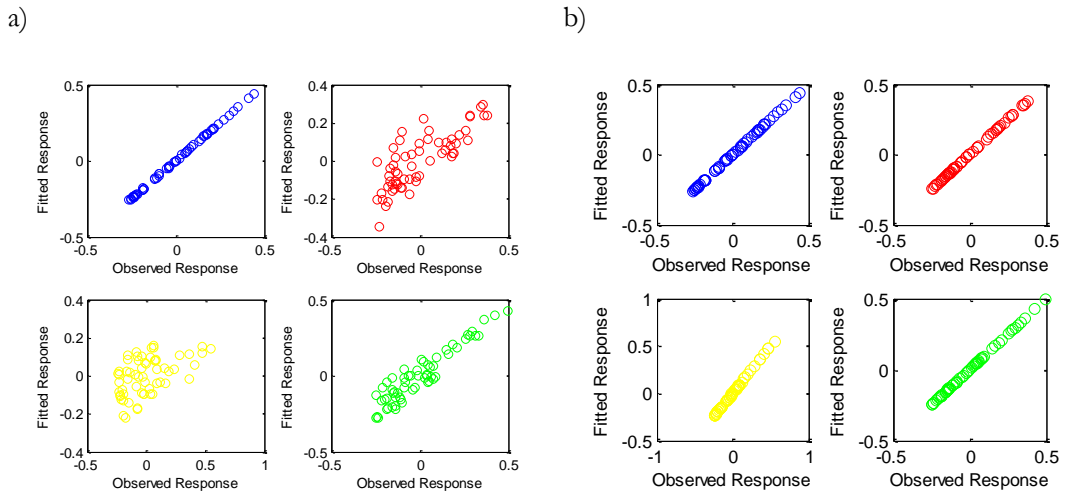


Figure 2.10. Scatter plot of fitted vs. observed response value per each endmember; a) $g=2$, b) $g=4$.

Cumulative percentage of the variance in matrices X and Y explained by the developed model are illustrated in Figure 2.11. This model explains the variance of the predictors' matrix relatively well already after computation of first component g , but at this stage, it explains only about 33% of variance in Y. With the two components, it explains already 70% of variance in Y while after adding the third one, it explains 100% of the variance for both X and Y.

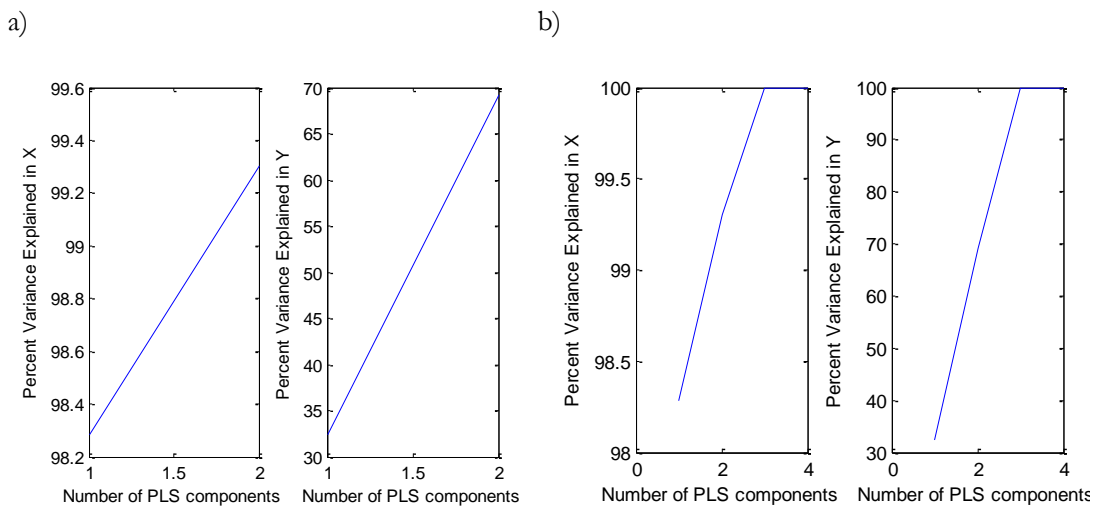


Figure 2.11. Cumulative percentage of the variance in X and Y explained by the model; a) $g=2$, b) $g=4$.

Figure 2.12 presents Estimated Mean Squared Prediction Error graphs as a function of PLS components. The MSE of the model with 2 components (Figure 2.12 (a)) shows a value of about 0.65 while for model with 4 components (Figure 2.12 (b)) this value equals 0. Actually, with the chosen dataset, the MSE is zero already after the third iteration and therefore 3 components would be sufficient for a good predictive performance of the model. This proves the observation that 3 PLS components are recommended for this model with the given data set. It is worth mentioning that this perfect fit of the model after the third iteration is related to the artificial data

set, while in reality it is expected that at the certain moment, the model gets close to but will not reach 100%. It can be related to the noise that exists not only in the prediction data, but also in the calibration set. The quality of the response data gathered by the other testing method also constitute for the overall noise in the data.

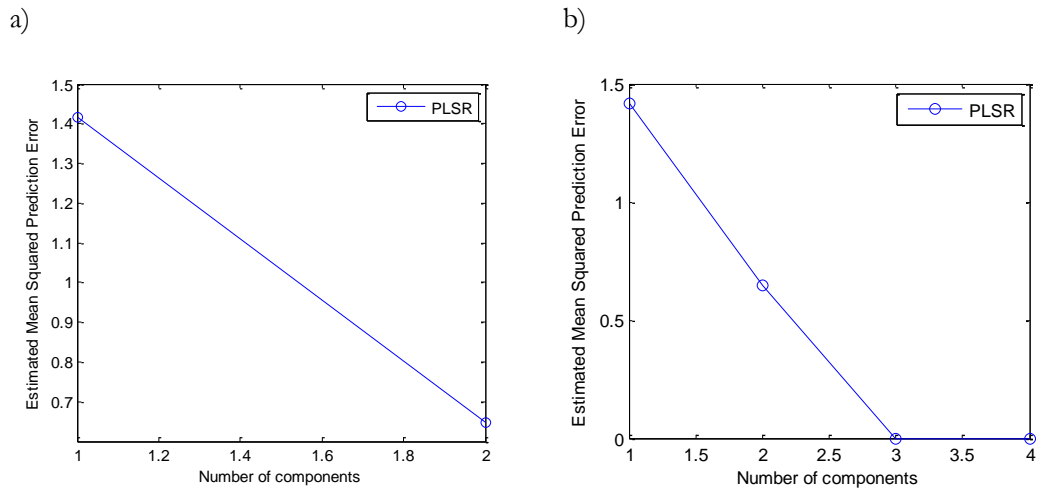


Figure 2.12. Estimated Mean Squared Prediction Error graph as a function of PLS components; a) $g=2$, b) $g=4$.

The comparison of the spectral profile created based on the simulated fractions and the one reconstructed from the predicted numbers is illustrated in Figure 2.13. Despite the fact that the model with 2 components explains only 70% of variance in responses matrix, the fit of the predicted signal with observed one can be considered as satisfying. One should also notice that the ‘original noise free test signal’ (green plot) is given only for reference and the model predicts the signal based on noisy test data (blue). The predicted signal (red) is plotted based on summation of predicted fractions (given in Table 2.1) multiplied by spectra of pure constituents, according to the Equation 2.12.

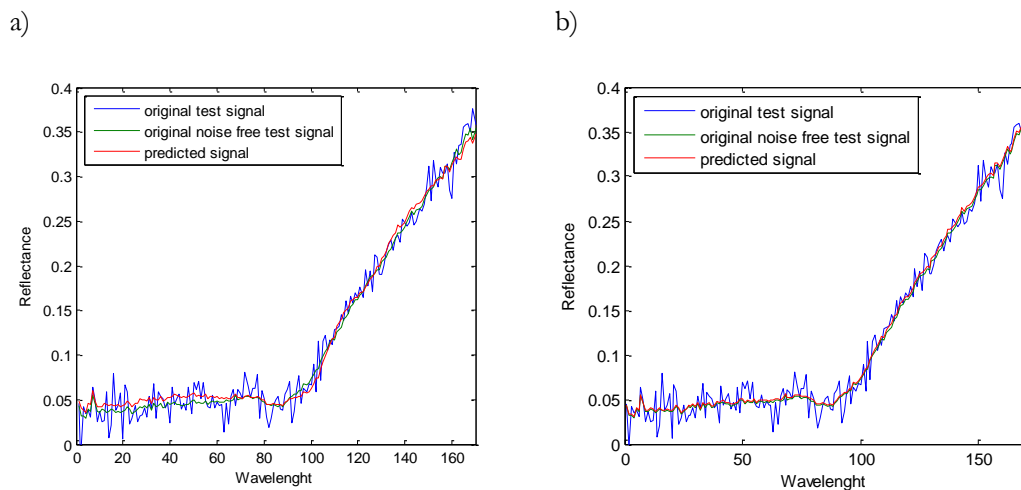


Figure 2.13. Comparison of the spectrum, generated based on the observed (simulated) fractions with the one based on the prediction with number of PLS components: a) $g=2$, b) $g=4$.

Table 2.1. Observed and predicted fractions of all 4 endmembers with $g=2$ and $g=4$, coefficient of determination R^2 for each component and MSE of these predictions.

	g=2				g=4			
Number of endmember	1	2	3	4	1	2	3	4
Observed fractions	0.6540	0	0.2340	0.1120	0.6540	0	0.2340	0.1120
Predicted fractions	0.6327	0.1174	0.0539	0.1961	0.6265	0.0099	0.2339	0.1299
R2	0.9998	0.9927	0.9858	0.9965	0.9997	0.9999	1.0000	0.9998
MSE for prediction	0.0134				2.9372 e-04			

Table 2.1 contains the observed and predicted fractions of all 4 endmembers for a selected mixed spectrum, coefficient of determination R^2 for each component as well as MSE of the predictions constructed with 2 and 4 PLS components. The model with 4 components gives very good prediction values that are also reflected in R^2 numbers. In case of $g=2$, the predicted fractions differ from the observed ones. This is especially noticeable in cases of the second and the third constituent as presented on the plots in Figure 2.10 (a), which illustrates the low predictive ability of the model for these variables. Although the differences between observed and fitted fractions values are apparent, the R^2 ones are still relatively high. This is caused by the fact that these figures were derived from a single spectrum (presented in Figure 2.13) and that there was not any inter-sample variation affecting this measure. The MSE value for the whole model confirms again that the model is under-fitting the data with two components.

Figures 2.15 and 2.16 demonstrate the typical form of residual analysis for the matrices of responses and predictors respectively. Figure 2.14 (a) clearly reveals that the model with $g=2$ predicts well only first constituent and the residuals for other endmembers are relatively large. There is no indication about the presence of any outlier data points. As illustrated in Figure 2.15, the model with 2 components has relatively large variation in X-residuals, suggesting the under fitted performance. This comparison of the overall standard deviation and DMoX per all observations proves that there are no outliers in this data set. The overall standard deviation of the model with $g=4$ equals $2.5E-17$, illustrating the very low level of residual information lost with the well-designed algorithm.

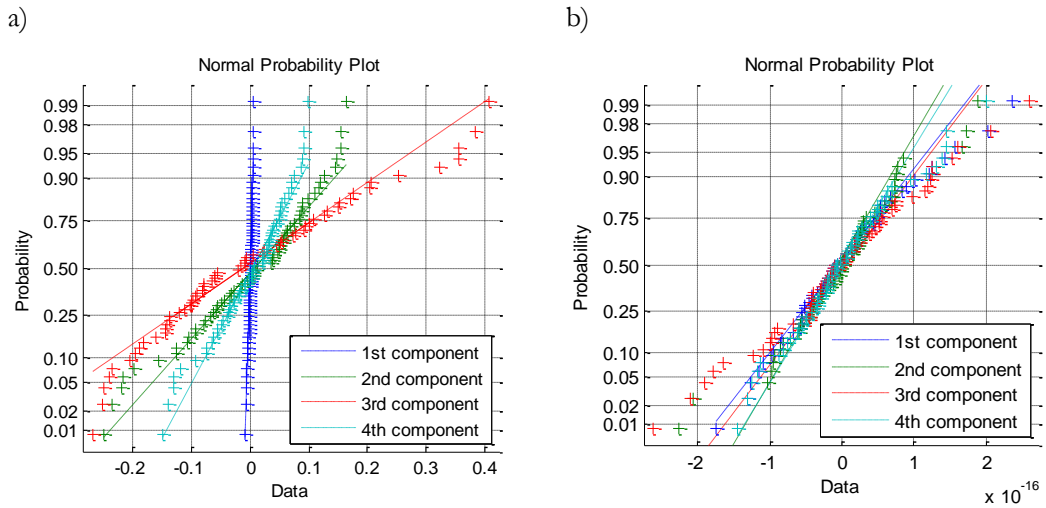


Figure 2.14. Normal probability plot for Y -residuals; a) $g=2$, b) $g=4$.

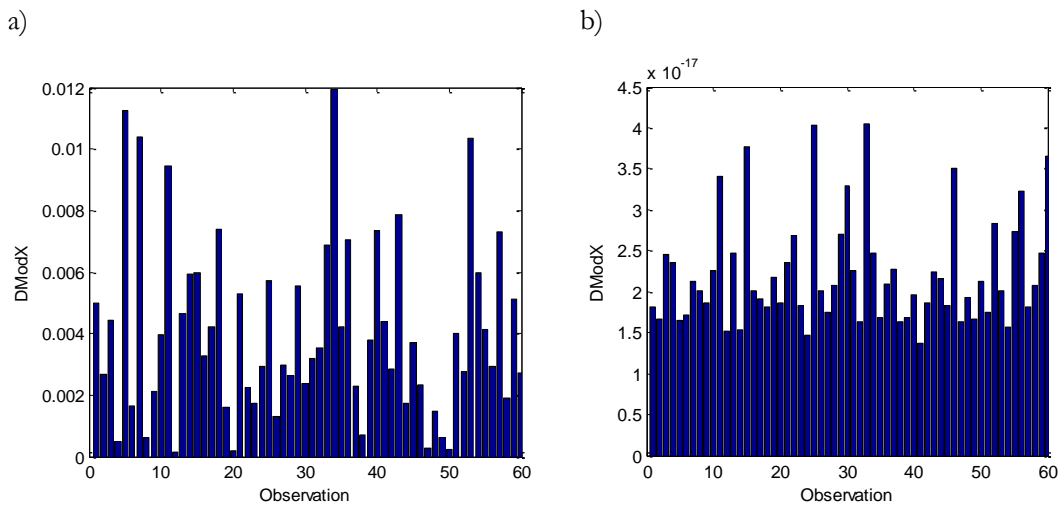


Figure 2.15. Distance to the model in X -space ($DModX$) per observation for X -residuals; a) $g=2$, b) $g=4$.

2.2.4.4. Data size reduction

Applying the spectral profiles as the matrix of predictors in the PLS model results in an extensive data set that needs to be processed by the algorithm. Although the PLS model can easily handle a lot of data points in observations, it is usually recommended to reduce the size of predictors' matrix. As indicated in Section 2.2.1, dimensionality reduction is a common approach for successful feature extraction during any classification process. Application of this method helps to save computational power and increase the speed of the algorithm, but predominantly it minimises the amount of "void data" in the model. This void data may be understood as the noise that was acquired with the signal of interest, however it is not related to it, or it may be a part of the actual signal that does not carry any information significant to solve a given problem. The first one is usually approached by dimensionality reduction techniques, like principal components analysis, maximum noise fraction (MNF), independent component analysis (ICA) and various

other methods [75, 76, 77, 78, 79]. Reduction of the signal data can be done by selecting a specific part of the spectral profile carrying meaningful information or by subsampling the data. Subsampling of the whole signal data may be very fast method of data reduction, but special care must be taken to not remove any meaningful data from the spectral profile. An alternative approach is based on the selection of a fraction of the profile, maintaining full available spectral resolution. This technique is often used when it is known that only selected part of the predictor signal is correlated with a specific response. This knowledge can come from physical properties of studied objects or other data accessible prior the model development. However, when this prior information is not available, this technique can still be applied by studying the training set during the algorithm development.

The proposed technique is based on the MSE calculation for the model trained with data reduced over varying parts of the spectrum. Figure 2.16 illustrates the simulation results of this concept applied to the dataset described in Section 2.2.4.2. This graph illustrates changes of prediction error derived from the model built with selected spectral region (window) cut-out from the original data. In this simulation, it was assumed that the removal of the data was done by increasing the size of the window, changing from 0 up to 100 bands with the 5 bands steps.

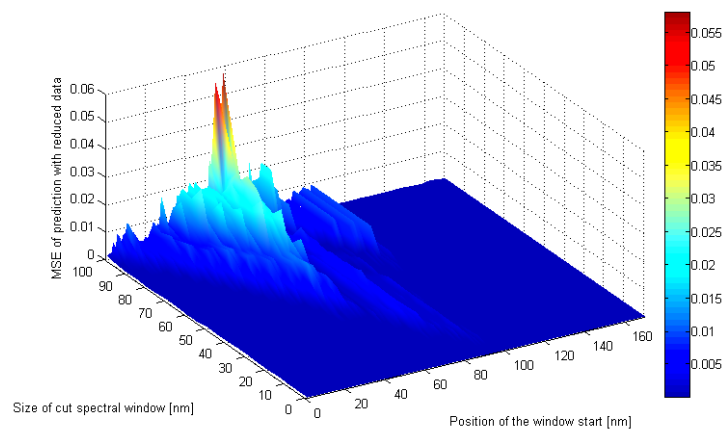


Figure 2.16. Surface graph of MSE variation as a function of spectrum window size and position.

For each simulated length, the window was sliding over the whole spectrum, imitating the data reduction in various positions of the profile. The MSE data is illustrated on the graph as a function of the size and starting position of the spectral window. Based on this test, a conclusion can be drawn, that the presence of the spectral range containing inflection of the reflectance curve is critical for the prediction quality (see Figure 2.13). This inflection is located between the bands 80 and 100. Clearly, removal of this region can result in increased MSE, despite the window size. It can be also seen that removal of significant portion of the original spectrum does not affect the Mean Square Error for prediction and could be considered as redundant for this task.

Demonstration of this PLS implementation based on simulated data illustrates the importance of proper algorithm development. The model performance will be satisfactory only if adequate training data can be provided and the algorithm structure is suitable for the given task. Presented tools can help to assess the quality of the model and tune it to the optimal performance before the implementation phase.

2.3. Optical Parametric Oscillators

Optical parametric oscillators are extremely flexible sources of broadly tuneable coherent radiation. As indicated in Chapter 1, these devices are based on a nonlinear optical frequency conversion and in principle can be considered as photon splitters. They operate by dividing the incoming energy from the high energy pump photon into two lower energy photons, named as signal and idler (see Figure 2.17). To satisfy the conservation of energy, the summation of the energy of these newly created photons must be equal to that of the pump photon. Energy of a photon can be derived as $h\nu$, where h is the Planck's constant and ν the energy of given photon. With this in mind, the conservation of energy can be written as [80]:

$$\nu_p = \nu_s + \nu_i \quad [2.13]$$

where the subscripts p , s and i stand for pump, signal and idler respectively. Typically signal is the higher energy (shorter wavelengths) photon and respectively, idler denotes the lower energy counterpart photon [80, 81]. Therefore, when applied to the mid-infrared spectroscopy, usually the idler output is the one of interest. This split of the pump photon into two lower energy photons is called parametric down-conversion.



Figure 2.17. Schematic of the parametric frequency down-conversion process where high energy pump photon is split into lower energy signal and idler photons [81].

2.3.1. Parametric process

For any pump frequency there is a vast selection of photon pairs that will satisfy the conservation of energy rule. However, only the photons that fulfil the conservation of momentum, which maintains the relative phase between the pump, signal and idler waves, are efficiently

generated. The process is commonly called the phase matching. To meet this relation, the wave vectors k of the created photons must be equal to the wavevector of the pump photon i.e. [82]:

$$k_p = k_s + k_i \quad [2.14]$$

where k_p , k_s and k_i are the wave vector magnitudes of pump, signal and idler waves respectively [80]. Usually the phase matching condition is described by the wave vector mismatch Δk , derived from the formula 2.14 as [82]:

$$\Delta k = k_p - k_s - k_i = \frac{2\pi}{c} \cdot (n_p v_p - n_s v_s - n_i v_i) = 0 \quad [2.15]$$

where n_p , n_s and n_i are the refractive indices of the pump, signal and idler waves within the nonlinear material [82]. To achieve perfect phase matching, the relative phase must be maintained between all waves throughout the nonlinear medium. Initially the most common method to satisfy this requirement was to use birefringent crystals, of which refractive index depends on the polarisation state of the radiation and its direction of propagation. Across the transparency range of such an optical material, with the increase of the photon frequency, the rise of refractive index caused by the dispersion of the material can be observed. As a consequence, the refractive indices of all pump, signal and idler waves are different within the medium. The phase mismatch has direct effect on the efficiency of the nonlinear process. With an analogy to conventional laser gain medium, a parametric gain bandwidth of a nonlinear crystal used in parametric process can be defined. The gain lineshape follows a \sin^2 function and its generic representation is shown in Figure 2.18.

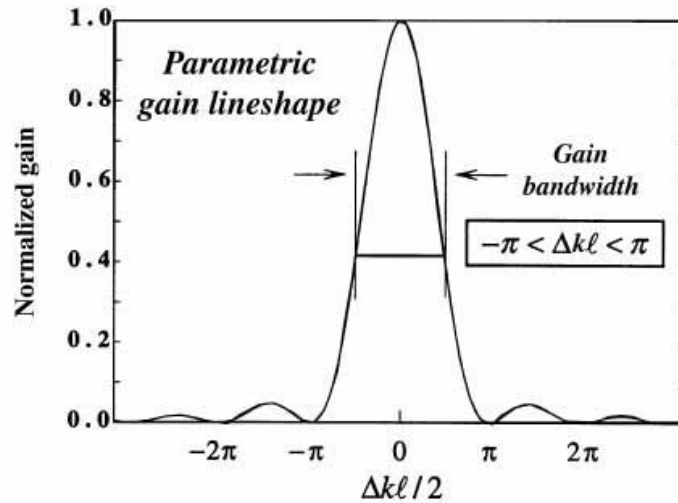


Figure 2.18. The dependence of parametric gain on the phase matching parameter $\Delta kl/2$ [83].

In the arrangements using birefringent materials, the phase matching condition is often controlled by the orientation and temperature of the nonlinear crystal and these impinge on the mechanical

complexity of the optical setup to assure stability of the crystal during the tuning process. Additionally, angles of propagation granting the phase matching rarely coincide with the one resulting in optimal nonlinearity of given material. This results in the parametric process, based on birefringent crystals, having overall relatively lower nonlinear coefficients [81]. Detailed description of birefringence-based phase matching tuning can be found at [84].

These drawbacks of birefringent materials were overcome by the development of periodically poled nonlinear gain media. The advent of this technology was triggered by the development of a quasi-phase matching concept, where the phase mismatch between the interacting waves is corrected at regular intervals using a periodical structure (see Figure 2.19 (a)) engineered into the nonlinear crystal [82]. This new technique not only removed the problems of birefringent materials but also allows one to access the extremely large nonlinear gain as very high nonlinearity of the crystal can be exploited. Although this technique does not allow for perfect phase matching and therefore the highest theoretical nonlinear coefficient is not attainable (due to slight phase mismatch in each domain of periodically poled material), in practice it is much higher than the largest achievable ones with birefringence based phase matching [82]. The crystallographic structure in these materials is periodically inverted inducing continuous change of the phase between incident pump and the generated signal and idler waves. Precise choice of the poling period Λ leads to the phase mismatch correction, so that the phase matching is achieved along the whole optical axis of the crystal. This can be written as [82]:

$$\frac{n_p(\lambda_p, T)}{\lambda_p} - \frac{n_s(\lambda_s, T)}{\lambda_s} - \frac{n_i(\lambda_i, T)}{\lambda_i} - \frac{1}{\Lambda(T)} = 0 \quad [2.16]$$

As indicated in the Equation 2.16, refractive index of the material is a function of the wavelength of interacting fields as well as temperature. Additionally, these crystals are also susceptible to thermal expansion and therefore the designed grating period alters with the change of the temperature. The dependence of these parameters on wavelength and temperature, along with the need for the conservation of energy, enables the OPO utilising these crystals to be tuned by the temperature of the crystal as well as the pump wavelength. This technology was then further expanded, incorporating linear grating period variation across the horizontal axis of the crystal. As a consequence, very rapid tuning of the signal and idler can be achieved by translating the crystal through the circulating pump field [81]. Due to their shape this type of gratings is called a fan-out design, of which an example is illustrated in Figure 2.19 (b). In recent times, more innovative fan-out grating patterns have been demonstrated where the fan distribution of these was slanted (see Figure 2.19 (c)), helping to realise continuous frequency tuning coverage of the crystal [85].



Figure 2.19. Periodically poled nonlinear crystal structure with a) single, b) fan-out [81] and c) slanted fan-out [85] grating periods.

OPOs are highly flexible with regard to both the temporal and the spectral coverage. They operate all the way from the ultra-short (femtosecond) pulse to the continuous-wave (CW) regime and extend from ultraviolet through visible and near-infrared to mid-infrared [86, 80], additionally, with the development of new nonlinear crystals, to the deep-infrared and terahertz spectral regions [80, 87]. This unprecedented flexibility in spectral output is granted by continuously expanding access to various nonlinear crystals. The parametric process of the pump photon down-conversion into the signal and idler ones is not restricted by a particular electronic or vibrational transition. Therefore, the tuning ranges of both these down converted photons are limited only by the transparency of the nonlinear material in which they are generated. Thanks to this property, it is possible to manufacture devices with very broad tuning range in the signal and idler waves. Figure 2.20 depicts the selection of various materials and their operational regimes.

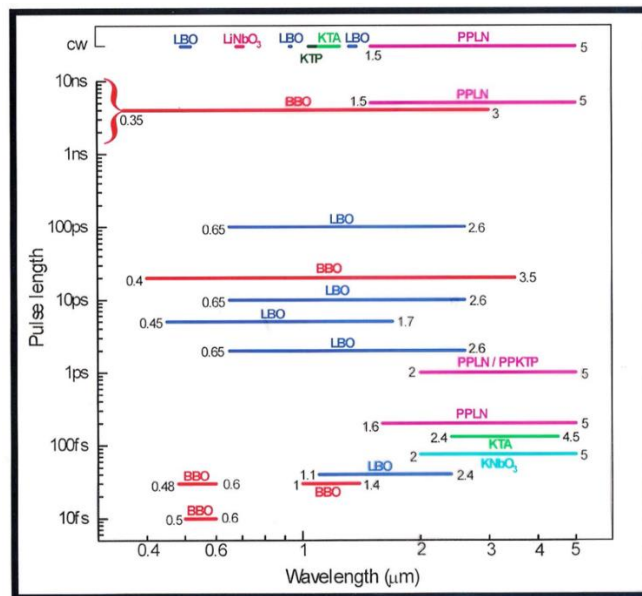


Figure 2.20. Spectral (up to mid-infrared) and temporal coverage of OPOs based on selection of nonlinear crystals [86].

In this dissertation, only the quasi phase matching scheme based OPOs with the periodically-poled LiNbO₃ (PPLN) as the nonlinear crystal are considered, as only this technique was used in all the presented developments. As indicated in Figure 2.20, this type of material operates across the near- and mid-infrared. Wavelength tuning of the OPO, based on single grating crystal, can be achieved by variation of the temperature. Data presented in Figure 2.21 (a) illustrate the tuning achieved based on crystal's temperature variation over the range 35–180 °C. This graph demonstrates the spectral coverage of the OPO with 8 different grating periods Λ , ranging from 28.5 μm up to 29.9 μm [88, 81]. Figure 2.21 (b) demonstrates the tuning of the OPO, based on fan-out design. In this configuration, the main route for the frequency selection is created by the translation of the crystal through the pump beam, continuously changing the grating period at the spot of the incident pump beam.

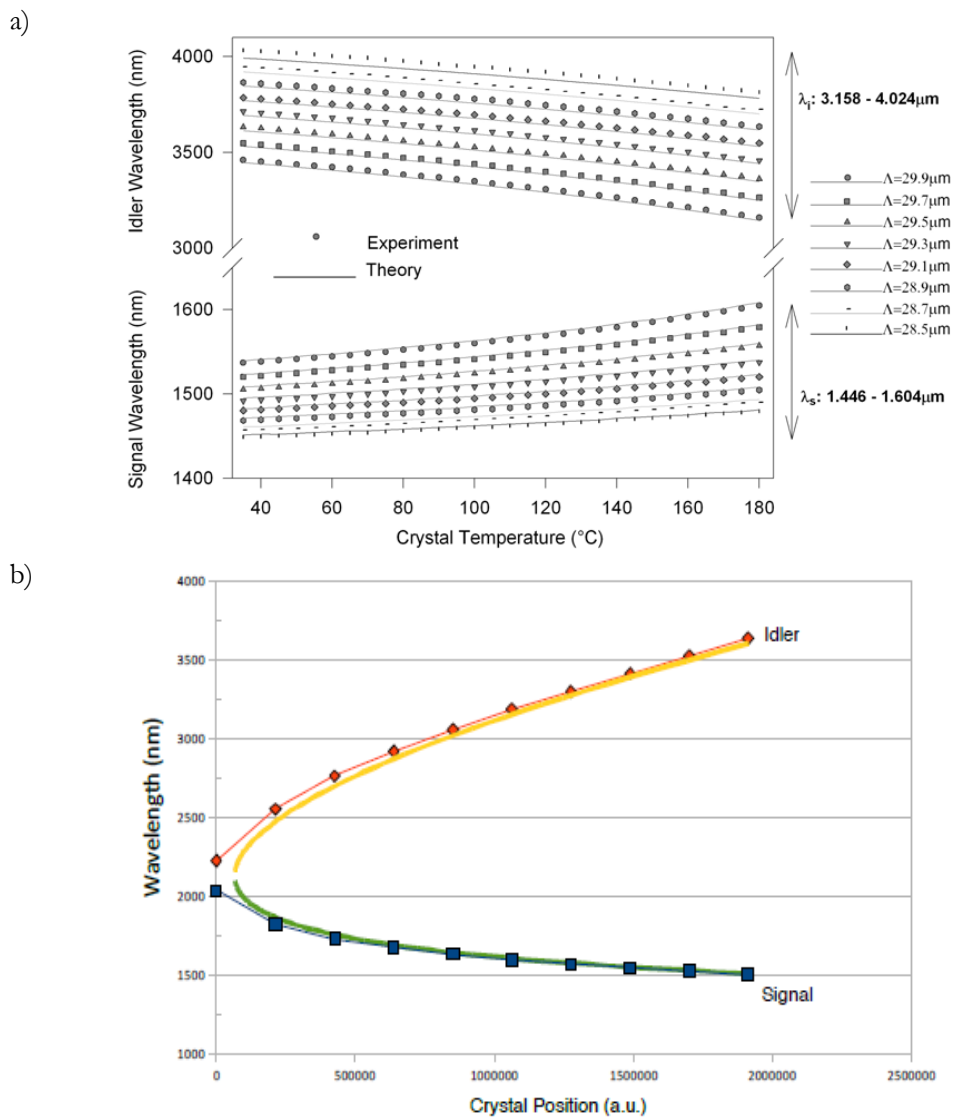


Figure 2.21. Wavelength tuning with a) single grating PPLN crystal with the temperature and grating tuning [81] and b) fan-out grating PPLN crystal with the crystal position changing [89].

In this example wavelength tuning covered the range of $1.5 - 2.1 \mu\text{m}$ and $2.2 - 3.7 \mu\text{m}$ for the signal and idler waves respectively. It is noticeable that the near-IR signal band does not meet the mid-IR band of idler. The point where the pump photon is split equally into the two photons is called degeneracy and results in generating the signal and idler waves at the same frequency. Even if it is possible, this was not achieved in demonstrated example due to the limitations of the chosen poling period, coatings of optical components and practicality of the temperature tuning [88].

With these exceptional tuning capabilities, OPOs found their strong position in near- and especially mid-infrared spectroscopy applications. Although, all temporal configurations are suitable for this purpose, requirements of the selected high-resolution spectroscopic applications can be met only by the very narrow linewidth achieved in the CW regime [90, 91]. Various configurations of Optical Parametric Oscillators have been developed over the years and each of them has a set of specific characteristics.

2.3.2. Cavity configurations

In the previous section, the nonlinear crystals were mentioned as the gain media of the parametric process. The gain of a device is regulated by the properties of these crystals and the applied pumping intensities. The majority of the available configurations conform to the low gain limits (corresponding to parametric generation when using CW or low to moderate peak power pulsed pump sources) [83]. Due to this fact, the single pass of the pump field through the crystal does not cause the macroscopic down-conversion effects. With analogy to the classical laser configuration, where the lasing is achieved with sufficient feedback to the crystal by the optical oscillation, the low gain arrangements induce the macroscopic level parametric waves through sufficient feedback of the generated waves. This is achieved by enclosing the nonlinear gain medium within the optical cavity, and devices employing this configuration are called the optical parametric oscillators. On the other hand, macroscopic levels of generated waves, with single (or few) passes through nonlinear material, are possible through the arrangements with very high parametric gain. These devices are called optical parametric generators (OPGs) and amplifiers (OPAs) [83]. The details of these systems can be found in literature [92] but in this dissertation only the OPO configuration will be investigated.

To discuss the cavity configurations of the OPOs, it is important to define the pump field affecting this arrangement. As indicated above, these devices split the higher energy (shorter wavelength) photons to the lower energy ones (of longer wavelengths). As such, OPOs are typically pumped by well-behaved, solid-state lasers, such as Nd:YAG and Nd:YVO₄. These are used at their output wavelength (1064nm) but also frequency doubled (532nm) and quadrupled

(266nm) [93, 80]. Many other lasers, such as Ti:sapphire [94], semiconductor disk laser (VECSEL) [95], Ho:YLF [96] and Er:YLF [97], have been utilised as a pump for successful operation of optical parametric oscillators. The pump field is irradiated onto the nonlinear crystal placed within the optical cavity and as soon as the pump power reaches the threshold of parametric process, the down-converted waves are generated. Over the years, various configurations of the optical cavities as well as arrangements of oscillating and generated fields were developed. Figure 2.22 demonstrates an overview of selected cavity configurations, illustrating the most common OPO arrangements. Since there are two down-converted fields created as the result of the parametric process, signal and idler, there are two generic groups of OPOs in which only one field resonates in the cavity (singly resonant oscillator, SRO – Figure 2.22 (a)) or the one, where both fields oscillate simultaneously (doubly resonant oscillator, DRO – Figure 2.22 (b)). The main advantage of the latter configuration is the fact that presence of both created waves in the field resonating through the gain medium, significantly reduces the required pump power for the device to reach threshold. However, the stability of such a cavity, as well as smooth tuning, are difficult to obtain and these are their main disadvantages. The instabilities of this configuration are mainly caused by very high resonance requirements. In order to keep both signal and idler waves on resonance, the cavity length of the OPO must be stabilised to within 1nm [82]. Additionally, there is also the doublet constraint of phase matching and frequency conservation between pump, signal and idler waves [83]. The same limitations make smooth tuning of the DRO configuration very difficult. The successful mitigation of these drawbacks was the introduction of the dual cavity doubly resonant configuration – Figure 2.22 (e). In this approach one oscillating field acts as a master and the other a slave adjusted by an actively actuated mirror to produce single mode pair output. This configuration significantly improves optical stability and allows a smooth tuning of both down-converted waves. Alternatively, an SRO approach can be utilised, where only one down-converted wave oscillates in the cavity but the parametric threshold is supported by additional resonance of the pump field through the nonlinear crystal. There are two configurations enabling this method. The first one relies on the resonance of the pump wave irradiated onto the nonlinear medium, in so called enhancement cavity, from a separate pump laser (pump enhanced singly resonant oscillator, PE-SRO – Figure 2.22 (c)), which also may benefit from the dual cavity configuration – Figure 2.22 (g). The other method utilises very high oscillating pump field by placing the nonlinear medium directly inside the pump cavity (intracavity singly resonant oscillator, IC-SRO – Figure 2.22 (d)). Additionally, both these configurations can be also developed in doubly resonant scheme [83]. These are only the main operation modes of OPOs, but novel configurations are being demonstrated, overcoming various problems of these systems and exploiting advantages of numerous arrangements. For instance, a new method for building a doubly resonant OPO – nested cavity doubly resonant optical parametric oscillator, NesCOPO –

improves the stability and tuning process of this technique allowing generation of broadly tuneable, single frequency mid-infrared radiation in very compact cavity arrangement [98, 85]. The introduced above OPO configurations operate as the standing wave oscillators, however ring resonators are also valid as OPO cavities, especially for generation of single-frequency radiation [94, 99].

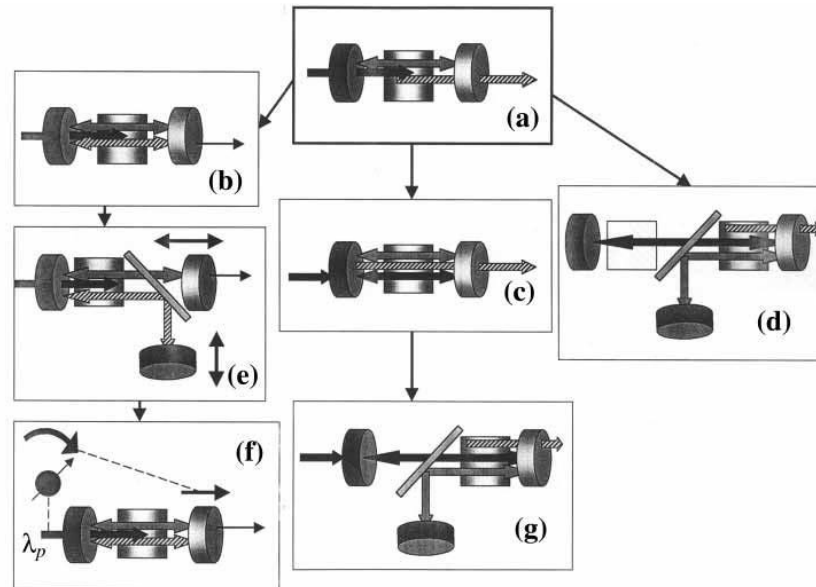


Figure 2.22. Cavity configurations for CW OPOs: (a) singly resonant; (b) doubly resonant; (c) pump enhanced; (d) intracavity; (e) dual cavity, doubly resonant; (f) doubly resonant, with pump tuning; and (g) dual cavity, pump enhanced. Black, grey, and striped arrows indicate the pump, signal and idler waves, respectively. Nonlinear media and gain media are shown by darker and lighter shading, respectively [83].

All the cavity designs described above consider continuous wave operation. However, as indicated earlier in this text and shown in Figure 2.20, the OPOs work in variety of temporal regimes. In conclusion, the singly resonant oscillator is the simplest and, due to its high stability, the most practical configuration. Nevertheless, from all available OPOs' designs, SRO requires the highest pump power in order to reach the threshold of parametric process. Next to very high power CW lasers, this configuration can be pumped by high peak-power pulsed laser sources. Variety of systems, spanning from nano- to femtosecond pulse duration, are suitable for pumping the OPOs. Basic principles of these systems are similar to those of CW oscillators, but their temporal characteristics can be changed by the pulsed regime. Overview of these features for each temporal domain is presented in [83].

Considering the location of the nonlinear gain medium with relation to the pump laser cavity, all the aforementioned configurations can be classified as externally pumped, or more commonly as: extra-cavity (EC) and intracavity (IC). The former, as described above, consist of

an optical parametric oscillator which is pumped from an external laser cavity. When the parametric gain overcomes the round-trip loss experienced by the resonant wave, the OPO reaches the threshold and the down-conversion from the incident pumping wave to signal and idler begins [81]. However, in these arrangements, especially EC-SRO, large pumping powers are required to cross the threshold level (which initially was the main obstacle for wide application of these devices). Introduction of the periodically-poled nonlinear materials, most notably the now ubiquitous PPLN crystal and low loss optical coatings, helped to lower the threshold to the required pumping power of 3-5W [81]. Important characteristic of these devices is the fact that they exhibit good down-conversion efficiency only when pumped sufficiently far (about 2.5 times) above their threshold condition. This indicates their very high efficiency when generating multi-watt output in the down-converted fields. On the other hand, due to the work close to the threshold regime, they are very inefficient when operated in relatively low powers (lower than 1W) [100]. This characteristic of EC-OPO, next to requirement of high power pump lasers, may be considered a disadvantage because many potential applications of a broadly tuneable mid-IR source only require moderate power levels.

In the other category – the intracavity geometry – the nonlinear medium of the optical parametric oscillator is placed inside the cavity of the parent pump laser. Due to a much higher intensity of the circulating coherent radiation within the cavity, compared to what can be out-coupled from it (typically between 10 to 20 times greater [100]), the parametric generation process can be brought to the threshold with a much smaller pump laser (in terms of both its power and size) compared to the EC-OPO geometry. More detailed description of this technique is presented in the following section.

2.3.3. IC-OPO

As indicated in previous section, the intracavity configuration of the OPO is created by placing the nonlinear gain material inside the optical cavity of the parent laser. This provides the parametric process with access to the very high oscillating pump field, enabling the OPO to reach the threshold at much lower primary power levels when compared to extra-cavity arrangements. Additionally, as a result of this geometry, the creation of very compact and efficient devices, capable of emitting hundreds of milliwatts of down-converted waves with as low as 1W of primary pump is possible [81]. Lower power requirement obviates the need for bulky pump lasers, water cooling and high electrical power consumption. It releases these devices from research labs, exposing them to new ranges of applications.

Before describing the other properties of the IC-OPO devices, their basic structure is presented below. It is done on the example of basic design that was a precursor of all developments across the projects presented in this dissertation. Figure 2.23 shows an illustrative diagram of this device.

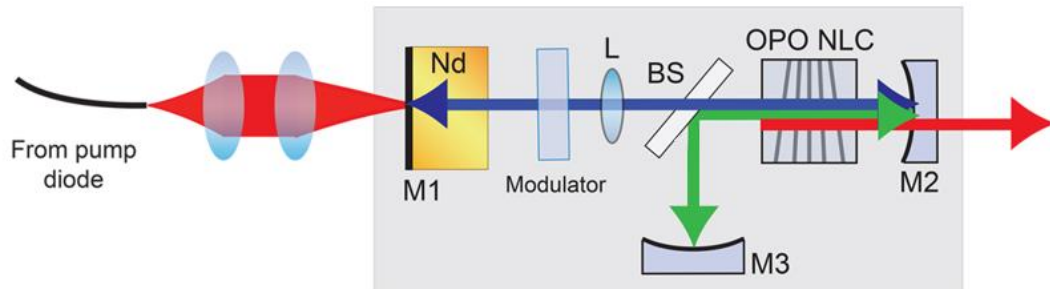


Figure 2.23. Basic diagram of an IC-OPO.

In this example the parent laser is based on the Nd:YVO₄ crystal pumped by fibre coupled laser diode. Typically, this type of gain material is pumped at its strongest absorption line, 808nm [81], and this is used in this example, however other pumping wavelengths have also been demonstrated for the same laser gain medium [101]. The primary pump illumination is at first collimated and subsequently focused into the gain material. The parent pump laser cavity, oscillating at 1064nm, is set by mirrors M1 and M2. The former one is a coating applied onto the outer surface of the laser gain crystal providing anti-reflective (AR) property for the primary pump at 808nm and high reflectivity for the oscillating 1064nm wave. The second mirror (M2) is also highly-reflecting (HR) coated for pump wavelength, but since it creates one end of the cavity for the oscillating down-converted field, it is also HR coated for these wavelengths – for the purpose of the example the HR coating is for the range of 1400nm – 1800nm, enabling oscillation of the signal wave. Within the pump cavity there is an optional (in case of pulsed operation regime) modulator (for instance acousto-optic for nanosecond operation), with crystal surface AR coated for 1064nm. An intracavity lens L, also AR coated for pump wavelength, assures suitable focus of the resonating field into the nonlinear gain material – here the fan-grated PPLN crystal. The beam splitter (BS) is a dichroic element that is highly transmissive for pump wave (also AR coated) but on one side it's highly reflective for the wavelengths of the oscillating down-converted field. This element bends the resonating arm of the OPO, arranged between mirrors M2 and M3. Mirror M3, similar to M2, is HR coated for the band of oscillating signal wave (in this example), with the exception of the HR requirement for the pump. Mirror M2 is highly transmissive for the other down-converted field (in this example idler) and therefore this one is directly irradiated outside the cavity. Since the parent laser and OPO have merged into single cavity in the IC-OPO configuration, there is no more direct output coupling of the 1064nm wave and the leaking non-

resonant down-converted field is the only output of this arrangement (neglecting the pump and signal fields that leak through M2, M3 and BS due to imperfect coatings). In fact, the parametric process indeed acts as the output coupler for these devices and the relation between pump field and the output-coupled power is discussed in the following section.

2.3.3.1. Threshold, power and efficiency

Before the power characterisation of the IC-OPO are discussed, it is important to define the meaning of the down-converted field. Although two separate waves, signal and idler, are created during parametric process, when this system is considered as an output coupler of the pump laser, the out-coupled field is the total down-converted one, consisting of both signal and idler. The power P_{DC} of such defined field can be expressed as a function of input laser power and threshold levels [82]:

$$P_{DC} = \sigma_{max}(P_{in} - P_{th}^{OPO}) \left(1 - \frac{P_{th}^L}{P_{th}^{OPO}}\right) \quad [2.17]$$

where P_{in} is the primary input power at 808 nm, P_{th}^L is the pump power at laser threshold and P_{th}^{OPO} is the pump power at OPO threshold and σ_{max} stands for the output slope efficiency of the pump laser that accounts for the coupling efficiency between the power of external primary pump source and oscillating laser field at 1064 nm. It can be expressed as [82]:

$$\sigma_{max} = \eta_{in}\eta_{abs} \frac{\lambda_{p-in}}{\lambda_p} \quad [2.18]$$

Where η_{in} is the optical coupling efficiency of the primary pump laser at λ_{p-in} to the parent laser gain medium, η_{abs} is the amount of this pump power that is absorbed and λ_{p-in} and λ_p are the wavelengths of the primary pump source (808 nm) and parent pump laser (1064 nm), respectively.

As presented in the previous section, the reduced pumping power threshold of the parametric process in the IC-OPO configuration (in comparison to externally pumped devices), and in result, reduced requirement for primary pump power, is one of its most significant advantages. However, using the maximum power of given primary source for pumping to obtain an arrangement characterised by a very low parametric threshold level, does not necessary mean the highest possible down-converted output. Since the IC-OPO should be considered as an output coupler for the parent laser, for maximum down-conversion efficiency it must be designed to act as an optimal output coupler for a laser pumped by the given primary source. As demonstrated by Colville et al. [102], the threshold of the OPO resulting in optimal performance and maximised output coupling (efficiency) is a function of the threshold power of parent laser and the primary pump power [82]:

$$P_{th}^{OPO} = \sqrt{P_{th}^L \cdot P_{in}} \quad [2.19]$$

Under this condition, the maximum total down-converted power, indicated as P_{DC_max} , attainable for specific input pump power can be presented as [82]:

$$P_{DC_max} = \sigma_{max} \left(\sqrt{P_{in}} - \sqrt{P_{th}^L} \right)^2 \equiv P_{out_max}^L \quad [2.20]$$

As shown in this equation, identically to the maximum total down-converted power P_{DC_max} , it describes the maximum obtainable output power from the pump laser $P_{out_max}^L$ at given input power. When operating the OPO in accordance with formula 2.19, its performance is analogous to an optimal output coupler of its parent laser and, for given primary pump, the maximum down-conversion occurs. This means that, while the system is designed to obey this equation, 100% of the maximum output power potentially attainable from the optimally output coupled parent laser at the fundamental frequency, can undergo down-conversion in the parametric process. This optimal condition can be derived by comparing the Equations 2.17 and 2.20, resulting in [82]:

$$P_{in} = \frac{(P_{th}^{OPO})^2}{P_{th}^L} \quad [2.21]$$

These optimisation conditions are illustrated in Figure 2.24, which demonstrates the characteristics of output power and efficiency of the IC-OPO as a function of primary pump power.

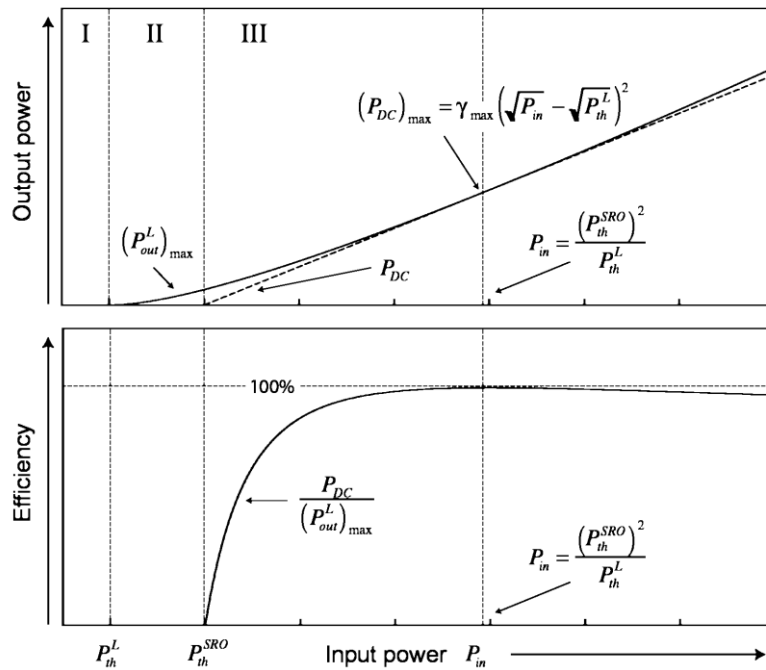


Figure 2.24. Down-conversion parameters of an IC-OPO [82].

Realistically, it is difficult to obtain 100% efficiency in experimental setup. However, the suitable designs of the IC-OPO cavity and its parent laser one allow to readily obtain the efficiency performance over 90% [103]. If the OPO would be brought to threshold too soon, then at the maximum of accessible primary pump power, the laser will be over-coupled, which results in reduced efficiency. Although, very low value of the threshold for parametric process that enables applying the lower power primary pumping sources is highly desirable, this over-coupling effect explains why use of very powerful pump lasers in this threshold configuration may lead to reduced down-conversion.

As shown in Figure 2.24, the operation of IC-OPO can be characterised by three regions that are examined with respect of primary input power. Across the first region, the input power is below the parent laser threshold $P_{in} < P_{th}^L$. As the laser in this region is unable to sustain oscillation, the intracavity field remains negligible. With further increase of the input power, the laser gain saturation occurs and lasing threshold is obtained. From that moment, the oscillating pump field rises linearly with the primary input power and continue until the threshold of the parametric process P_{th}^{OPO} is reached, that defines the second operational region $P_{th}^L < P_{in} < P_{th}^{OPO}$. When the parametric oscillator is brought above threshold, the system enters the third region $P_{in} > P_{th}^{OPO}$. These three regions are once again shown in Figure 2.25 where the behaviour of the down-converted power and the intracavity pump power are illustrated as a function of the input power.

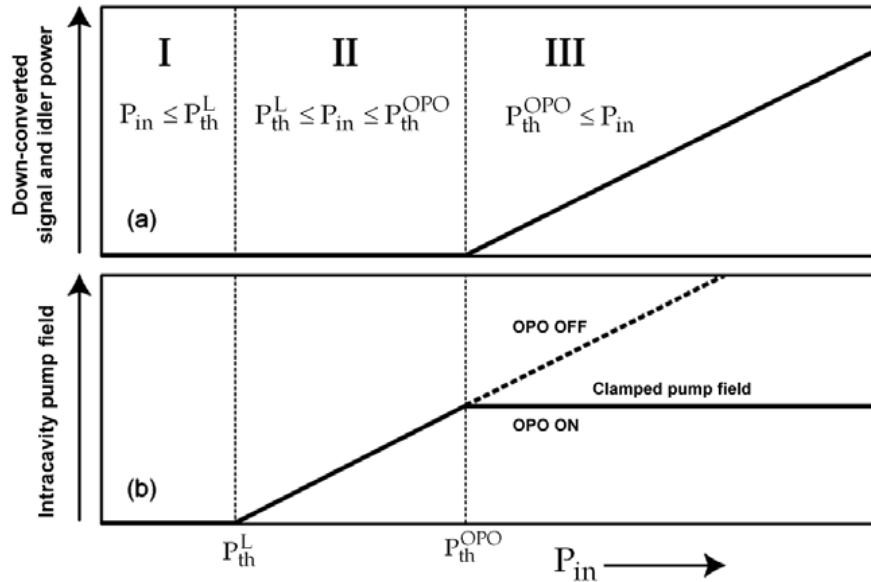


Figure 2.25. (a) Linear output power of OPO once above threshold and (b) clamping effect of the IC-OPO upon the circulating field [81].

When the threshold of the parametric process is reached, the resonating pump field is ‘clamped’ at the P_{th}^{OPO} value. As such, it can be compared to an optical version of Zener diode, where the Zener Current increases with rising of the reverse voltage, up to the specified Breakdown Voltage, at which point the current gets stabilised over very wide range of voltages. Similarly, IC-OPO stabilises the pump power beyond the P_{th}^{OPO} value and further increase of the primary pump is transferred through the oscillating field of parent laser and converted by the parametric process to the linear growth of power in down-converted signal and idler waves. This effect is shown in Figure 2.25 (b). Good quality clamping is one of the inspection criteria during characterisation of the IC-OPO, it indicates a well-designed parent laser and signal cavities as well as good stability against any thermal effects present in laser gain and nonlinear crystals [81]. Thermal effects, such as thermal lensing and thermal expansion of nonlinear crystal grating period, can have significant influence on the behaviour of the laser system [82]. Regardless if this impact is induced internally by interaction of the oscillating optical field with the optical material or is it an external effect caused by thermal air currents, thermal control of the laser gain and nonlinear crystals plays important role in the stabilisation of the system’s performance. Detailed analysis of optical parametric oscillators’ power characteristics can be found in [81, 82, 83, 104, 103].

2.3.3.2. Relaxation oscillations

As introduced above, the IC-OPOs exhibit the high-power output and very good down-conversion efficiency. That, together with very broad tuning range and compact structure of the device, make them a desirable choice as illumination sources for spectroscopic applications. However, it has been found that the intracavity concept also makes them prone to outbursts of spontaneous and long-lived relaxations oscillations. These are the erratic power variations around the steady state value, caused by a mutual coupling of the energy stored in the upper state of the lasing transition in the gain medium and the mode oscillating in the optical cavity. This process impacts the amplitude and frequency stability of these devices and, if not managed, can limit their applications to very crude operations in CW mode [105, 100].

Neodymium-based lasers, due to their high gain, ease of pumping and technological maturity, are ideally suited as pump sources for IC-OPOs. Generally, these lasers are susceptible to relaxation oscillations, because the upper state lifetime in this gain material is much longer than the typical decay times for laser radiation inside the optical cavity. Nevertheless, they are generally strongly damped and typically are well-managed, not hampering practical development of CW operating devices. Figure 2.26 (a) shows a regular trace of neodymium-based laser achieving the steady state operation through the highly damped relaxation oscillation. Placing the OPO within the laser

cavity and operating in an IC-OPO configuration has significantly worsened this process as shown in Figure 2.26 (b). In this arrangement, aside from the parent pump laser, there is also another optical cavity sustaining oscillation of one down-converted wave (e.g. signal wave in SRO design) and the energy stored in this field, coupled through the nonlinear crystal to the pump field introduces the third factor affecting relaxation oscillations. As illustrated in Figure 2.26 (b), under this circumstance, the frequency and damping time of relaxation oscillations are significantly increased [104, 105]. This very long damping time leads to quasi-random and long-lived oscillatory outbursts of the pump field translating to high level of amplitude and frequency fluctuations in the idler output.

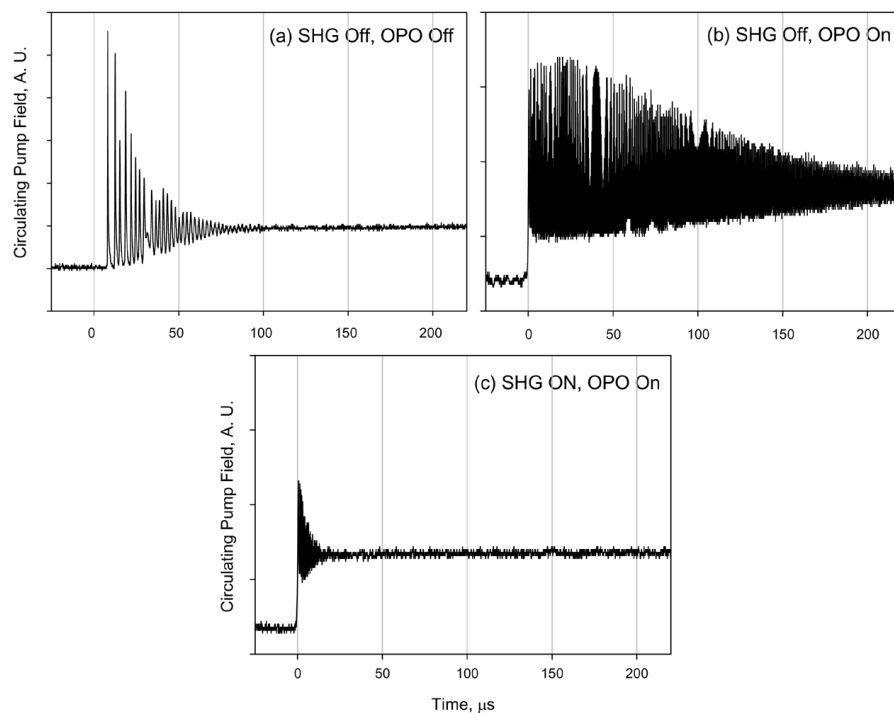


Figure 2.26. Typical measured traces of the transient behaviour of the ICOPO with (a) down-conversion suppressed (i.e. laser operation only), (b) down-conversion permitted (with no SHG) and (c) both down-conversion and SHG enabled [100].

Several methods for smoothing the relaxation oscillations has been suggested [81, 100]. One potential solution mitigating this phenomenon is to operate the pump laser in the Q-switched, pulsed mode. This helps to avoid the issue of relaxation oscillations because of the short pulse duration [106]. An additional advantage of this arrangement is that the very high peak powers, circulating within the parent laser cavity, make the total system insensitive to the effects of optical loss, which in turn significantly extends the tuning range of such a device [107]. However, operation of the IC-OPO in a pulsed regime leads to significant broadening of the line-width of

the down-converted waves and as such, it limits the use of the technique for applications where detection of very fine spectral features is required.

An alternative solution is based on the introduction of a frequency doubling crystal inside the pump cavity. This method significantly reduces the damping time (by a factor of approximately 50,000 [81]) of the relaxation oscillations and leads to the steady state even faster than the pump laser itself. The performance is shown in Figure 2.26 (c). This technique exhibits such an outstanding performance because the second harmonic generation (SHG) can be considered as an optical loss, placed within the cavity of pump laser, which is proportional to the square of the power oscillating. It is fully passive and instantaneous which makes it a very attractive solution for practical implementation in IC-OPO based devices. Applying this technique induces an optical loss, however it incurs only a marginal (approximately 5% [81]) drop in down-converted power and it is an insignificant price to pay for the transient stability of the system.

The final method relies on selecting the different pump lasers. The relaxation oscillation is especially a problem for Neodymium based gain materials. However, this effect is completely eliminated when choosing a pump laser with significantly shorter upper-state lifetime. Figure 2.27 illustrates the comparison of transient behaviour of IC-OPO based on Nd:YVO₄ and a VECSEL, showing excellent performance of the former laser without any oscillation at all. A detailed study and description of relaxation oscillations mitigation techniques can be found in [81, 100, 95, 82, 105].

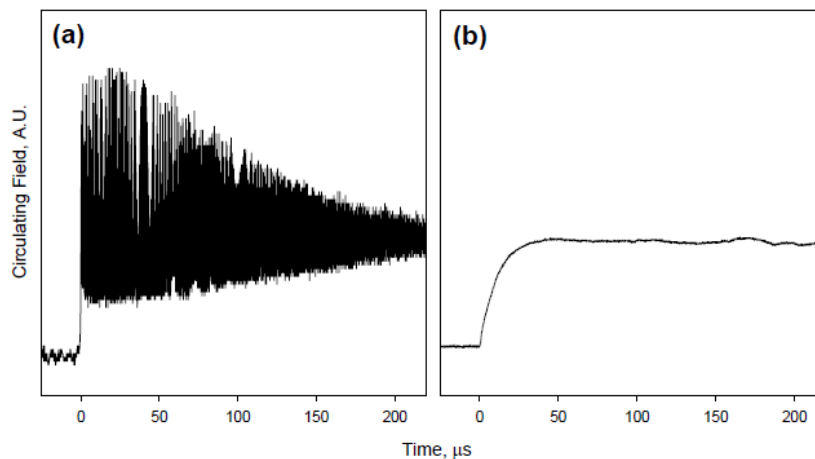


Figure 2.27. Recovery transient dynamics after perturbation of the steady state of an IC-OPO pumped internal to (a) an Nd:YVO₄ and (b) VECSEL laser [95].

This is a very brief introduction to the optical parametric oscillators and in particular the intracavity configuration of these devices. Extensive information about these systems can be found for instance in [80, 83, 82, 103, 81].

2.4. Laser scanning

As indicated in the introduction to this dissertation, a big part of the work done over the course of this programme was focused on the laser-based imaging and application of optical parametric oscillators as a broadly tuneable illumination sources for hyperspectral imaging. The description of merits of lasers for spectroscopic applications (including imaging spectroscopy), as a technology enabling access to the mid-IR bands, can be found in Chapter 1. Given that the illumination source and co-aligned single point detector create the core of the optical arrangement for the point spectroscopy, the imaging setup requires further consideration with respect to the optical path.

In general, there are two common methods for performing the laser-based imaging that can be distinguished by point or flood illumination. The difference between these two is manifested in the shape of optical beam and the type of detector. The former technique employs a high intensity, small diameter and collimated beam, scanned across the object of interest, where the back reflected radiation is captured by a single element detector and the collected data is reconstructed to form an image. The latter method requires a broad-beamed illumination of the scene (achieved by the controlled divergence of the laser beam) with the 2D detector array recording the reflected energy directly in the form of an image. There may be other embodiments of laser-based imaging that employ linear detector arrays, and these utilise either of the two illumination methods. Although, the flood illumination techniques has been demonstrated in practice (e.g. [108]), it requires a very high intensity beam that, even after divergence, will provide sufficient illumination of the scene and a detector array. This is increasingly important for the longer wavelengths of the illumination source, as the Black Body Radiation of all the elements of the inspected scene would have significant impact on the detected signal. Additionally, such a detector is a very expensive element, significantly affecting the cost of the whole imaging system. In this text, only the point illumination technique with a single point detector will be described, as employing this method allows one to achieve solutions at significantly lower costs and increased flexibility in spatial and spectral coverage of the device.

The key component to the single point imaging is a scanning setup. The scan can be done on the side of the illumination/imaging device, on the side of the inspected scene or as a combination of both. When the data acquisition is done with the device without a scanner, the imaged object must be translated in front of the fixed beam (for instance, mounted on the linear translation stages in X-Y arrangement) and pixels of the image linked with the coordinates of the translation mechanisms. Although, this configuration is possible and it may be used in some specific applications, it is not very practical, as it requires interaction with the imaged object in order to capture the data. When the scanner is in proximity (or even integrated) to the illumination

source, the image acquisition is independent from the inspected scene. Scans performed by these devices can be uni- or bidirectional and can be done employing a multitude of solutions. When a unidirectional scanner (line scan) is used, there is usually a requirement for relative movement between imaging device and the scene of interest. This can be achieved by mounting the linear scanner on a moving vehicle (e.g. airplane) where the carrier's motion provides the other dimension necessary to create an image. Although, in this situation, the imaging device has only a single axis scanner, it is mounted on moving platform and therefore is independent from imaged scene. In another example, the linear scanner is installed above the moving objects (e.g. conveyor belt transporting objects of interest) which provides the relative movement necessary to recreate an image. Even if, this kind of imager cannot work on its own, it is a desirable scheme for selected applications.

There are several common modalities of scanners used with the laser arrangements and, to some extent each of them could be used for imaging applications. The most common ones are oscillating mirrors, rotating polygons [109, 110], acousto-optic deflectors [110, 111], Palmer scanners [109], Risley prisms [112] and recently, also scanners based on microelectromechanical systems (MEMS) [111]. Other scanning configurations, like pan-tilt, rotation or F-theta are also available but are rarely used for 2D imaging applications. Palmer scanners and Risley prisms, the bidirectional devices (that by their nature scan in two dimensions), are also not used for imaging as often as the alternative arrangements, due to the circular nature of their scan pattern. Oscillation mirrors and rotating polygons in their basic state are unidirectional (single axis scan), however they are usually arranged as a pair of mirrors or polygon and mirror set, assuring two-dimensional scan. Figure 2.28 illustrates the imaging arrangement used during the development of the OPO based hyperspectral imager - Firefly IR Imager [89], where the rotating polygon and oscillating mirror provide the two-dimensional data set. The radiation from the optical parametric oscillator (red lines) is sent along its optical axis, reflected by a small plane mirror m placed on axis in front of the calcium fluoride (CaF_2) collection lens L towards the polygon scanner PS and subsequently through the tilting mirror TM to the scene of interest. The back-scattered radiation returning from the scene (blue lines) is collected via the same tilting mirror and the polygon scanner, then focused by the collection lens L onto the detector D located in the image plane of this collection lens.

The setup presented in Figure 2.28 ensures that the detector D always inspects the same scene that is currently illuminated by the radiation extracted from OPO. This means that the observation direction is spatially synchronised with the illuminating beam. The lens LC placed before the micro mirror m enables the focusing of the illuminating radiation on the imaged object. Since the employed detector D displays sensitivity over a broad range of wavelengths, a band passing filter F is placed in close distance from the MCT detector to minimise the influence of

the stray infrared radiation that could be potentially recorded from hot objects or signal field leaking from the OPO. A Helium-Neon laser and detector *TD* are used for triggering the image acquisition process and controlling the polygon rotation [113]. In the final, commercialised equipment, this system has been replaced by two oscillating mirrors, providing a physically more compact device of similar functionality.

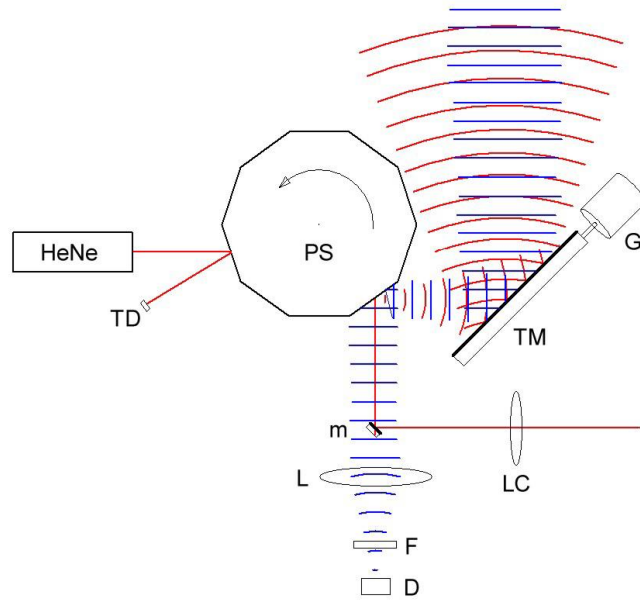


Figure 2.28. Sketch of the imaging set-up from [113]: HeNe – helium neon laser, TD – triggering detector, PS – polygon scanner, TM – tilting mirror, G – galvanometer, m – micro-mirror, LC – illumination focusing lens, L – collection lens, F – band pass filter, D – MCT detector.

Overall, a set of various parameters can describe the image scanning setup, such as maximum angles of the beam deflection, spot size of illuminating laser, distance from the object, spacing and number of points per one line of scan. They are different for each scanning embodiment and will not be discussed in this chapter. Some of these parameters are presented in Chapter 3 with respect to the imaging process with the Firefly IR Imager.

2.5. Conclusions

The two fields of science which underpin the projects presented in the remainder of this dissertation portfolio – classification algorithms and optical parametric oscillators – have been introduced and briefly discussed in this chapter. Various signal processing techniques can be employed to extract the sought after information from the sensor output data and simplify the analysis of the problem. Out of many processes necessary for this information extraction, the

classification techniques are the ones of high importance. The initial introduction to all the standard steps that are necessary to perform a successful classification has been done and subsequently, a survey of various approaches for this task demonstrated with examples of corresponding algorithms that can be applied to perform it. From this extensive list of available tools two have been chosen – Support Vector Machine and Partial Least Squares regression, for detailed introduction of their key aspects and demonstration of data analysis and results representation.

Optical parametric oscillators represent the other technology key for the demonstrated research. In this chapter, the underpinning parametric process, enabling the frequency down-conversion and ultimately providing the tuneable source to access the mid-infrared spectral range has been presented. The discussion on various configurations of these devices, mainly focussing on the intracavity type, as this arrangement was used in all the projects demonstrated in this dissertation was described.

Finally, the laser scanning techniques that allows acquisition of spatial data with single point illumination and detection have been introduced and an example of such a setup shown, describing its mechanism and the propagation of optical waves. This chapter introduces the necessary background information for the following three chapters.

References

- [1] S. Murai, Remote sensing note, Japan association on Remote Sensing, 1993.
- [2] J. J. Furtado, Z. Cai and L. Xiaobo, “Digital image processing: supervised classification using generic algorithm in Matlab toolbox,” *Report and Opinion*, vol. 2, no. 6, pp. 53-61, 2010.
- [3] D. Lu and Q. Weng, “A survey of image classification methods and techniques for improving classification performance,” *International Journal of Remote Sensing*, vol. 28, no. 5, p. 823–870, 2007.
- [4] L. Jiang, B. Zhu and Y. Tao, “Hyperspectral Image Classification Methods,” in *Hyperspectral Imaging for Food Quality Analysis and Control*, London, Elsevier, 2010, pp. 79-98.
- [5] H. Yao and D. Lewis, “Spectral Preprocessing and Calibration Techniques,” in *Hyperspectral Imaging for Food Quality Analysis and Control*, London, Elsevier, 2010, pp. 45-78.
- [6] M. Dash and H. Liu, “Feature selection for classification,” *Intelligent Data Analysis*, vol. 1, no. 1-4, pp. 131-156, 1997.

- [7] G. Hughes, "On the mean accuracy of statistical pattern recognizers," *IEEE Transactions on Information Theory*, vol. 14, p. 55–63, 1968.
- [8] J. Tang, S. Alelyani and H. Liu, "Feature Selection for Classification: A Review," in *Data Classification: Algorithms and Applications*, CRC Press, 2014, pp. 1-29.
- [9] J. d. Leeuw, H. Jia, L. Yang, X. Liu, K. Schmidt and A. K. Skidmore, "Comparing accuracy assessments to infer superiority of image classification methods," *International Journal of Remote Sensing*, vol. 27, no. 1, pp. 223-232, 2007.
- [10] I. Lizarazo, "Accuracy assessment of object-based image classification: another STEP," *International Journal of Remote Sensing*, vol. 35, no. 16, pp. 6135-6156, 2014.
- [11] D. Huang, S. Xu, J. Sun, S. Liang, W. Song and Z. Wang, "Accuracy assessment model for classification result of remote sensing image based on spatial sampling," *Journal of Applied Remote Sensing*, vol. 11, no. 4, p. 046023, 2017.
- [12] J. Cihlar, Q. Xiao, J. Chen, J. Beaubian, K. Fung and R. Latifovic, "Classification by progressive generalization: a new automated methodology for remote sensing multispectral data," *International Journal of Remote Sensing*, vol. 19, pp. 2685-2704, 1998.
- [13] R. S. Defries and J. .. Chan, "Multiple criteria for evaluating machine learning algorithms for land cover classification from satellite data," *Remote Sensing of Environment*, vol. 74, pp. 503-515, 2000.
- [14] P. M. Harris and S. J. Ventura, "The integration of geographic data with remotely sensed imagery to improve classification in an urban area," *Photogrammetric Engineering and Remote Sensing*, vol. 61, p. 993–998, 1995.
- [15] W. L. Stefanov, M. S. Ramsey and P. R. Christensen, "Monitoring urban land cover change: an expert system approach to land cover classification of semiarid to arid urban centers," *Remote Sensing of Environment*, vol. 77, p. 173–185, 2001.
- [16] A. Polak, T. Kelman, P. Murray, S. Marshall, D. J. M. Stothard, N. Eastaugh and F. Eastaugh, "Hyperspectral imaging combined with data classification techniques as an aid for artwork authentication," *Journal of Cultural Heritage*, vol. 26, pp. 1-11, 2017.
- [17] L. Kuncheva, C. Whitaker, C. Shipp and R. Duin, "Limits on the Majority Vote Accuracy in Classifier Fusion," *Pattern Analysis and Applications*, vol. 6, pp. 22-31, 2003.
- [18] W. Liu, G. S. and C. E. Woodcock, "Uncertainty and confidence in land cover classification using a hybrid classifier approach.," *Photogrammetric Engineering and Remote Sensing*, vol. 70, p. 963–972, 2004.
- [19] P. Kamavidar, S. Saluja and S. Agrawal, "A Survey on Image Classification Approaches and Techniques," *International Journal of Advanced Research in Computer and Communication Engineering*, vol. 2, no. 1, 2013.
- [20] K. Ding and S. Gunasekaran, "Shape feature extraction and classification of food material using computer vision," *Transactions of American Society of Agricultural Engineers*, vol. 37, no. 5, pp. 1537-1545, 1994.

- [21] M. N. Patel and P. Tandel, "A Survey on Feature Extraction Techniques for Shape based Object Recognition," *International Journal of Computer Applications*, vol. 137, no. 6, pp. 16-20, 2016.
- [22] H. Soltanian-Zadeh, S. Pourabdollah-Nezhad and F. R. Rad, "Shape-based and texture-based feature extraction for classification of microcalcifications in mammograms," in *Proceedings Volume 4322, Medical Imaging 2001: Image Processing*, San Diego, 2001.
- [23] R. N. Hota, V. Venkoparao and A. Rajagopal, "Shape Based Object Classification for Automated Video Surveillance with Feature Selection," in *10th International Conference on Information Technology (ICIT 2007)*, Orissa, 2007.
- [24] P. Revesz and T. Triplet, "Temporal data classification using linear classifiers," *Information Systems*, vol. 36, pp. 30-41, 2011.
- [25] I.-Y. Jeong and K. Lee, "Learning temporal features using a deep Neural network and its application to music genre classification," in *Proceedings of the 17th ISMIR Conference*, New York, 2016.
- [26] L.-Q. Xu and Y. Li, "Video classification using spatial-temporal features and PCA," in *International Conference on Multimedia and Expo ICME'03*, Baltimore, 2003.
- [27] F. Ma, L. Yu, M. Bajger and M. J. Bottema, "Mammogram Mass Classification with Temporal Features and Multiple Kernel Learning," in *2015 International Conference on Digital Image Computing: Techniques and Applications (DICTA)*, Adelaide, 2015.
- [28] A. Ahmad and S. Quegan, "Analysis of Maximum Likelihood Classification on Multispectral Data," *Applied Mathematical Sciences*, vol. 6, no. 129, pp. 6425 - 6436, 2012.
- [29] S. M. Moorthi, I. Misra, R. Kaur, N. P. Darji and R. Ramakrishnan, "Kernel based learning approach for satellite image classification using support vector machine," in *2011 IEEE Recent Advances in Intelligent Computational Systems*, Trivandrum, 2011.
- [30] H. Jin and R. Wang, "Robust Image Set Classification Using Partial Least Squares," in *IScIDE 2013: Intelligence Science and Big Data Engineering*, Beijing, 2013.
- [31] C. Liu, C. Wang and R. Dai, "Text detection in images based on unsupervised classification of edge-based features," in *Eighth International Conference on Document Analysis and Recognition (ICDAR'05)*, Seoul, 2005.
- [32] J.-S. Lee, M. Grunes, T. Ainsworth, L.-J. Du, D. Schuler and S. Cloude, "Unsupervised classification using polarimetric decomposition and the complex Wishart classifier," *IEEE Transactions on Geoscience and Remote Sensing*, vol. 37, no. 5, pp. 2249 - 2258, 1999.
- [33] V. V. Chamundeeswari, D. Singh and K. Singh, "An Analysis of Texture Measures in PCA-Based Unsupervised Classification of SAR Images," *IEEE Geoscience and Remote Sensing Letters*, vol. 6, no. 2, pp. 214 - 218, 2009.
- [34] J. Ediriwickrema and S. Khorram, "Hierarchical maximum-likelihood classification for improved accuracies," *IEEE Transactions on Geoscience and Remote Sensing*, vol. 35, no. 4, pp. 810 - 816, 1997.

- [35] Q. Du and H. Ren, "Real-time constrained linear discriminant analysis to target detection and classification in hyperspectral imagery," *Pattern Recognition*, vol. 36, pp. 1-12, 2003.
- [36] L. Mussone, A. Ferrari and M. Oneta, "An analysis of urban collisions using an artificial intelligence model," *Accident Analysis and Prevention*, vol. 31, pp. 705-718, 1999.
- [37] C. Huang, L. S. Davis and J. R. G. Townshend, "An assessment of support vector machines for land cover classification," *International Journal of Remote Sensing*, vol. 23, no. 4, pp. 725-749, 2010.
- [38] M. P. Vayssières, R. E. Plant and B. H. Allen-Diaz, "Classification trees: An alternative non-parametric approach for predicting species distributions," *Journal of Vegetation Science*, vol. 11, no. 5, pp. 679-694, 2000.
- [39] C. Hecker, J. H. Dilles, M. v. d. Meijde and F. D. v. d. Meer, "Thermal infrared spectroscopy and partial least squares regression to determine mineral modes of granitoid rocks," *Geochemistry, Geophysics, Geosystems*, vol. 13, no. 3, pp. 1-15, 2013.
- [40] R. Pande-Chhetri, A. Abd-Elrahman, T. Liu, J. Morton and V. L. Wilhelm, "Object-based classification of wetland vegetation using very high-resolution unmanned air system imagery," *European Journal of Remote Sensing*, vol. 50, no. 1, pp. 564-576, 2017.
- [41] D. Geneletti and B. Gorte, "A method for object-oriented land cover classification combining Landsat TM data and aerial photographs," *International Journal of Remote Sensing*, vol. 24, p. 1273-1286, 2003.
- [42] P. M. Harris and S. J. Ventura, "The integration of geographic data with remotely sensed imagery to improve classification in an urban area," *Photogrammetric Engineering and Remote Sensing*, vol. 61, p. 993-998, 1995.
- [43] C. D. Lloyd, S. Berberoglu, P. J. Curran and P. M. Atkinson, "A comparison of texture measures for the per-field classification of Mediterranean land cover," *International Journal of Remote Sensing*, vol. 25, no. 19, pp. 3943-3965, 2010.
- [44] M. Pedley and P. Curran, "Per-field classification: an example using SPOT HRV imagery," *International Journal of Remote Sensing*, vol. 12, p. 2181-2192, 1991.
- [45] P. Atkinson and A. Tantall, "Neural networks in remote sensing," *International Journal of Remote Sensing*, vol. 18, p. 699-709, 1997.
- [46] E. Binaghi, P. Madella, M. Montesano and A. Rampini, "Fuzzy contextual classification of multisource remote sensing images," *IEEE Transactions on Geoscience and Remote Sensing*, vol. 35, p. 326-339, 1997.
- [47] G. Foody, "Approaches for the production and evaluation of fuzzy land cover classification from remotely-sensed data," *International Journal of Remote Sensing*, vol. 17, pp. 1317-1340, 1996.
- [48] C. Ozkan and F. Erbek, "The comparison of activation functions for multispectral The comparison of activation functions for multispectral," *Photogrammetric Engineering and Remote Sensing*, vol. 69, pp. 1225-1234, 2003.

- [49] S. Magnussen, P. Boudewyn and M. Wulder, "Contextual classification of Landsat TM images to forest inventory cover types," *International Journal of Remote Sensing*, vol. 25, no. 12, pp. 2421-2440, 2010.
- [50] J. Benediktsson and I. Kanellopoulos, "Classification of multisource and hyperspectral data based on decision fusion," *IEEE Transactions on Geoscience and Remote Sensing*, vol. 37, no. 3, pp. 1367-1377, 1999.
- [51] B. M. Steele, "Combining Multiple Classifiers: An Application Using Spatial and Remotely Sensed Information for Land Cover Type Mapping," *Remote Sensing of Environment*, vol. 74, no. 3, pp. 545-556, 2000.
- [52] N. Baaziz, O. Abahmane and R. Missaoui, "Texture feature extraction in the spatial-frequency domain for content-based image retrieval," *arXiv: Computer Vision and Pattern Recognition*, pp. 1-19, 2010.
- [53] A. Yeo and Z. Yun, "Texture classification using Wavelet Transform and Support Vector Machines," Faculty of Information and Communication Technology, University Tunku Abdul Rahman, 2011.
- [54] K. Rajpoot and N. Rajpoot, "Wavelets and support vector machines for texture classification," in *8th International Multitopic Conference*, Lahore, 2004.
- [55] M. Venkataramana, E. S. Reddy, C. Satyanarayana and S. Anuradha, "A Review of Recent Texture Classification: Methods," *IOSR Journal of Computer Engineering*, vol. 14, no. 1, pp. 54-60, 2013.
- [56] T. J. Yi, "Texture classification on wood images for species recognition," Faculty of Information and Communication Technology, University Tunku Abdul Rahman, 2009.
- [57] S. Li, J. T. Kwok, H. Zhu and Y. Wang, "Texture classification using the support vector machines," *Pattern Recognition*, vol. 36, p. 2883 – 2893, 2003.
- [58] J. K. Annavarapu, "Statistical Feature Selection for Image Texture Analysis," *International Research Journal of Engineering and Technology*, vol. 2, no. 5, pp. 546-550, 2015.
- [59] J. W. Cooley and J. W. Tukey, "An algorithm for the machine calculation of complex Fourier series," *Mathematics of Computation*, vol. 19, no. 2, pp. 297-301, 1965.
- [60] R. Polikar, "The Engineer's Ultimate Guide to Wavelet Analysis: The Wavelet Tutorial," 5 November 2006. [Online]. Available: https://cseweb.ucsd.edu/~baden/Doc/wavelets/polikar_wavelets.pdf. [Accessed 17 June 2018].
- [61] S. G. Mallat, "A Theory for Multiresolution Signal Decomposition: The Wavelet Representation," *IEEE Transactions on Pattern Analysis and Machine Intelligence*, vol. 11, no. 7, pp. 674-693, 1989.
- [62] J.-P. Vert, "Introduction to support vector machines and applications to computational biology.," MINES ParisTech University, Paris, 2001.

- [63] C. J. Burges, "A Tutorial on Support Vector Machines for Pattern Recognition," Kluwer Academic Publishers, Boston.
- [64] C. Cortes and V. Vapnik, "Support-Vector Networks," *Machine Learning*, vol. 20, no. 3, pp. 273-297, 1995.
- [65] E. Kim, "Everything You Wanted to Know about the Kernel Trick (But Were Too Afraid to Ask)," 20 December 2017. [Online]. Available: http://www.eric-kim.net/eric-kim-net/posts/1/kernel_trick_blog_ekim_12_20_2017.pdf. [Accessed 18 June 2018].
- [66] Z. Wang and X. Xue, "Multi-Class Support Vector Machine," in *Support Vector Machines Applications*, Cham, Springer, 2014, pp. 23-48.
- [67] B. S. Everitt and G. Dunn, *Applied Multivariate Data Analysis*, John Wiley & Sons, Ltd., 2013.
- [68] S. Wold, L. Eriksson, J. Trygg and N. Kettaneh, "The PLS method -- partial least squares projections to latent structures -- and its applications in industrial RDP (research, development, and production).," Prague, 2004.
- [69] S. Wold, M. Sjostrom and L. Eriksson, "PLS-regression: a basic tool of chemometrics," *Chemometrics and Intelligent Laboratory Systems*, vol. 58, pp. 109-130, 2001.
- [70] M. Khelifa, "Linear Regression Models," [Online]. Available: <https://www.zu.ac.ae/main/files/contents/research/training/BivariateandmultipleLinearRegression.pdf>. [Accessed 20 June 2018].
- [71] H. Abdi, "Partial least squares regression and projection on latent structure regression (PLS Regression)," *WIREs Computational Statistics*, pp. 1-10, 2010.
- [72] P. Geladi and B.R.Kowalski, "Partial Least Squares Regression: A Tutorial," *Analytica Chimica Acta*, vol. 185, pp. 1-17, 1986.
- [73] V. E. Vinzi and G. Russolillo, "Partial least squares algorithms and methods," *WIREs Computational Statistics*, vol. 5, pp. 1-19, 2013.
- [74] B. Jørgensen and Y. Goegebeur, *ST02: Multivariate Data Analysis and Chemometrics*, Odense: University of Southern Denmark, 2007.
- [75] C. Chang, "Data Dimensionality Reduction," in *Hyperspectral Data Processing: Algorithm Design and Analysis*, John Wiley & Sons, Inc., 2013, pp. 168-199.
- [76] L. Cao, K. Chua, W. Chong, H. Lee and Q. Gu, "A comparison of PCA, KPCA and ICA for dimensionality reduction in support vector machine," *Neurocomputing*, vol. 55, no. 1, pp. 321-336, 2003.
- [77] X. Fu and L. Wang, "Data dimensionality reduction with application to simplifying RBF network structure and improving classification performance," *IEEE Transactions on Systems, Man, and Cybernetics, Part B (Cybernetics)*, vol. 33, no. 3, pp. 399-409, 2003.
- [78] S. T. Roweis and L. K. Saul, "Nonlinear Dimensionality Reduction by Locally Linear Embedding," *Science*, vol. 290, no. 5500, pp. 2323-2326, 2000.

- [79] M. Belkin and P. Niyogi, "Laplacian Eigenmaps for Dimensionality Reduction and Data Representation," *Neural Computation*, vol. 15, no. 6, pp. 1373-1396, 2003.
- [80] F. Duarte, *Tunable Lasers Handbook*, Academic Press, 1995.
- [81] D. J. M. Stothard, "Practical Continuous-Wave Intracavity Optical Parametric Oscillators," in *Advances in Optical and Photonic Devices*, InTech, 2010, pp. 293-328.
- [82] D. J. M. Stothard, "Continuous-wave, singly-resonant optical parametric oscillators pumped internal to Nd:YVO4 lasers," University of St Andrews, 2001.
- [83] M. Ebrahimzadeh and M. H. Dunn, "Optical Parametric Oscillators," in *Handbook Of Optics*, St. Andrews, McGraw-Hill, 2004, pp. 1-72.
- [84] I. D. Lindsay, "High spatial and spectral quality diode-laser-based pump sources," St. Andrews University, St. Andrews, 1999.
- [85] J. G. d. Aulnois and B. Szymanski, "Tunability improvement of a doubly resonant OPO for fast and high resolution gas spectroscopy.," in *SPIE Defense + Commercial Sensing 2018*, Orlando, 2018.
- [86] M. H. Dunn and M. Ebrahimzadeh, "Parametric Generation of Tunable Light from Continuous-Wave to Femtosecond Pulses," *Science*, vol. 286, pp. 1512-1517, 1999.
- [87] J. E. Schaar, K. L. Vodopyanov, P. S. Kuo, M. M. Fejer, X. Yu, A. Lin, J. S. Harris, D. Bliss, C. Lynch, V. G. Kozlov and W. Hurlbut, "Terahertz Sources Based on Intracavity Parametric Down-Conversion in Quasi-Phase-Matched Gallium Arsenide," *IEEE JOURNAL OF SELECTED TOPICS IN QUANTUM ELECTRONICS*, vol. 14, no. 2, pp. 354-362, 2008.
- [88] D. J. M. Stothard, M. Ebrahimzadeh and M. H. Dunn, "Low-pump-threshold continuous-wave singly resonant optical parametric oscillator," *OPTICS LETTERS*, vol. 23, no. 24, pp. 1895-1897, 1998.
- [89] M Squared Lasers Ltd, "Firefly-IR Widely Tunable, Mid- & Near-IR Hyperspectral Imager, User Manual v2.0".
- [90] R. F. Curl and F. K. Tittel, "Tunable infrared laser spectroscopy," *Annu. Rep. Prog. Chem., Sect. C: Phys. Chem.*, vol. 98, pp. 219-272, 2002.
- [91] F. Tittel, D. Richter and A. Fried, "Mid-Infrared Laser Applications in Spectroscopy," in *Solid-State Mid-Infrared Laser Sources. Topics in Applied Physics*, Berlin, Heidelberg, Springer, 2003, pp. 458-529.
- [92] R. Danielius, A. Piskarskas, A. Stabinis, G. P. Banfi, P. D. Trapani and R. Righini, "Traveling-Wave Parametric Generation of Widely Tunable, Highly Coherent Femtosecond Light Pulses," *Journal of the Optical Society of America B*, vol. 10, no. 2, p. 222-2231, 1995.

- [93] I. D. Lindsay, D. J. M. Stothard, C. F. Rae and M. H. Dunn, "Continuous-wave, pump-enhanced optical parametric oscillator based on periodically-poled RbTiOAsO₄," *OPTICS EXPRESS*, vol. 11, no. 2, pp. 134-140, 2003.
- [94] D. J. M. Stothard, I. D. Lindsay and M. H. Dunn, "Continuous-wave pump-enhanced optical parametric oscillator with ring resonator for wide and continuous tuning of single-frequency radiation," *OPTICS EXPRESS*, vol. 12, no. 3, pp. 502-511, 2004.
- [95] D. J. M. Stothard, J.-M. Hopkins, D. Burns and M. H. Dunn, "Stable, continuous-wave, intracavity, optical parametric oscillator pumped by a semiconductor disk laser (VECSEL)," *OPTICS EXPRESS*, vol. 17, no. 13, pp. 10648-10658, 2009.
- [96] R. C. Eckhardt, Y. X. Fan, R. L. Byer, C. L. Marquardt, M. E. Storm and L. Esterowitz, "Broadly Tunable Infrared Parametric Oscillator Using AgGaSe₂," *Applied Physics Letters*, vol. 49, pp. 608-610, 1986.
- [97] N. Barnes, K. E. Murray, J. R. Hietanen and R. A. Iannini, "Er:YLF Pumped AgGaSe₂ Optical Parametric Oscillator," *Proc. OSA Advanced Solid State Lasers*, pp. 322-328, 1990.
- [98] B. Hardy, A. Berrou, S. Guilbaud, M. Raybaut, A. Godard and M. Lefebvre, "Compact, single-frequency, doubly resonant optical parametric oscillator pumped in an achromatic phase-adapted double-pass geometry," *OPTICS LETTERS*, vol. 36, no. 5, pp. 678-680, 2011.
- [99] W. R. Bosenberg, A. Drobshoff, J. I. Alexander, L. E. Myers and R. L. Byer, "93% pump depletion, 3.5-W continuous-wave, singly resonant optical parametric oscillator," *OPTICS LETTERS*, vol. 21, no. 17, pp. 1336-1338, 1996.
- [100] D. J. M. Stothard and M. H. Dunn, "Relaxation oscillation suppression in continuous-wave intracavity optical parametric oscillators," *OPTICS EXPRESS*, vol. 18, no. 2, pp. 1336-1348, 2010.
- [101] Q. Sheng, X. Ding, C. Shi, S. Yin, B. Li, C. Shang, X. Yu, W. Wen and J. Yao, "Continuous-wave mid-infrared intra-cavity singly resonant PPLN-OPO under 880 nm inband pumping," *OPTICS EXPRESS*, vol. 20, no. 7, pp. 8041-8046, 2012.
- [102] F. G. Colville, M. H. Dunn and M. Ebrahimzadeh, "Continuous-wave, singly resonant, intracavity parametric oscillator," *Optics Letters*, vol. 22, no. 2, pp. 75-77, 1997.
- [103] M. Ebrahimzadeh, G. A. Turnbull, T. J. Edwards, D. J. M. Stothard, I. D. Lindsay and M. H. Dunn, "Intracavity continuous-wave singly resonant optical parametric oscillators," *J. Opt. Soc. Am. B*, vol. 16, no. 9, pp. 1499-1511, 1999.
- [104] G. Turnbull, M. Dunn and M. Ebrahimzadeh, "Continuous-wave, intracavity optical parametric oscillators: an analysis of power characteristics," *Applied Physics B: Lasers and Optics*, vol. 66, pp. 701-710, 1998.
- [105] G. A. Turnbull, D. J. M. Stothard, M. Ebrahimzadeh and M. H. Dunn, "Transient Dynamics of CW Intracavity Singly Resonant Optical Parametric Oscillators," *IEEE JOURNAL OF QUANTUM ELECTRONICS*, vol. 35, no. 11, pp. 1666-1672, 1999.

- [106] T. Debuisschert, J. Raffy, J. P. Pocholle and M. Papuchon, "Intracavity optical parametric oscillator: Study of the dynamics in pulsed regime," *Journal of the Optical Society of America B*, vol. 13, no. 7, p. 1569–1587, 1996.
- [107] D. J. M. Stothard, C. F. Rae and M. H. Dunn, "An Intracavity Optical Parametric Oscillator With Very High Repetition Rate and Broad Tunability Based Upon Room Temperature Periodically Poled MgO LiNbO With Fanned Grating Design," *IEEE JOURNAL OF QUANTUM ELECTRONICS*, vol. 45, no. 3, p. 256–263, 2009.
- [108] L. Maidment, Z. Zhang, C. R. Howle, S. T. Lee, A. Christie and D. T. Reid, "Stand-off detection of liquid thin films using active mid-infrared hyperspectral imaging," in *2015 Conference on Lasers and Electro-Optics (CLEO)*, San Jose, 2015.
- [109] A. Wehr and U. Lohr, "Airborne laser scanning—an introduction and overview," *ISPRS Journal of Photogrammetry & Remote Sensing*, vol. 54, pp. 68-82, 1999.
- [110] D. Rockwell, C. Magness, O. A. J. Towfighi and T. Corcoran, "High image-density particle image velocimetry using laser scanning techniques," *Experiments in Fluids*, pp. 181-19214, 1993.
- [111] S. T. S. Holmström, U. Baran and H. Urey, "MEMS Laser Scanners: A Review," *Journal Of Microelectromechanical Systems*, vol. 23, no. 2, pp. 259-275, 2014.
- [112] M. Ostaszewski, S. Harford, N. Doughty, C. Hoffman, M. Sanchez, D. Gutow and R. Pierce, "Risley prism beam pointer," in *Proceedings Volume 6304, Free-Space Laser Communications VI*, San Diego, 2006.
- [113] D. J. M. Stothard, M. H. Dunn and C. F. Rae, "Hyperspectral imaging of gases with a continuous-wave pump-enhanced optical parametric oscillator," *Optics Express*, vol. 12, no. 5, pp. 947-955, 2004.

Chapter 3: INHERIt project

3.1 Project background

According to a recent study, in 2014 the global art market reached its highest ever-recorded level of just over €51 billion worldwide [1]. This represents a 7% year-on-year increase from €47.4 billion documented in total sales of art and antiques in 2013, consisting of more than 36 million transactions [2]. The vast majority of these high value dealings were made without scientific or forensic testing to assure the authenticity of the traded objects. Non-scientific art expertise – known in the art world as connoisseurship – is a common practice to assess the authenticity. Nevertheless, an experienced specialist can only evaluate a limited amount of the artwork and when not supported by additional scientific tests, that evaluation is subjective and as such it is not infallible [3, 4]. Services using scientific approaches to determine the authenticity of artworks are available; however, these can have perceived issues, including the time involved and the need to remove sample material for a number of the techniques [3]. There is consequently a need for efficient, portable and cost-effective non-destructive methods of art analysis to serve a broader range of the market. In some cases, due to the high value and unique nature of the objects, the paint sampling required by certain types of examinations may also be restricted. Non-destructive tests provide the possibility to use complementary techniques and obtain more information from the same sample. Several such methods, for instance X-ray fluorescence and FTIR (Fourier Transform Infrared) or Raman spectroscopy, exist and are applicable for studying artwork [5, 6]. Although these methods are commonly used for scientific art investigation as well as for some other applications, there is still a need for new, non-invasive techniques that could extend the amount of information obtained from the artwork analyses and limit the number of required invasive tests. In this chapter, Hyperspectral Imaging (HSI) combined with chemometrics algorithms is proposed as a novel, non-invasive analysis method for classification and mapping of paints and pigments. The purpose of this study is to utilise these tools as an aid for artwork evaluation and specifically, the identification of counterfeits.

In recent years Hyperspectral Imaging has undergone significant development. There is an increasing amount of camera technologies that, with different configurations, provide many ways to obtain hyperspectral data over several spectral ranges. This emerging technology is rapidly finding applications in different fields, including pharmaceuticals [7], agriculture [8] and food quality control [9, 10, 11, 12], as well as the art world, for material identification and mapping of

the works of art [13, 14, 15, 16, 17, 18]. To date, most applications of hyperspectral (and multispectral) technology in the art world are for the restoration and conservation of paintings [19, 20, 21, 22]. Pigment analyses provided by HSI systems, together with dedicated classification algorithms, allow the identification of “restored zones” in tested paintings and differentiate these from significant areas of the original canvases, which then are suggested for detailed evaluation [19, 23, 24, 18]. The use of HSI in the infrared spectral range has also helped to reveal features of artists’ techniques such as their preparatory drawing [25, 22]. Due to the very broad range of wavelengths available for hyperspectral systems, the transmittance and reflectance response of different layers of paintings and drawings is frequently observed during data analyses. When material that is transparent at a specific wavelength range (but opaque at others) covers the one that is reflective within the same spectral range, the underlying material can be detected by the HSI system and is hence revealed in the data acquired. Empowered by signal processing techniques, this facilitates a detailed study of the artwork creation process and enables identification of the materials used [26]. Beyond the world of art, spectral selectivity of HSI data had been used on various occasions to analyse texts of historic value [27, 28, 29]. Identification of pigments and inks facilitated by HSI had also been used to aid in assigning the date of manuscripts [27]. Furthermore, HSI technology empowers the recovery of erased and overwritten scripts as well as it allows the determination of appropriate bands for monitoring laser and non-laser cleaning processes [28].

Alongside the aforementioned benefits for art documentation and conservation, the potential of hyperspectral imaging in forgery detection has also been recognised. The application of HSI to address the challenge of forensic analysis of documents was successfully applied in the past [30, 31, 32]. Classification of different inks after obliteration of the text and the ‘crossing lines problem’ [30] were studied and analysed with chemometrics-based tools. These techniques applied to HSI data have had a significant impact on forgery recognition and provided objective results compared to traditional visual inspection-based judgments [30]. Other forensic applications of HSI were also reported, such as fingerprint detection [33] and blood stain dating at crime scenes [34].

Typically, the success of the above mentioned HSI activities have been critically dependent upon bespoke signal processing, making non-expert use difficult. In some cases the application of pure spectroscopic techniques achieved sufficient results [25], while in others, more advanced algorithms had to be employed in order to analyse the data [23, 24, 26]. It was also recognised that the full diagnostic potential of HSI may be improved by the implementation of robust data processing algorithms [28].

As demonstrated above, HSI technology combined with advanced signal processing techniques have already found numerous applications in the art world. However, to date these have focused on supporting various aspects of conservation and have allowed researchers to better understand assorted paintings by enabling observation of materials below the surface of the completed work. A novel combination of Near- and Mid-infrared hyperspectral imaging with state-of-the-art signal processing algorithms and background information from experts in the field of art analysis is presented in this chapter in order to provide HSI data-based classification of paints and artwork for the purposes of authentication. Although the Near-infrared range can be reached with widely known HSI technology, access to the Mid-IR region was granted by the novel application of an active, laser-based Mid-IR Imager. Although a similar wavelength range was already explored with a passive system [35], this work presents unique application of this active device for the artwork analysis. This project demonstrates infrared hyperspectral imaging empowered by automated paint classification techniques as a non-invasive method supporting the identification of counterfeit paintings. The goal of this project was not to compare performance of this technique based on the data from Near- and Mid-IR region with the one acquired in visible range, but rather explore the viability of infrared imaging spectroscopy to find and analyse subtle differences in the paints' spectra, that are not distinguishable in visible range. The presented work was divided into four parts: 1) verification of the IR Imager facility to produce valid data and determining the best image acquisition technique with this specific piece of hardware; 2) development of the OPO systems and an investigation into the potential techniques to improve the laser imaging quality in this project; 3) establishment of algorithms using bespoke paintings which were created for this study and imaged in a well-controlled environment under laboratory conditions; 4) application of the developed techniques to hyperspectral images of paintings held by the Berlin Landeskriminalamt which contained known and suspected forgeries, including, for the first time the analysis with HSI, paintings from the infamous Beltracchi case [36, 37, 38, 39, 40]. The activities discussed in parts 1) and 2) above constitute a major part of the work described in this chapter. Acquisition of good quality data proved to be a challenging task with this imager and therefore the experimental aspects of this process – and the steps we took to improve them – are described in detail. Significant effort was also placed on the identification, quantification and mitigation of noise factors affecting this imaging device, including per-pulse jitter, specular reflections and speckle, and these are also discussed in the following sections. The overall structure of this chapter is based on the preceding points and after initial focus on explaining the system development and testing, the details of the art analysis and the final results achieved during this work are provided. Some aspects of this study were described and published in [41, 42].

3.2 Hyperspectral equipment

Applications of HSI systems operating in the visible-near-infrared (Vis-NIR) spectrum (400 nm – 1000 nm) have already been presented in the literature and tend to focus on performing and supporting various tasks including spectral characterisation of pigments [17, 18, 20, 23, 26, 27, 28]. InGaAs detector based hyperspectral imagers are also reaching further into near-infrared region (900 nm – 1700 nm, and in some cases extended up to 2500 nm) and these also found application in the study of artworks [16, 17, 18, 25]. However, relevant literature showing the use of sensors operating in longer wavelengths, approaching up to 4000 nm, which are known to contain rich spectral information and useful chemometric descriptors, is not so readily available. In this work, two hyperspectral imaging systems operating in different (but overlapping) regions of the infrared portion of the electromagnetic spectrum were utilised. The choice of these two systems allowed a study of the image acquisition and illumination methods and how these impact on the performance of the proposed image processing techniques designed to automatically analyse the near- and mid-infrared range data. This work is driven by the motivation that in addition to the colour information contained in the visible spectrum, often sufficient to identify various pigments, a range of paint types (including pigments, binders and solvents) also have spectral features in the longer wavelengths. Hence, this study is focussed on exploring these characteristics for the accurate discrimination of paints. It should be noted however, that while the intention of this research is to investigate the usefulness of these longer wavelengths, many pigments can be discriminated using the Vis-NIR region and this could be beneficial for the final application of presented in this chapter technology by art scientists. As such, this topic is further discussed in Section 3.5.1.

Under evaluation in this study is a Firefly IR Imager (M Squared Lasers), an active laser-based HSI system that provides point-by-point scanned illumination to the analysed object (paintings in this case). The device operates mainly in the mid-IR region (2500nm to 3750nm), whereas it also acquires images from a narrow wavelength band of the NIR spectral range (1490nm to 1850nm). Firefly's vertically polarised laser source operates in a pulsed regime at 150 kHz repetition rate, <10 ns pulse duration and average powers of 140 ± 30 mW in near-IR and 90 ± 40 mW in mid-IR respectively. It should be noted that both average powers quoted here are variable as a function of wavelength. The image acquisition process is based on single point detection of reflected laser energy. The nominal laser beam radius at the output port is 2mm ($1/e^2$ intensity) with 1.5mrad half angle beam divergence. A spatial scan is made possible by two galvanometer-mounted gold mirrors which deflect the illuminating laser beam, then direct the collected and reflected energy back to the single-element IR photovoltaic detector. Firefly is able to capture images up to maximum pixel count of 512x512 that may have varying spatial resolution,

depending on the beam deflection settings as well as the distance between the imager and the object. Moreover, 3 lower options are available - 64x64, 128x128 and 256x256 pixels. However, due to the sinusoidal movement pattern of the vertical galvanometer, the image is spatially distorted nearly 12% at the bottom and the same at the top of it. Therefore, these regions of each tested image are cropped in this work before data analysis. A hyperspectral image can be captured by performing the sequential collection of spatial images across the spectral range that is accessible by the device.

Access to the Mid-IR is granted by the fact that the Firefly IR Imager uses an Intracavity Optical Parametric Oscillator (IC-OPO) technology which transforms the radiation of a 1064nm pump laser into two beams at longer wavelengths, corresponding to the aforementioned spectral range of this system (also see Chapter 2 and [43]). As explained in Chapter 2, when the pump photon passes through the non-linear crystal (in this case fan grating, periodically poled lithium niobate – PPLN), where the parametric process takes a place, its energy is converted into two lower energy photons called signal and idler. The summed energy of the signal and idler photons is equal to the energy of the pump photon. The split of the energy between signal and idler depends on the position of the crystal relative to the pump laser and therefore its translation across the pump beam allows spectral tuning of the imager. While the technology is highly innovative, the requirement for a physical translation of the crystal accompanied by the time required for image collection at each wavelength makes the acquisition of hyperspectral cube time consuming. In fact, the total acquisition time is determined by the required spectral and spatial resolution of the hyperspectral data cube to be acquired. Since the down-converted spectral region is continuous across the entire accessible bandwidth, the spectral resolution of the hyperspectral data cube is determined by the step size of the crystal translation. As a result, the spectral tuning may be as fine as 0.1nm. However, due to the finite linewidth of the illuminating laser ($\sim 5\text{cm}^{-1}$), in this work the hyperspectral data cubes (hypercubes) were acquired with a spectral resolution of 6nm. It should be noted that an option for the spectral tuning of this imager allows it to function as a hyperspectral, multispectral or single band imager depending on user requirements.

In the coming sections, the performance of the Firefly IR Imager is compared with that of a Red Eye 1.7 (Inno-spec GmbH) passive hyperspectral camera. This system employs the widely used pushbroom data acquisition method [44] that is common with this kind of hardware. The Red Eye 1.7 uses a transparent grating which provides 256 spectral image bands across the NIR operating range (900nm – 1700nm). As a passive system, the Red Eye 1.7 requires external illumination, thus 12V DC off-the-shelf halogen lamps were used during imaging, to ensure a sufficient amount of infrared illumination. The halogen lamps, as an incandescent light source,

emit not only a portion of energy in the visible band of the electromagnetic spectrum, but also provide excellent illumination in the near-IR range as required by this system [45].

3.2.1 Image acquisition with Red Eye 1.7

Image acquisition with the Red Eye 1.7 passive imaging system was performed following typical for such systems operating procedures and provided high quality data. A Zolix KSA 11-200S4N linear translation stage was used to provide the relative movement between scanned pieces and the detector. This is required by pushbroom imaging systems which capture images in a line scan fashion. By providing sufficient and even illumination from halogen lamps and the scanning mechanism, the hyperspectral data cubes were acquired for a number of different paintings. During each data acquisition run, reflectance calibration was also performed to ensure that background spectral responses of the instrument and illumination, as well as the ‘dark’ current of the camera, were accounted for in the data set and therefore do not affect the results of any subsequent analysis. The relative reflectance for the raw images can be calculated using [46]:

$$I_R = \frac{I_0 - I_D}{I_W - I_D} \quad (3.1)$$

where I_R is the relative reflectance image, I_0 is the raw reflectance image, I_D is the dark reference image, and I_W is the white reference image [46]. The spectral background I_W was obtained by scanning a white reference tile made from Spectralon - a material of high Lambertian reflection over its reflective spectral range of 250 nm – 2500 nm [47]. The dark reference I_D was captured by fully obscuring the camera objective using an opaque black cap.

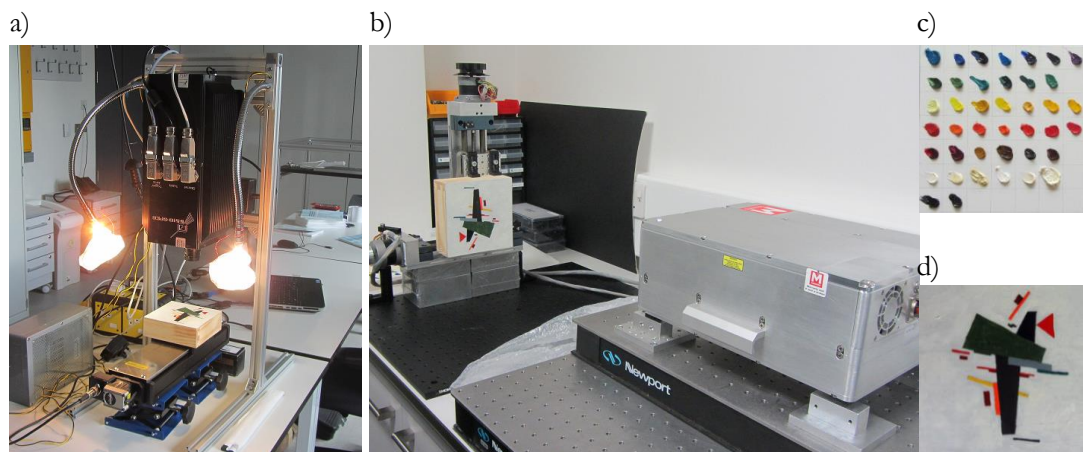


Figure 3.1. Illustration of the scanning set-up for Red Eye 1.7 camera (a) and Firefly IR Imager (b), along with the two targets: grid canvas (c) and test painting (d).

As the data acquisition software provided with Red Eye 1.7 camera incorporates the traditional calibration procedure, the captured data was saved directly in the reflectance format and no further calibration or correction was required. Figure 3.1 (a) illustrates the set-up of the full scanning system which incorporates the Red Eye 1.7 camera. In this figure a scan of the test painting is shown. The test painting shown in this figure and the grid canvas (Figure 3.1 (c) and (d)) are used as targets in the following sections and will be fully introduced in Section 3.4.1.

3.2.2 Image acquisition with Firefly IR Imager

The mid-infrared imager used in this work was originally developed as a device for the standoff detection of gases and explosive materials, where only the presence or absence of a compound would be judged based on the detected reflected energy at a specific wavelength. Therefore, the hyperspectral data acquired with this device are obtained in a form of individual images illustrating absorption at one specific wavelength. It runs by saving a single image and stream of images: automatic record of images from the same wavelength at the maximum frame rate given by chosen spatial resolution. There is also an option of spectral scan: automatic record of images with tuning of the optical frequency that allows selection of the start and the end wavelength as well as the step interval. Each monochromatic image captured by the Imager is by default saved as compressed, 8-bit JPEG file. The Imager's operating system also provides access to the 16-bit, raw data, but this is encoded (file is unreadable without decoding algorithm) and not available for automatic spectral scan. For this project it was decided that the full, uncompressed file would be required to capture all the spectral information and therefore the raw files were necessary. Due to the time-consuming process of the image acquisition, manual tuning and recording the data would be unacceptable. Two different solutions were developed to overcome this obstacle. First was automatic control of the mouse pointer on the screen of the Imager's Graphical user Interface (GUI) which imitated an operator's actions of tuning and saving data. This approach would suffice, although, in the initial stages of the project, the GUI experienced multiple errors that interfered with the automated mouse movement pattern making the saving process of full HSI data unsuccessful. While the problem of erratic errors was solved in cooperation with the Imager's supplier by updating the device's firmware, a new automated acquisition method was developed. This was based on the remote access (achieved under Matlab environment) to the operating system of the Imager and by sending a specific sequence of JavaScript Object Notation (JSON) commands (provided by device manufacturer) that corresponded to tuning and saving actions of the Firefly. This provided raw data in individual, encoded files. Next to the JSON commands, the raw data file decoding algorithm was also obtained from equipment' supplier, opening the access to the encoded files. A Matlab code was

prepared to reshape these files into a standard format for HSI data (a three-dimensional image stack) and perform selection of pre-processing operations. The Matlab GUI is presented in Figure 3.2. With this algorithm the selected files were decoded, cropped (as mentioned above, parts distorted by the sinusoidal movement of the galvanometer were discarded), registered and stacked as a hypercube.

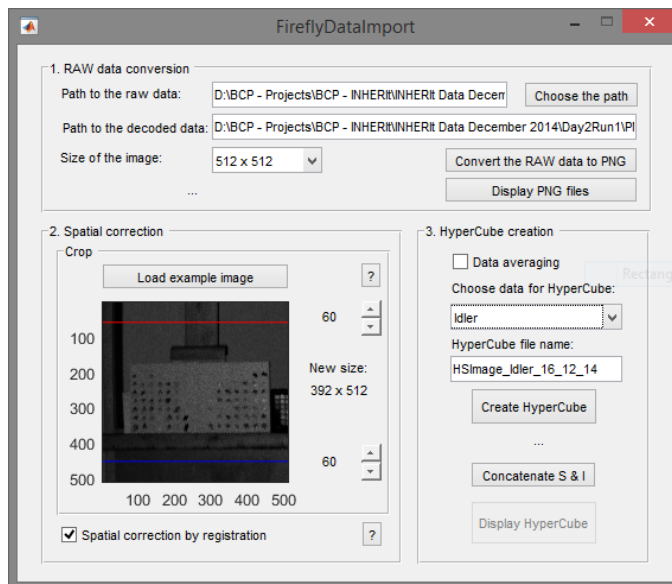


Figure 3.2. Graphical User interface of the software for decoding and pre-processing images acquired with the Firefly IR Imager.

An image registration technique was implemented due to a spatial shift observed between the images captured in left-to-right and right-to-left movements of the horizontal scan galvanometer. As there is no option to control the direction of the galvanometer movement during image acquisition, the shifts created by its position variations were randomly present in all the monochrome images of the hyperspectral data. The magnitude of these shifts was not extensive (2 to 5 pixels difference in horizontal position of imaged object). However, it was sufficient to corrupt the spectral footprint of an object's edges. Upon attempts of various techniques, a SURF (Speeded-Up Robust Features) method [48] was chosen as the one with the best performance for image registration. Figure 3.3 illustrates (a) an example of SURF features extraction, which with variable scale factor are used to register (realign) the images, and (b) a comparison of the location of these features that demonstrates the offset between the two images.

Although simple in principle, imaging with the laser-based Firefly IR device proved to be a more complicated process. The initially captured data contained several features, inherent to the underlying physics driving this imager, that made direct application of chemometrics challenging. The main difficulty brought by the hardware arrangement onto the analysis of the data it produces is that the spatial intensity distribution across the image is not uniform. To overcome this problem,

a series of image acquisition methods aiming to mitigate this phenomenon was attempted. The classification algorithms were used on the produced data, as a tool for verification of the uniformity. While the results of these analyses are demonstrated in this section, the details of the algorithm will be introduced only in Section 3.4.2. The target used during these tests is a ‘grid canvas’ that will be introduced in Section 3.4.1. The other two features affecting the quality of the data were the noise level and the presence of specular reflections but these were not handled during the imaging with the Firefly IR. However, to verify the potential hardware-based solutions for reduction of these features, lab bench setups were built as presented in Section 3.3.

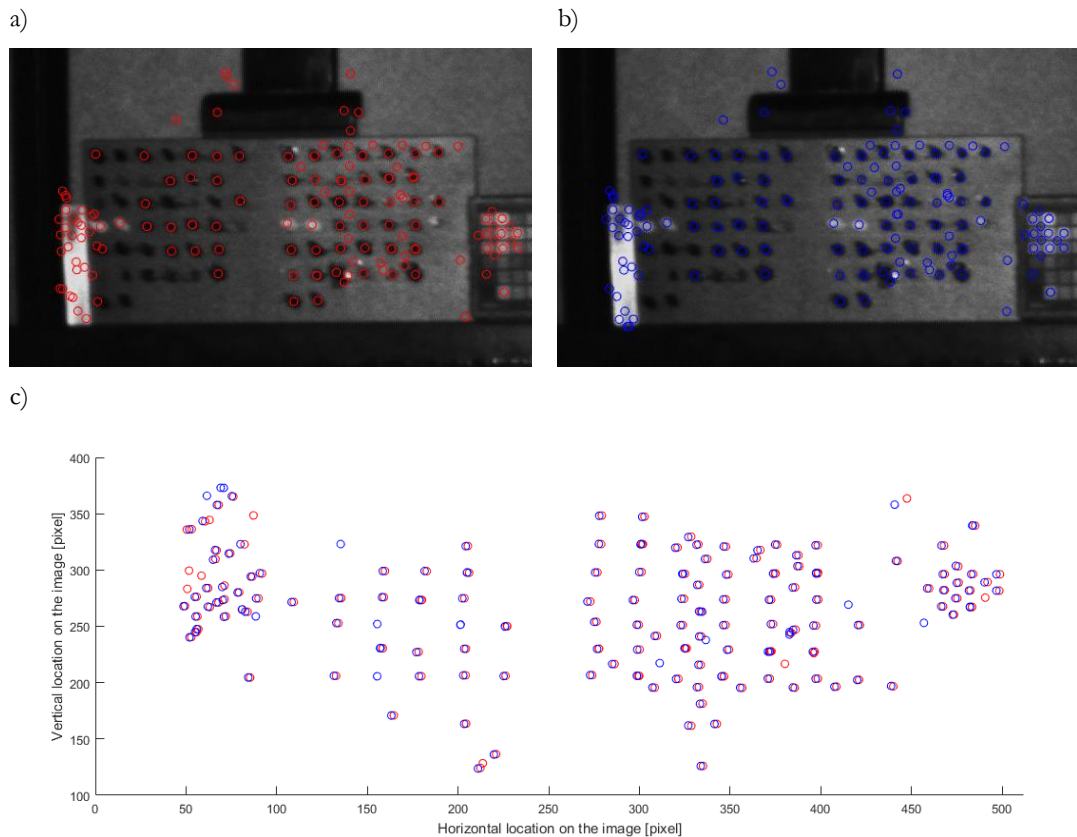


Figure 3.3. Example of the SURF registration algorithm, where single band image at 3050.1nm with overlaid circles indicating location of features used for registration is shown in panel a), single band image at 3053.6nm with overlaid circles indicating features location is shown in panel b) and graph in panel c) demonstrates a comparison between the two; Note that the axes of figure c) are not in scale to better illustrate the phenomenon.

3.2.2.1 2D Galvanometer scan – full field of view

As introduced above, the direct method for image acquisition with the described device is a two-dimensional scan with two embedded mirrors. Unfortunately, due to the deflection of the illuminating beam (process inherent in the scanning thru galvanometer mounted mirrors), the collection efficiency of the reflected energy varies with respect to the angle of incidence of the

beam on the object. This phenomenon results in a varying reflectance response of objects which are spectrally identical and should therefore produce the same spectrum regardless of spatial location. In this and all the following subdivisions of Section 3.2, a Support Vector Machine (SVM) classifier (introduced in more detail in Section 3.4.2) is used to analyse and illustrate the uniformity of the image. In this case the classifier is trained with several classes of paints, but rather than identify various objects in the image, this algorithm is used to observe if the whole background is assigned to a single class. This approach was chosen to assess which image acquisition technique will provide sufficient uniformity to perform successful paint identification. Figure 3.4 (a) illustrates a single band image (at 3000nm) of two grid canvases, where the whole spatial area was captured with one scan. The 7 colours on the left painting indicate Regions of Interest (ROIs). Data from these regions was used as the training set for the classifier. Figure 3.4 (b) illustrates graphical representation of the classification result. The background of these two canvases is covered with one type of paint and, in the absence of the aforementioned issue, should have the same intensity across the whole analysed image.

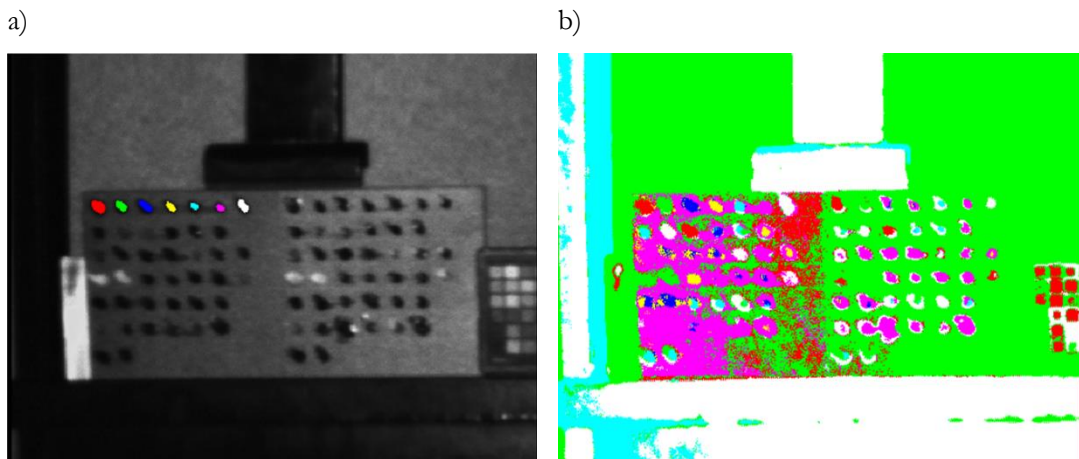


Figure 3.4. Single band image (at 3000nm) of the two grid canvases placed next to each other, with indicated regions of interest (a) and graphical representation of the classification algorithm based on this data set (b).

It is apparent that the background of these paintings (although identical in reality) was categorised as several different regions. This is caused by gradual intensity change across the image. It must be noted here that the classifier was not trained with the background data itself, and this result is brought out only to demonstrate the number of different classes that the background has been labelled with. At the same time, the 7 paints that constitute the training set have also not been properly classified on the second (right hand side) painting.

The imaging setup and laser scanning incidence angles were analysed further to provide a better understanding of this problem. Figure 3.5 provides a schematic diagram of the imager position shown with respect to the image plane. The schematic illustrates the approximate laser beam

angles during the scanning process. This image also demonstrates the off-normal incidence of the illumination beam on the object placed parallel to the housing of the imager. For roughened surfaces the diffuse reflections are best observed when the scanning beam is at a near-normal angle of incidence with respect to the object. According to the bidirectional reflectance distribution, with an increasing angle of incidence, the main intensity of the reflected radiation will be directed away from the detector [49]. This phenomenon accurately describes the observed behaviour of the Firefly IR Imager.

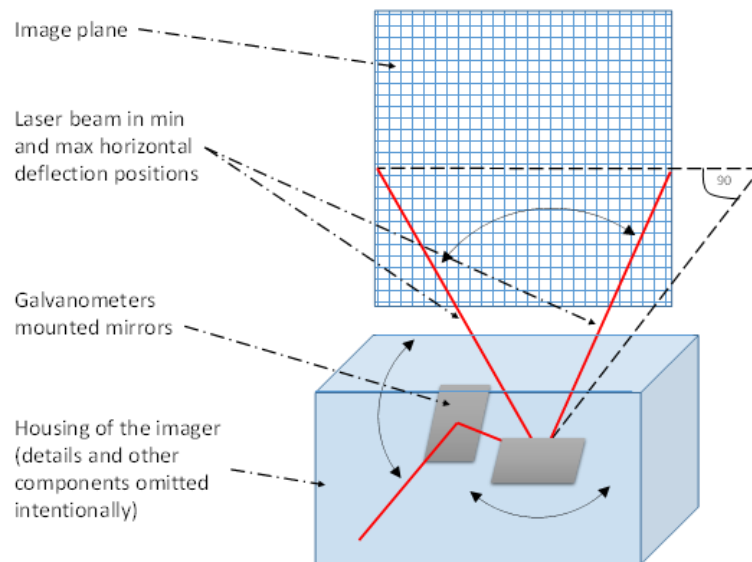


Figure 3.5. Simplified diagram of the minimum and maximum beam positions at one horizontal plane during the image scan.

Due to the off-normal incidence of the laser beam when imaging the painting placed parallel to the front of the Imager housing, it was decided to image the painting at three different orientations as illustrated in Figure 3.6. This helped to verify the impact that the incidence angles of the scanning beam have on the intensity of the reflected radiation that is collected. The grid canvas was first placed parallel to the imager housing, then $+45^\circ$ and finally at -45° from the normal parallel position. Since it was also noted that the intensity variation is stronger in the longer wavelength range, this test was performed in the Near-IR operating band of the system where this phenomenon is weaker. Any undesired artefacts observed in images at these wavelengths are expected to be amplified in the Mid-IR range. The results shown in Figure 3.6 confirmed the expected impact of the imaging setup and are consistent with the bidirectional reflectance distribution studies – increasing the angle of incidence results in a reduction in the amount of radiation that is reflected back to the detector. The data produced by the imager in this form was not acceptable.

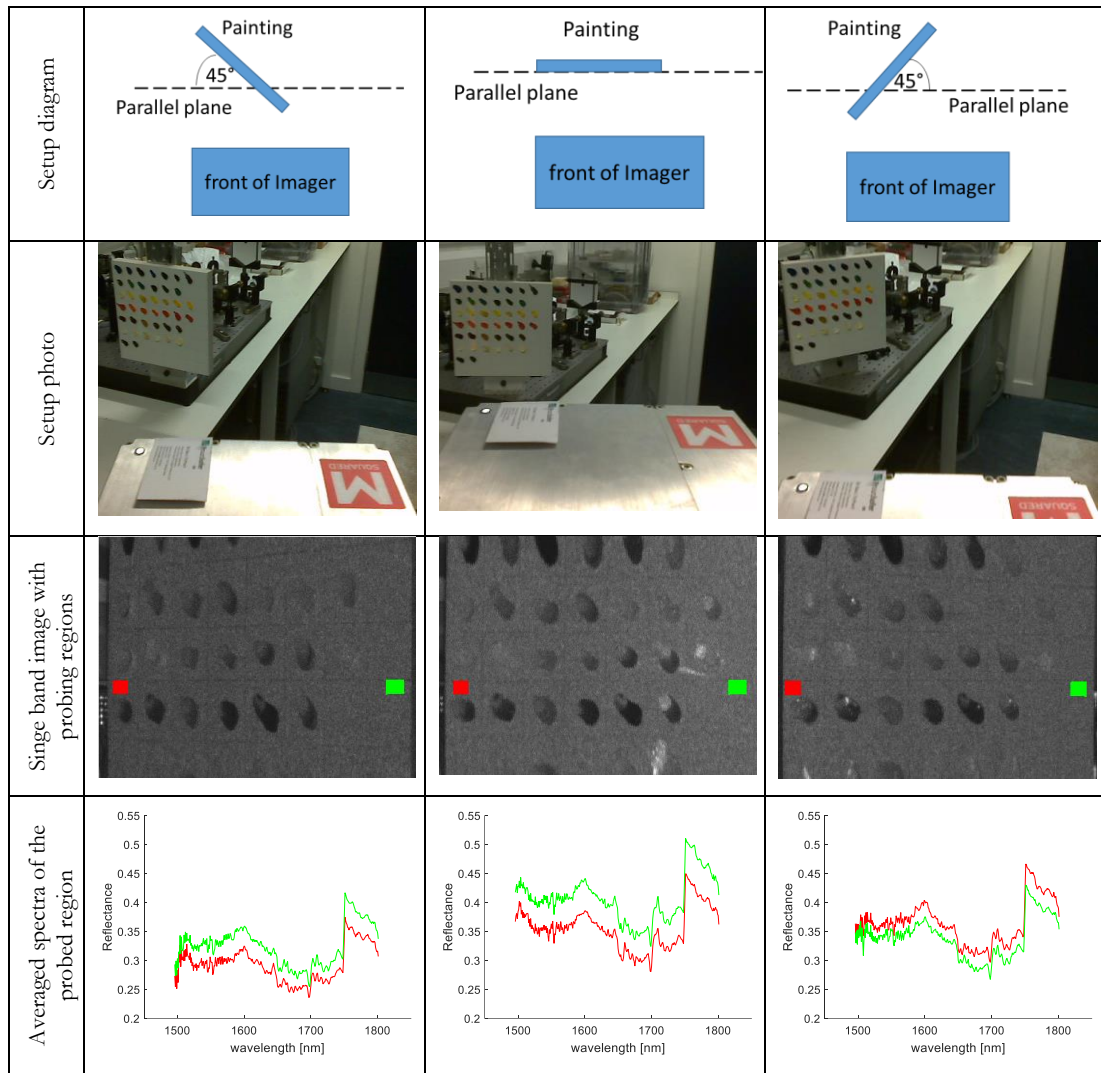


Figure 3.6. Results of the test for the impact of painting position on the intensity variation across the image. Colours of the lines in the graphs correspond to regions selected on the single band image.

3.2.2.2 Normalisation with the calibration image

The first attempt to mitigate the above-mentioned phenomenon was to normalise and correct the data with a uniform target, similar to white reference target approach. Knowing the technique described in Section 3.2.1, where a Spectralon tile is used for normalisation of the data from passive system, it was assumed that any uniformity of intensity can be removed from the image by use of similar approach. The Spectralon material is not applicable for mid-infrared region as its high reflectivity falls-off beyond 2500nm. As an alternative, a flat sheet of shotblasted aluminium was proposed. It is a very good infrared reflector and the shotblasting process provided the diffuse reflection property to its surface. In Figure 3.7 (a) a single band image of this aluminium sheet is demonstrated. Figure 3.7 (b) shows the same data set as illustrated in Figure 3.4 but normalised by the data of the calibration tile. Figure 3.7 (c) displays the graphical representation of the classification result.

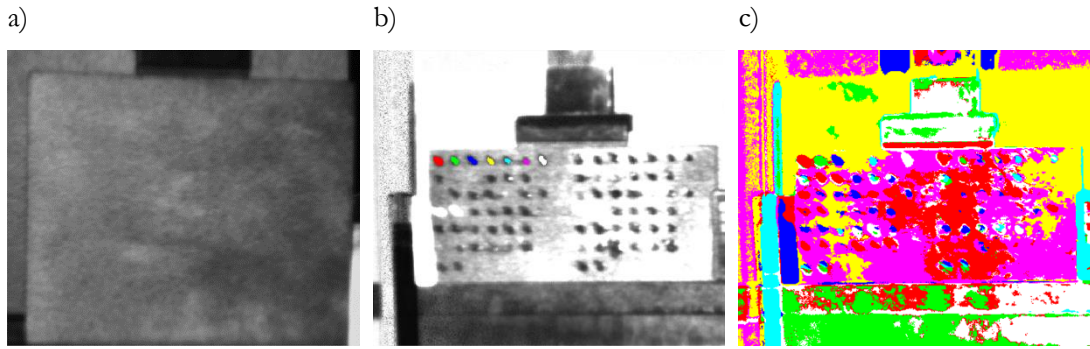


Figure 3.7. Single band image (at 3000nm) of the shotblasted aluminium sheet used as the calibration tile (a), normalised image of two grid canvases placed next to each other, with indicated regions of interest (b) and graphical representation of the classification algorithm based on this data set (c).

While a certain level of correction is observed, the intensity on the normalised data is still not uniform. Although this may be partly caused by imperfections of the target object, it was also discovered that spatial uniformity in the image data is highly dependent on the imaging wavelength as well as the type and surface roughness of the material(s). Therefore, performing normalisation with single reference target was not sufficient in order to match the properties of all potentially inspected materials.

The magnitude of the intensity variation observed during all the trials with the two-dimensional scan made any successful classification impossible, therefore it was decided that this image collection approach - the full field of view (FoV) with one 2D scan – is not acceptable for this project.

3.2.2.3 1D Galvanometer scan (line scan)

It was observed that the most significant difference in the amount of collected energy is due to the horizontal scan, while the impact of beam deflection in the vertical plane was less substantial. Following this remark, it was proposed to combine only one-dimensional scan, done by the embedded galvanometer, with scan of the other dimension, by translation of the object in front of the line of scan. With that approach, the actual collection efficiency in the horizontal plane was not important, as it would be the same for all the lines composing the image. The same linear translation stage that was used to provide movement in the pushbroom scans with passive system (Zolix KSA 11-200S4N) was employed to translate the grid canvas in front of the Firefly.

Although it is possible to disable the galvanometer controlling the horizontal movement, the data recorded with this system is always saved to a 2D matrix. The image size chosen in acquisition settings determines how many vertical lines compose one data set. As a result, the state of the object in front of the imager is affecting the shape of the data. For example, imaging a static

object with the size set of 512x512 pixels will result in 512 very similar copies of the same vertical line of the scan. Any movement of the object, only if the translation speed is equal to the speed of the galvanometer scan, will result in an undistorted image, but any other speed will appear as stretched (slower movement) or compressed (faster movement) one.

3.2.2.3.1 Fast translation

To explore this technique, the first approach undertaken was to scan the object with arbitrary speed (slower than the speed of the galvanometer scan). The grid canvas was positioned in front of the imager in such way that the region of interest filled the whole area of the image and was mounted on the translation stage capable of moving the painting through the line of the scan. Since there is no trigger signal available with the Firefly, the translation stage movement and image acquisition could not be synchronised, resulting in a set of images (for each individual wavelength) containing a random amount of background lines and fragments of the grid canvas in a form of stretched images, as in example is presented in Figure 3.8 (a) - (d). These results required a set of actions to reshape the data to a proportional image of the grid canvas. The lack of trigger, in addition to the random scan start time, caused more difficulties. Due to the left-to-right and right-to-left movement of the horizontal scanner, every second time the intensity values are acquired in reversed order. The manufacturer of this system accounted for it and it is programmed in the imager operating system to flip every second matrix to properly represent the oriented image. This automatic operation was in this case not desired and to proceed with this data, every other image had to be flipped back (Figure 3.8 images (b) and (d)). When this was performed, all the images from the set were stitched (Figure 3.8 (e)), and then every other such composition had to be flipped. This time it was caused by the reverse travel direction of the translation stage. Rearranged files were then all cropped and subsampled leaving only every third vertical line to remove the stretch (Figure 3.8 (f)).

Due to the continuous movement of the translation stage it was critical for the data to be acquired continuously. Continuous image recording was used to avoid any loss of information caused by the latency of the remote data acquisition and recording raw files. This mode is accessible only directly from the user interface and it records 8-bit compressed files. It was decided that for the purpose of this demonstration 8-bit data will be sufficient. However, at that time the operating system was still not updated and the amount of errors occurring during imaging resulted in a significant number of images missed from the transfer. Due to this fact, the whole recorded data set had to be first manually inspected to select an error free subset of images.

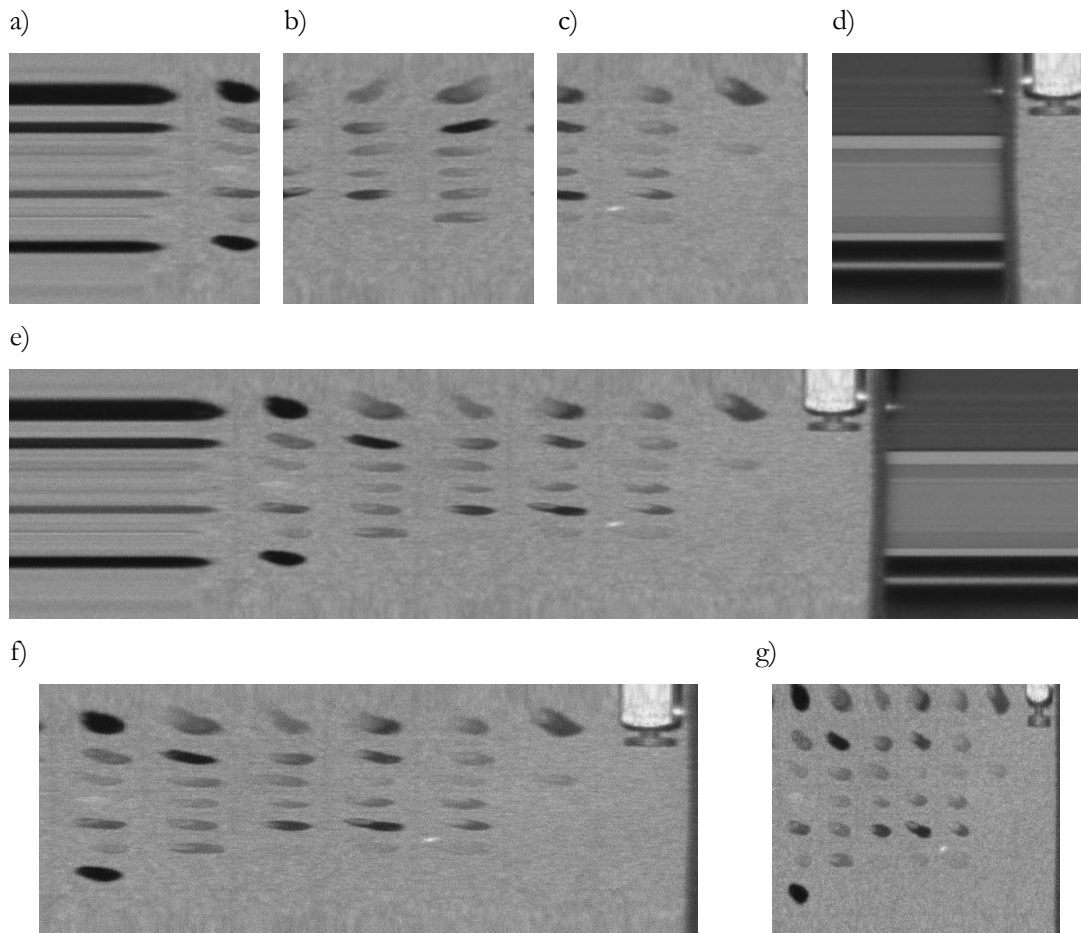


Figure 3.8. Subsequent steps of line scan imaging approach with fast painting translation (based on single band image at 1550nm), where (a) to (d) represent initial data, (e) rearranged and stitched composition, (f) cropped and (g) subsampled image.

This test was performed in the signal range (1490nm to 1850nm) but only images from the range 1620nm up to 1800nm could successfully be obtained using the aforementioned image reconstruction process. These images were then stacked into a hyperspectral cube and the quality of the data produced was assessed. At first, four regions of interest were selected in the four corners of the image, covering only the background of the grid canvas. Then average spectra were extracted from these regions. Comparison of these profiles demonstrated that intensity variation across the spatial domain was successfully minimised. The result of this test is shown in Figure 3.9.

After obtaining the positive result of this initial test, the classification algorithm was run on the data. Figure 3.10 (a) illustrates single band image with indication of ROIs used for extraction of training data. Figure 3.10 (b) shows a graphical representation of the classification result where a single class has been assigned to the whole background. The colours on this result correspond to the colours used for the selection of training data.

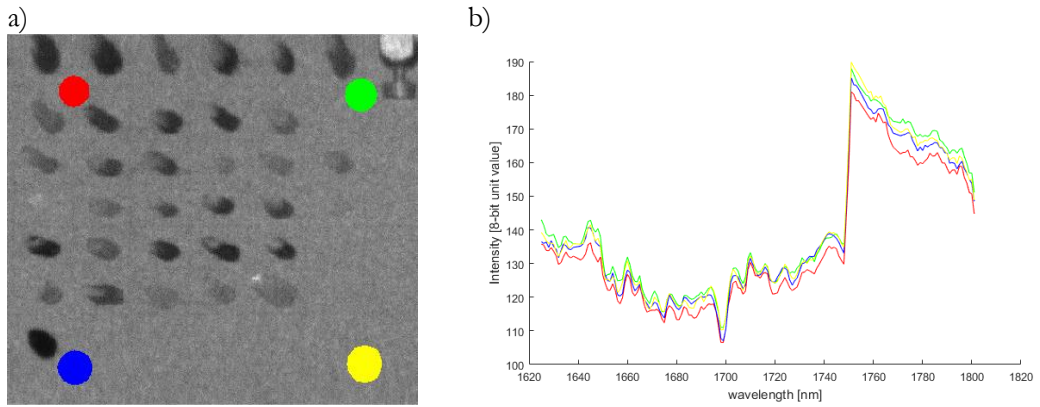


Figure 3.9. Single band image at 1710nm with four regions of interest indicated by coloured ellipses (a) and average spectral profiles extracted from these regions (b).

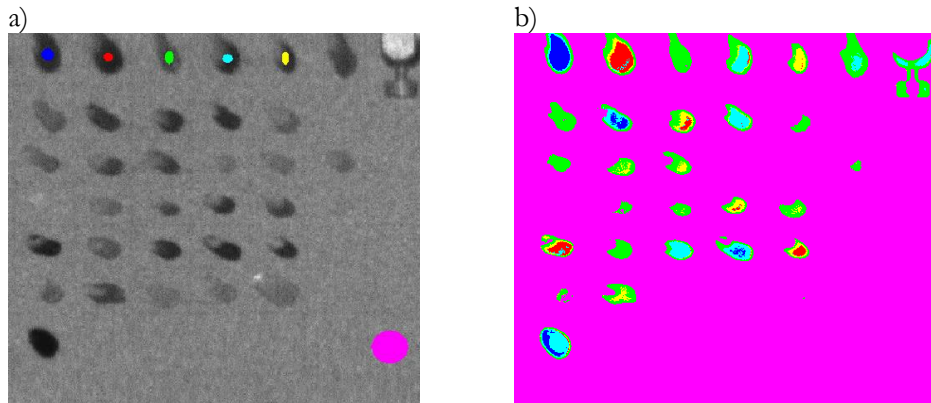


Figure 3.10. Single band image at 1710nm with regions of interest indicating selected training data (a) and graphical representation of the classification result (b). Note: classification of the paint samples is valid only for the paints selected in the training data, classification of other paints was not the purpose of this exercise and the result demonstrate the best match from the algorithm.

This short test demonstrated a way to reduce the spatial intensity variation. Unfortunately, due to errors in the user interface and resulting random loss of data this method was not reliable and as such was not chosen for this project.

3.2.2.3.2 Gradual translation

After the observation of a successful mitigation of the spatial intensity variation by the line scan approach presented above, it was decided to attempt a similar technique, however this time with the target stationary during each line acquisition. This method was believed to be less susceptible to the data loss issues observed during previous experiment. In this test the two grid canvases were rotated 90 degrees and top-to-top put next to each other – this way in case of successful reduction of intensity variation the actual classification on unseen data can be observed. The paintings mounted on the translation stage were moved sideways 0.5mm each time and for each position one full image was recorded. With the disabled galvanometer responsible for

horizontal scan, this resulted in 512 repeats of the same line. By calculation of a median value for each row in the image, one vertical line was created and all lines per one wavelength were concatenated to form an actual 2D image. Other methods to extract single line were also tested, such as the use of a maximum or minimum value and discarding all lines but the one at fixed location. The minimum and maximum values were introducing spikes of random noise and for this reason they were abandoned. Use of fixed line was a viable alternative to the chosen approach, however the median additionally helped to minimise the speckle noise (see Section 3.3.1.2), therefore this one was chosen for image reconstruction. Each image was composed of 383 lines (resulting from 196mm travel of the translation stage, with the step of 0.5mm).

Due to the extended duration of the capture process (about 1 hour per 1 image per 1 wavelength) it was decided to populate the cube in a way that its spectral resolution could increase gradually (as opposed to fixed, high resolution cube with gradually increasing wavelength span). Figure 3.11 represents the image collection sequence, where the data was first acquired at the edges of the signal range and subsequently the imager was tuned to the middle at the range between previously recorded spectral points. This way each new acquired wavelength created a new range and iteratively the next data point was taken in the middle of this range. This process took about 1 week of non-stop operation and resulted in a resolution of 3-4 nm (in NIR wavelength range).

During the acquisition and stitching of all the monochrome images a slight distortion in each single captured image was discovered. Although this was not fully understood, some lines seemed to be missing and other seemed to be multiplied, causing the objects (paints) to be randomly shifted and stretched/compressed along the horizontal edge. In the vertical dimension the images were also varying between each other, which was most obvious by the varying position of the top edge of the canvas.

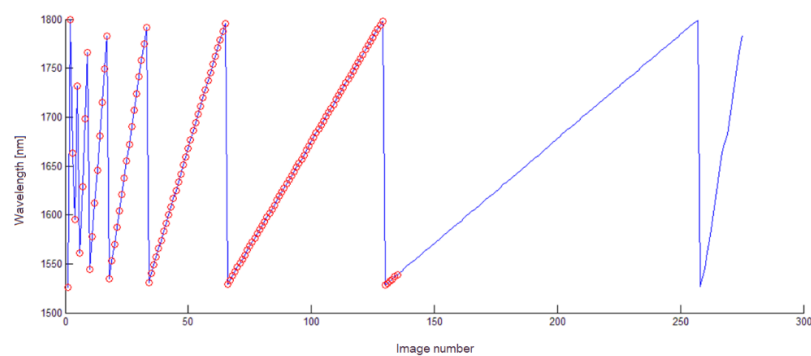


Figure 3.11. Data acquisition sequence with gradual increase of the spectral resolution, where blue line indicates the data collection sequence and red circles mark the images that were actually acquired within available time.

This was expected to be caused by the changes in thermal dynamics of the oscillating galvanometer performing vertical scan in the course of all the days of this scan. Some of these distortions were successfully reduced by the image registration applied during the conversion of the single band images to the hyperspectral cube. Figure 3.12 (a) illustrates an example single band image (at 3200nm) acquired with this technique with the four ROIs selecting background of the imaged painting in its corners, to extract average spectra at these regions as shown in Figure 3.12 (b).

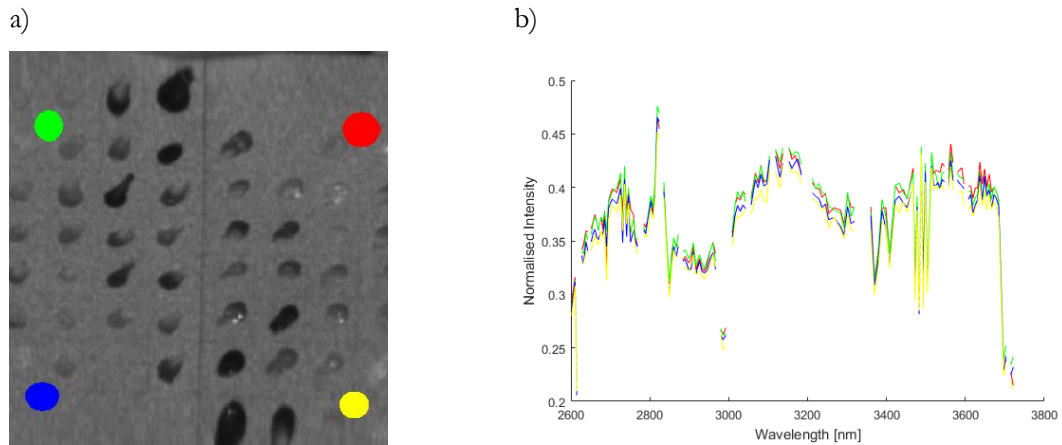


Figure 3.12. Single band image at 3200nm with four regions of interest indicated by coloured ellipses (a) and average spectral profiles extracted from these regions (b).

A classification algorithm was also run on this data. Figure 3.13 demonstrates the training data and graphical representation of the classification result. It can be noted that the line scan method again resulted in a single class being assigned to the background, which confirms the high level of uniformity in illumination. Additionally, the first column of paints from right canvas was generally positively classified based on the training data from the last column of the left canvas.

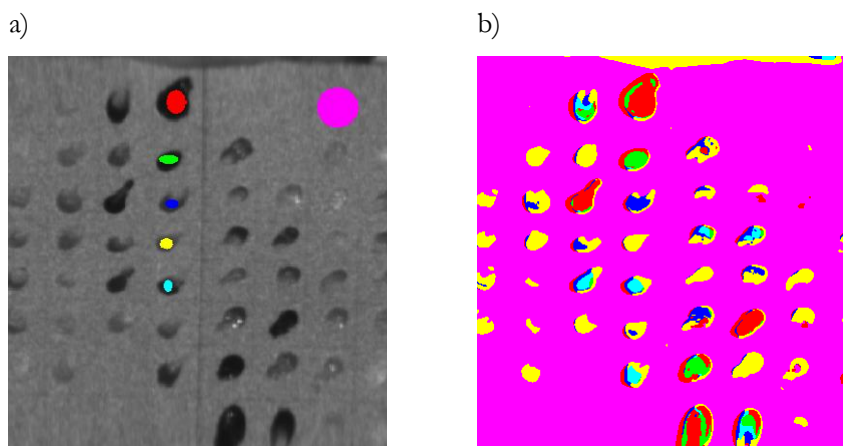


Figure 3.13. Single band image at 3200nm with regions of interest indicating selected training data (a) and graphical representation of the classification result (b). Note: classification of the paint samples is valid only for the paints selected in the training data, classification of other paints was not the purpose of this exercise and the result demonstrate the best match from the algorithm.

Although this method followed the previous one, with demonstration of the line scan as a successful approach for reducing the intensity variation, its prohibitively long acquisition time made it very impractical and not effective to proceed within this project.

3.2.2.4 Segmental 2D Galvanometer scan

Elimination of the beam deflection in the horizontal plane proved to be a very successful method to improve intensity uniformity on the image, at the same time however, a very impractical one. Following the 1D scan testing the idea was brought up, which is in between full field of view and line scan imaging. To perform it the ‘Zoom’ function of the Firefly IR Imager was exploited. Adjusting this feature is changing the extent of the galvanometer rotation and therefore the maximum angle of beam deflection. While doing this, the amount of scan points is not changed therefore as a result, the produced image has the same spatial size but is featuring much smaller object – thus this function is called ‘Zoom’. The potential of this procedure was recognised as the finite size of the target paintings could be divided into smaller regions. Resulting images would be subsequently stitched together to form a single image representing the whole canvas at each wavelength. Thanks to this procedure the deflection of the scanning beam was reduced and thus improved the spatial intensity distribution across the scanned area whilst maintaining workable image acquisition time. The size of the segments was empirically derived to be 50 x 75mm. With such a field of view, the whole grid canvas was acquired with 9 scans while the ‘test painting’ (see Section 3.4.1) with 6 of them. To assure accurate and repeatable image portioning into the small blocks described above, the scanned painting was placed on a remotely controlled linear x-y translation stage. Figure 3.1 (b) demonstrates the scanning system including the Firefly IR Imager and the painting placed on the translation stages. Figure 3.14 illustrates the segmentation of both these targets and example single band intensity images in near- and mid-wave infrared regions for both of them.

Figure 3.15 illustrates the training data and graphical representation of the classification result, performed to demonstrate one-to-one comparison with the line scan results. As it can be seen in Figure 3.15 (a), within each small region there are still variations in collected intensity, and these are especially apparent in selected bands of the mid-IR data.

Although the differences in intensity are still present and the uniformity of the image acquired with this technique was not as good as the one from the line scan, this result demonstrates significant improvement with respect to the full FoV scan. On the other hand, the imaging could be done with remote control (assuring reliable saving of the data) with acceptable acquisition time (approximately 5 hours for the grid canvas). Due to the nature of the hardware

(complexity of detector settings), the reflectance calibration was not possible for this equipment. To rescale the spectral data to the reflectance range [0-1], the 16-bit intensity data acquired on each wavelength was divided by the maximum value (65,536). After completing the data stitching and rescaling, no further pre-processing was applied.

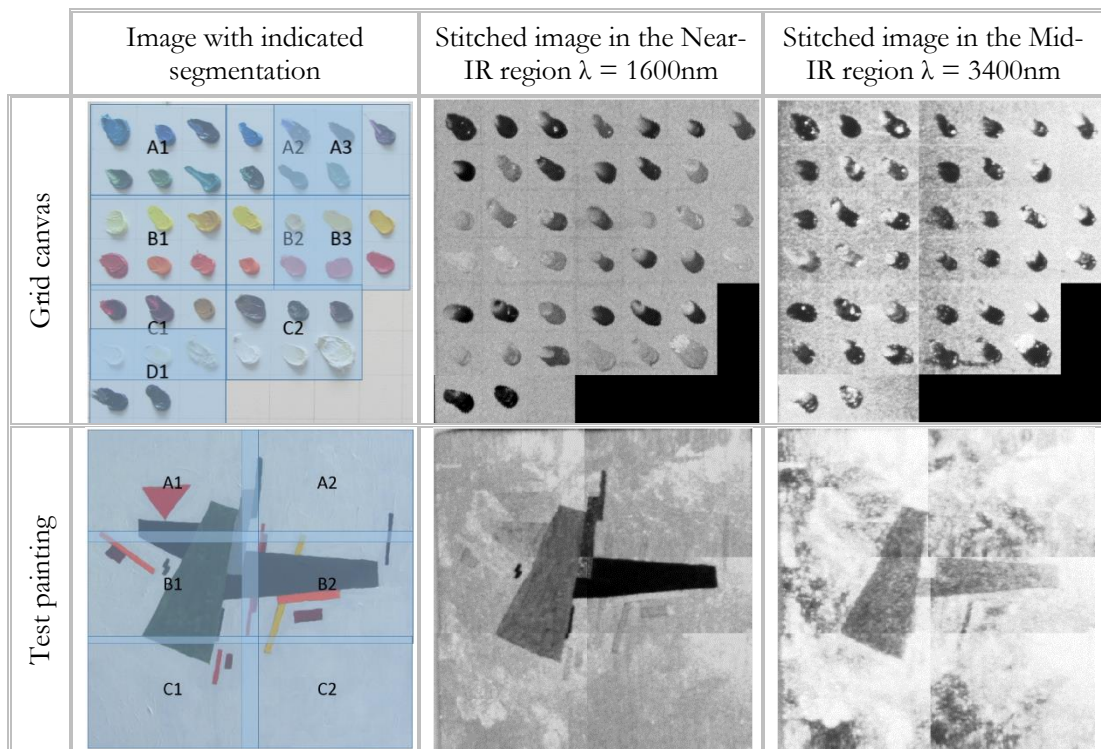


Figure 3.14. Illustration of the segmentation procedure for the two target paintings with examples of the stitched single band images in near- and mid-IR regions. Note: the black colour at the bottom right corner of the grid canvas HSI data represent lack of data.

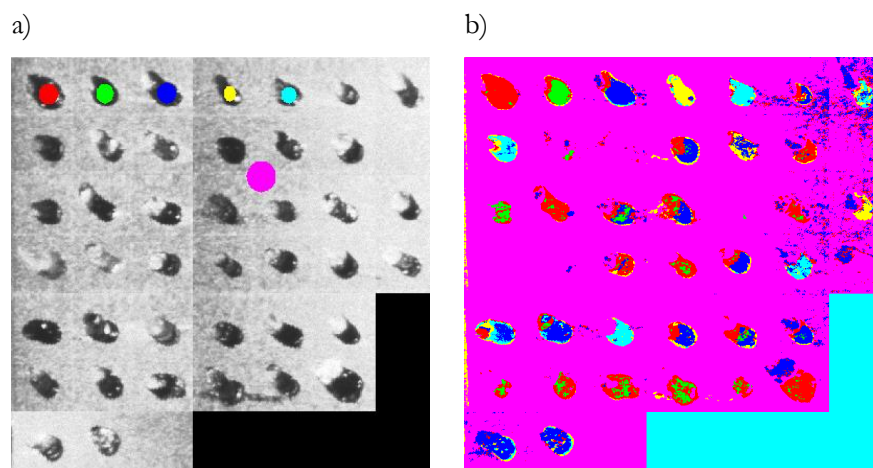


Figure 3.15. Single band image at 3400nm with regions of interest indicating selected training data (a) and graphical representation of the classification result (b). Note: classification of the paint samples is valid only for the paints selected in the training data, classification of other paints was not the purpose of this exercise and the result demonstrate the best match from the algorithm.

3.3 Hardware improvement techniques for imaging artefacts

In Section 3.2 various attempted image acquisition modalities have been presented. This work was triggered by the challenge to minimise of the intensity variation across the spatial domain of the image, caused by the varying collection efficiency of the reflected radiation. This was however not the only undesirable artefact caused by the laser-based nature of the employed imager. Two other issues that were affecting the quality of the data were the noise level and the presence of the specular reflections. Unlike the collection efficiency variation, these did not hamper the progress of the project, but they did affect the quality of the collected data. Figure 3.16 illustrates 2 segments of the grid canvas, before stitching into a whole image. Each of these segments contains 6 paint blobs on the plain background. Though, when imaged, the background does not appear uniform. Next to the aforementioned change in intensity, the salt-and-pepper type of noise affecting this image is very apparent in this region. This noise is equally present everywhere in the image, yet the intensity of these regions is much lower than the background, caused by higher absorption of paints, making the noise less obvious. The paint blobs on the other hand, due to their three-dimensional structure, feature large specular reflections. It can be clearly seen in Figure 3.16 that within one object (paint blob) the spectra extracted from regions captured from a specular reflection are significantly different from those not affected by this phenomenon. Examples of a paint spectrum were extracted from the segment C2 and are shown together with the average spectral profile of the background. Noticeably, the region affected by specular reflection is spectrally more similar to the background rather than to the other regions of this paint's image.

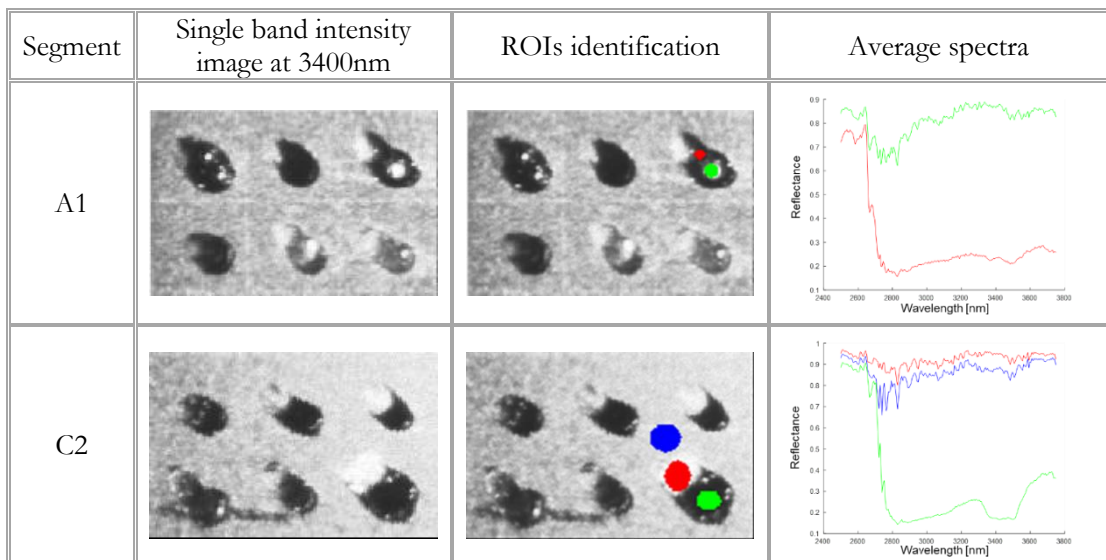


Figure 3.16. Image examples demonstrating salt-and-pepper type of noise as well as the impact of the specular reflection on the spectral signature of the area affected by this phenomenon.

Despite these observations, for the purpose of the classifier training, it was decided to extract the data from the whole paint regions regardless of obvious intensity variations within these regions, to label them as one class, expecting that similar imaging artefact could be present in the tested data. Therefore, training of the classifier on a combination of non-specular and specular reflection data was chosen. Hence, despite manifestation of these artefacts in acquired images, the main strand of the project continued with the Firefly IR Imager. In parallel, the above-mentioned issues were investigated and mitigation techniques proposed as a separate work package in this programme. This resulted in employing custom build, lab bench-based imaging systems. All procedures will be presented below as potential techniques that could be employed in new embodiment of Firefly-like, laser-based imaging devices.

3.3.1 Noise

The salt-and-pepper noise observed in the acquired images manifests itself in regions of randomly distributed higher and lower intensity pixels or groups of pixels. As a result of the analysis of this noise's nature it was concluded that its presence has a double root cause. First, the per-pulse jitter in illumination energy that the Firefly imager exhibits, which is dictated by the operational mode of the laser driving the Firefly imager. Second is the speckle effect which is typical for any laser-based imaging systems. Both of them have different physical principles and their mitigation would require two independent mechanisms, so as such, both these will be considered separately.

To quantify the noise level N_L measured from the tested system, a measure of variability was introduced in this study, and it is expressed by the Formula 3.2

$$N_L = \frac{\max(D) - \min(D)}{\text{median}(D)} \cdot 100\% \quad (3.2)$$

where $\max(D)$, $\min(D)$ and $\text{median}(D)$ correspond respectively to the maximum, minimum and median value from the data set D . This parameter directly relates to the noise level in the data set, therefore low value is desired for a best quality data. Improvement of the noise level resulting from the use of the normalisation electronics will be derived as:

$$I_N = \frac{N_{orig}}{N_{norm}} \quad (3.3)$$

where N_{orig} is the noise level measured directly from the laser system, without the use of boxcar electronics while N_{norm} is the noise level of the normalised signal.

The performance of the system was also analysed by the signal-to-noise ratio SNR defined in a way typical for the image processing community as:

$$SNR = \frac{mean(D)}{\sigma(D)} \quad (3.4)$$

where $mean(D)$ represents the mean value from the data set D and $\sigma(D)$ is the standard deviation derived from the same data. Since (as its name indicates) this is the ratio between signal and the noise, higher value corresponds to better quality data. Same as for the noise level, an improvement in SNR was calculated to observe the impact of proposed technique. This was defined as:

$$I_{SNR} = \frac{SNR_{norm}}{SNR_{orig}} \quad (3.5)$$

where SNR_{norm} is the signal-to-noise ratio of the normalised signal while SNR_{orig} is the signal-to-noise ratio of the original, unprocessed signal.

Two tests modes were prepared to study the performance of the proposed normalisation: single point in time and spatial scan. In both cases a plane, white paper was used as the target object. Measurement of a single point in time allowed the test of the pulse-by-pulse jitter based noise reduction only, without the impact from any other noise sources. Data set of 1000 samples was collected for each test, which took approximately 3.5 minutes per run. For the purposes of this investigation, to obtain the spatial scan the galvanometer-based, angular scanning approach which the Firefly employs was replaced by a fixed-beam, linear target scanning configuration using a stepper-motor driven x-y translation stage (the same translation stage arrangement as demonstrated in Figure 3.1 used for moving of the test painting). The key point of this test was to demonstrate the advantage in noise reduction achieved by the proposed approach. Replicating the angular scanning mechanism could complicate this demonstration by the intensity variation from which the Firefly device suffers (see Section 3.2.2). Potentially also by the transition from the highly reflecting specular regime (when the beam is fully or nearly perpendicular to the target) and the Lambertian regime, where one relies on back scatter alone. During this test there was no speckle reduction technique implemented, therefore this data set will represent the combination of the noise from pulse-by-pulse jitter and the speckle effect.

For each spatial scan test, a region of 20mm x 20mm was scanned with the 1mm step. This created an image with size of 20x20 pixels – very modest data set, however sufficient for the demonstration purpose.

3.3.1.1 Per-pulse jitter

The nature of this noise source lies in the intensity variation of the per-pulse emitted energy from a laser system. This amplitude jitter comes from the physics driving the pulsing mechanism employed in the Firefly IR Imager, i.e. Q-switching. Q-switching is one a number of approaches to run a laser system in a pulsed mode. It is the most common technique to achieve pulsing on the nanosecond time scale. During each high-loss period of the switching cycle the population inversion accumulated in the gain medium will vary, resulting in inconsistent energy released from this arrangement during the low-loss switch period. The physics of Q-switching and all its jitter characteristics could by itself constitute a separate project so these will not be further discussed in this work.

Therefore, the output of a laser system is a jittery pulse train which, when used in imaging, illuminates the point in space with erratic energy levels, then when reflected and captured in a form of an image is manifested as a noise. To minimise this effect a normalisation technique was proposed, where the amplitude of the reflected, returning pulse is divided by the information about the amplitude of the same pulse, outgoing from the laser setup, resulting in a pulse train, in theory free from the jitter caused by the laser, with intensities varying only due to the changing absorption of objects reflecting the illumination. To demonstrate this concept, a laser setup with monitored output and fast electronics able to process and normalise the acquired pulses were required. The former was a lab bench based OPO setup while the later was realised in a form of the electronic arrangement containing two channels of boxcar integrator combined with a division process to perform the normalisation. Each of these are presented below, followed by the results achieved from their integration.

3.3.1.1.1 Optical Pulsed Source

The intracavity OPO upon which the Firefly depends, is optimised for high repetition rate, high mean power and low per-pulse energy operation. In order to maximise the chances of success in this development phase, it was presumed that a low repetition rate and high per-pulse energy OPO would be advantageous, as it would lead to approximately two orders of magnitude greater energy per pulse, therefore raising the signal significantly further above the noise floor. Therefore, an extra-cavity singly resonant OPO (EC-OPO) pumped by a Q-switched neodymium-doped yttrium aluminium garnet (Nd:YAG) laser was constructed (as shown in Figure 3.17 (a)).

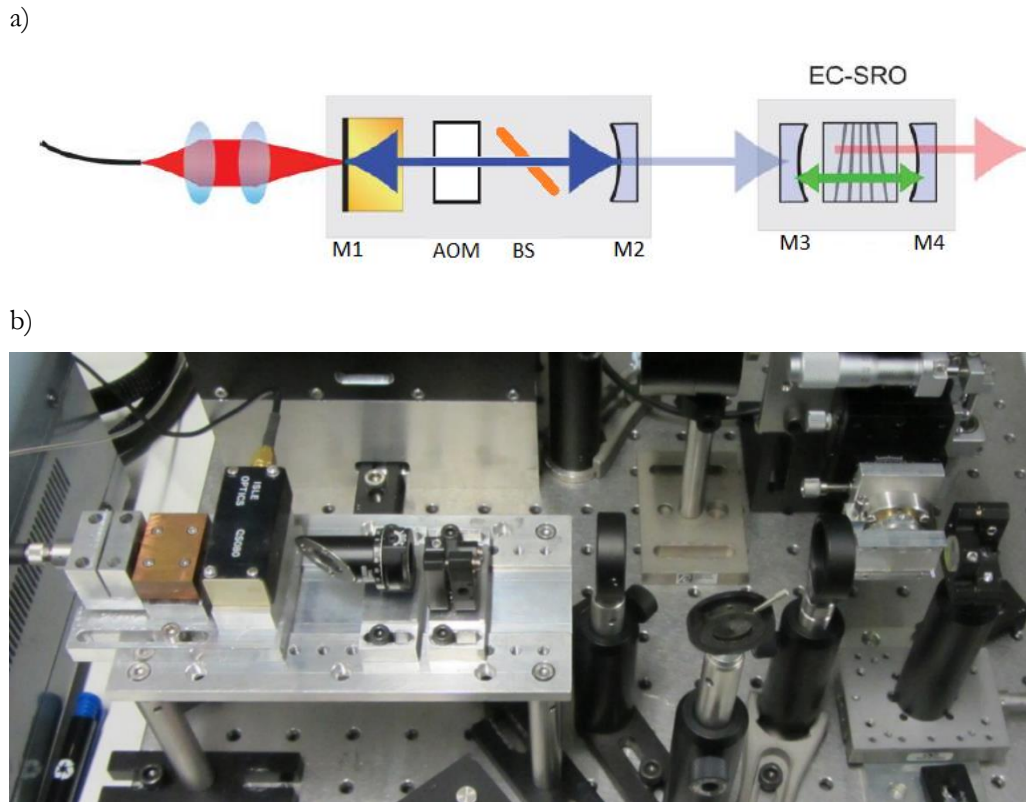


Figure 3.17. A diagram (a) and a photograph (b) of the EC-OPO developed in this test.

The pump laser was initially pumped by 3W of radiation at 808nm wavelength from a fibre coupled laser diode. The cavity of this laser was formed between the mirrors M1 and M2. The M1 mirror was achieved by high reflection (HR) coating of one facet of the Nd:YAG crystal at the 1064nm radiation of this laser. It was also anti reflection (AR) coated for the primary pump at 808nm. The M2 mirror was a 90% reflecting output coupler. Within the cavity an acousto-optic modulator (AOM) was introduced to enable Q-switched operation of this laser. Additionally, due to the fact that Nd:YAG based lasers emit non-polarised radiation and a PPLN based OPO requires polarised input pump radiation, a Brewster surface (BS) was introduced to the cavity to transmit only the horizontally polarised component of the oscillating field. The OPO was built as a short cavity between mirrors M3 and M4, in singly resonant arrangement. The mirror M3 was AR coated for the 1064nm pump radiation and HR coated for the signal range 1400nm – 1700nm. The mirror M4 was HR coated for the signal waveband letting the whole down-converted mid-infrared idler radiation pass through. The heart of this OPO was made by the 30mm x 11mm x 1mm, Periodically Poled Lithium Niobate crystal employing the fan grating structure, allowing the wavelength tuning by the translation of crystal's position through the beam. The grating period ranged from 27-32.5 μm over the 11mm axis of the crystal resulting in phase matching range of 1380 - 1790nm ($\Delta\lambda_s \approx 410\text{nm}$) for signal and 2620 - 4645nm ($\Delta\lambda_i \approx 2025\text{nm}$) for idler. The orientation of this PPLN crystal in the EC-OPO cavity required the horizontal polarisation of the

pump, which defined the orientation of the aforementioned Brewster plate. Figure 3.17 depicts the basic diagram and photograph of constructed EC-OPO.

Only a modest characterisation of this system was performed to test the per-pulse energy performance of the described arrangement. Initially the average power and peak energy were tested as function of Q-switching repetition rate for the stand-alone pump laser. This was performed to define the repetition rate that gave the optimal per-pulse energy from the experimental setup. Figure 3.18 illustrates result of this test where the pulse energy rapidly increases with decreasing repetition rate, until it reaches a plateau at approximately 15kHz switching rate, when the pulse energy stays at the level of 0.17mJ.

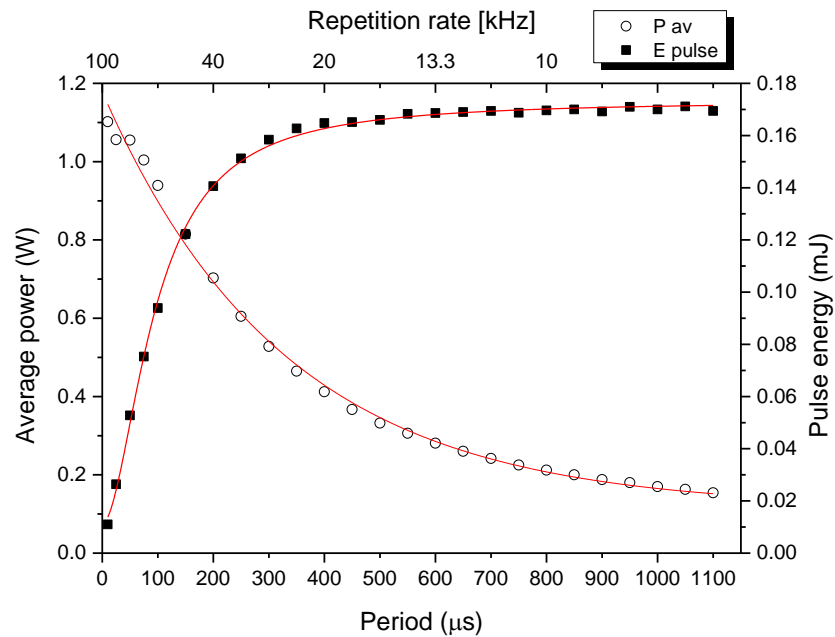


Figure 3.18. Pump laser characteristic of average power and peak energy as function of Q-switching repetition rate.

The average power of the laser behaved inversely to the pulse energy and from approximately 1.1W at the 100kHz repetition rate it dropped to approximately 200mW at 1kHz. Operation at 10kHz repetition rate was chosen for the whole duration of this experiment, which corresponds to an average power of 1.1W and pulse energy of 0.17mJ.

Following this measurement, the pump laser was integrated with the OPO cavity and extra-cavity operation of this OPO was realised. This was characterised for the mid-IR idler pulse energy performance. The results of these measurements are demonstrated in Figure 3.19, where is noticeable that 0.17mJ of pump energy induced approximately 20 μJ pulses of idler radiation (which results in approximately 2kW peak power, considering 10ns pulses). Based on this characteristic it can be deduced that the slope efficiency for idler pulse energy reached 16%.

This system produced approximately 20 μ J pulses in the tunable mid-infrared spectral region, compared to \sim 0.5 μ J as produced by the intracavity OPO (IC-OPO) based Firefly, pulsed with high repetition rate of approx. 350kHz. At this stage, the goal was to show the potency of the per-pulse energy normalisation method and therefore it was intended to do so with this higher energy system to relax the tolerance on the produced electronic instrumentation. Once proven, the speed and sensitivity of the developed electronics would need to be improved in order to accommodate the higher repetition rate, lower per-pulse energy which the Firefly produces.

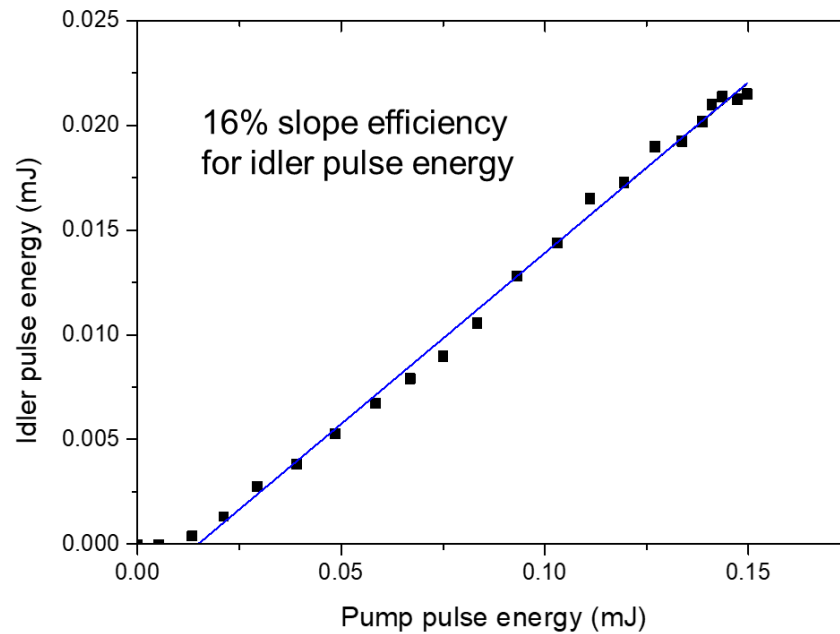


Figure 3.19. Pulse energy of the idler as a function of pump pulse energy.

While in operation, the full tuning range of the EC-OPO was characterised versus the position of the PPLN crystal. As presented in Figure 3.20, only 8mm out of 11mm crystal width was used to generate the down-converted wave. This was caused by the coatings on the OPO mirrors running out of their high reflectivity range, therefore not supporting the parametric process anymore. As demonstrated, the signal and idler waves tune over the range 1.49 μ m-1.70 μ m and 2.84 μ m-3.72 μ m respectively, recreating similar spectral range to that available from the Firefly imager.

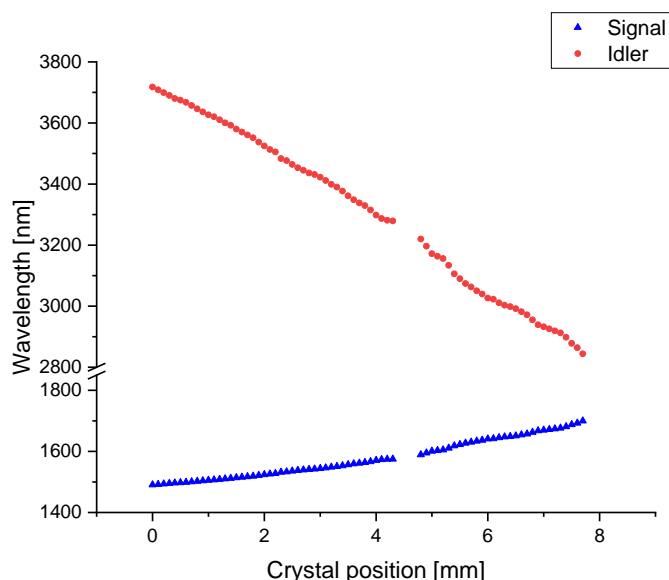


Figure 3.20. Tuning range of the EC-OPO through its phase matching range.

Having identified the most significant aspects of the system performance for the project, the work proceeded towards the main part of the experiment. In order to do so, the bare EC-OPO was now equipped with the optics controlling the propagation of the main output beam as well as the additional, reference arm, sampling a fraction of the main beam to enable the normalisation process.

The idler beam outcoupled from the OPO cavity was first collimated to assure a beam size suitable for imaging at varying distances. Subsequently a germanium filter was used to spectrally clean the beam, passing only the idler wavelengths, while blocking all the other frequencies produced in the parametric process. Then the beam passed through the uncoated calcium fluoride (CaF_2) window which, while allowing the majority of this radiation to pass, was reflecting approximately 3% of its power, thereby creating the reference arm for the imaging beam. This sampled radiation was then reflected for the second time from a similar CaF_2 window and the reflected beam was focused to a photovoltaic, thermoelectrically cooled and optically immersed IR detector (PVI-2TE from VIGO Systems S.A.). This double stage power reduction was needed in order to bring the optical power in the reference arm closer to the one detected after reflection from the scanned object. The main beam was directed to the scanning arrangement (as described below in Sections 3.3.1.1.3 and 3.3.1.1.4) and the reflected beam was focused through a 2" lens to another VIGO detector. The large, 2" diameter lens provided sufficient collection aperture for this optical system. During the experimental phase it was discovered that the mismatch between the detected reflected power and the one in the reference arm is still too big to perform successful normalisation. To bring these closer, two continuously variable neutral

density filters were introduced in both arms to provide controlled attenuation. Figure 3.21 demonstrates the setup and illustrates the different beams.

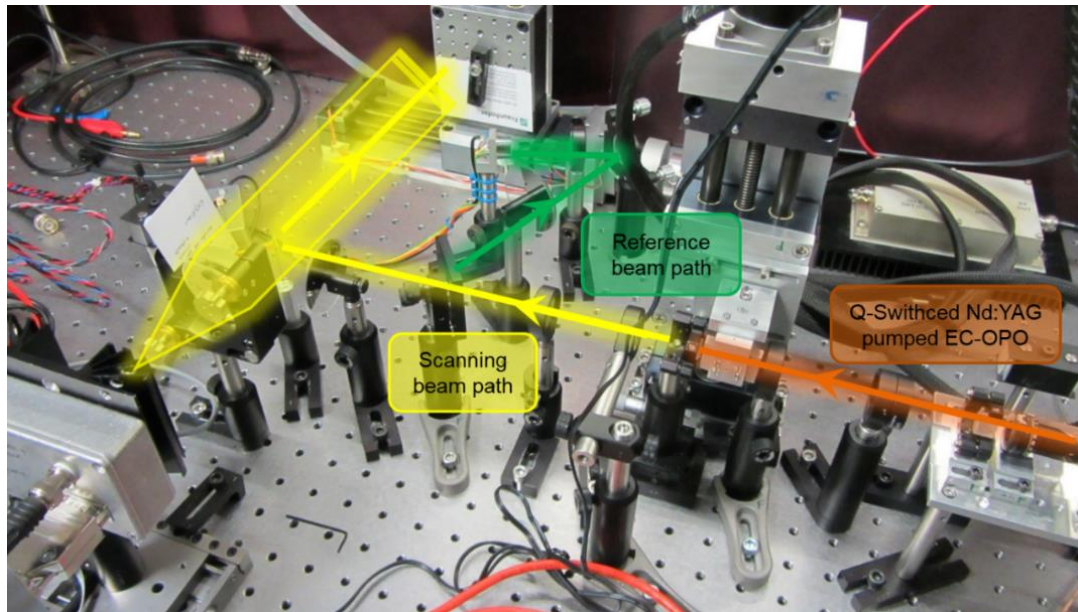


Figure 3.21. Test bed of the EC-OPO based imaging setup for the normalisation experiment.

3.3.1.1.2 Boxcar integrator and normalisation electronics

The methodology chosen for noise reduction was to measure the outgoing pulse energy (further referred to as Channel B) and use that to normalise the returned signal (further referred to as Channel A), reflected from the target. Therefore, any jitter in the emitted energy will be eliminated through the A/B normalisation (values from Channel A divided by these from Channel B). Both, the intracavity OPO which forms the basis of the Firefly IR imager and the extra-cavity OPO that is used in this study served as pulsed sources, with an optical pulse width (taking into account the speed of the detector) of approximately 10ns. Due to the short pulse, it was not possible to simply feed the signals into an analogue multiplier (configured for division). Additionally, the pulses were significantly separated in time due to the time-of-flight difference between the local reference detector and the imaging detector. Therefore, it was necessary to construct electronic instrumentation which was fast enough to measure the area under the pulse envelope, and then hold this value whilst normalisation takes place. To this end, a very high bandwidth, dual channel boxcar integrator was adapted, which then feeds in, after signal conditioning steps, into an analogue normalisation chip. Figure 3.22 shows the layout of the PCB design with photograph of the boxcar integrator board and circuit diagram of the heart of this device – the integrator section. This device was designed and built by Dr David Stothard.

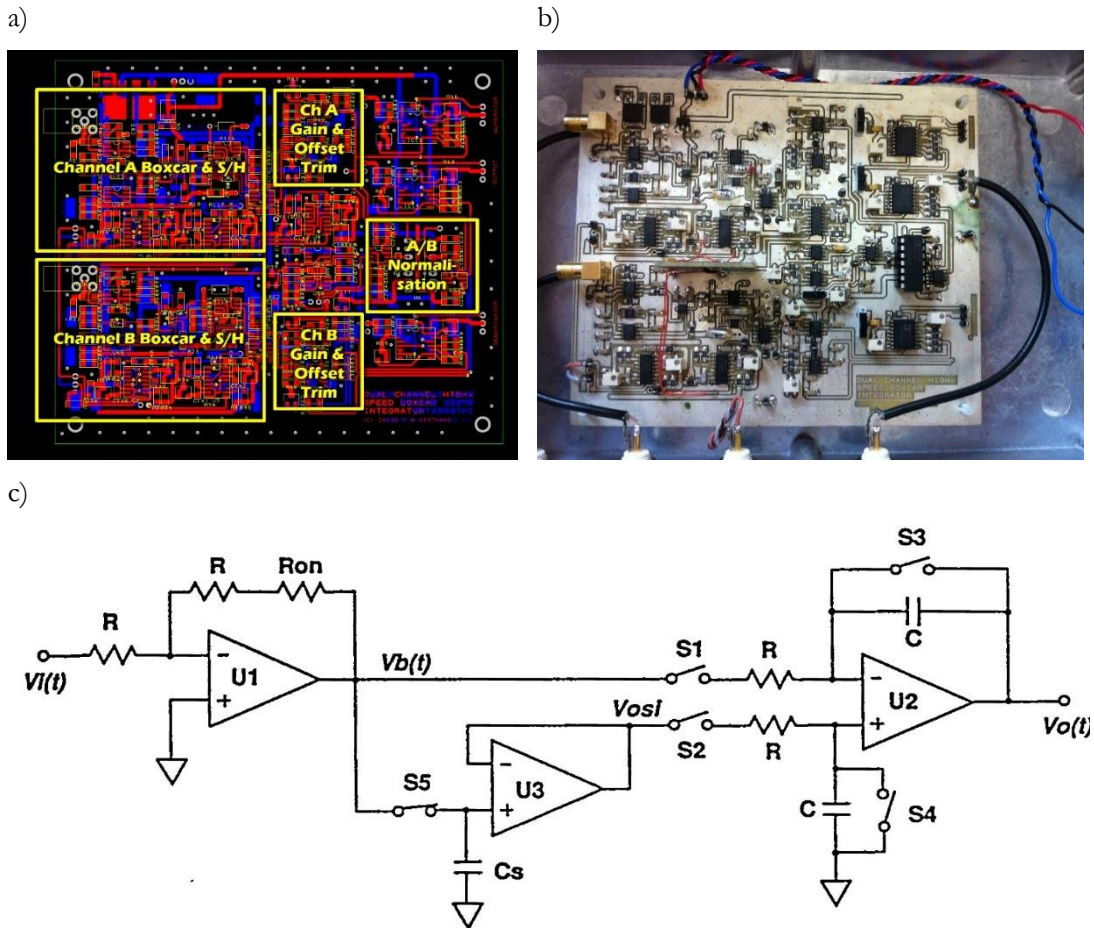


Figure 3.22. The Boxcar Integrator electronics: PCB layout (a), photograph of ready board (b) and the electronic circuit of the integrator part (c).

The oscilloscope screens in Figure 3.23 demonstrate step by step the critical operations performed on the board of the integrator to achieve the normalised signal. In this description, the specific operation is illustrated by the respective traces, assigned as numbers (1) – (9) corresponding to the traces shown in Figure 3.23 (a)-(f). The initial trigger for the Boxcar operation is linked to the TTL (Transistor–Transistor Logic) signal (1) activating the AOM, and in result generating a laser pulse (2). For each channel separate boxcar timing (position and width) is set (3). At the same time, reset of the integrated signal can be set, latest before the new integration takes place (4). When the boxcar is aligned with the pulse, it is integrated and this value is kept in continuous state until the reset timer will clear this signal in preparation for next integration.

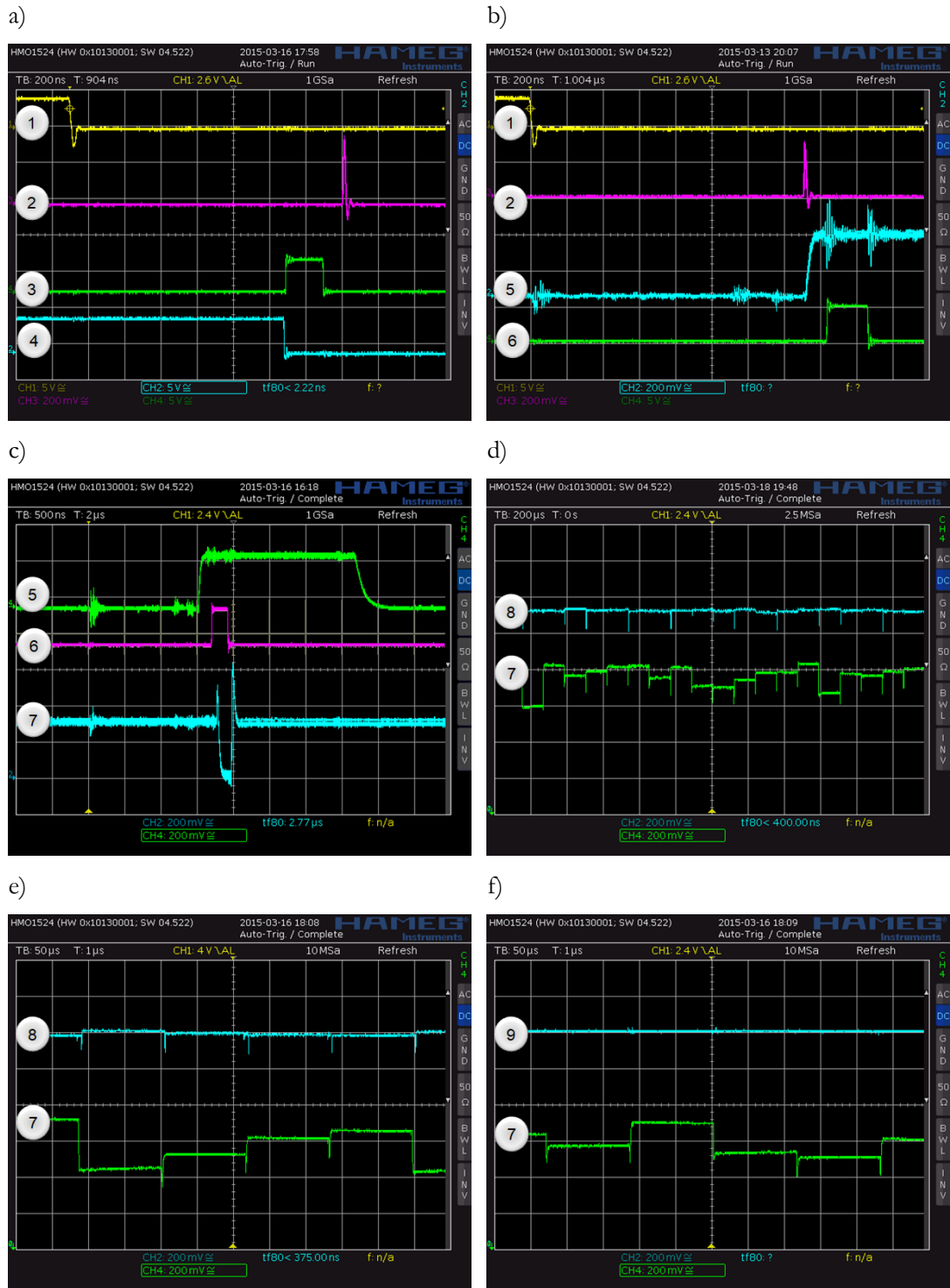


Figure 3.23. Oscilloscope screens (a) - (f) demonstrating the operation of the boxcar integrator electronics where trace 1 illustrates TTL trigger signal, subsequent traces constitute as follow: 2 - the laser pulse, 3 - the boxcar timing, 4 - the reset signal, 5 - the integrated signal, 6 - the "sample and hold" timing, 7 - the quasi-continuous integrated signal of one channel, 8 - the normalised signal, 9 - the averaged normalised signal.

It should be noted that even though the position of the boxcar is correct for the pulse integration, due to the latency of the electronic components, its trace displayed on the oscilloscope screens does not overlap with the position of the pulse. Trace (5) illustrates the voltage resulting from the integration of the laser pulse over the time of the boxcar. Integrated signal is being sampled during “sample and hold” time (6) and is stored in quasi-continuous train of voltage values corresponding to the integrated laser pulses (7). All the steps from (1) to (7) are repeated for both channels (A and B) and the normalised signal resulting from division of Channel A by the Channel B is presented as one trace (8). This process is significantly minimising pulse-by-pulse jitter in the measured amplitude, though an additional step can be implemented, where the signal is averaged across a selected number of pulses resulting in a continuous signal (9).

The use of this device in the imaging application required very good linearity of the boxcar’s response. Expecting the laser radiation to illuminate a highly reflective as well as highly absorbing materials, the boxcar integrator was required to be able to integrate the pulse signal in a repeatable way, independent from the pulse intensity. The linearity of this process was checked by measuring peak value of the pulse and quasi-continuous value of the integrated signal voltage. Figure 3.24 (a) demonstrates the result of this test, showing very good performance of the tool.

Additionally, a test of residual noise in the system was measured. The boxcar was operated as described above, however the laser was switched off. Without any signal to integrate, in perfect condition there should be no signal at the output of the boxcar. Nevertheless, even with the laser switched off, there was still a detectable noise signal at the output of the Boxcar Integrator. The oscilloscope trace in Figure 3.24 (b) depicts example of integrated signal from both channels measured under these conditions (note 10mV/division setting of the oscilloscope). It demonstrates approximately $\pm 10\text{mV}$ signal variation, while no signal would be expected on any of the channels. These signals may originate from the components used to build the normalisation tool (especially caused by the charge injection on the fast digital switches and by ground bounces) or from the detectors connected to both channels. Having no means to further mitigate this residual noise its presence was acknowledged and it will constitute the main limiting factor of the pulse-by-pulse jitter reduction.

After alignment and verification of the boxcar behaviour, its performance as a normalisation tool for jitter reduction was tested and results are presented in the following Section 3.3.1.1.3.

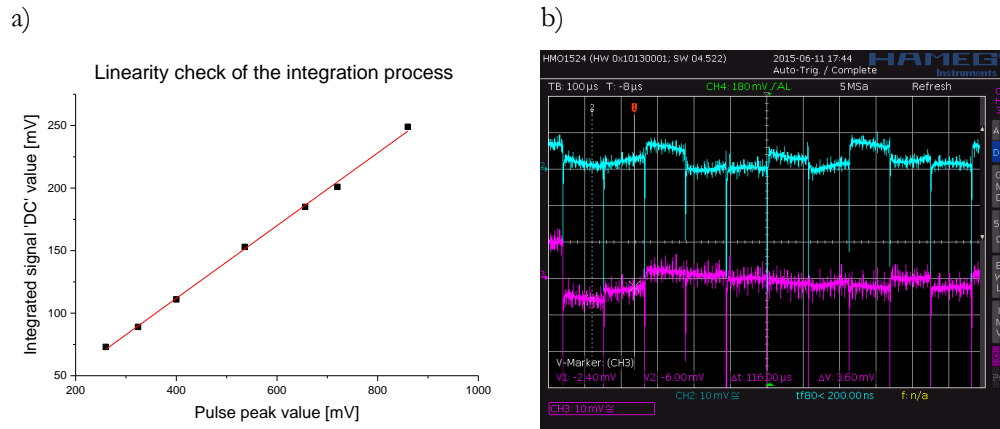


Figure 3.24. Tests of the boxcar integrator performance: linearity check (a) and test of any residual noise (b) where the traces represent the measured signal on both channels of the normalisation circuitry with laser being switched off.

3.3.1.1.3 Results

The first experiment conducted to test the normalisation performance was based on a single point in time measurement, where both channels of the boxcar electronics were fed with signal from one detector (Channel A = Channel B). This concept allowed establishment of the best case scenario, maximum reduction of the noise induced by pulse-by-pulse jitter coming from Q-switched laser with the use of proposed normalisation electronics. Running this test eliminated any differences in the alignment of the optical paths and detectors performance. As can be observed in Figure 3.25, there is still minor difference between the output from the two channels, which is caused by the physical differences in electronic components used to build the device and by the settings of both boxcar channels.

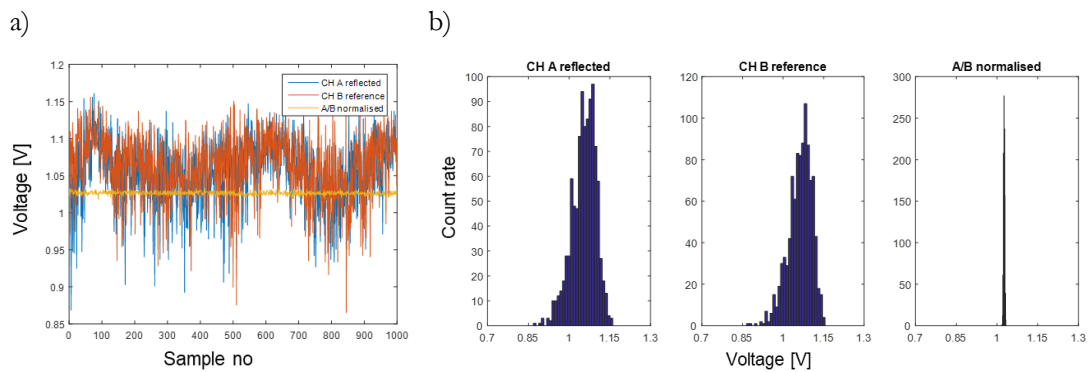


Figure 3.25. Time series (a) and signal voltage level distribution (b) in the channels A (reflected), B (reference) and A/B (normalised) of the boxcar electronics in the Channel A = Channel B case.

Table 3.1. Calculated performance indicators for the Channel A = Channel B case.

	Ch A = Ch B	Ch B = Ch A	A/B - normalised	Improvement
Noise level – N_L [%]	27.6	27.2	1.5	~18 times
SNR	23.7	24.2	444.0	~18.5 times

As demonstrated in Table 3.1, despite of mentioned minor differences between the two channels, the normalisation performance of the boxcar device is excellent with the noise level improving from approximately 27% to only 1.5% after normalisation, and SNR from approximately 24 to 444, this way showing the hardware limitations of this device. However, it is only the best case scenario, and in actual setup, where each channel is fed by respective signal, the difference in the optical path, alignment of components and any variation between detectors will cause deterioration of this result. Figure 3.26 shows two oscilloscope screens, demonstrating the difference between Channel A = Channel B and Channel A \neq Channel B cases.

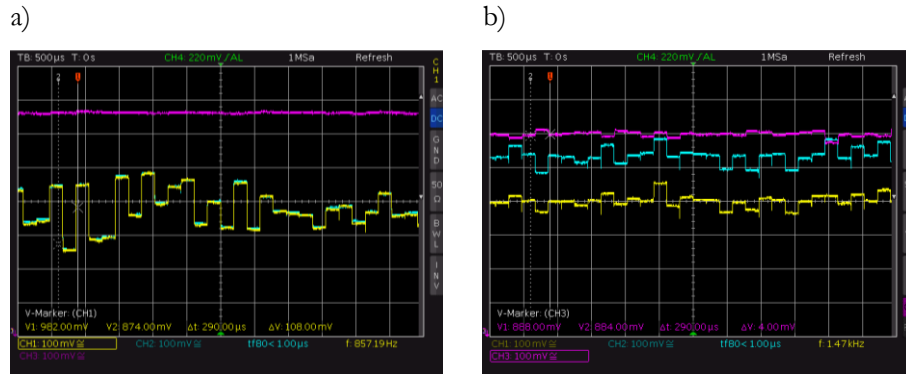


Figure 3.26. Oscilloscope traces for Channel A = Channel B (a) and Channel A \neq Channel B (b) cases. Yellow and cyan traces represent signals in channels A and B while magenta trace is the normalised A/B signal.

With reflected and reference signals coupled respectively to channels A and B, the single point in time experiment was repeated, demonstrating maximum improvement via normalisation in the realistic conditions. The results of this test are shown in Figure 3.27 and Table 3.2.

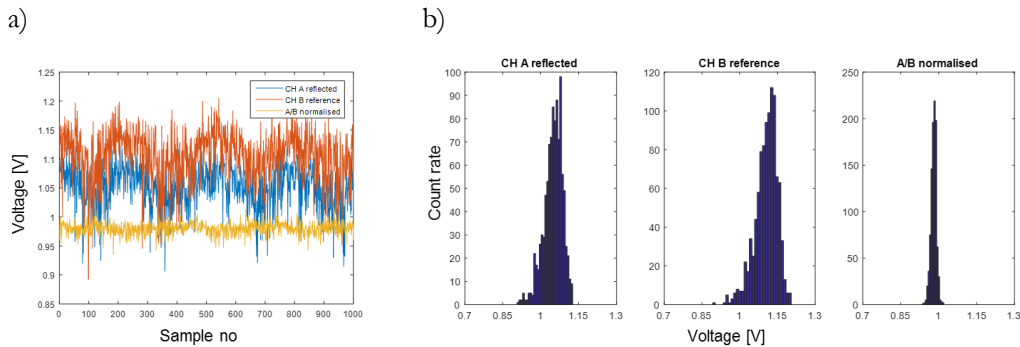


Figure 3.27. Time series (a) and signal voltage level distribution (b) in the channels A (reflected), B (reference) and A/B (normalised) of the boxcar electronics for the single point in time test.

Table 3.2. Calculated performance indicators for the single point in time test.

	CH A reflected	CH B reference	A/B - normalised	Improvement
Noise level – N_L [%]	20.9	28.1	8.7	~2.5 times
SNR	28.5	24.9	92.2	~3.5 times

The improvement shown in this experiment is not as significant as in the previous case and the difference in the signals fed to the both channels are definitely affecting the results, however these still represent an approximate improvement by a factor of 3 in the data quality after normalisation.

Although, using actual reflected and reference signals on respective channels, this test was still only collecting the data from a single spot over time. Since the main concern was improvement of image quality, verification of the normalisation impact on image noise level was also performed. The image data was acquired as described in Section 3.3.1 and collected data is presented in Figure 3.28.

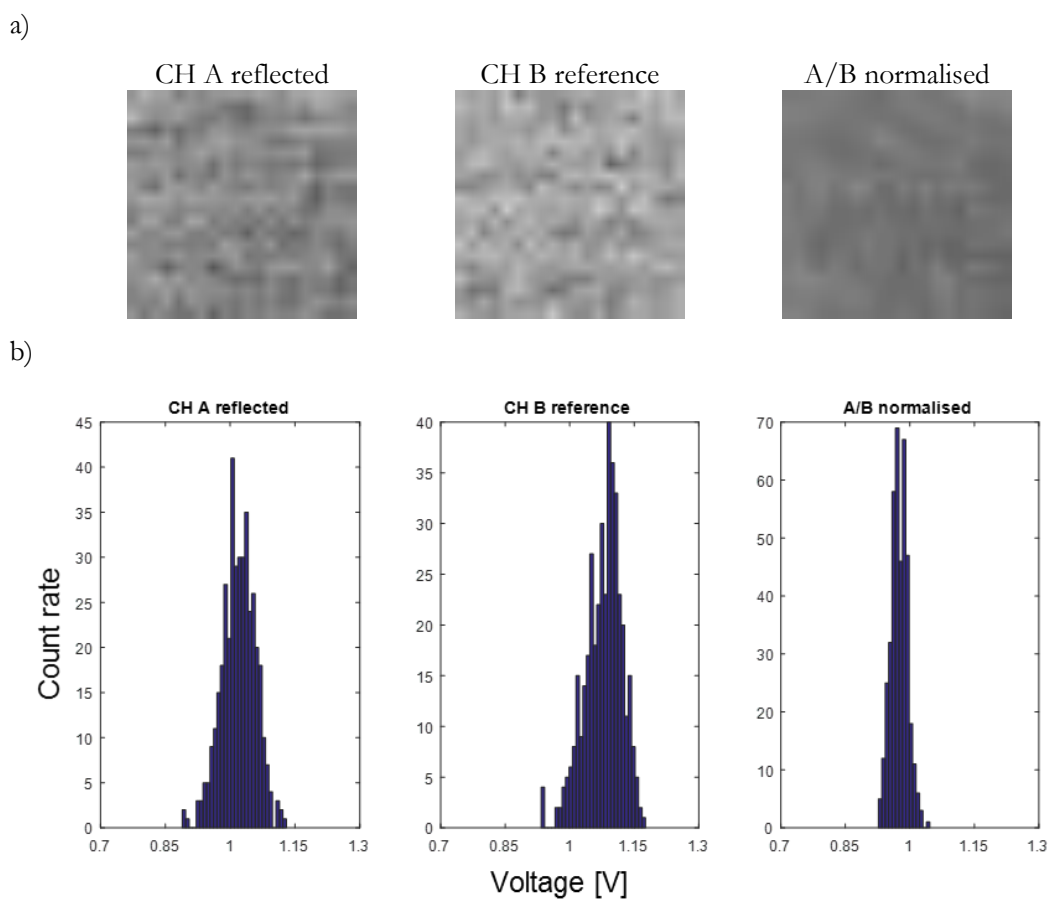


Figure 3.28. Time series (a) and signal voltage level distribution (b) in the channels A (reflected), B (reference) and A/B (normalised) of the boxcar electronics for the spatial scan test.

Table 3.3. Calculated performance indicators for the spatial scan test.

	CH A reflected	CH B reference	A/B - normalised	Improvement
Noise level – N_L [%]	23.6	22.4	12.3	~2 times
SNR	26.2	25.4	50.7	~2 times

As demonstrated above, the noise level and SNR did not change much in case of both, the reference and reflected signals, however the normalised signal deteriorated in the spatial scan, comparing to the single point test. It was understood that the performance of the laser setup behaved the same in both test cases and the speckle effect affecting the reflected signal had statistically uniform impact on amplifying some pixels as on attenuating others (due to the interference constituting the basis of the speckle effect – see Section 3.3.1.2), resulting in similar quantified noise measures for both cases. Nonetheless, due to the fact that the reference beam is probed directly after laser output and only reflected beam is affected by the speckle, the normalisation process is disturbed by the random, speckle induced intensity mismatch between these two beams. As a result, the improvement caused by the normalisation electronics had even smaller impact in this case. Despite this phenomenon, use of this method still gives a factor of 2 increase of the signal-to-noise ratio. The proposed noise reduction device aimed to reduce the noise coming from pulse-by-pulse jitter, however further improvement would be expected if some speckle reduction techniques could also be applied [50, 51, 52, 53]. No speckle reduction techniques were applied during this project, nevertheless the presence and impact of the speckle was tested, and the results of this test are discussed below.

3.3.1.2 Speckle effect

In the previous section, the speckle phenomenon was mentioned several times, however it was not described. Speckle is a granular appearance of a physical object observed when it is illuminated with coherent laser radiation and as such it is a significant issue when using a laser such as an OPO. It is caused by the interference between beams reflected from different areas of the illuminated object. On the scale of an optical wavelength, the majority of surfaces have very rough structure which when illuminated with a coherent laser, produce multiple independent scatter areas. At a distant observation point, the reflected waves interfere with each other, producing a granular pattern – speckle [54] (see Figure 3.29 (a)). In an imaging arrangement this phenomenon is also present and is also caused by the roughness of the observed surface. In this case, the granular structure in the observation plane is produced by the superposition of multiple amplitude spread functions, where each of these comes from different a point on the object's surface. The addition of amplitude spread functions with varying phase results in the speckle pattern on the image plane (see Figure 3.29 (b)).

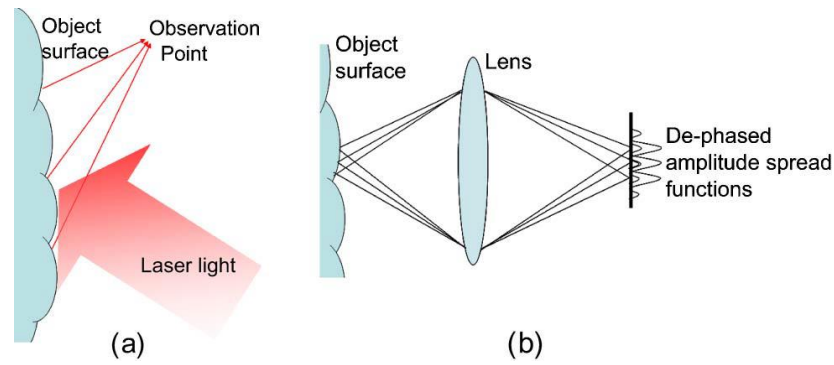


Figure 3.29. Speckle formation in (a) free space and (b) an imaging system [55].

Speckle is a very complex structure, seemingly chaotic that does not hold any connection with the macroscopic structure of the inspected object. Although it appears disordered, it carries a lot of information about the illuminated objects as well as the optical system [56]. This additional information carried by the speckle effect will not be considered here since within this project this phenomenon was perceived only as an unwanted imaging artefact, introducing the salt-and-pepper noise to the acquired data.

When the speckle is observed by an imaging system (as illustrated in Figure 3.29 (b)) the precise structure of its pattern depends on the parameters of the imaging system. Size of the speckle is highly affected by the diffraction-limited resolution of the optical system and therefore the aperture size of the lens used to project the image onto the detector. To demonstrate the presence of the speckle effect during the collection of the experimental data, the test illustrating the effect of aperture change on the speckle size was performed. Speckle size can be described by the formula [57]:

$$\sigma_s = \frac{\lambda \cdot z}{d} \quad (3.6)$$

where λ is the radiation wavelength, z is the distance from the lens to the screen (detector surface) and d is the diameter of the lens. The diameter of the lens can be varied by a physical change of the lens or implementation of adjustable iris in front of a fixed lens, affecting the transmission aperture of the optical arrangement. Here the latter approach was taken. Figure 3.30 presents the composite of two images where left side illustrates a speckle pattern obtained with larger aperture, showing very fine size of the speckle, while the right side was captured with smaller aperture (both the 'larger' and 'smaller' dimensions were not defined by the author) resulting with pattern of coarse granulation. [56]

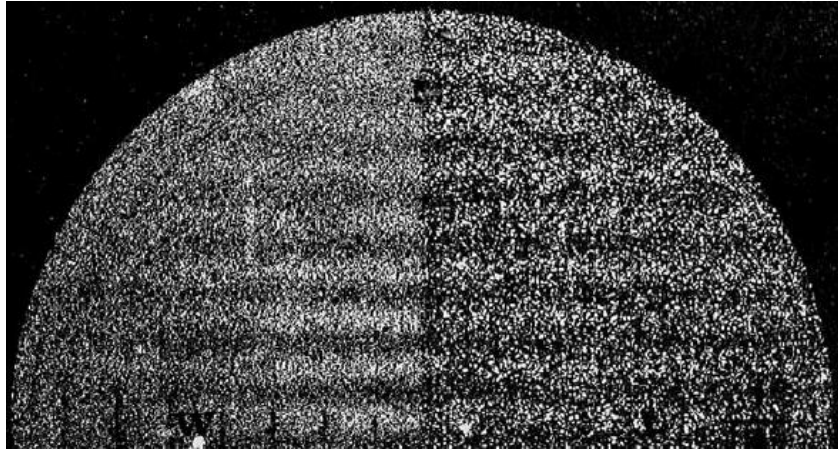


Figure 3.30. Composite of two images showing varying granulation of speckle pattern when observed via larger (left) and smaller (right) size of the aperture placed in the optical path [56].

This phenomenon can be directly explained by the Formula 3.6 as the diameter of the lens D is inversely proportional to the speckle size. From physical point of view, it is driven by the fact that the small aperture makes it impossible for the finest speckles to be created and therefore the pattern is aggregated into the large ones. In speckle photography this effect is often used to match the speckle granulation to the pixel size of the detector. On the other hand, in this experiment use of very coarse scanning resolution was planned (as described before in section 3.3.1), with one pixel (acquired by single point detector) corresponding to 1mm x 1mm surface. With such a low resolution, it was expected that very fine speckle pattern would be averaged over the whole pixel and statistically will be very similar across all the pixels, while speckle with larger size would significantly dominate the intensity of individual pixels in captured image and be observed as increased noise level. To verify these expectations an adjustable iris was placed in front of the lens focusing the reflected beam to the detector. During this experiment the per-pulse jitter reduction electronics was included (see Section 3.3.1.1) to observe direct relation between the two noise factors. Due to the fact that the performance of the boxcar integrator depends on the ratio of the signal power collected by the two detectors, the reference beam was appropriately attenuated by adjustment of the continuous neutral density filter, during gradual decrease of the aperture size in the reflected path. Similar to the per-pulse jitter reduction experiment, this test was also performed first as single point in time and only subsequently as the 2D scan measurement. Figure 3.31 demonstrates the relation between the signal-to-noise ratio extracted from the single point in time data and the varying aperture diameter, for the signal from reflected beam as well as the normalised one. The impact of the normalisation can be again clearly observed by approximately 3 times higher SNR, however the change of the aperture size has virtually no impact on this data. This is exactly what was expected, as in the static arrangement (single point

observation) the speckle impact on the collected signal intensity exists, but remains constant for the whole data series as confirmed and presented in Figure 3.31.

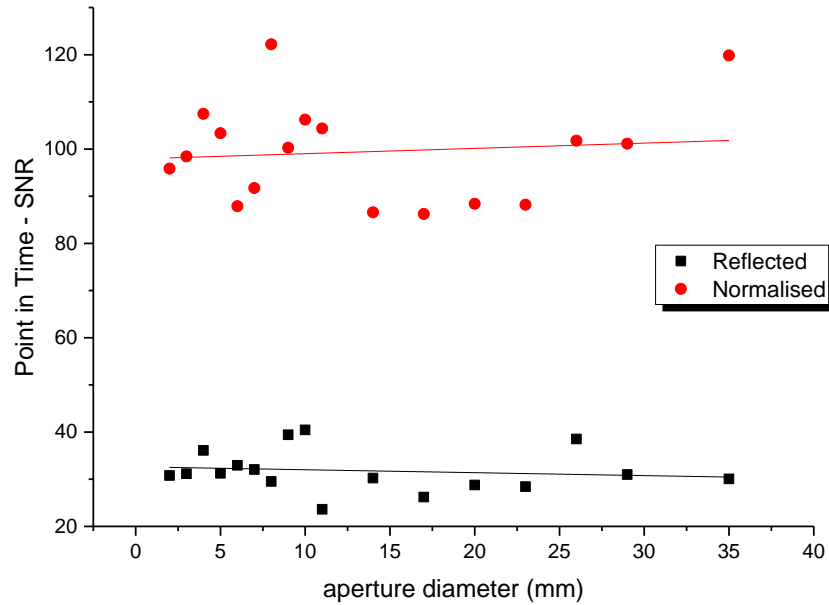


Figure 3.31. Signal-to-noise ratio derived for the single point in time data from the directly reflected and normalised signals, as a function of the aperture diameter.

In the imaging arrangement, the speckle effect became clearly visible, driving SNR to approximately half of the one derived from the single point data acquisition. Also, in line with the above described expectations, this phenomenon is more apparent when the aperture diameter decreases. As illustrated in Figure 3.32, pixels of images acquired with small aperture diameter feature much higher intensity variation than these observed through larger aperture. This is true for both directly captured reflected signal as well as the normalised one. Figure 3.33 demonstrates the relation between the signal-to-noise ratio extracted from the acquired images and the varying aperture diameter, for both signals - reflected and normalised one. It can be observed that although the smallest apertures affect the SNR of the signal (by changing the speckle pattern), increase of aperture's diameter would not indefinitely improve the image quality as the speckle impact reached a plateau at the aperture diameter of approximately 10mm. From this stage, the beams travelling on the optical path were able to pass the aperture without significant impact on their interference and modification of speckle pattern.

This test demonstrated the presence of the speckle in constructed imaging setup and quantified its impact on the data acquired in order to characterise the pulse-by-pulse jitter reduction. As mentioned before, elimination of this speckle based noise was out of the scope of this project and presented results concluded this speckle impact study.


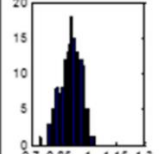
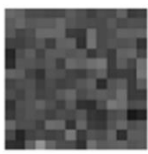
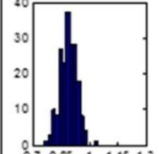
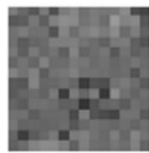
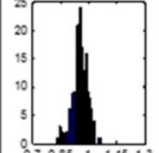
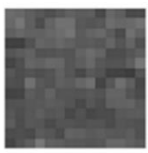
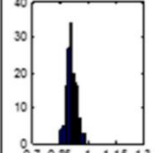
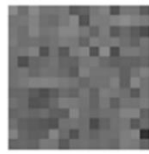
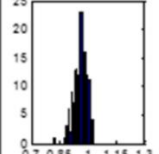
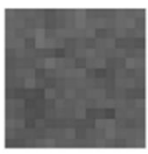
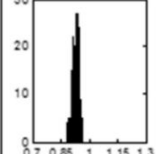
Aperture size [mm]	Reflected signal			Normalised signal		
	Image	Histogram	SNR	Image	Histogram	SNR
2			17.4			20.2
4			24.0			34.3
10			28.3			54.9

Figure 3.32. Illustration of selected aperture diameters and corresponding acquired images with the data represented in a form of histogram and derived SNR for the reflected and normalised signals.

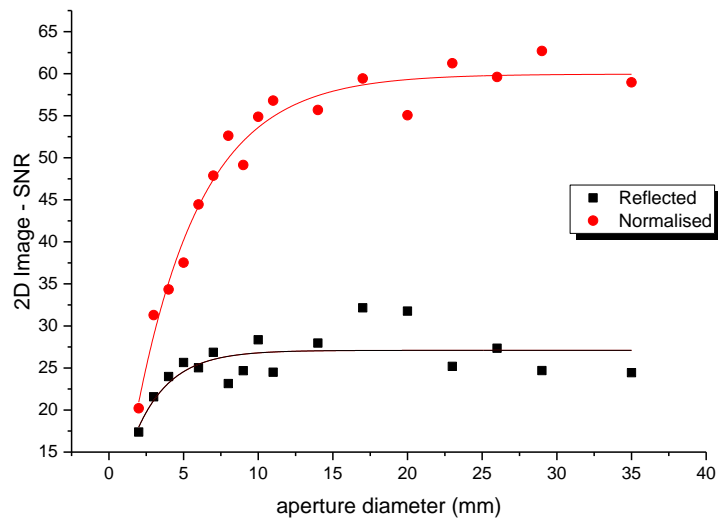


Figure 3.33. Signal-to-noise ratio derived for the 2D imaging scan data from the directly reflected and normalised signals, as a function of the aperture diameter.

3.3.2 Specular reflection

As demonstrated in Section 3.3, specular reflection can introduce significant distortion to the acquired data. Although in some cases the information it carries may be beneficial for a specific task (for example recovery of surface shape in computer vision [58]) usually it is an unwanted artefact of the imaging process and, when possible, effort should be made to avoid it.

Reflection of light from the surface was extensively studied in the past and the physics of both the diffuse (unordered, scattered in all directions) and specular (mirror-like) components are well understood [49, 59, 60]. Among many physical properties describing the reflection of electromagnetic radiation, the most significant for this study is its relationship with the polarisation of incident and reflected waves. If unpolarised light undergoes diffuse reflection, the reflected beam will remain unpolarised. When the same unpolarised radiation is specularly reflected from a gloss surface, it will be to a greater or lesser extent polarised. However, when linearly polarised light is diffusely reflected from a surface, the polarisation information is nearly completely destroyed. On the other hand, specular reflection preserves the polarisation of incident light [59, 60, 61]. This very basic principle of the behaviour of light can be used for the removal of the specular component of the reflection. Although this concept was already presented before [58, 62], it was never attempted in the context of imaging with Firefly IR Imager and this method was proposed to minimise the problem of specular reflections in acquired data. The Firefly device, being based on the IC-OPO, emits linearly polarised radiation. In line with presented above phenomenon accompanying to the specular reflection of polarised light, a cross-aligned polariser in front of the imaging detector was introduced, to eliminate this component from captured signal.

To validate this idea for the laser-based imaging system, a demonstration experiment using a Helium-Neon (HeNe) laser operating in visible range (632.8nm) was performed. For these tests the scanning system was changed, replacing the linear translation stage arrangement with a system of two galvanometer based mirrors, similar to the scanner built into the Firefly imager. The control of the galvanometers and data acquisition were performed by the Red Pitaya board - Dual core ARM Cortex A9+ CPU (central processing unit) and FPGA (field-programmable gate array), enabled development board including two 125 mega sample per second (MS/s) radio frequency (RF) input and two 125MS/s RF outputs, with 50 MHz analogue bandwidth and 14 bit analogue-to-digital and digital-to-analogue converters [63].

The experiment was performed in two scanning configurations – 1D (scan of a single vertical line) and 2D (image acquisition). 1D scan was performed across 0.3m on the target object with 1.15m distance between the object and the scanner, resulting in a beam deflection range of $\sim 15^\circ$. Although, cross polarisation (90° with respect to the polarisation of output beam) is expected to remove specific component of linearly polarised reflected light, data was captured with gradually rotating polariser to fully characterise this phenomenon. Two target objects were chosen – one of highly specular nature (sheet of black metal) and second characterised by strong diffuse reflectivity (sheet of white paper). Figure 3.34 demonstrates the acquired intensity characteristics as a function of deflection angle, with changing angle of the polariser analysing the

reflected light (polarisation of incident beam was constant). Figure 3.34 (a) represents data acquired from highly specular object while Figure 3.34 (b) from highly diffusive one.

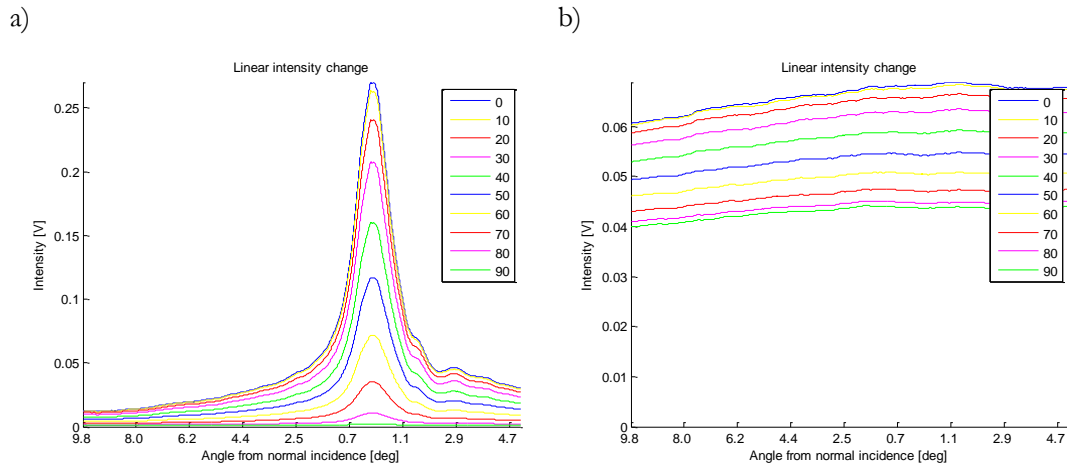


Figure 3.34. Intensity of reflected light from highly specular (a) and highly diffusive (b) objects, as a function of beam deflection angle, with varying angle of the polariser analysing the reflected beam.

As displayed in Figure 3.34, the intensity detected at normal and near-normal angle of incidence is higher for both scanned objects, however only for the metal sheet (Figure 3.34 (a)) the mirror-like reflection results in very high spike of intensity (notice: nearly an order of magnitude difference on the intensity axis of these graphs). It can be observed that the diffuse reflection change of the polarisation is fractionally attenuating the signal, which is expected since a component of light that is blocked by crossed aligned polariser will be present in randomly polarised reflected light. However, this effect is nearly the same for all the deflection angles, including near-normal ones. The variation in the intensity of the collected light across the whole scanning range can be explained by the varying collection efficiency as discussed in Section 3.2.2.1.

The specular reflected signal is orders-of-magnitude greater than the diffuse, causing a dynamic range issue. It is very highly polarised. Whilst a polariser does lead to a factor of two reduction in the diffuse, randomly-polarised light, the attenuation of the specular light – containing near perfectly linearly polarised light – is such that it leads to almost complete rejection, thereby leading to preferential suppression of the troublesome specular component whilst still preserving a significant proportion of the diffuse signal for subsequent detection.

After this test, the same two objects were scanned with second galvanometer enabled, allowing for acquisition of 2D image. To allow for the same amount of data points captured as an image (predetermined by the buffer size of the Red Pitaya), the scan width and distance between scanner and object were decreased resulting in the acquisition of image corresponding to 85mm x 90mm on the surface of the target object. Figures 3.35 and 3.36 demonstrate the data recorded

for specular and diffusive objects respectively, with varying angle of analysing polariser. As it can be clearly observed by the position of specular reflection in Figure 3.35, the normal beam was incident at the top left corner of the imaged scene. This test confirmed again that introduction of analyser cross-aligned to the polarisation of illumination beam helps to eliminate specular reflection. As demonstrated in Figure 3.36, cross-polarisation also improves the intensity uniformity of the image of highly diffusive object. In Figures 3.35 and 3.36 the pixel intensity range was fixed between the maximum pixel intensity (depicted as white colour) from image captured at 0° condition and absence of any detected signal (depicted as black colour). This allows demonstration of the specular reflection elimination, however also reduction in image intensity.

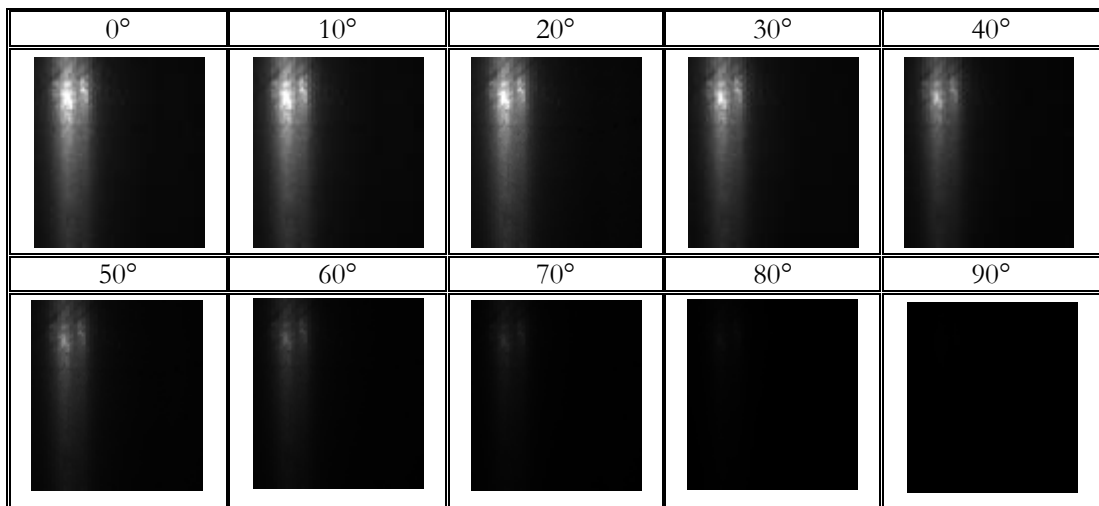


Figure 3.35. Series of images of the same highly specular object with varying angle of the polariser analysing the reflected beam. The pixel intensity range on all pictures was fixed to the one from 0° polariser alignment.

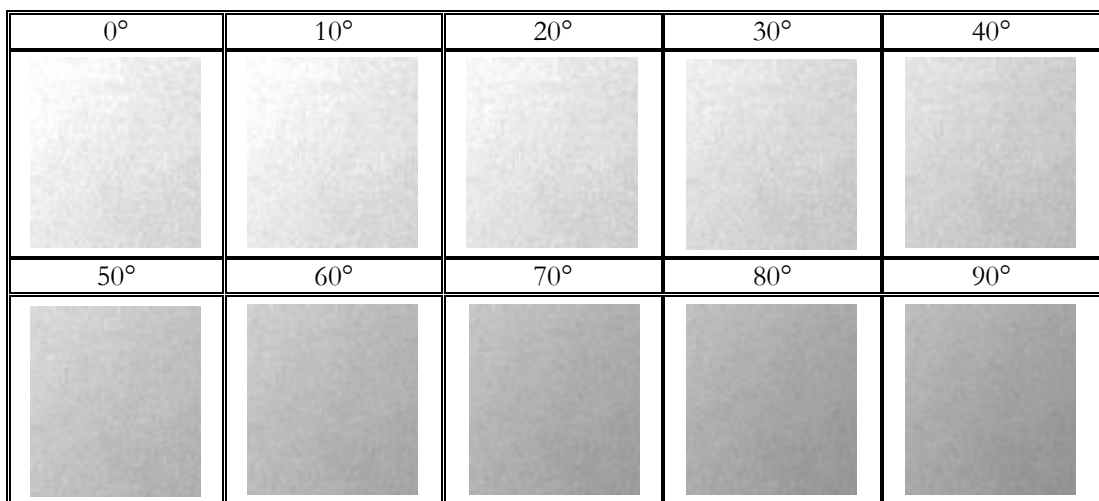


Figure 3.36. Series of images of the same highly diffuse object with varying angle of the polariser analysing the reflected beam. The pixel intensity range on all pictures was fixed to the one from 0° polariser alignment.

The two objects used in aforementioned test featured uniform surface. Although it was beneficial for verification of the process performance, it was not possible to check how this process can affect any other features of the imaged objects. For that purpose, a cardboard box with highly glossy surface was chosen. This time the pixels' intensity in the images was fixed to the range in the single image acquired at 90° condition and whole specular reflection is demonstrated as saturation of the detector (values above the fixed range, demonstrated as white colour) as it takes place in the Firefly device. The result of this imaging is shown in Figure 3.37.

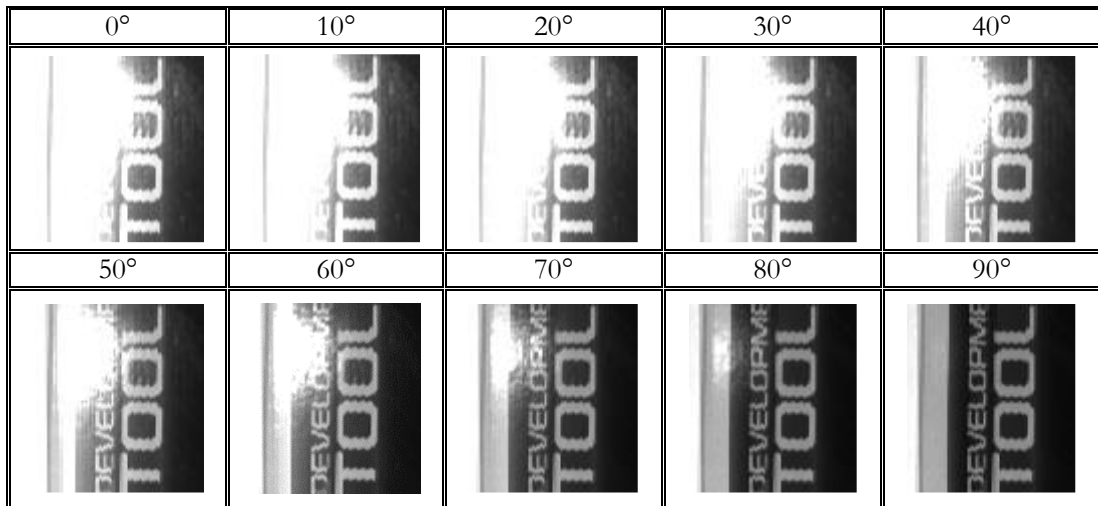


Figure 3.37. Series of images of cardboard box with highly glossy surface with varying angle of the polariser analysing the reflected beam. The pixel intensity range on all pictures was fixed to the one from 90° polariser alignment.

This experiment demonstrates that if there is a sufficient amount of reflected radiation being captured by the imaging detector, the cross-polarisation of the collected radiation reduces the specular reflection artefact in the image. Upon successful demonstration of this effect in the visible range it was decided to attempt the translation of this technique to mid-IR regime, combining it with the OPO-based imaging setup.

3.3.3 Integration with the mid-infrared illumination source

To verify the performance of the proposed techniques, the galvanometer-based scanner was mounted in place of the linear translation stages of the EC-OPO based imaging arrangement. Following the main strand of the project, this time the two grid paintings were placed next to each other (where columns 1&6, 2&5 and 3&4 feature the same paints, but horizontally flipped) and sections of both served as a target scene (similar arrangement to the one presented in Section 3.2.2.3.2).

At this stage, significant effort was made to upgrade the data acquisition using the Red Pitaya board. Images taken during the experiment described in previous section were based on a single buffer (16k samples) of data acquired through fast (125MS/s) analogue input port (while galvanometers were driven by fast analogue output ports). With use of the default FPGA code this was the maximum sample size that could be continuously acquired, significantly restricting the resolution of captured image. The first attempt to overcome this limitation was to use slow (100kS/s) analogue input and output ports available on the Red Pitaya that with direct sampling implemented on the CPU allow continuous data transfer. The result of this attempt is demonstrated in Figure 3.38 (a) where a single band intensity image (at arbitrary position of the PPLN crystal, specific wavelength not measured) of the target acquired with this technique is shown. As can be seen in the figure, the quality of the obtained image was poor, featuring artificial segmentation and offset within the image. This was caused by the fact that although bespoke code was created and upload to the CPU, the actual behaviour of the analogue ports was still determined by the default FPGA code on the board. As this standard FPGA code was not suitable for this application, it was necessary to modify it appropriately. Being faced with this task, it was decided to use again the fast analogue ports, however this time with the continuous sampling mode enabled on the FPGA. Additionally, to facilitate the appropriate image reconstruction, the board was also used to trigger the Q-switching of the OPO and boxcar normalisation electronics. With this update, acquisition of good quality imagery was possible, with the size set to 498x512 pixels. Figure 3.38 (b) illustrates the picture of the same scene recorded with the same optical settings, but this time taken with the updated FPGA code (recorded from directly reflected, non-normalised, signal).

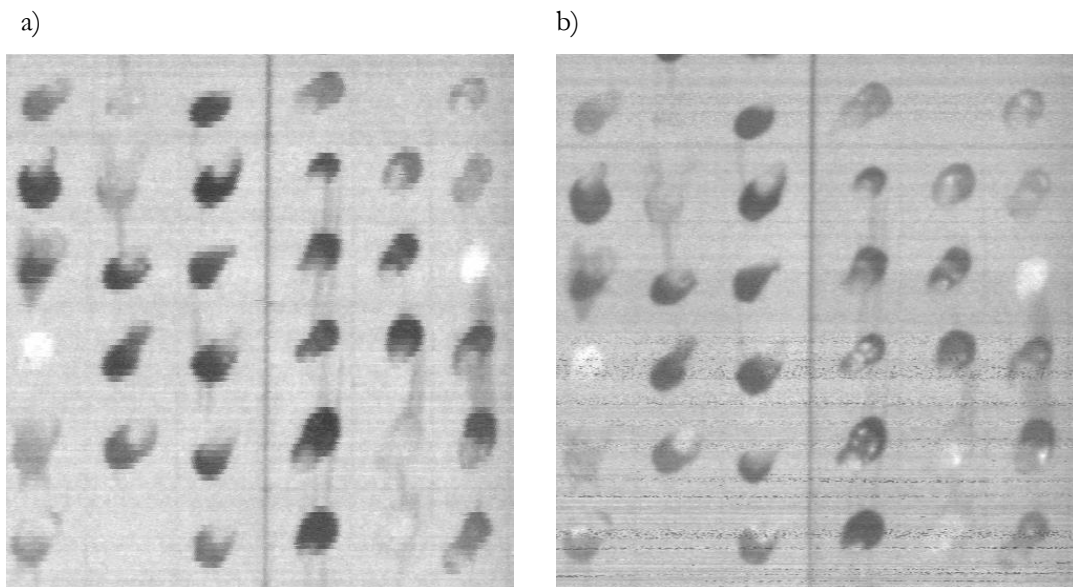
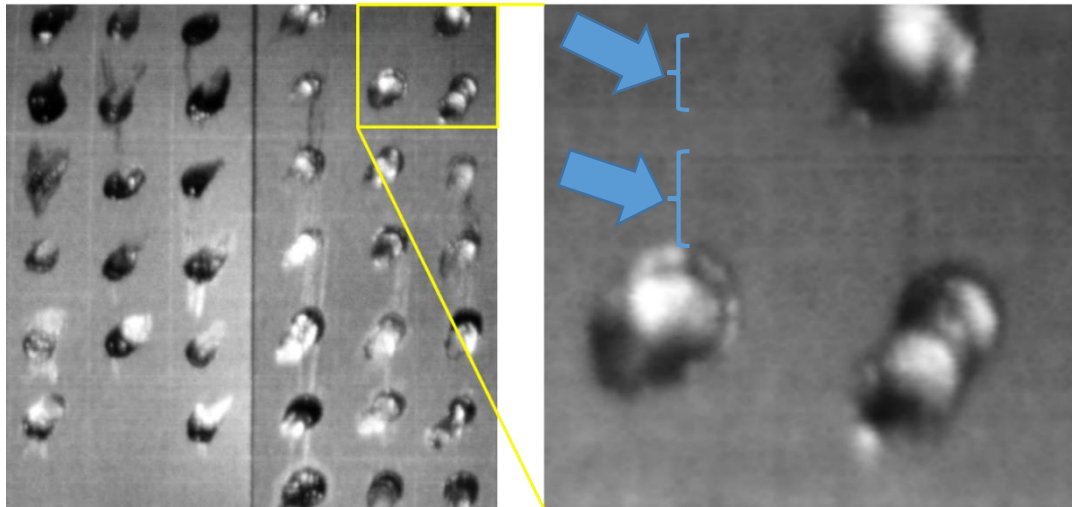


Figure 3.38. Single band intensity images of the grid painting recorded by slow analogue channels with default FPGA code of Red Pitaya (a) and by fast analogue channels with updated FPGA code (b); polariser setting - 90° .

Now, with significantly increased image resolution, any instability of the laser source becomes much more apparent. In Figure 3.38 (b) horizontal noise lines can be clearly seen, resulting from significant long-term (as opposed to pulse-by-pulse) laser intensity fluctuation. This phenomenon reveals another reason for the application of signal normalisation in similar laser imaging arrangements. In Figure 3.39 a comparison of directly acquired, reflected signal and normalised signal is presented, demonstrating the advantage of normalisation process in image noise reduction. In this case the intensity fluctuation induced by both long-term laser instability and pulse-by-pulse jitter were not as severe as shown in Figure 3.38 (b). Yet, thanks to the normalisation process, detection and correction of even low amplitude noise was possible.

a)



b)

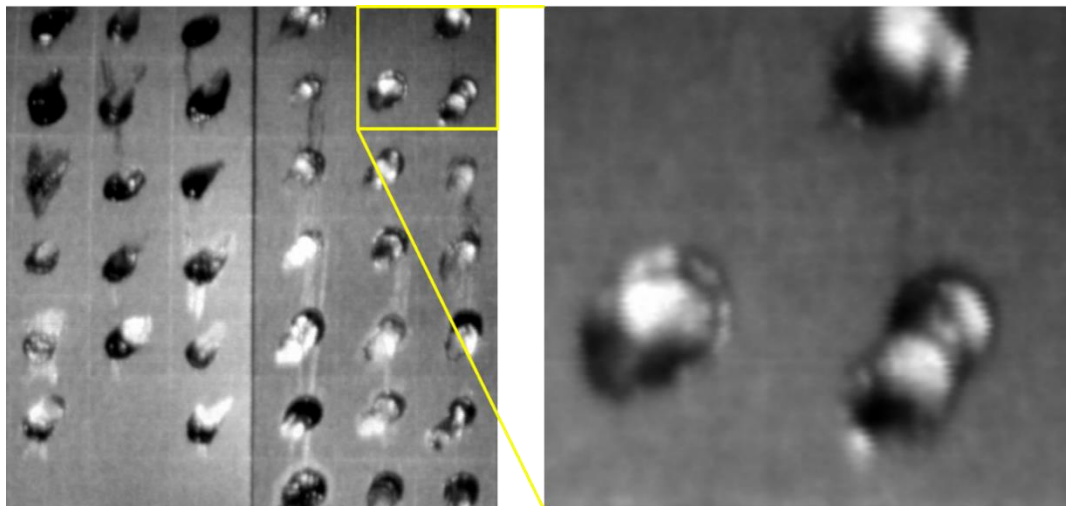


Figure 3.39. Single band intensity images of the grid painting reconstructed from directly reflected (a) and normalised (b) signal, with inserts demonstrating the low-amplitude, long-term intensity fluctuations in reflected signal (marked by arrows and curly brackets), removed from the image by the normalisation process; polariser setting - 0° .

In the above tests two polarisers working in the short- and mid-wave infrared regions (1500nm – 5000nm – Thorlabs, LPMIR050-MP2) were implemented both on the scanning and reference beam paths. Implementation of the polarisation control on both paths was predetermined by the use of the normalisation electronics, as it was observed that any discrepancy in the signal on both arms has significant impact on the performance of the boxcar device. The effect of the polarisation was already demonstrated in Figures 3.38 and 3.39. The data displayed in Figure 3.38 was recorded with the polariser in the crossed-aligned position (90°) featuring good removal of the specular reflection, while the one in Figure 3.39 was acquired with the polariser co-aligned with the polarisation of incident beam, so strong specular reflections are noticeable.

It was observed that performance of this technique is wavelength dependant and although it may be a good solution in some cases (as demonstrated in Figure 3.38), at other wavelengths the polarisation effect is not so effective. The images shown in Figure 3.40 were acquired on different band (exact wavelength not measured – arbitrary position of PPLN crystal) when polarisers in front of the detectors were set to 0° , 60° and 90° respectively. It can be seen that without cross-polarisation the specular reflection is very strong. With partial (60°) cross-polarisation the overall intensity drops, limiting also extent of specular reflections, while for fully (90°) crossed polariser the intensity of the image dropped down significantly in the middle of the image, while the edges were still featuring specular reflections.

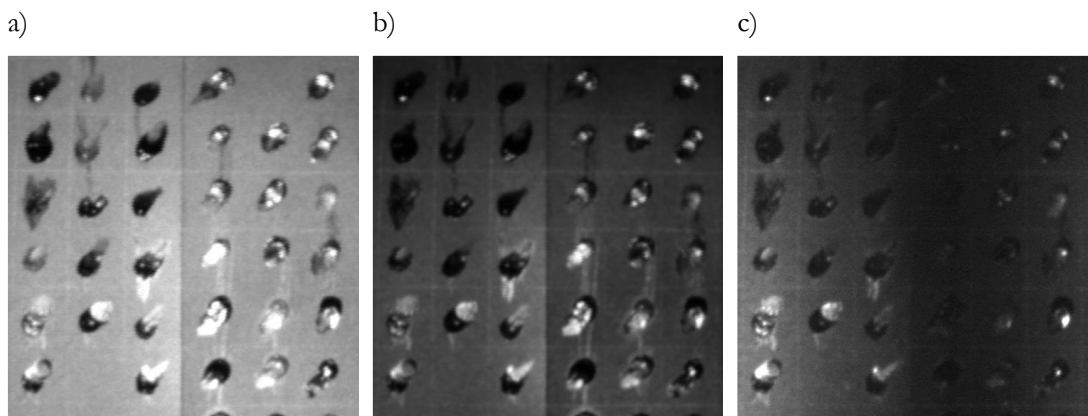


Figure 3.40. Single band intensity images of the grid painting reconstructed from normalised signal, captured with the polariser set to 0° (a), 60° (b) and 90° (c).

Since this effect could not be directly explained, an additional test was performed, where images of highly specular (sheet of metal) and highly diffusive (cardboard painted with diffusive paint) objects were captured in collinear and cross-aligned positions of polariser – see Figure 3.41. As can be observed in the recorded images, while operating in this spectral band, the cross-polarisation is somewhat effective, significantly reducing the extent of specular reflection. However, it is introducing very strong intensity variation, considerably decreasing the transmitted

signal from near-normal incidence angles, while still allowing very strong signal towards both sides from normal. This effect is much more apparent for mirror-like surfaces, however it can be also observed for highly scattering surfaces. A detailed study of this phenomenon was discontinued as it extended already beyond the framework of the INHERIt project and time and effort was moved to other activities.

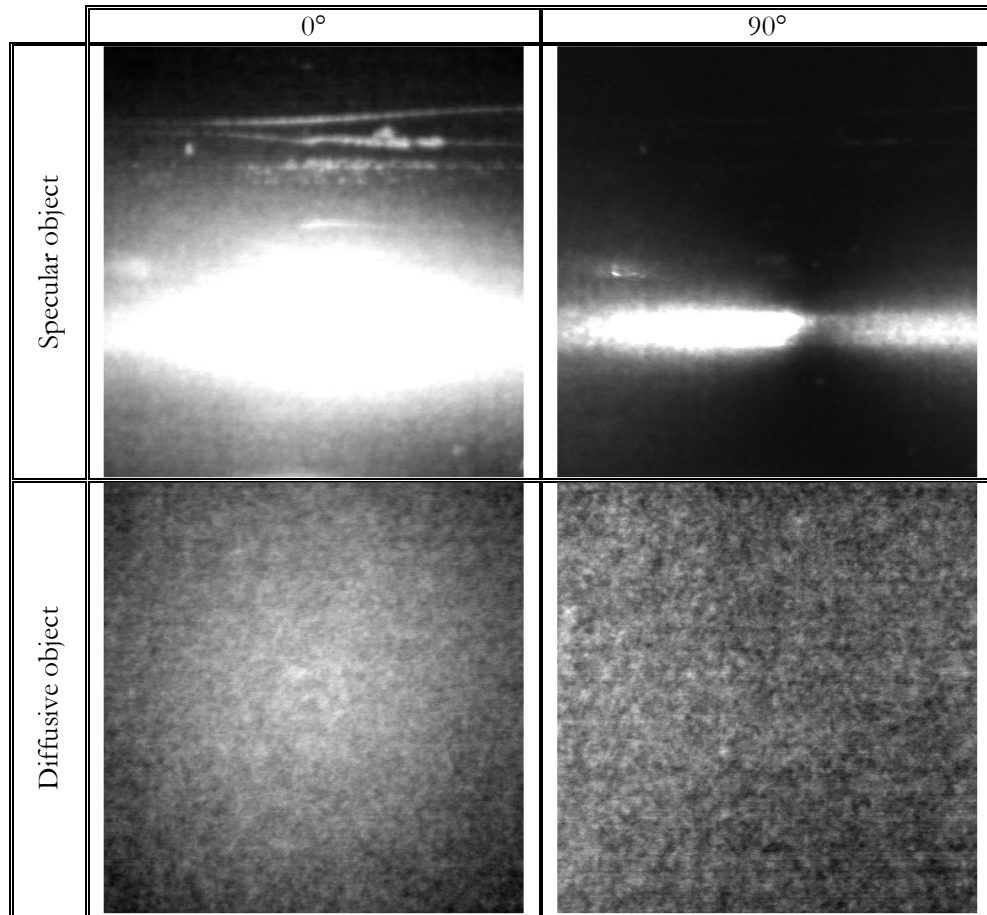


Figure 3.41. Single band intensity images of highly specular and highly diffusive surfaces, reconstructed from normalised signal, captured with the polariser set to 0° and 90°.

Summarising these lab-bench-based activities, it can be concluded that there is an extensive field of hardware solutions that can be implemented with the laser-based imaging system, that can lead to the improvement of the image quality. The normalisation procedure for pulse-by-pulse jitter removal, which is also capable also of removing various other long-term laser fluctuations, and specular reflection removal by cross-polarisation of the captured beam have been demonstrated in this chapter. Both these methods would require further engineering work to improve alignment and wavelength dependencies to exploit these solutions, however this study demonstrated the potential of these techniques. Additionally, supported by any suitable speckle removal modality, these approaches could lead to the successful reduction of various unwanted artefacts of laser-based imaging.

3.4 Development of algorithms for artwork classification

As indicated previously, the main strand of the project was focused on the implementation of HSI for the artwork authentication process. Next to the high-quality data acquired from the hardware, a specific set of algorithms and training data were required and their development is described in this Section.

3.4.1 Building and validating a spectral library using bespoke paintings

Two different paintings were prepared specifically to allow the construction of a “spectral library” from HSI data sets containing only known paints at specific locations. Both paintings were used for algorithm development and validation after the spectral library was created. One type of painting used mainly for development was constructed in the form of a grid of 41 oil-based paints covering a representative selection of the materials commonly used by artists during the 20th century (see Figure 3.42 (a)). Exemplar paints were purchased from a number of professional artists' colourmen with particular reference to those offering ranges that include ostensibly “historically appropriate” materials (Michael Harding; Rublev; Blockx). The full description of all paints contained by this template can be found in Figure 3.42 (b) and Appendix A. All the paints were also analysed using other instrumental techniques such as scanning electron microscopy-energy dispersive X-ray spectrometry (“SEM-EDX”), FTIR spectroscopy and Raman microscopy, however these were performed by other partners of the project and as such are not part of this dissertation. Identifications of all the pigments were made with reference to the spectral libraries derived from the Pigmentum Project collection of historical pigments [64].

Two of these “grid canvases” as described above were used for development of new hardware solutions (see Section 3.3), signal processing algorithms and also served as training data for classifications of other unseen paintings that presumably contains at least one or more of these pigments. A second style of canvas, used for algorithm validation, was a pastiche of a Suprematist work by Kazimir Malevich (see Figure 3.42 (c)). This bespoke painting was created using a selective subset of the paints contained in the grid canvas (Figure 3.42 (a)), and was accompanied by labelled “ground-truth” data describing each area painted with different paint (see Figure 3.42 (d)). In this thesis it is referred to as a “test painting”.

a)



b)

Cerulean blue	Cobalt blue	Phthalo blue lake	Manganese blue	Ultramarine blue	Dioxazine violet	Manganese violet
Terre vert	Chrome oxide green	Cobalt turquoise	Phthalo green lake	Viridian	Chrome green	
Lemon yellow	Bright yellow lake	Aureolin	Yellow lake	Naples yellow	Cadmium gold yellow	Chrome yellow
Vermilion	Minium	Orange molybdate	Pyrrulo vermilion	Napthol red	Scarlet lake	Cadmium red
Alizarin crimson	Magenta	French yellow ochre	Raw sienna	Raw umber	Transparent oxide red	
Cremnitz white	Flake white	Barite white	Zinc white	Flemish white	Titanium white #3	
Ivory black	Lamp black					

c)



d)

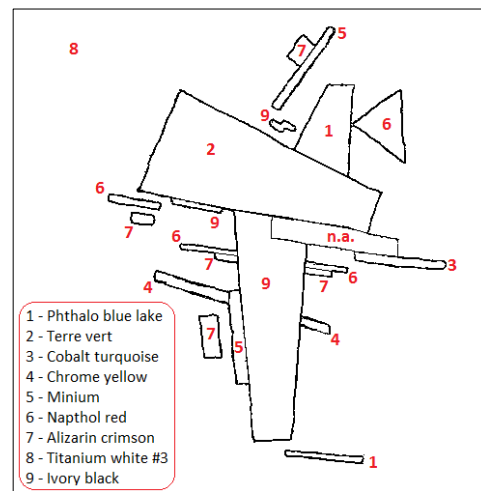


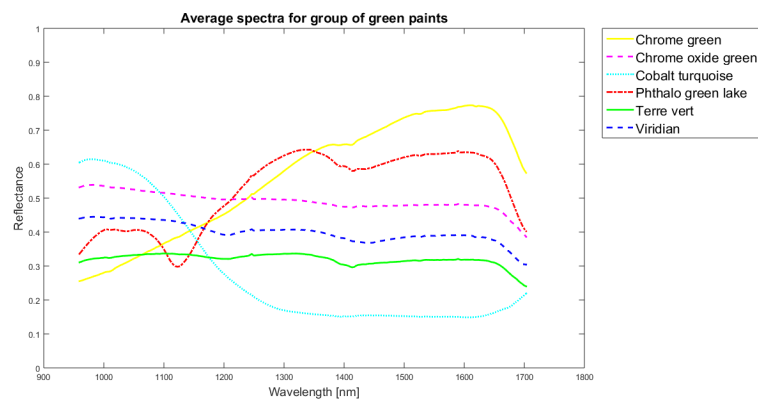
Figure 3.42. Illustration of paintings used during the lab stage of the project and their ground truth description: a) the pigment grid canvas serving as a training data; b) description of the pigments used in the grid canvas; c) Pastiche of "Untitled (Suprematist Composition)," by Kazimir Malevich as testing painting; d) ground truth data of pigments used for creation of the Kazimir Malevich pastiche.

Examination of the second painting provided controlled conditions for validation of the algorithms developed for automatic paint recognition. These two analysed paintings (grid canvas and pastiche) constituted not only a very well controlled but also a realistic data set of paints which are commonly used in 20th century artwork, upon which the methods developed in this work could be assessed.

3.4.2 Algorithm development and feature extraction

After the pre-treatment to normalise and calibrate the data (see Section 3.3), subsequent processing was the same for both data sets and an algorithm was designed to facilitate hyperspectral analysis of the artwork. Since this work aimed at the identification of different paints, the main aspect of algorithm development was focused on the application of robust statistical classification techniques. Both supervised (guided by human provided training data) and unsupervised (fully based on software analysis of the image) techniques (see Chapter 2) were considered [65]. Since the objective of this work is the detection of counterfeit paintings by the classification of known paints, supervised classification was chosen as the most suitable for this application. The grid canvas presented in Figure 3.42 (a) was used to build a spectral library of selected pigments and this served as the training data for the algorithm. Figure 3.43 illustrates the average spectra (acquired by both systems) of the group of green paints presented on the grid canvas that is shown in Figure 3.42. All the average spectra from the 41 paints in the library are presented in Appendix A.

a)



b)

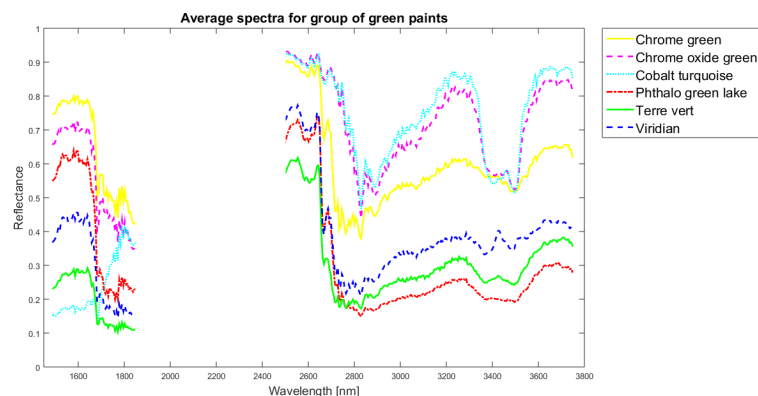
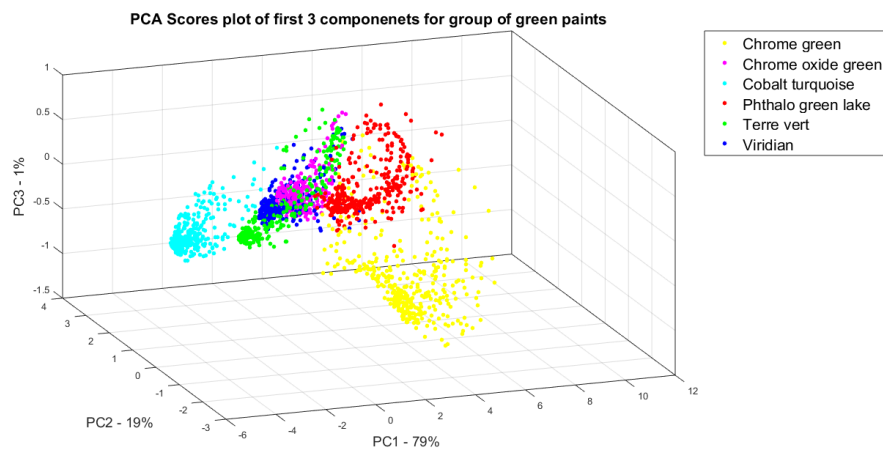


Figure 3.43. Average spectral response of all the green coloured pigments acquired by passive (a) and active (b) system.

Although this figure illustrates the averaged spectral response from the entire paint regions, the algorithm is trained to recognise all variations of this response resulting from the uneven paint surfaces when imaged. It is expected that during the analysis of the artwork the captured data will include various artefacts of the imaging process, all these variations were also allowed in the training set classes. The training data therefore included examples of specular reflections and intensity variations coming from the three-dimensional structure of the paint blobs and their thickness (see Section 3.3). A Principal Component Analysis (PCA) [66] was performed to assess the quality of this training set and the PCA scores plot shows that the first three principal components explain over 95% of variance in the data. The examples of these plots for the group of green paints acquired by both imaging systems are shown in Figure 3.44. For completeness, all PCA scores plots for the full acquired library are shown in Appendix A.

a)



b)

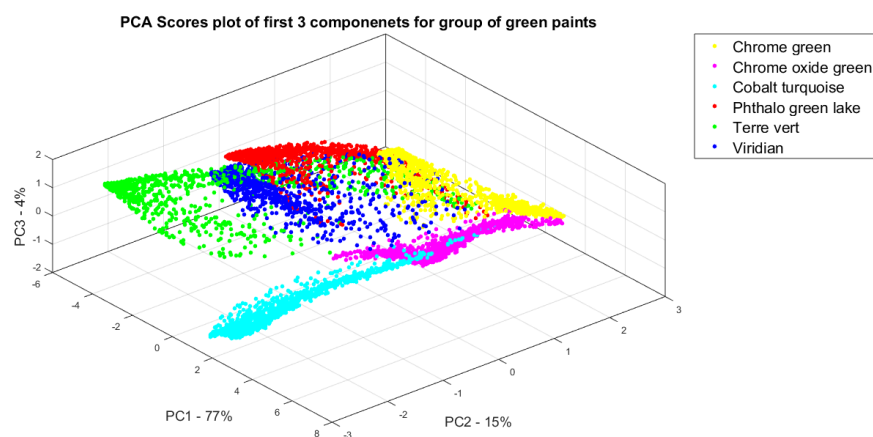


Figure 3.44. PCA scores plot of first three principal components for the group of green paints imaged with passive (a) and active (b) system.

Although there is a wide range of algorithms which could be chosen to perform multivariate analysis using supervised classification, a Support Vector Machine (SVM) (see Chapter 2) was identified as the most suitable method for this project due to its robustness and consistent classification accuracy [67, 68, 69]. SVMs consist of a family of learning algorithms that can be used for data classification, that demonstrate very good performance in many applications [67, 68, 70]. For this reason, it is one of the most popular machine learning algorithms and it is often used to solve classification problems. The specific algorithm used for the paint classification in this study is contained in the LIBSVM package [71] for Matlab, which uses a Classification SVM Type 1 (C-SVM). As the SVM is a binary classifier, the multiclass problem was approached using a ‘one-against-one’ technique. The quality of the model was also evaluated using Cross Validation Accuracy scores acquired during model training and final Classification Accuracy [71].

In order to facilitate the construction of a spectral library and algorithm development, two of the “grid canvases” (see Section 3.4.1 and Figure 3.42) were imaged side by side, and one was used as training data set while the other as validation set (see Figure 3.45 (a)). This approach alleviates the need for k-fold cross validation, as it introduces new, ‘unseen’ data for the classifier. Regions of interest - subsets of the image manually selected to contain a group of pixels corresponding to a single paint - were defined for all 41 paint samples of the grid canvas. Since each row in the canvas represents one group of colours (see Figure 3.42 (a)), each row of the grid, labelled 1-7, was considered separately in the HSI data for algorithm development. For each paint a label was allocated as denoted by colours in Figure 3.45.

The leftmost painting (Figure 3.45 (a)) was used as training data and with use of ROIs, each paint of the selected row was assigned a colour label for classification (see Figure 3.45 (b)). During this project it was chosen not to compress the spectral dimension and instead the full spectral profile was used as the data features for algorithm training. After training, the classification was performed on both paintings and the whole process was repeated for each row 1 - 7 in turn. Satisfactory classification results were obtained for both – the data set that the classifier was trained on, as well as the new, previously unseen data set to which the classifier was applied. A graphical illustration of the combined result for individual row after applying the proposed technique to each row separately is presented in Figure 3.45 (c). The same set of colours was used as the visual labels representation in each row, but since each row was analysed separately, repeating of the colour in each observation of a single column is only caused by row-wise result combination, and has no other meaning.

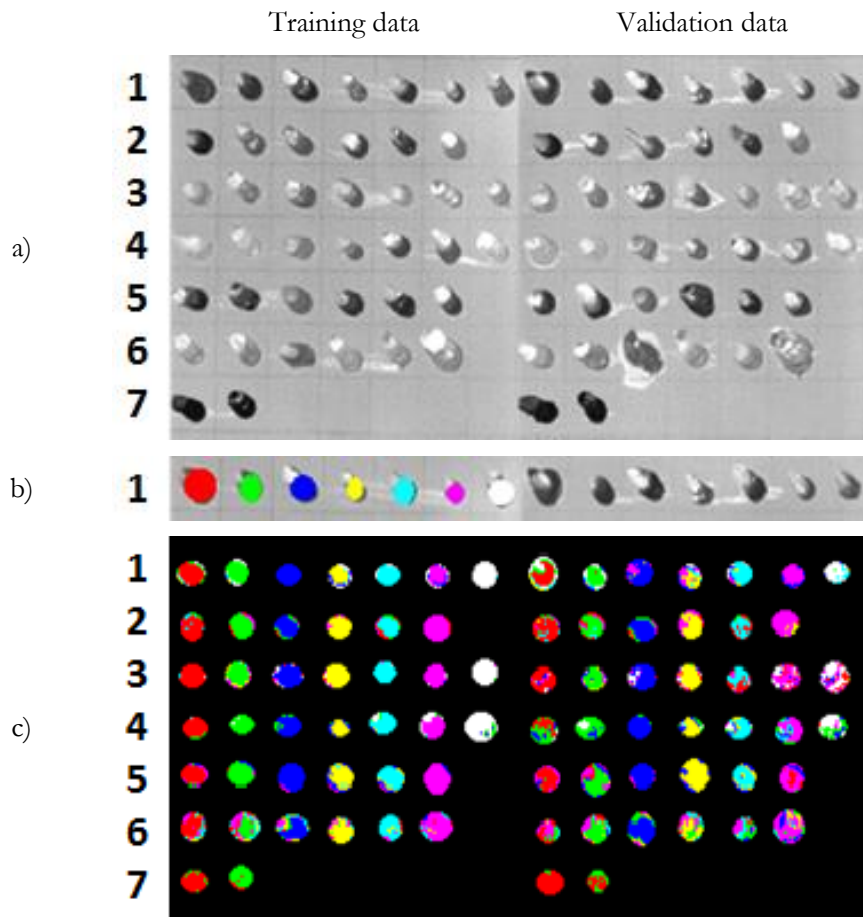


Figure 3.45. Illustration of the classification algorithm validation based on Red Eye 1.7 data: a) intensity image on one wavelength for two grid canvases; b) single row with assigned colour labels to each paint c) classification result of the training data set (on the left side) and validation data set (on the right).

To facilitate the classification process on a variety of the acquired images, all the relevant algorithms were built into a Matlab-based software for which the GUI is presented in Figure 3.46.

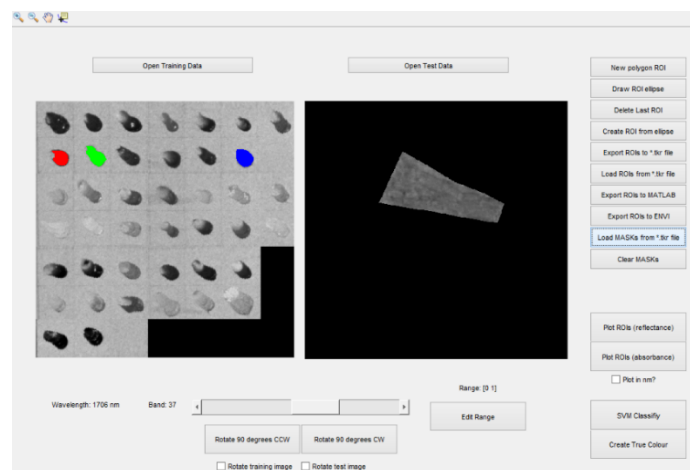


Figure 3.46. Illustration of the analysis software developed for painting analysis with demonstration of ROI's implemented on the training and mask on the testing image.

3.5 Results

3.5.1 Candidate paint selection

In this work, a dual stage classification process was proposed, to limit the amount of training data built into the classification model and to recognise an individual paint. The first stage of classification aimed at choosing a subset of 3 potential paints from the hyperspectral image of the “grid canvas”. This method not only accelerated the classification process and reduced computing power required for the problem by comparing only likely candidates, but also reduced the chance of misclassification. In practice, it does not make sense to attempt to recognise a one single paint by referencing and comparing it with the entire spectral library of all paints available – especially those which are clearly a different colour. It should be noted that many pigments can be accurately distinguished by analysing the visible region of the spectrum and, for these, this primary classification may be sufficient. For all others, shortlisting possible candidates based on the colour and appearance is a practical solution to reduce computational overhead and the likelihood of error. In fact, while the presented concept has already demonstrated its potential with a training set of only 41 paints, with the expected extension of the library to contain hundreds of different pigments, a pre-selection such as that mentioned above would be necessary for efficient performance of spectral data-based classification. To date, the selection of candidate paints has been carried out manually – by visual inspection based on paint colour, however an RGB or a visible range HSI system could also be used for this task and algorithms would have to be developed to perform this initial candidate selection step before the final spectral classification part. Furthermore, based on the ground truth data, the described visual inspection always shortlisted the correct paint and therefore it was clearly a viable solution and one which could be easily performed - even by a non-expert user of the technology.

3.5.2 Spectral classification of the test painting

Figure 3.47 provides examples of regions selected for classification and paint candidates chosen as training data for their labelling. Due to the highly geometrical structure of the painting analysed in Figure 3.47 (also shown in full and in colour in Figure 3.42 (c)), masks (binary images used to specify regions of the image for processing) were created for each painting area. Each structure on the painting was prepared with a single, unmixed paint. Therefore, to make demonstration of the classification results simpler, regions of the painting corresponding to a single colour were classified separately, with the remainder of the image being disabled from classification by application of the masks.

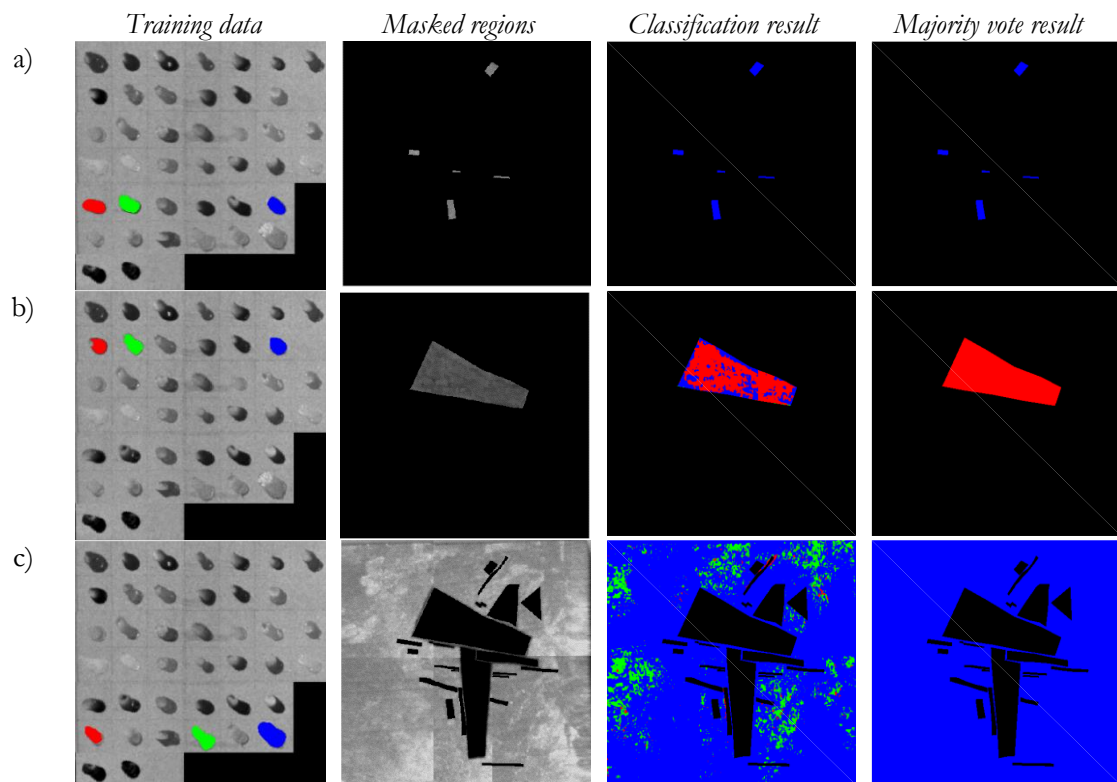


Figure 3.47. Illustration of the analysis approach for pigment classification on tested painting. For each colour on the painting, a subset of training paints was chosen (first column – Training data) and classification was performed on the masked area of the painting corresponding to this colour (second column – Masked regions). It resulted in per-pixel classification of the selected area (third column – Classification result) and majority vote was drawn for these regions effecting in selection of one pigment corresponding to one colour (fourth column – majority vote result). Three examples of this approach are shown in here, for the regions of brown (a), green (b) and white (c) paint (demonstration based on Firefly IR Imager data).

After the candidate pre-selection, a spectral classification stage using a SVM classifier and majority voting scheme was applied to assign the chosen paint section to one of the selected classes based on the spectral signature in each pixel of the masked region in the test painting. The classification was performed on a pixel-by-pixel basis, but with the prior knowledge that each section of the test painting was created with one type of the pigment – i.e. no mixtures or other impurities. Figure 3.47 illustrates this approach and provides the classification and majority vote results for selected example regions. The colour of the label assigned to each pixel and subsequently each region of paint corresponds to the “class colour” assigned to the ROI selected from the training data set.

The approach shown in Figure 3.47 was applied to all regions of the painting, assigning one class from the training set to each of them in turn. A total of 10 different paints were used to prepare the painting under study, from which 9 were available in the “grid canvas” and were therefore contained within the constructed spectral library. From this perspective, using the Firefly IR Image data, it was possible to automatically classify 67% of the pigments (6 out of 9)

correctly, while the correctness ratio for data from the Red Eye 1.7 system reached 78% (7 out of 9). Figure 3.48 shows the classification results for both imaging systems when compared with the ground truth data.

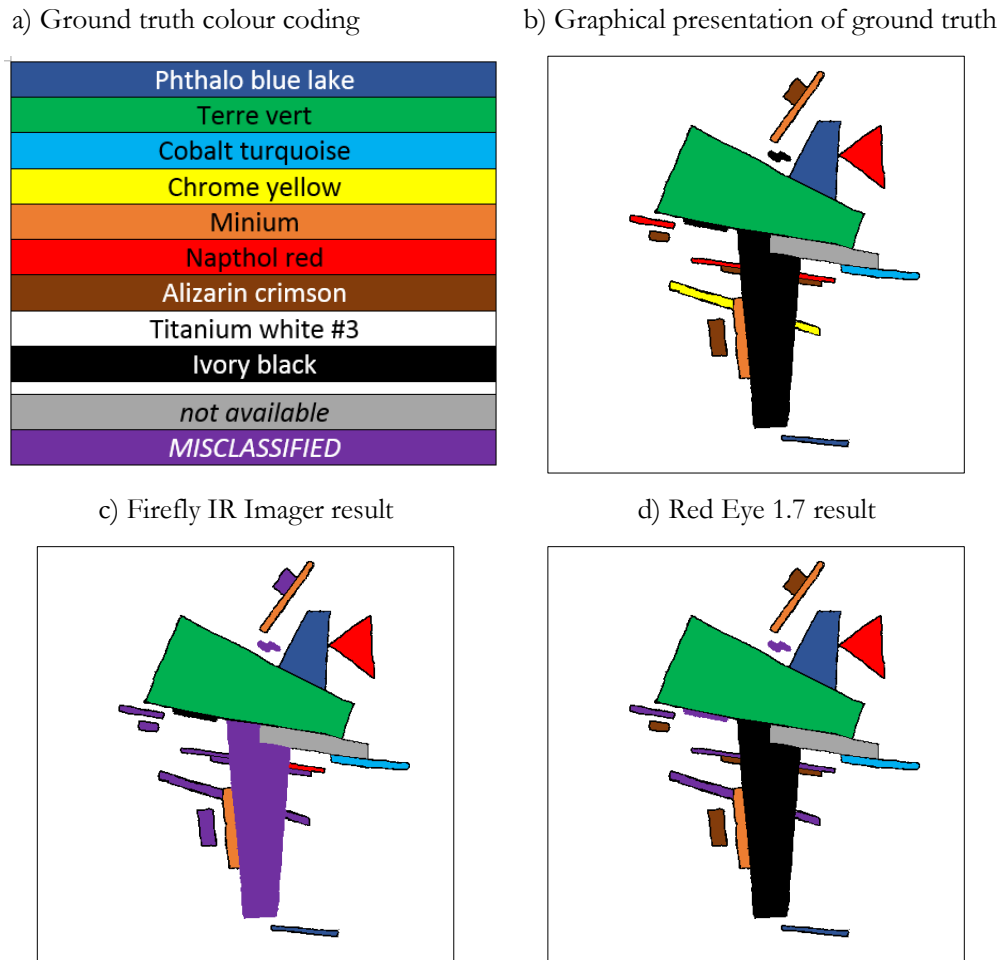


Figure 3.48. Graphical illustration of class labelling for all the regions of the test painting: a) the colour coding of the result demonstration; b) ground truth data illustration; c) the result based on data from Firefly IR Imager; d) the result based on data from Red Eye 1.7 system.

It is clear that in some cases, if the classification of data from one device is wrong, it may be accurate if the other is used, and vice versa. For example, one of the regions painted with Ivory black paint is always classified correctly by both systems, but it exists in a different region for both of them (see Figure 3.48 (c) and (d)). This demonstrates the complementary nature of the two devices and also shows that the full range of considered wavelengths is useful for discriminating different paints. Whilst the classification accuracies did not reach 100%, the potential of automated techniques based on the hyperspectral data has been clearly demonstrated.

The percentage of correctly classified pixels varied significantly between different regions in spite of the fact that each region was known as painted by a unique paint from the library. The

misclassification problem was most likely due to the spectral similarity of the candidate paints or as a result of the imaging artefacts discussed in Section 3.3. Figure 3.49 shows the Receiver Operating Characteristic (ROC) curves for both used HSI sensors.

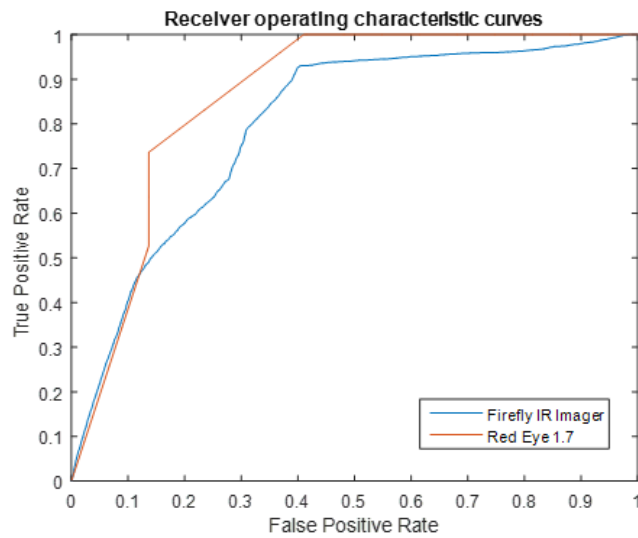


Figure 3.49. Example of receiver operating characteristic (ROC) curves for both tested HSI sensors.

The ROC curves were generated by applying the classifier to the data from both HSI systems and performing a binary comparison with the output and a set of manually generated ground truth data. It is clear that the performance of the classification using the data from the passive system is better than the active one. This reduced accuracy in the active system can be explained by the presence of the aforementioned imaging artefacts (as discussed in Section 3.3) which are present in the data set.

3.5.3 Analysis of forged paintings

Having demonstrated the proposed system's ability to recognise the paints based on spectral signatures in a well-controlled lab-based environment, this technology was applied to assess other paintings, suspected or, by other means, already identified as forgeries. Thanks to the courtesy of the Berlin Police it was possible to image several paintings from their collection of forged paintings created by the infamous Wolfgang Beltracchi [38].

Due to the practicalities in transporting the equipment to Berlin, only the Red Eye 1.7 camera was used during this experiment. Data acquisition, pre-processing and analysis steps followed the approach described in Sections 3.2, 3.4 and 3.5. The only difference was at the stage of classification since the analysed paintings did not feature the simple geometric properties of the one designed for this work as shown in previous sections. For this reason, the application of

binary masks was not a feasible approach to allow individual regions of the paintings to be processed separately. Additionally, they contained a variety of pigments, both in pure and mixed form. To overcome these challenges, the proposed techniques were applied to selected regions of the two paintings, chosen based on other instrumental testing techniques (see Section 3.4.1), which contained “*Titanium white*” paint known in this case to be anachronistic (i.e. the pigment was not yet developed at the period in which the painting was supposedly produced). As shown in Figure 3.50 (b) and (c), the two selected paintings are displayed, where the green boxes outline the regions chosen for the analysis alongside a magnification of the colour representation of the classification result.

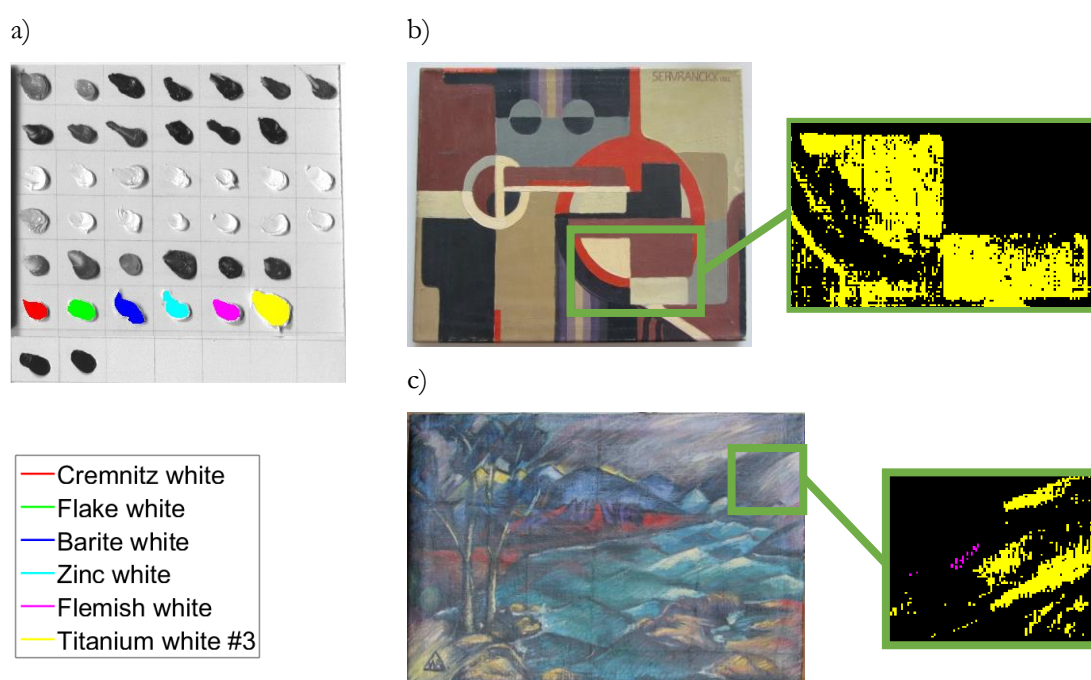


Figure 3.50. Illustration of two forged paintings with indication of analysis region and classification result of selected colours: a) intensity image of grid canvas with selection of paints used for training and the legend identifying the colour coded pigments; b) painting described as *Sevrancx* with white/cream colour classification result; c) painting referred as *HM501* and white colour classification.

Figure 3.50 (b) shows a painting referred to as ‘Sevrancx’ in which the white/cream regions have been identified as *Titanium White* in a separate invasive tests. The developed software was trained on all of the white/cream paints in the spectral library constructed in this study using pigments in the “grid canvas” painting (see Figure 3.50 (a)) and included: *Cremnitz white*, *Flake white*, *Barite white*, *Zinc white*, *Flemish white* and *Titanium white #3*. The right hand part of the figure shows the classification result for a small region of the painting. Yellow in this image corresponds to *Titanium White* in the spectral library. The black regions correspond to pixels in the image where no classification has been made by the system as it does not recognise the spectra of these pixels

as belonging to any paint in the spectral library provided. Furthermore, no other classification labels/colours are visible in the image. The reason for this is that the classifier did not identify any other part of this section of the painting as containing any of the other white paints. From this result, it is clear that two of the white/cream regions have been correctly identified and this was validated by comparing with previously captured ground-truth information. A analogous situation can be observed in Figure 3.50 (c) demonstrating a painting referred to as ‘HM501’, where similar classification steps successfully identified *Titanium White* in agreement with the result of the aforementioned separate analysis. It may be noticed that several pixels were misclassified as Flemish white (marked with magenta in Figure 3.50 (c)). However, the number of pixels in error is very small as this is to be expected of any automated classification scheme. In both these test cases the correct identification of *Titanium White* was very important for the art scientists, as this was the anachronistic pigment used in Beltracchi forgeries. Moreover, this combined with other evidence, such as the use of another anachronistic paint, Phthalocyanine Green, and a very limited pool of re-used canvases and stretchers, confirmed the counterfeit nature of these paintings [36].

3.6 Conclusions

Hyperspectral Imaging combined with advanced signal processing techniques is a valid and potent method which can be used as a tool to support the process of artwork authentication by identification and classification of pigments. The work presented above revealed the development of the software-based signal processing algorithms to facilitate feature extraction and classification of paints from hyperspectral images of bespoke and fraudulent artwork captured in the infrared spectral region. A wide range in the infrared was accessed by use of a conventional Near-IR HSI camera as well as a novel laser based imager, extending the readily accessible bandwidth of this portion of the Near-IR spectrum with a subset of the Mid-IR region. Collaboration of art historians and signal processing specialists made it possible to create a small spectral library of pigments, based on the tailored grid canvas, and to apply the classification techniques to distinguish different paints used on a specially prepared painting. Additionally, thanks to unique access to an extremely high-profile data set, developed algorithms enabled a test - for the first time with this technique - of a set of known Beltracchi forged paintings. The classification results showed the moderate-high correct classification rate already after the first attempt to solve this problem. In fact, up to 78% of pigments used in the bespoke test painting were correctly classified using the Red Eye 1.7 HSI imaging sensor. Ultimately, and perhaps most importantly, an anachronistic paint - *Titanium White* - was identified from real forged paintings

using evaluated system in real world conditions, and utilising the separately acquired spectral library of pigments as reference.

The data in this work was acquired using a state-of-the-art laser-based hyperspectral imager and the results of analysed images have been compared to those obtained when analysing data captured by a conventional hyperspectral camera. It is shown that there are various challenges associated with capturing wide area hyperspectral images using active laser-based imaging systems such as the Firefly IR. These occur as a result of non-uniform back-scatter reflectance, per-pulse jitter, speckle effect and specular reflections which affect the nature of the spectral signatures observed. To address these challenges, various workable solutions were demonstrated and it was shown that it is possible to successfully apply signal processing algorithms to the resulting data set in order to achieve accurate classification in most cases. Additionally, a set of hardware improvement techniques was proposed and it was concluded that their implementation could lead to significant enhancement of the image quality.

This initial study demonstrates the effectiveness of hyperspectral imaging in combination with image processing and classification techniques. However, it should be noted that some pigments were undistinguishable with the SVM classifier and further investigation would be required to determine which paints can be reliably identified with this method. Additionally, other spectral bands, feature extraction techniques and classification algorithms should be considered to further explore the effectiveness and improve the robustness of the final system. A comprehensive spectral library of pigments is also crucial for successful classification. Various thicknesses of the paints, different base (e.g. wooden board or canvas), background painting surface and presence of varnish may affect the spectral profile and should be considered for an implementable system.

The application of scientific methods to reveal forgeries has recently gained significant public profile [4]. With increased demand for such analysis, the introduction of hyperspectral imaging can enhance the portfolio of available techniques and tools as a rapid and non-destructive method of artwork examination. Even if the results based solely on HSI data cannot provide full confirmation that a painting is genuine or forged, current practices of art historians employ a combination of background knowledge and scientific data in the authentication process. By adding hyperspectral imaging to their already sophisticated toolkit, the analysis procedures could become faster, easier and more accessible to a larger portion of the market resulting in more affordable services for customers. Ultimately, the techniques proposed herein could limit the amount of destructive tests required for final validation and consequently increase the amount of analysed artwork making the whole procedure even more cost effective.

3.7 Acknowledgments

This study was carried out within the framework of an Intelligent Hyperspectral Imaging (INHERIt) Project financed by Innovate UK, Technology Strategy Board in collaboration between Department of Electronic & Electrical Engineering, University of Strathclyde, (Glasgow, UK), M Squared Lasers (Glasgow, UK), Fraunhofer UK (Glasgow, UK) and Art Analysis & Research (London, UK). Thanks to Berlin Landeskriminalamt for granting access to their paintings and supporting this study. This project was also supported by the EPSRC Centre for Doctoral Training in Applied Photonics, funded by the UK Engineering and Physical Sciences Research Council (grant EP/G037523/1) and by an Industrial Fellowship from the Royal Commission for the Exhibition of 1851. Thanks to Pavel Demin from Université catholique de Louvain for support in preparation of FPGA code for RedPitaya board.

References

- [1] C. McAndrew, "TEFAF Art Market Report 2015," The European Fine Art Foundation (TEFAF), Helvoirt, 2015.
- [2] C. McAndrew, "TEFAF Art Market Report 2014: The Global Art Market, with a focus on the US and China," The European Fine Art Foundation (TEFAF), Helvoirt, 2014.
- [3] S. Hardach, "BBC - Culture - The surprising secrets of busting art forgeries," 19 October 2015. [Online]. Available: <http://www.bbc.com/culture/story/20151015-the-surprising-secrets-of-busting-art-forgeries>. [Accessed 08 January 2016].
- [4] N. Eastaugh and J. Nadolny, "Science for the Art Market: A Buyer's Guide," *ArtBanc Market Intelligence*, no. 7, pp. 33-37, April 2007.
- [5] A. Adriaens, "COST Action G8: Non-destructive analysis and testing of museum objects," in *Benefits of non-destructive analytical techniques for conservation*, Kalkara, 2004.
- [6] G. D. Smith, J. F. Hamm, D. A. Kushel and C. E. Rogge, "What's Wrong with this Picture? The Technical Analysis of a Known Forgery," in *Collaborative Endeavors in the Chemical Analysis of Art and Cultural Heritage Materials*, American Chemical Society, 2012, pp. 1-21.
- [7] Y. Roggo, A. Edmond, P. Chalus and M. Ulmschneider, "Infrared hyperspectral imaging for qualitative analysis of pharmaceutical solid forms," *Analytica Chimica Acta*, vol. 535, pp. 79-87, 2005.
- [8] B. D. Jadhav and P. M. Patil, "Hyperspectral Remote Sensing For Agricultural Management: A Survey," *International Journal of Computer Applications*, vol. 106, no. 7, pp. 38-43, 2014.

- [9] G. K. Naganathan, L. M. Grimes, J. Subbiah, C. R. Calkins, A. Samal and G. E. Meyer, "Visible/near-infrared hyperspectral imaging for beef tenderness prediction," *Computers and Electronics in Agriculture*, vol. 64, no. 2, pp. 225-233, 2008.
- [10] T. Qiao, J. Ren, C. Craigie, J. Zabalza, C. Maltin and S. Marshall, "Comparison between near infrared spectroscopy and hyperspectral imaging in predicting beef eating quality," in *Hyperspectral Imaging and Applications Conference (HSI 2014)*, Coventry, 2014.
- [11] T. Qiao, J. Ren, C. Craigie, J. Zabalza, C. Maltin and S. Marshall, "Quantitative prediction of beef quality using visible and NIR spectroscopy with large data samples under industry conditions," *Journal of Applied Spectroscopy*, vol. 82, no. 1, 2015.
- [12] T. Qiao, J. Ren, J. Zabalza and S. Marshall, "Prediction of lamb eating quality using hyperspectral imaging," in *OCM (Optical Characterization of Materials) 2015*, Karlsruhe, 2015.
- [13] S. Legrand, F. Vanmeert, G. V. d. Snickt, M. Alfeld, W. D. Nolf, J. Dik and K. Janssens, "Examination of historical paintings by state-of-the-art hyperspectral imaging methods: from scanning infra-red spectroscopy to computed X-ray laminography," *Heritage Science*, vol. 2, pp. 13-24, 2014.
- [14] C. Fischer and I. Kakoulli, "Multispectral and hyperspectral imaging technologies in conservation: current research and potential applications," *Studies in Conservation*, vol. 51, no. Supplement-1, pp. 3-16, 2006.
- [15] F. Rosi, C. Miliani, R. Braun, R. Harig, D. Sali, B. G. Brunetti and A. Sgamellotti, "Noninvasive Analysis of Paintings by Mid-infrared Hyperspectral Imaging," *Angewandte Chemie International Edition*, vol. 52, no. 20, p. 5258–5261, 2013.
- [16] K. A. Dooley, S. Lomax, J. G. Zeibel, C. Miliani, P. Ricciardi, A. Hoenigswald, M. Loew and J. K. Delaney, "Mapping of egg yolk and animal skin glue paint binders in Early Renaissance paintings using near infrared reflectance imaging spectroscopy," *Analyst*, vol. 138, p. 4838–4848, 2013.
- [17] J. K. Delaney, J. G. Zeibel, M. Thoury, R. Littleton, M. Palmer, K. M. Morales, E. R. d. I. Rie and A. Hoenigswald, "Visible and Infrared Imaging Spectroscopy of Picasso's Harlequin Musician: Mapping and Identification of Artist Materials in Situ," *Applied Spectroscopy*, vol. 64, no. 6, pp. 584-594, 2010.
- [18] J. K. Delaney, M. Thoury, J. G. Zeibel, P. Ricciardi, K. M. Morales and K. A. Dooley, "Visible and infrared imaging spectroscopy of paintings and improved reflectography," *Heritage Science*, vol. 4:6, pp. 1-10, 2016.
- [19] H. Liang, "Advances in Multispectral and Hyperspectral Imaging for Archaeology and Art Conservation," *Applied Physics A*, vol. 106, no. 2, p. 309–323, 2012.
- [20] A. Casini, C. Cucci, M. Picollo, L. Stefani and T. Vitorino, *Creation of a hyper-spectral imaging reference database of red lake pigments*, COSCH e-Bulletin, 2015.
- [21] A. Casini, F. Lotti, M. Picollo, L. Stefani and E. Buzzegoli, "Image spectroscopy mapping technique for noninvasive analysis of paintings," *Studies in Conservation*, vol. 44, no. 1, pp. 39-48, 1999.

- [22] M. Kubik, "Hyperspectral Imaging: A New Technique for the Non-Invasive Study of Artworks," *Physical Techniques in the study of Art, Archaeology and Cultural Heritage*, vol. 2, p. 199–259, 2007.
- [23] F. Daniel, A. Mounier, J. Pérez-Arantegui, C. Pardos, N. Prieto-Taboada, S. F.-O. d. Vallejuelo and K. Castroc, "Hyperspectral imaging applied to the analysis of Goya paintings in the Museum of Zaragoza (Spain)," *Microchemical Journal*, vol. 126, p. 113–120, 2016.
- [24] S. Baronti, A. Casini, F. Lotti and S. Porcinai, "Multispectral imaging system for the mapping of pigments in works of art by use of principal-component analysis," *Applied Optics*, vol. 37, no. 8, pp. 1299-1309, 1998.
- [25] C. Cucci, J. K. Delaney and M. Picollo, "Reflectance Hyperspectral Imaging for Investigation of Works of Art: Old Master Paintings and Illuminated Manuscripts," *Accounts of Chemical Research*, vol. 49, no. 10, p. 2070–2079, 2016.
- [26] M. Attas, E. Cloutis, C. Collins, D. Goltz, C. Majzels, J. R. Mansfield and H. H. Mantsch, "Near-infrared spectroscopic imaging in art conservation: investigation of drawing constituents," *Journal of Cultural Heritage*, vol. 4, pp. 127-136, 2003.
- [27] K. Melessanaki, V. Papadakis, C. Balas and D. Anglos, "Laser induced breakdown spectroscopy and hyper-spectral imaging analysis of pigments on an illuminated manuscript," *Spectrochimica Acta Part B*, vol. 56, pp. 2337-2346, 2001.
- [28] C. Balas, V. Papadakis, N. Papadakis, A. Papadakis, E. Vazgiouraki and G. Themelis, "A novel hyper-spectral imaging apparatus for the non-destructive analysis of objects of artistic and historic value," *Journal of Cultural Heritage*, vol. 4, pp. 330-337, 2003.
- [29] M. E. Klein, B. J. Aalderink, R. Padoan, G. d. Bruin and T. A. Steemers, "Quantitative Hyperspectral Reflectance Imaging," *Sensors*, vol. 8, pp. 5576-5618, 2008.
- [30] C. S. Silva, M. F. Pimentel, R. S. Honorato, C. Pasquini, J. M. Prats-Montalban and A. Ferrere, "Near infrared hyperspectral imaging for forensic analysis of document forgery," *Analyst*, vol. 139, pp. 5176-5184, 2014.
- [31] Z. Luo, P. Shafait and A. Mian, "Localized Forgery Detection in Hyperspectral Document Images," in *13th International Conference on Document Analysis and Recognition (ICDAR)*, Nancy, France, 2015.
- [32] Z. Khan, F. Shafait and A. Mian, "Towards Automated Hyperspectral Document Image Analysis," in *Proceedings of the 2nd International Workshop on Automated Forensic Handwriting Analysis: A Satellite Workshop of International Conference on Document Analysis and Recognition (ICDAR 2013)*, Washington DC, USA, 2013.
- [33] T. Chen, Z. D. Schultz and I. W. Levin, "Infrared spectroscopic imaging of latent fingerprints and associated forensic evidence," *Analyst*, vol. 134, p. 1902–1904, 2009.
- [34] G. Edelman, E. Gaston, T. v. Leeuwen, P. Cullen and M. Aalders, "Hyperspectral imaging for non-contact analysis of forensic traces," *Forensic Science International*, vol. 223, p. 28–39, 2012.

- [35] C. Daffara, D. Ambrosini, L. Pezzati and D. Paoletti, “Thermal quasi-reflectography: a new imaging tool in art conservation,” *Optics Express*, vol. 20, no. 13, pp. 14746-14753, 2012.
- [36] C. Finn, “The Devil in the Detail,” *Apollo: The international art magazine*, vol. CLXXIX, no. 616, p. 50 – 54, January 2014.
- [37] H. Keazor and T. Öcal, Eds., *Der Fall Beltracchi und die Folgen. Interdisziplinäre Fälschungsforschung heute.*, Berlin: De Gruyter, 2014.
- [38] J. Hammer, “The Greatest Fake-Art Scam in History?,” *Vanity Fair*, 10 October 2012. [Online]. Available: <http://www.vanityfair.com/culture/2012/10/wolfgang-beltracchi-helene-art-scam>. [Accessed 22 March 2016].
- [39] S. Koldehoff and T. Timm, *Falsche Bilder, Echtes Geld (Fake paintings, real money)*, Berlin: Verlag Galliani, 2012.
- [40] M. Sontheimer, “A Cheerful Prisoner: Art Forger All Smiles After Guilty Plea Seals Deal,” *Der Spiegel*, 27 October 2011. [Online]. Available: <http://www.spiegel.de/international/germany/0,1518,794454,00.html>. [Accessed 18 March 2016].
- [41] A. Polak, T. Kelman, P. Murray, S. Marshall, D. Stothard, N. Eastaugh and F. Eastaugh, “Use of infrared hyperspectral imaging as an aid for paint identification,” *Journal of Spectral Imaging*, vol. 5, no. 1, pp. 1-10, 2016.
- [42] A. Polak, T. Kelman, P. Murray, S. Marshall, D. J. M. Stothard, N. Eastaugh and F. Eastaugh, “Hyperspectral imaging combined with data classification techniques as an aid for artwork authentication,” *Journal of Cultural Heritage*, vol. 26, pp. 1-11, 2017.
- [43] D. J. M. Stothard, M. H. Dunn and C. F. Rae, “Hyperspectral imaging of gases with a continuous-wave pump-enhanced optical parametric oscillator,” *Optics Express*, vol. 12, no. 5, pp. 947-955, 2004.
- [44] H. Grahn, *Techniques and Applications of Hyperspectral Image Analysis*, Chichester: Wiley, 2007.
- [45] M. W. Davidson, “ZEISS Microscopy Online Campus | Tungsten-Halogen Lamps,” [Online]. Available: <http://zeiss-campus.magnet.fsu.edu/articles/lightsources/tungstenhalogen.html>. [Accessed 15 January 2016].
- [46] G. ElMasry and D.-W. Sun, “Principles of Hyperspectral Imaging Technology,” in *Hyperspectral Imaging for Food Quality Analysis and Control*, London, Elsevier Inc., 2010, pp. 32-36.
- [47] Labsphere, Inc, “Spectralon Diffuse Reflectance Standards,” [Online]. Available: https://www.labsphere.com/site/assets/files/2628/spectralon_diffuse_reflectance_standards.pdf. [Accessed 30 November 2016].
- [48] H. Bay, T. Tuytelaars and L. V. Gool, “SURF: Speeded Up Robust Features,” in *Computer Vision – ECCV 2006*, Graz, Springer, Berlin, Heidelberg, 2006, pp. 404-417.

- [49] K. E. Torrance and E. M. Sparrow, "Theory for Off-Specular Reflection From Roughend Surfaces," *Journal of the Optical Society of America*, vol. 57, no. 9, pp. 1105-1114, 1967.
- [50] B. Redding, G. Allen, E. R. Dufresne and H. Cao, "Low-loss high-speed speckle reduction using a colloidal dispersion," *Applied Optics*, vol. 52, no. 6, pp. 1168-1172, 2013.
- [51] B. Redding, M. A. Choma and H. Cao, "Speckle-free laser imaging using random laser illumination," *Nature Photonics*, vol. 6, pp. 355-359, 2012.
- [52] G. Ouyang, M. N. Akram, K. Wang, Z. Tong and X. Y. Chen, "Laser speckle reduction based on angular diversity induced by Piezoelectric Benders," *Journal of the European Optical Society: Rapid publications*, vol. 13025, no. 8, pp. 1-4, 2013.
- [53] J. I. Trisnadi, "Hadamard speckle contrast reduction," *Optics Letters*, vol. 29, no. 1, pp. 11-13, 2004.
- [54] J. W. Goodman, "Some fundamental properties of speckle," *Journal of the Optical Society of America*, vol. 66, no. 11, pp. 1145-1150, 1976.
- [55] K. V. Chellappan, E. Erden and H. Urey, "Laser-based displays: a review," *Applied Optics*, vol. 49, no. 25, pp. 79-98, 2010.
- [56] G. Cloud, "Optical Methods in Experimental Mechanics; Part 24: Demonstrations of Laser Speckle Phenomena," *Experimental Techniques*, vol. 30, no. 6, pp. 27-30, 2006.
- [57] K. J. Gåsvik, *Optical Metrology*, Chichester: John Wiley & Sons, Ltd., 2003.
- [58] H. Ragheb and E. R. Hancock, "A probabilistic framework for specular shape-from-shading," *Pattern Recognition*, vol. 36, pp. 407-427, 2003.
- [59] M. Born and E. Wolf, *Principles of Optics*, Liverpool: Pergamon Press Ltd, 1970.
- [60] I. Overington, *Vision and acquisition: fundamentals of human visual performance, environmental influences, and applications in instrumental optics*, Pentech Press, 1976.
- [61] G. A. Atkinson and E. R. Hancock, "Recovery of Surface Orientation From Diffuse Polarization," *IEEE Transactions on Image Processing*, vol. 15, no. 6, pp. 1653-1664, 2006.
- [62] V. Müller, "Elimination of specular surface-reflectance using polarized and unpolarized light," in *ECCV 1996*, Cambridge, 1996.
- [63] StemLabs, "STEMLab," 2018. [Online]. Available: <https://www.redpitaya.com>. [Accessed 7 May 2018].
- [64] N. Eastaugh, V. Walsh, T. Chaplin and R. Siddall, *The Pigment Compendium*, Elsevier, 2008.
- [65] eXtension.org, "What's the difference between a supervised and unsupervised image classification?," eXtension.org, 17 October 2013. [Online]. Available: <http://articles.extension.org/pages/40214/whats-the-difference-between-a-supervised-and-unsupervised-image-classification>. [Accessed 18 March 2016].

- [66] S. Wold, K. Esbensen and P. Geladi, "Principal Component Analysis," *Chemometrics and Intelligent Laboratory Systems*, vol. 2, no. 1-3, pp. 37-52, 1987.
- [67] C.-W. Hsu, C.-C. Chang and C.-J. Lin, "A Practical Guide to Support Vector Classification," National Taiwan University, Taiwan, 2010.
- [68] N. Cristianini and J. Shawe-Taylor, *An Introduction to Support Vector Machines and Other Kernel-based Learning Methods*, Cambridge: Cambridge University Press, 2000.
- [69] P. Du, G. Li, W. Zhang, X. Wang and H. Sun, "Consistency Measure of Multiple Classifiers for Land Cover Classification by Remote Sensing Image," in *Multiple Classifier Systems: 8th International Workshop, MCS 2009, Reykjavik, Iceland, June 10-12, 2009, Proceedings*, Reykjavik, 2009.
- [70] MathWorks, "Support Vector Machines (SVM)," MathWorks, [Online]. Available: <http://uk.mathworks.com/help/stats/support-vector-machines-svm.html>. [Accessed 19 January 2016].
- [71] C.-C. Chang and C.-J. Lin, "LIBSVM : a library for support vector machines," *ACM Transactions on Intelligent Systems and Technology*, vol. 2, no. 3, pp. 27:1--27:27, 2011.

Chapter 4: ROSDAM

4.1. Project background

To date, oil which has been spilt in ice-affected water tends to disappear beneath the ice layer and it is not possible to detect and monitor where it travels or at which point it emerges from the ice edge into open sea. This poses very significant challenges to any extenuating activities until long after the emerging oil has been located.

There is vast range of techniques available for monitoring open water oil spills, including various satellite and airborne remote sensing methods [1, 2]. However, the detection of oil spills in ice-affected waters differs significantly and the presence of ice limits the amount of applicable monitoring as well as the detection techniques. Current approaches for the detection of oil under ice can be divided into two groups: (I) on or above the surface sensing and (II) detection from underneath ice. Extensive surveys of available techniques for surface remote sensing have been presented in literature [3, 4, 5] as well as a study of oil detection from underneath the ice surface [6]. Various detection techniques, including for example Synthetic Aperture Radar (SAR), Microwave Radiometers (MWR) and Tunable Diode Laser Spectroscopy (TDLS) were presented in the above-mentioned reviews, but most of them are described as not applicable for the oil under ice detection problem. Hyperspectral imaging (HSI) was also included in these reviews and similar to the other techniques it was identified as not applicable for this task.

The majority of hyperspectral imaging systems, independent from their operating spectral range, require external illumination in order to observe the scene (passive systems). Most of the imagers operating in visible and near-infrared (NIR) range of the electromagnetic spectrum utilise halogen lamps as the illumination source or rely on solar light. This feature may limit their use in an Arctic environment and the systems that actively illuminate the scene of interest could overcome this limitation. Although HSI systems with active illumination were reported [7], they constitute the minority of HSI systems and are not readily available. Due to the unique access to the laser-based, active hyperspectral imager, it was decided to verify its applicability or otherwise for the oil under ice detection problem.

The work described in this chapter was done under the short study 'Hyperspectral Ice/Oil Detection Experiment' (HIDE) followed by the project 'Remote Oil Spill Detection And Monitoring on ice-covered waters' (ROSDAM) funded by the R&D Award from the International

Tanker Owners Pollution Federation Limited (ITOPF). It focused on testing if the available hyperspectral devices (see Chapter 3.2) could be applied for the detection of oil in ice-affected waters.

The HIDE experiment demonstrated promising results of the HSI application for the oil under ice detection [8]. Encouraged by the results of this proof of concept, an extensive feasibility study of HSI application for the detection of oil beneath the sea ice was initiated (ROSDAM project). Although the project ultimately proved this technique unfeasible for this application. The experimental approach for oil and ice treatment as well as series of results confirming that the HSI hardware used during this study is not applicable for the oil under ice detection are demonstrated throughout this chapter. During the work on this project, a series of pitfalls were encountered, therefore, along with the findings and lessons learned, these will be also discussed in this chapter.

4.2. HIDE – the initial proof of concept study

4.2.1. Passive system setup

A test with a passive HSI system was performed on the premises of University of Strathclyde. A small container (width x length x height: 5x15x3cm) was half filled with the sea water (about 15 mm depth) obtained from the Scottish shore (salinity ~30 psu (practical salinity unit), this is the salinity of the water referred to as the “sea water” across this chapter) and was frozen in a small upright laboratory freezer at a temperature of -30°C (see Fig. 1 a).

The RedEye 1.7 camera was used in the configuration identical to the one described in Chapter 3.2.1. The container with ice was taken from the freezer and imaged at room temperature. After imaging the pure ice, the ice block was removed from the container and a layer of about 15 mm off-the-shelf engine lubrication oil was poured into the container and the ice block was placed on top of the oil sample (see Fig. 1 b).

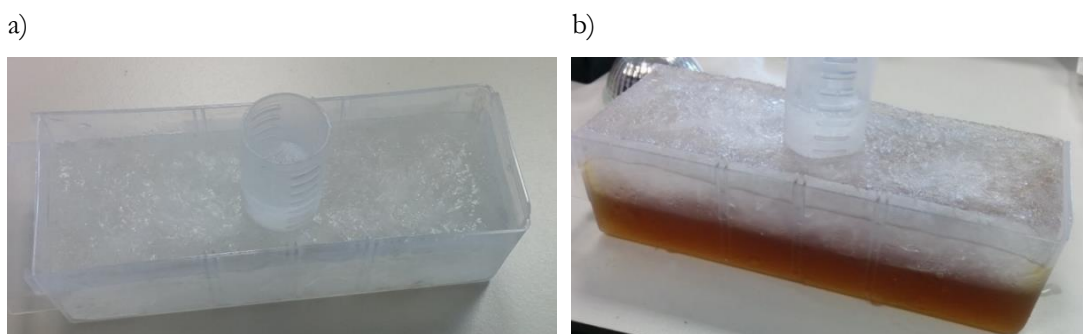


Figure 4.1. Small container with ice (a) and oil introduced beneath the ice layer (b).

There was no liquid sea water beneath the oil layer during this test. The imaging of this new condition was performed in the same way as for the pure ice block. The whole imaging procedure was finished before any melting of the ice could be observed.

4.2.2. Active system setup

Test with the active system was performed on the premises of Scottish Association for Marine Science (SAMS). The ice sample was grown in cylindrical container (height: 1 m, diameter: 0.7 m) placed in a cold room with a controllable temperature. The container was filled with the sea water obtained from Scottish shore (salinity ~ 30 psu) and was maintained at a temperature of -30°C for the time of the ice growth. Due to the restrictions in the operating temperature of the Firefly IR Imager (M Squared Lasers) (specified temperature range of operation: $+15^{\circ}\text{C}$ to $+30^{\circ}\text{C}$), the cooling in the cold room was disabled for the time of the imaging and the data collection was performed in the varying temperature, rising from approximately 10°C at the beginning of the data acquisition, to the room temperature at the end. It was observed that the ice surface was affected by this temperature increase. Additionally, the energy transferred from the Mid-IR affected the ice structure and intensified melting was observed in the area of the laser scanning. The imager was placed approximately 1 m above the ice container and an external gold mirror was applied to allow vertical data acquisition from the vertically located imager (see Fig. 2a).

Despite the observed melting effect (both caused by ambient temperature as well as the laser radiation) the experiment was continued on the same and only available, ice block. No refreezing of the ice was attempted and only (in between the imaging runs) the superficial water layer from melted ice was removed with a cloth. After collection of the pure ice data, a hole was drilled at the side of ice layer and the oil sample (the same engine lubrication oil as used for test with passive system) was introduced via a hose inserted through the drilled hole beneath the ice block. The thickness of the oil layer was not tested at that stage, but based on the dimensions of the container and the volume of injected liquid, the approximate oil layer thickness was 10 mm. The data for the new conditions were collected in the same way as for pure ice. After the test was completed, the tested ice was cut and it was measured to have a thickness of approx. 80mm (see Fig. 2 b), with cooled down liquid sea water underneath. The amount of ice melted during the experiment was negligible.



Figure 4.2. Scanning setup with the Firefly IR Imager above the container with ice (a); the ice block of approximately 80 mm thickness cut after the imaging (b).

4.2.3. Results

The initial proof of concept provided an assortment of promising results for both passive and active imaging systems [8]. The acquired average spectra varied between the pure ice case and the one with oil underneath (see Table 4.1.). The collected signal intensities were low, though it was expected for highly absorbing and scattering medium like ice. Despite these low signal levels, it was assessed that it was sufficient for further analyses. Due to the fact that the main objective of this experiment was to conclude if the HSI is able to detect the oil presence beneath the ice samples, the classification technique was employed to distinguish a pure ice and oil under ice scenarios. The analyses were performed using a Support Vector Machine (SVM) classifier.

Due to the limited amount of data available, the same hyperspectral images were used for training the algorithm as well as for classification purposes. The training of the classifier was performed on a subset of the analysed images (see coloured ellipses drawn on the intensity image of one chosen band from hyperspectral data cube presented in Table 4.1.). To check the classification performance on different sizes of the training data, two approximately 5% and 25% of total available data were tested. All classification results are presented in the graphical form, where an assigned colour illustrates the class given during the training process and the one

identified by the classification algorithm. In all the figures in Table 4.1., red colour of the training region ellipse and classification results represents the pure ice case, while green represents the situation with oil underneath the ice sample.

Table 4.1. HIDE experiment results based on the data acquired with passive and active systems. The left column illustrates the average spectra of pure ice and ice with oil underneath. The right column illustrates the two sizes of training data and colour representation of the Support Vector Machine classification result.

	Average Spectra	Classification result			
Passive system		Training data		Classification result	
		Ice	Ice & Oil		
Passive system		Low amount of training data (~5%)			
		Medium amount of training data (~25%)			
Active system (NIR)		Training data		Classification result	
		Ice	Ice & Oil		
Active system (NIR)		Near-IR region (1490-1850 nm)	Low amount of training data (~5%)		
		Medium amount of training data (~25%)			
Active system (Mid-IR)		Training data		Classification result	
		Ice	Ice & Oil		
Active system (Mid-IR)		Mid-IR region (2500-3750 nm)	Low amount of training data (~5%)		
		Medium amount of training data (~25%)			

The results obtained during this study were based on data sets acquired from a single ice container and no repeatability tests of these results were available at that point. Additionally, as mentioned above, at that stage the Firefly Imager was not ready for sub-zero temperature operation, therefore only measurements in approx. 15°C were possible. This resulted in gradual

melting of the ice during the imaging, proving to be a far from optimal arrangement. In spite of the aforementioned drawbacks, the presented data stood as very strong proof to proceed with the further study. Upon successful funding application, a 12-month feasibility study was initiated. It was completed within the framework of the ROSDAM project financed by the R&D Award from the International Tanker Owners Pollution Federation Limited (ITOPF). The following paragraphs of the current chapter encompass the work performed during this project. Some aspects of this study were described and presented to the funding body in the form of two technical reports.

4.3. ROSDAM project - Experimental setup

4.3.1. Imaging hardware arrangement

4.3.1.1. Passive system

Data acquisition with the Red Eye 1.7 camera (see Chapter 3.2.1) requires relative movement between the object and the detector, for that reason in this application it was practical to implement the movement of the camera above the static ice. Therefore, the camera was mounted on a Zolix KSA 11-200S4N linear translation stage that allowed the spatial scan. Due to the horizontal mounting of the camera, use of a gold mirror was required to acquire the data from ice containers located below the camera. Illumination was provided by one off-the-shelf 230V AC halogen reflector. The halogen lamp, as an incandescent light source, not only emits a portion of energy in the visible band of the electromagnetic spectrum, but also provides excellent illumination in the near-IR range as required by this system [9]. One of the specific requirements of this project was operation of the imaging hardware in sub-zero temperature. According to the specifications, the Red Eye 1.7 system has embedded temperature control with minimum allowed ambient temperature of -5°C , however it was tested (and confirmed with the manufacturer) that stable camera operation is available with ambient temperature dropping down to about -10°C . Therefore, no other temperature stabilisation was used for this system during the imaging. Figure 4.3 illustrates the camera and illumination used during the project.

In the course of each acquisition run, reflectance calibration was also performed to ensure that the background spectral responses of the instrument and the illumination source as well as the 'dark' current of the camera were captured in the data set. Consequently, these parameters could be used to calibrate the data before subsequent analysis.

4.3.1.2. Active system

The active Firefly IR Imager (see Chapter 3.2), in contrast to the passive system, does not require relative movement nor external illumination. However, it is not equipped with any temperature control and its operating ambient temperature is limited to the range of +15°C to +30°C (according to specifications). For the purpose of this project, an additional enclosure was prepared with insulated walls and heating elements provided to assure the operating temperature during the test stayed within the specified range for this equipment. The temperature was monitored and controlled in range of +20°C to +25°C.

The scanning mirrors embedded in the structure of the imager are designed to acquire the data horizontally to the imager. For this project, similar to the passive system, the use of an additional gold mirror was required to deflect the scanning beam and collect the data from the ice containers located below the camera. Figure 4.3 illustrates the camera enclosed within the insulation box used during the tests.



Figure 4.3. Firefly IR Imager in thermal enclosure (on left) and Red Eye 1.7 camera mounted on the translation stage with halogen illumination (on right) in the testing setup.

4.3.2. Ice growth and control

The experimental part of the work was conducted in two locations. The main part of the work was done in the cold room made available at the Scottish Association for Marine Science while small sample tests were done on the premises of the University of Strathclyde and are described in Section 4.6.2 of this chapter. For the experiments in the cold room, the ice samples were grown in four cylindrical containers (height: 62cm, diameter: 40cm). All of them were insulated from the bottom and the sides to assure ice growth from the top of the container, simulating the natural ice growth process (see Figure 4.4 (a)). Each container was equipped with

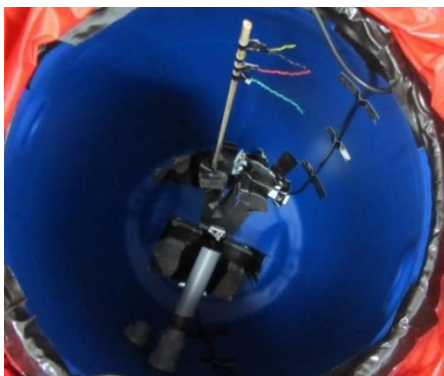
a waterproof RGB camera and height indicators as illustrated in Figure 4.4 (b). Use of this system allowed monitoring of the ice thickness during its growth and assessing the time intervals required between subsequent testing runs. The containers placed in the cold room were filled with sea water obtained from the Scottish shore (~ 30 psu) (see Figure 4.4 (c)).

The cold room used for this experiment allowed for control and monitoring of the temperature during the tests. Throughout the ice growth phase, the temperature was set for -30°C (actual temperature readings indicated approximately -25°C) while the temperature during the measurements was initially set for -5°C . Due to the complexity of the test schedule and necessity for multiple entries to the cold room, the temperature was oscillating between -5°C and $+1^{\circ}\text{C}$ during the imaging process. To mitigate this temperature rise, the cold room setting was changed for -10°C in later stage of the experiment. Although the temperature oscillations were still present during data acquisition, the average temperature did not rise above -5°C .

a)



b)



c)

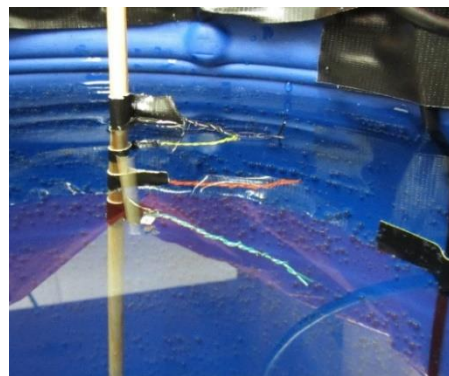


Figure 4.4. Insulated containers: used as ice tanks during the experiment (a), with underwater camera thickness indicators and oil injection piping (b), filled with sea water (c).

Within this project two ice growth modalities were explored. In an earlier stage of the test an ice layer attached to the container was grown (Figure 4.5. (a)), while during the later stage the approach of free floating ice was also developed (Figure 4.5 (b)). To achieve this system, the

edges of the ice samples were periodically cut and removed during the ice growing process, leaving a thick central part of the ice layer and very thin ice formed at the edges. The thin edge sections from the final growth were removed during the imaging process to assure free floating ice before oil injections.

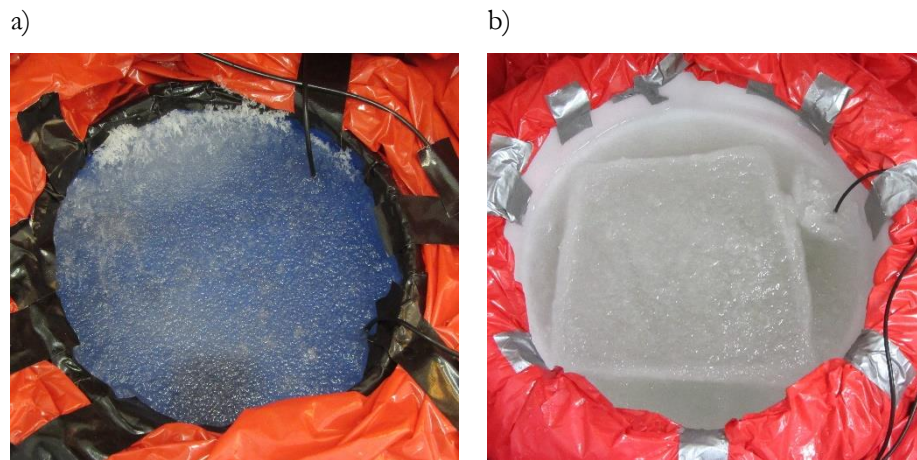


Figure 4.5. Ice formations: fully filling the container and attached to its wall (a), with thinner edges and thick middle part prepared for free floating ice (b).

4.3.3. Oil injection and monitoring

The containers used for ice growth were equipped with a system for oil injection underneath the ice specimens. Due to the fact that at the initial stage of presented work the grown ice was attached to the walls of the container, a pipe was provided to inject the oil contamination which entered the container below the ice layer. Additionally, there was a second pipe provided with a valve at one end to drain any excess water.

Since there was no preferred oil injection technique developed prior to the experiment, different techniques were used in order to choose the most suitable method. In general, these techniques can be divided into 3 groups:

- a. With the ice block fixed in the container, a defined volume of the oil sample was first introduced through the oil injection pipe. This additional fluid caused the penetration of the sea water onto the surface of ice. This excess of water was then drained to eliminate the effect of ice being overflowed. Subsequently the injection pipe was flushed with part of the drained water and its excess was then drained again.
- b. With the ice piece fixed in the container, a defined volume of the water was first drained from underneath ice and then the oil specimen was introduced to fill up this volume. Upon oil introduction, the injection pipe was flushed with a fraction of water previously

drained from the container. This approach aimed in reducing the problem of the surface overflowing with water penetrating through ice. Although this minimised the problem compared to the first approach, some drainage of water after the flushing was occasionally required.

- c. Providing the free-floating ice approach, adopted in the later stage of the work, the injection of oil was performed directly from the side of the ice block with the use of elastic hose. The injection of oil in this scenario did not generate the effect of the surface overflowing as the ice sample always floated on top of the increasing volume of the fluid.

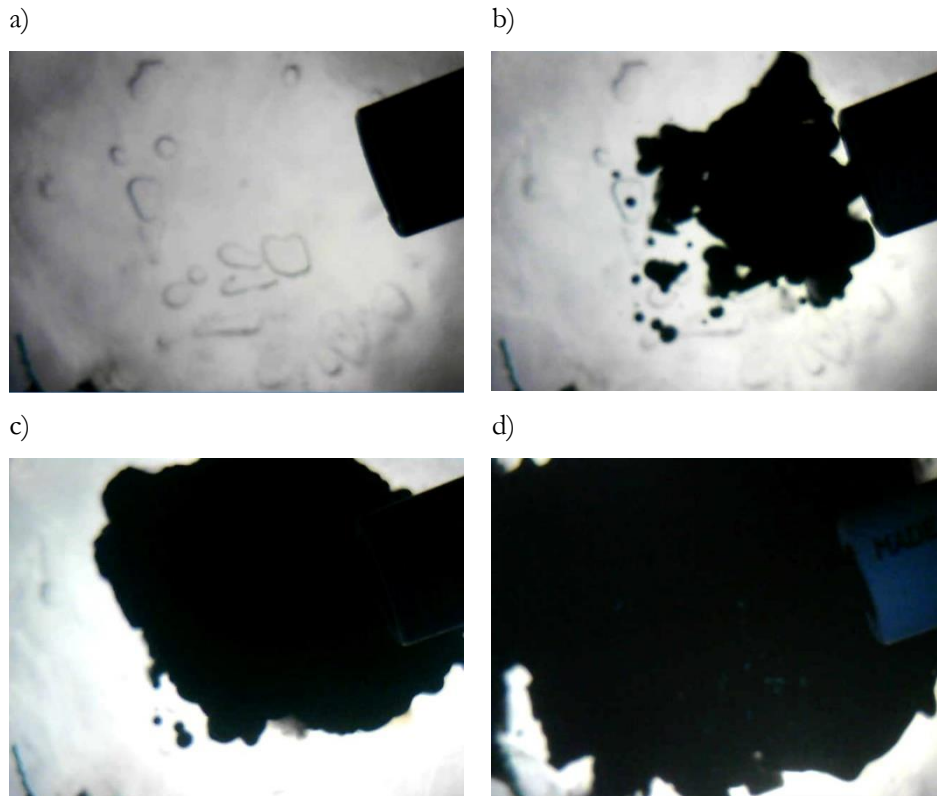


Figure 4.6. Underwater view images of one of the oil introduction cases (the case of 11cm thick ice) illustrating a situation with no oil (a) and the oil distribution in three oil thickness cases: 0.5cm (b), 1cm (c) and 2cm (d).

The ice thickness could be assessed with the help of underwater camera and prepared markers (see Figure 4.4), however the actual thickness was always confirmed after experiment on the block of ice removed from the container. In contrast, the thickness of the oil layer was more difficult to control. The volume of the oil sample was calculated under assumption that it would evenly fill the column of desired height across the whole surface of the container. However, early in the experiment it was observed that oil introduced under the ice specimen did not spread uniformly underneath the ice layer and as soon as it went through water and reached the ice surface, it stayed in one place. This usually caused accumulation of the oil layer in the centre of the container, and therefore also centre of the ice block. Due to the lack of a better control method,

the volume based indication of the oil amount to be injected under the ice block was maintained and the thickness value resulting from volume calculation was applied as reference description of the test cases. Figure 4.6 illustrates an example of the oil layer captured with the underwater camera across the 3 injections: 0.5cm, 1cm and 2cm of the oil thickness, in case of the 11cm thick ice. A crude oil was used as a contaminant during the whole experiment.

4.4. Background tests

4.4.1. Spectral response of water

The use of containers for ice growth results in a finite water column height beneath the ice samples. A very high absorption coefficient of water in the infrared region [10, 11] (see Figure 4.8) results in very short penetration depth, however to confirm that the signal response from the material on the bottom of the container would certainly not affect the experimental data, the spectral response of the background was verified.

To demonstrate the level of absorption, a spectral response of highly reflective material (ceramic plate) and highly absorbing material (polyethylene bucket) was obtained by direct imaging of these objects and subsequently by imaging through the layers of water. This experiment was done for both HSI systems and its arrangement of imaging is demonstrated in Figure 4.7.

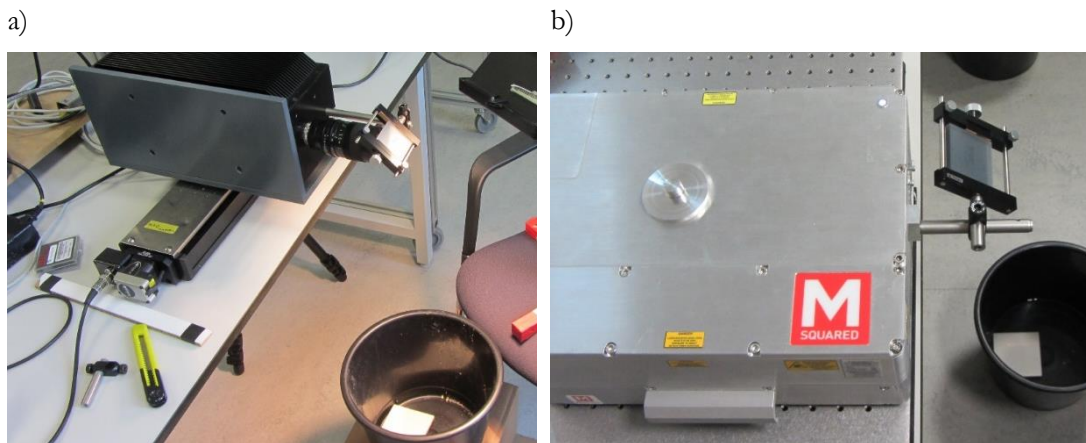
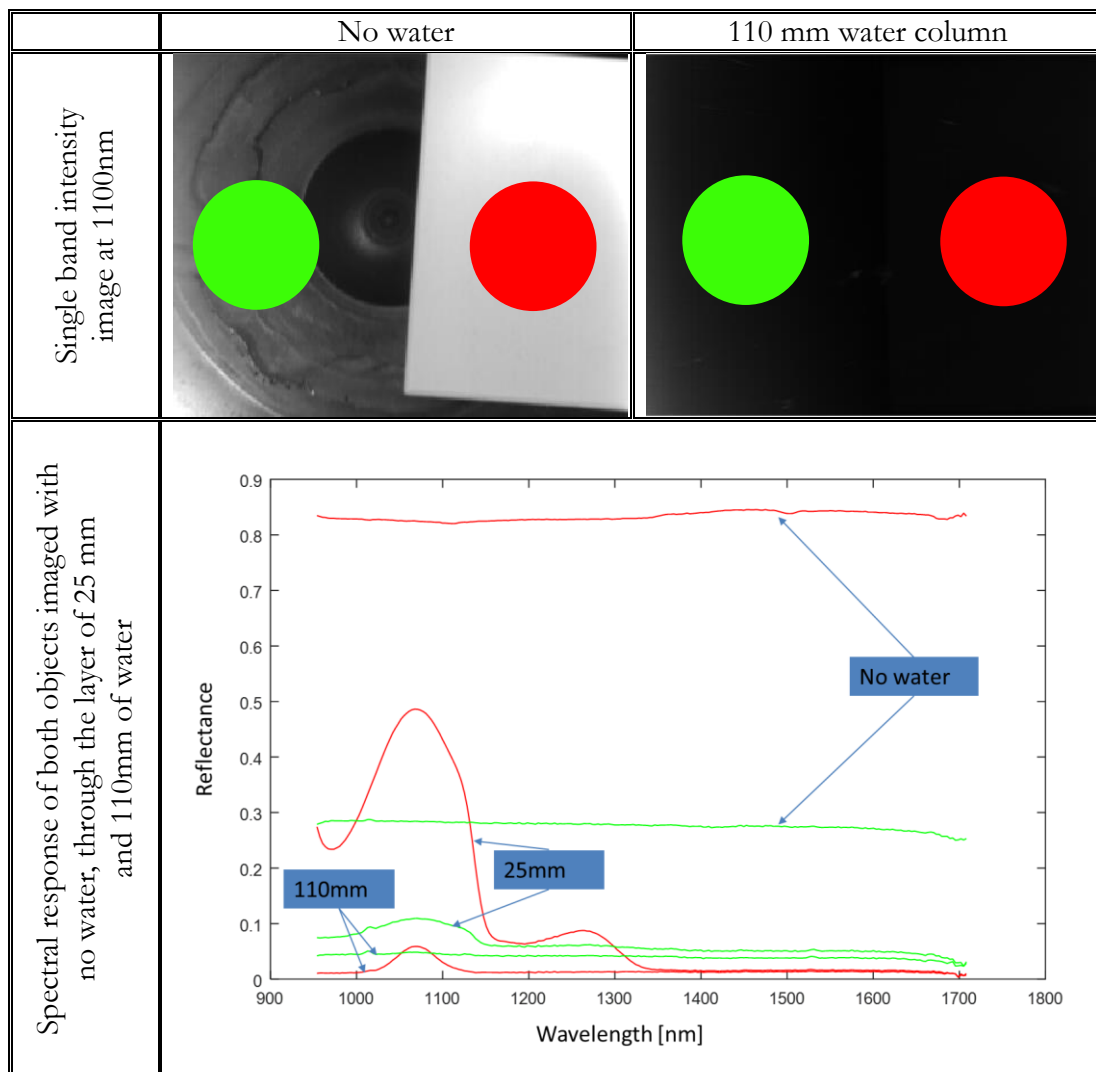


Figure 4.7. Background verification setup for imaging with (a) passive and (b) active HSI system.

The imaging results achieved with the passive system are presented in Table 4.2 while the results of imaging with active system are demonstrated in Table 4.3. It should be noted that (as introduced in Chapter 3.2.2.2), the spectra acquired with the active system are not corrected by any reference response. Therefore, these seemingly significant spectral signatures acquired through the water layer (presented in Table 4.3) are in fact only graphs of hardware determined baseline.

Table 4.2. Spectral response of highly reflective object (ceramic tile - region and graphs in red) and highly absorbing object (polyethylene bucket - region and graphs in green) imaged directly through 25 mm and 110 mm water layer.



Results of this test were corresponding to the published data of very high water absorption coefficient and very short penetration depth in this spectral region [10, 11]. As expected (see Figure 4.8), the penetration depth of water was the highest in the bands of Near-IR closest to visible range and it dropped significantly towards longer wavelengths. It was observed that the water column height beyond 110 mm can be sufficient to eliminate any risk of the background impact during imaging in Near-IR region. The penetration depth of Mid-IR radiation dropped down to micrometre scale of water layer and in line with expectations, the acquired spectra demonstrated only hardware baseline. For practical reasons and in agreement with presented above results, it was decided that a water column beneath the ice block of approximately 1m is sufficient in order to avoid any impact of the materials placed under water.

Table 4.3. Spectral response of highly reflective object (ceramic tile – red region and graphs) and highly absorbing object (polyethylene bucket – green region and graphs) imaged directly and through 40 mm water layer. The spectra presented here are not corrected by any reference response. The seemingly significant spectral signatures acquired through the water layer are, in fact, only graphs of hardware determined baseline.

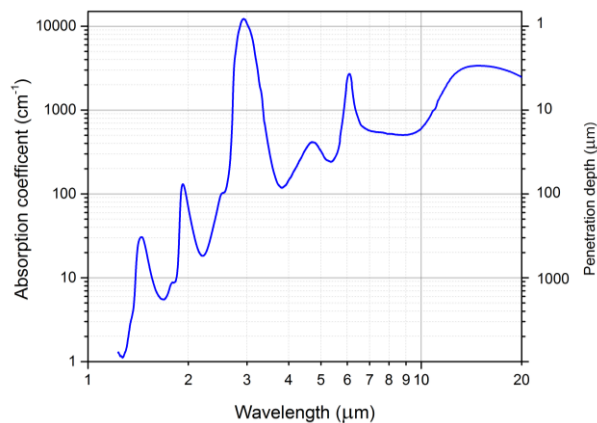
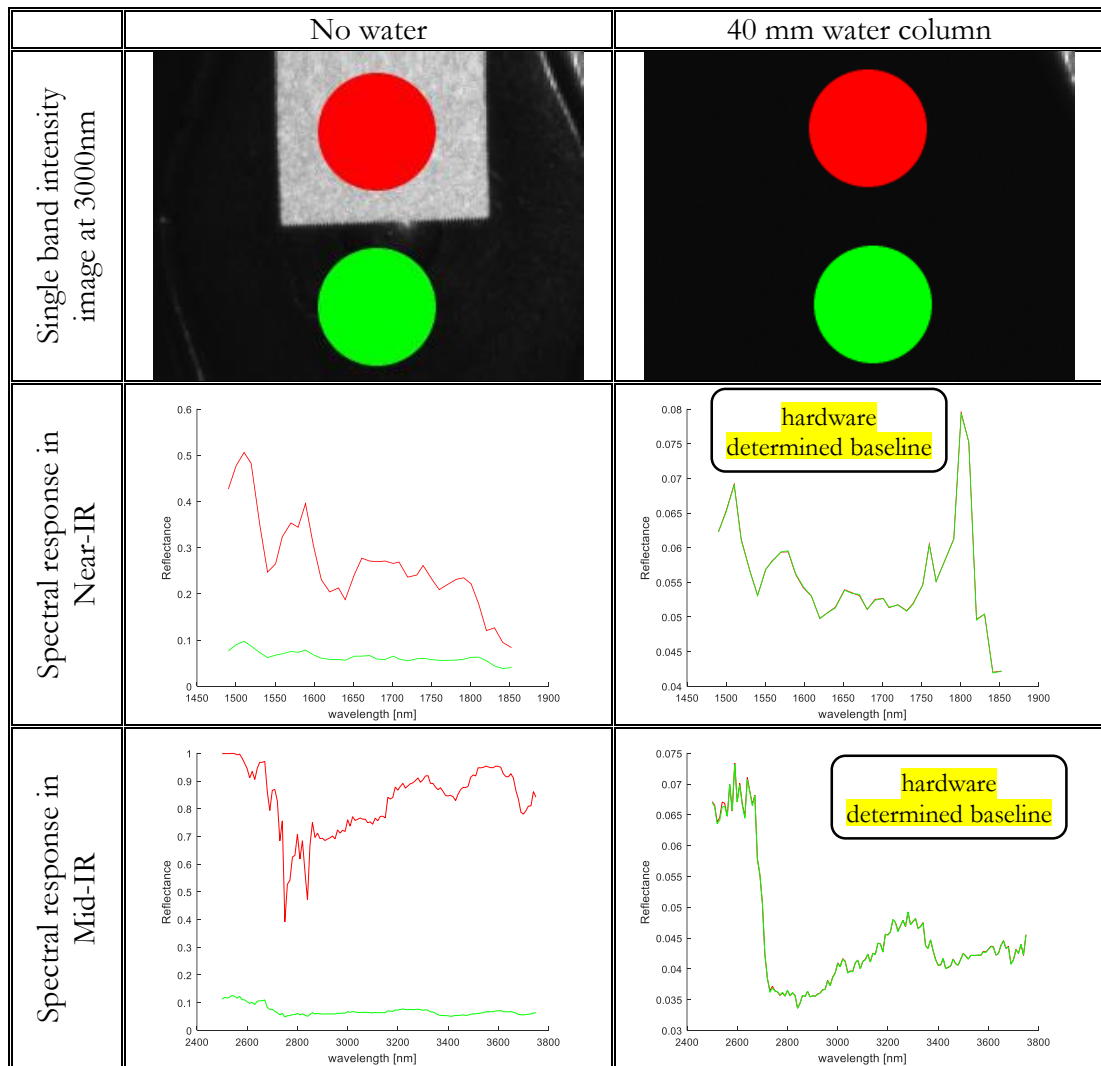


Figure 4.8. Absorption coefficient of water and matching penetration depth in the infrared region, based on the data from [11].

4.4.2. Spectral response of crude oil

During the experiment, a spectral signature of the crude oil was also captured with both employed imaging systems. Figure 4.9 illustrates the spectral response extracted from this data. It may be observed that although the data captured in Near-IR range (with both imaging systems) demonstrate a spectral signature, the spectrum acquired in Mid-IR represents only a hardware base line as the whole irradiated illumination was absorbed by oil and no reflectance response was measured.

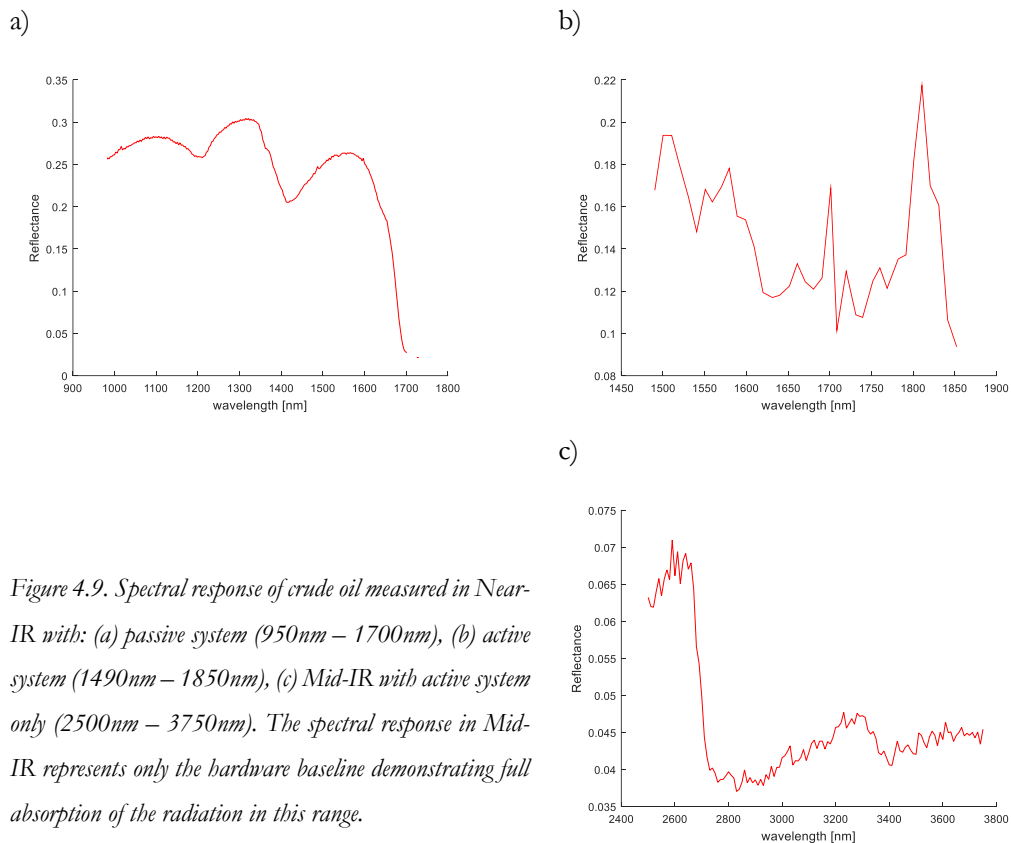


Figure 4.9. Spectral response of crude oil measured in Near-IR with: (a) passive system (950nm – 1700nm), (b) active system (1490nm – 1850nm), (c) Mid-IR with active system only (2500nm – 3750nm). The spectral response in Mid-IR represents only the hardware baseline demonstrating full absorption of the radiation in this range.

The choice of using the hyperspectral imager operating in Mid-IR range was greatly driven by the expectation of strong absorption features from the crude oil. Nevertheless, in result, total absorption was observed through the whole Mid-IR spectral bandwidth of the imager. Due to these facts, in combination with very high absorption of water, the chances to succeed in getting meaningful results were not high. However, counterintuitively the results of imaging with the active system provided surprising and initially promising results (see Section 4.6.1.5).

4.4.3. Refractive index considerations

As demonstrated in the two above sections, the absorption of light by all the substances of interest (sea water, sea ice and crude oil) is very high and use of reflectance spectroscopy could be potentially justified by the favourable reflectance conditions created on the interface between

these media. The refractive index of sea water at 589nm is approximately 1.338 (varies with the water temperature and salinity) [12, 13], for ice in temperatures -2°C to -32°C the refractive index changes in a range 1.341 – 1.397 [14], while the refractive index for crude oils varies with temperature between 1.453- 1.438 for light oils in 20 °C to 60°C and 1.667 – 1.640 for heavy oils in the same temperature region [15]. Additional effects could be brought by the fact that the refractive indices of water and ice are wavelength dependant and vary significantly across the operational bandwidth of the Firefly Imager – from 1.142 for the radiation at 2800nm up to 1.483 for the radiation at 3150nm [10]. Based on these values, the reflectance values on the interface sea ice – sea water and sea ice – crude oil can be derived with the Fresnel equations. For this consideration the reflection at normal incidence was calculated based on Formula 4.1,

$$R = \left| \frac{n_1 - n_2}{n_1 + n_2} \right|^2 \quad (4.1)$$

where the reflectance R depends on the relation between the refractive indices n_1 and n_2 of the two media creating the interface. For the sea ice – sea water interface the reflectance is approximately 0.046% while for the sea ice – crude oil interface it changes to range between 0.039% and 0.77%, depending on the oil type and environmental conditions. This change in reflectance was considered as a potential source of significant difference in the radiation reflected towards the detector from the spilled oil as compared to the sea water beneath the ice. At this stage it is also important to recall (as explained in Chapter 3) that only the data from the passive system is calibrated (and therefore can be referred to the physical properties of measured objects), while the one from active system, due to lack of proper calibration method, represents merely normalised radiation reflected toward the detector. All the reflectance graphs presented in this chapter follow this approach and should be read appropriately.

4.5. Imaging challenges and data extraction

Apart of the challenges caused by the temperature control, the growth of ice and oil injections, the imaging of ice with the two available systems faced additional challenges that resulted in a specific data analysis approach.

As described in Section 4.3.1.1, to provide relative movement between the object (ice) and the detector, the passive system was horizontally mounted on the translation stage. To allow observation of ice, a gold mirror was mounted on the camera (as can be observed in Figures 4.3. and 4.7.). The combination of this mirror with the short focal depth lens system, used as fore optics of the camera, resulted in difficulties to obtain a focused image of the full scene.

Compromising between the practicality of the experimental setup and image quality, only about half of the scene was set in focus (middle part) while other half (side edges) were blurred. Due to this fact, the data analysis was restricted to the parts of the image where the focus was obtained and the spectral information was extracted from these parts only. Figure 4.10 (a) demonstrates an example of the single band intensity image (at 1300nm) of ice with a rectangle indicating region of the image used for data extraction.

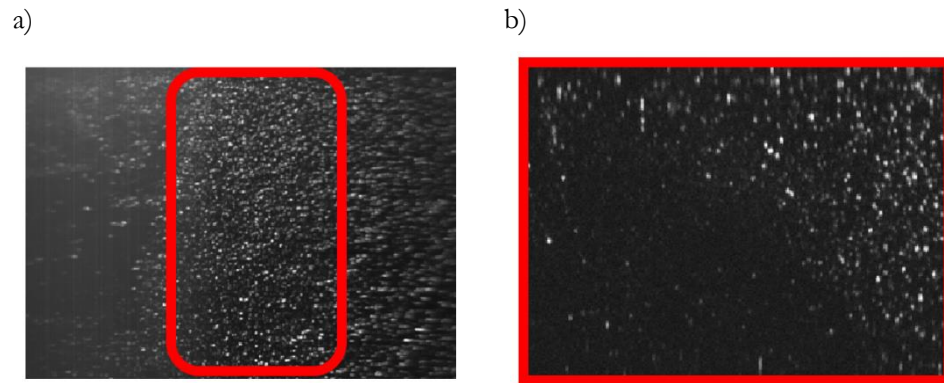


Figure 4.10. Single band intensity picture of ice imaged with passive system (a) and with active system (b) and their respective regions for spectral data extraction (red frame).

Imaging with the active system also required use of the mirror, however as this is a laser-based device, this approach did not cause any focusing difficulties. Yet, as a more fundamental problem, the active laser-based nature of this system introduced another imaging artefact that had direct impact on the data analysis. Due to the single-point scanning and detection used in this arrangement, acquired images showed intensity variations in the spatial domain. This phenomenon is directly related to the Bidirectional Reflectance [16] and it is a physical characteristic of this system. Moreover, it introduces regions of the image with significantly varying intensity, despite these having no physical differences observed in the imaged object. Figure 4.11 (a) illustrates a single band intensity image (at 3000nm) of the ice sample and Figure 4.11 (b) presents the colour coding for 5 regions of this image. Figures 4.11 (c) and (d) illustrate averaged spectra extracted from these regions (maintaining the colour coding) in Near-IR and Mid-IR bands of the imager respectively.

In view of the results described above, it was decided that at this stage of the project, the spectral data will be extracted and averaged over the whole acquired image (providing that the whole image represents one scene – only pure ice or only ice contaminated with oil) - see Figure 4.10 b).

Imaging of ice brings an additional challenge independent from the data acquisition technique. As presented in Figures 4.10 and 4.11, the images of ice are composed of pixels of very low signal (dark spots) and pixels of very high signal (bright spots) next to each other. This is

caused by crystalline structure of ice, trapped air bubbles, discontinuities and other imperfection, that in a highly specular way reflect the incident radiation in various directions. This generates data points of highly varying intensity representing the same object. For the duration of the project it was decided to deal with this feature by averaging over a region of neighbouring pixels (for spatially small objects) or by averaging over a large surface of the image to get the statistical representation of the spectrum.

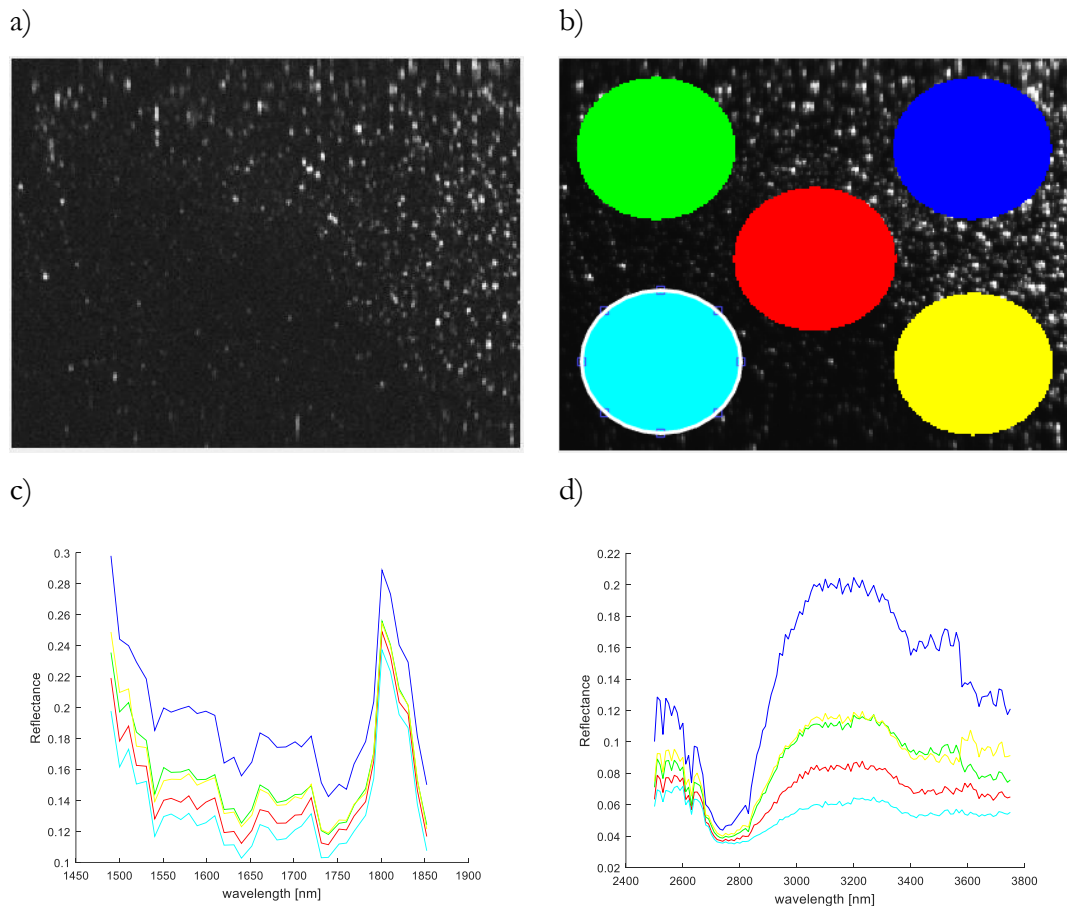


Figure 4.11. Single band intensity image (at 3000nm) of ice (a) and colour coding for 5 regions of this image (b), average spectra extracted from illustrated regions in Near-IR band (c) and Mid-IR band (d).

4.6. Experimental work

4.6.1. First full scale test

4.6.1.1. Test schedule

The data acquisition during the test was divided into two sessions. This was caused by an observation made throughout the first experimental run when beneath the main layer of ice, there was an ice formation in the water column suggesting insufficient insulation of the containers. It

was observed that the ice formation affected the oil injection and distribution process. Figure 4.12 illustrates the ice particles formed in water under the main ice structure that were stuck to the bottom surface of ice. The first part of data acquisition was done with this ice block, however before thicker ice was grown, the test was reset – whole ice was melted and the ice tanks were re-insulated allowing proper ice formation in the later part of the test.

Having the experience from the proof of concept study (HIDE experiment – see section 4.2), it was expected that the imaging process (especially the irradiation of ice with the laser) may affect the ice structure. To avoid this matter, the experiment was performed in ice maintaining temperature (see section 4.3.2), however to assure that the imaging process does not have any impact on the collected data, a verification run was performed. It was done by imaging one ice container with pure ice only following the same schedule (time intervals) as for another ice container that was imaged in parallel with all the oil injections scenarios. Table 4.4 illustrates a record of this data acquisition run.



Figure 4.12. Ice formation stuck to the bottom surface of the main ice layer – view of the bottom of the ice block cut out from the contained after imaging.

The results of the first imaging run helped to verify that the imaging process does not affect the analysed ice samples. Having this confirmation, the second session was focused on data acquisition for the ice - oil thickness relationship matrix (demonstrated in Table 4.4). It should be noted that for each element from the schedules presented in Table 4.4, the image was captured with both HSI systems. Additionally, the description of ice thickness was made based on actual thickness as measured at the end of data acquisition. The oil thickness descriptions are based on the total oil layer thickness, assuming the ideal oil under ice distribution upon injection of specified oil volume (see Section 4.3.3).

Table 4.4. Test schedule of two data acquisition runs of first full scale test.

First imaging session		Second imaging session		
4cm ice	4cm ice	3cm ice	7cm ice	11cm ice
Pure ice	Pure ice (1 st scan)	Pure ice	Pure ice	Pure ice
0.5cm oil	Pure ice (2 nd scan)	0.5cm oil	0.5cm oil	0.5cm oil
1cm oil	Pure ice (3 rd scan)	1cm oil	1cm oil	1cm oil
		2cm oil	2cm oil	2cm oil

The nomenclature presented in the Table 4.4 above will be used in the description of the results obtained in the following section.

4.6.1.2. Passive system results - first imaging run

The first session resulted in 2 data sets: (I) verification of the imaging impact on the spectral response of pure ice and (II) spectral response of 4cm ice layer without and with oil underneath. Figure 4.13 illustrates the colour coding and spectral response of pure ice scanned repeatedly (three times) in one of the ice containers (described as T3) and it is placed together with the spectral response of the pure ice measured in another container (described as T1). Figure 4.14 illustrates the colour coding and spectral response of pure ice and two scenarios with oil injected underneath (0.5cm and 1cm). As indicated in Figure 4.13, the spectral response of the pure ice from the same container was reproduced twice as identical, however third scan resulted in spectrum of similar shape, but with increased signal intensity. Although there was no specific reason found to explain this occurring, it is expected that a change in the illumination could generate it. In the same figure it can be seen that the spectral signature of the ice samples from two different containers varied significantly. There was no specific factor detected in order to explain why this variation would have to take place. Hence at that stage of experiments the quality of ice (imperfect insulation, as explained in Section 4.6.1.1) was suspected to be a potential root cause. Comparison of the pure ice spectrum with the spectra of oil under ice scenarios illustrated in Figure 4.14, demonstrates perplexing results, where no clear correlation could be found. Due to known issue with the ice condition, no further analysis was made at this stage and the test was repeated in Second imaging run.

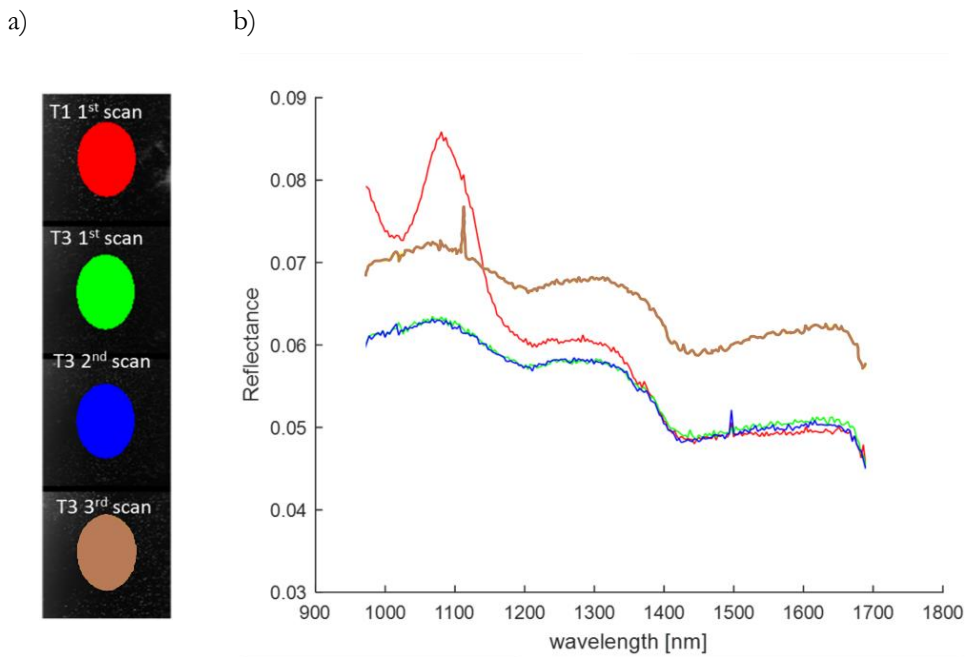


Figure 4.13. Colour coding (a) and averaged spectral response (b) of 4cm pure ice layer, extracted from the data acquired with passive system.

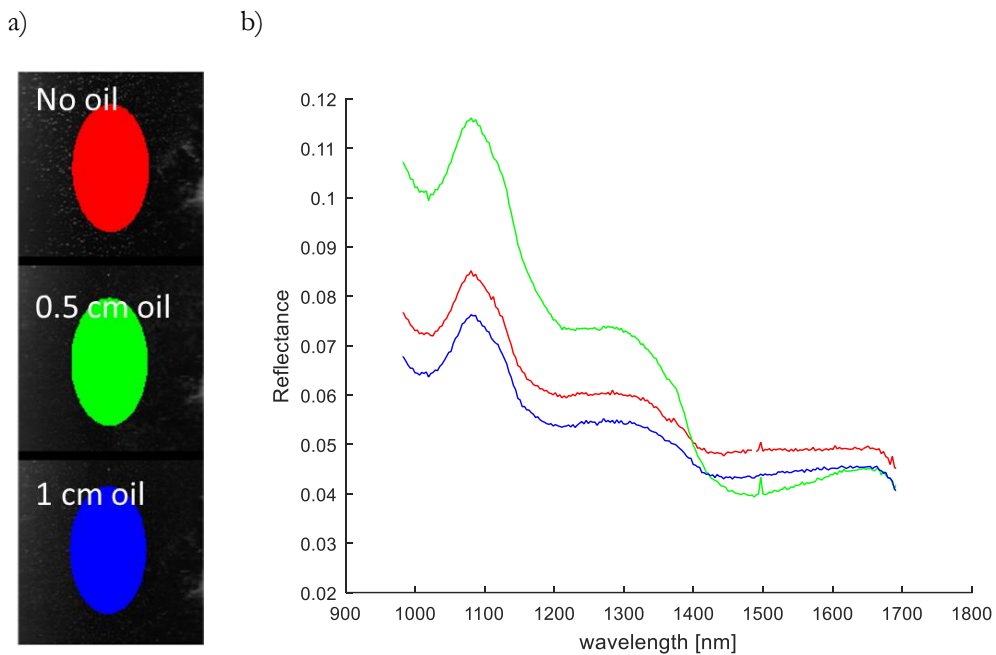


Figure 4.14. Colour coding (a) and averaged spectral response (b) of 4cm ice layer without and with oil injections underneath, extracted from the data acquired with passive system.

4.6.1.3. Passive system results - Second imaging run

As indicated in Section 4.6.1.1, the second imaging session was focused on the acquisition of spectral data with respect to different ice and oil layer thicknesses (data set graphically presented

in Figure 4.16). Moreover, a comparison of the pure ice spectra from three different containers, each holding ice of different thicknesses, is presented in Figure 4.15.

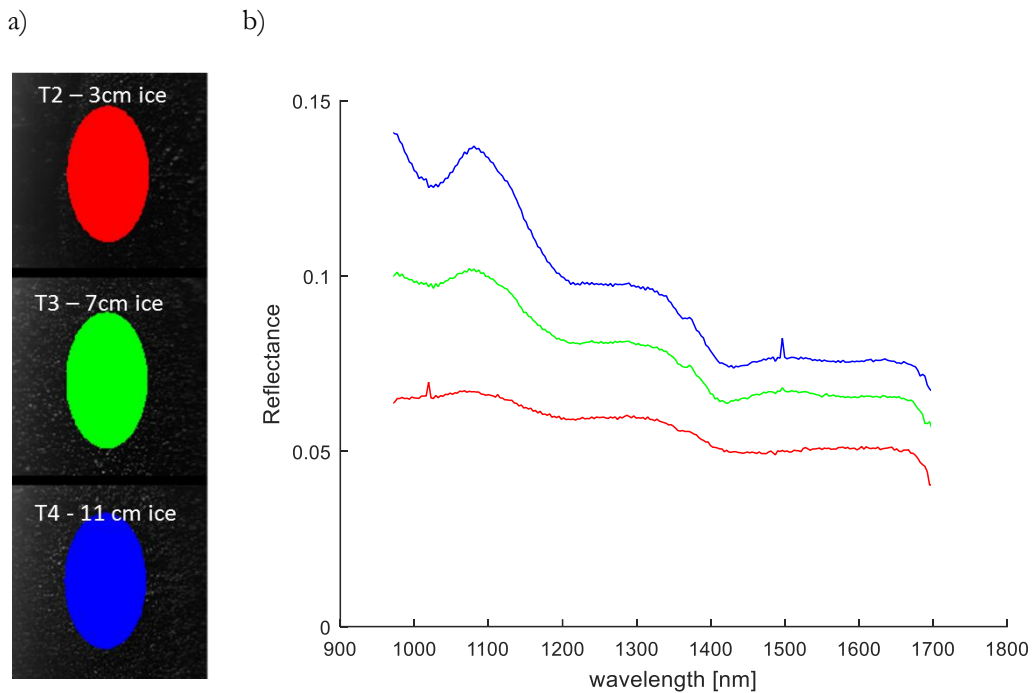


Figure 4.15. Colour coding (a) and averaged spectral response (b) of 3cm, 7cm and 11cm pure ice layers, extracted from the data acquired with passive system.

It was observed that the spectral signature of pure ice grown in all analysed containers varied in predictable manner, maintaining similar features but increasing in signal intensity with the elevation of ice thickness (see Figure 4.15). This gradual raise of the signal strength may be explained by incremented depth of material (ice), where more specular reflections take place, intensifying the amount of signal reflected towards the detector.

Analysis of the spectral response in the oil versus ice thickness was very difficult and eventually it was assessed that there is no consistency in the acquired data (see Figure 4.16). Similar to the pure ice spectra, the signal intensity of all the cases was increasing together with the higher ice thickness, which was considered as an expected result, however the relationship between data from analyses of pure ice and ice with oil underneath it could not be found. In each ice thickness scenario, the intensity of the spectra varied randomly - no specific relationship was found. From the perspective of finished project and final conclusions being known, it is understood that although a considerable effort was made to keep the illumination repeatable, the observed spectra possibly were caused by random amount of specular reflections from the ice surface. Therefore, it was decided that analyses with the passive system producing inconsistent data sets should be eliminated from further studies.

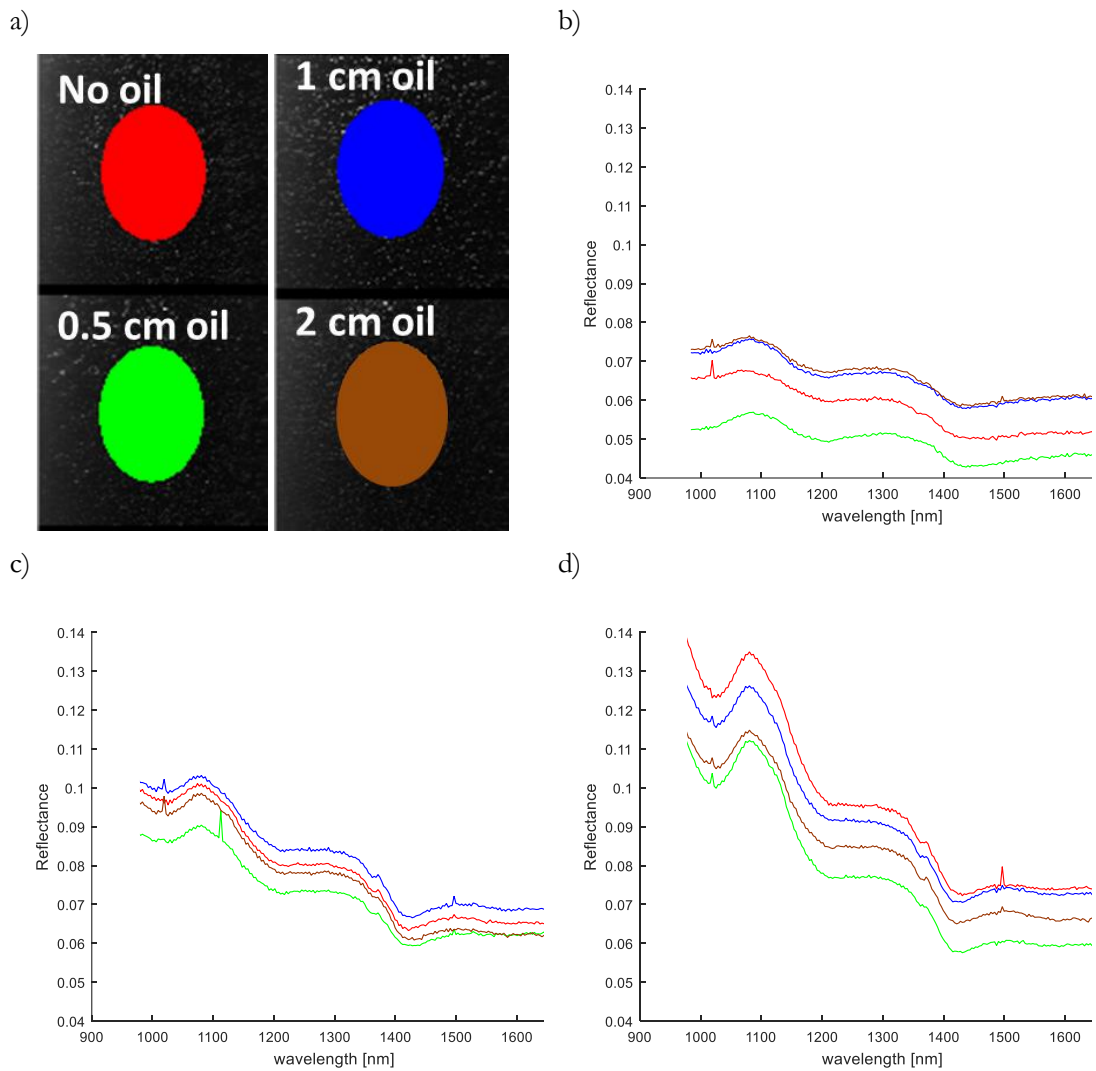


Figure 4.16. Colour coding (a) and averaged spectral response of 3cm (b), 7cm (c) and 11cm (d) ice layers without and with oil injections underneath, extracted from the data acquired with passive system.

4.6.1.4. Active system results – first imaging run

As presented in Section 4.6.1.2, the first experimental session resulted in 2 data sets – (I) verification of the imaging impact on the spectral response of pure ice and (II) spectral response of 4cm ice layer without and with oil underneath. Figure 4.17 illustrates the colour coding and spectral response of pure ice scanned twice in one of the ice containers (described as T3). These data are placed together with the spectral response of the pure ice measured in another container (described as T1). Although the ice sample in container T3 was scanned three times (similar as with passive system) the data from the first scan were discarded from the analysis, as it was noticed after the records were collected that the imaging was performed with a not stable laser system. The lack of laser stabilisation resulted in severe intensity variations revealed in the acquired

spectral signature. This data set was omitted and special attention was made to ensure enough stabilisation time before any subsequent imaging experiments. Figure 4.18 illustrates the colour coding and spectral response of pure ice and two scenarios with oil injected underneath (0.5cm and 1cm).

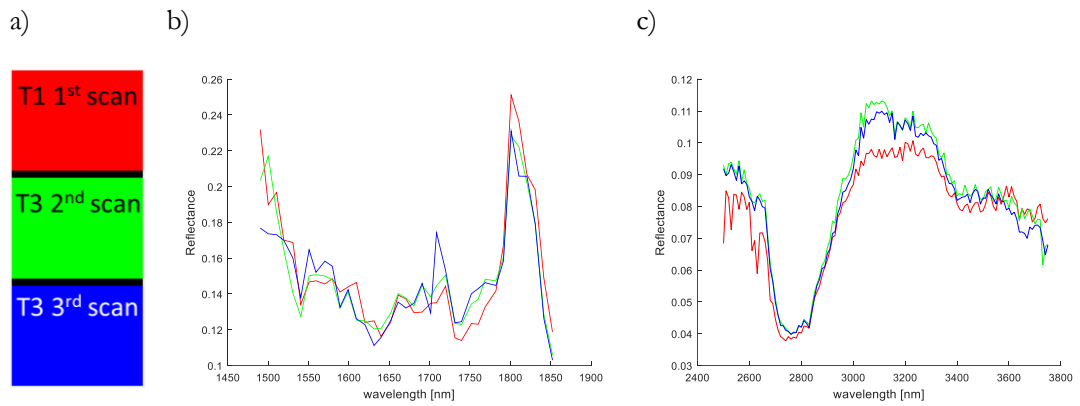


Figure 4.17. Colour coding (a) and averaged spectral response of 4cm pure ice layer in Near-IR (b) and Mid-IR (c) spectral region, extracted from the data acquired with active system.

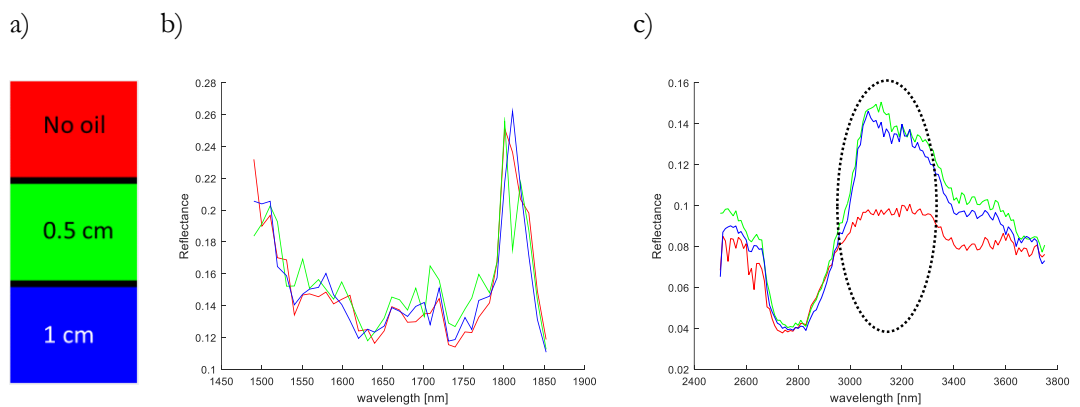


Figure 4.18. Colour coding (a) and averaged spectral response of 4cm ice layer without and with oil injections underneath, in Near-IR (b) and Mid-IR (c) spectral region, extracted from the data acquired with active system.

As presented in Figure 4.17, there was no significant difference in spectral signature of pure ice in repeated measurements. Noticeable difference in the spectral response of Mid-IR range was detected between ice samples from two different containers, however it was not considered as important when compared with the spectra presented in Figure 4.18. No significant alteration was observed in the Near-IR range. An outstanding spectral difference was detected in the Mid-IR region between pure ice and both oil under ice scenarios (see region marked by dashed ellipse on in Figure 4.18 (c)). Initially it was believed that these spectral differences were caused by the presence of the oil sample underneath the ice block and that, if reproducible in other experiments with ice, could be a significant feature to differentiate between the two cases. Similar to the pure

ice comparison, no major differences in pure ice and oil conditions were observed in the Near-IR band.

4.6.1.5. Active system results – second imaging run

In a similar way to the approach described in Section 4.6.1.3., two sets of results from this imaging session are presented below. Figure 4.19 shows the comparison of pure ice spectra extracted from the dataset of all analysed ice thicknesses while Table 4.5 demonstrates the results of the tests with varying ice and oil layers' thicknesses.

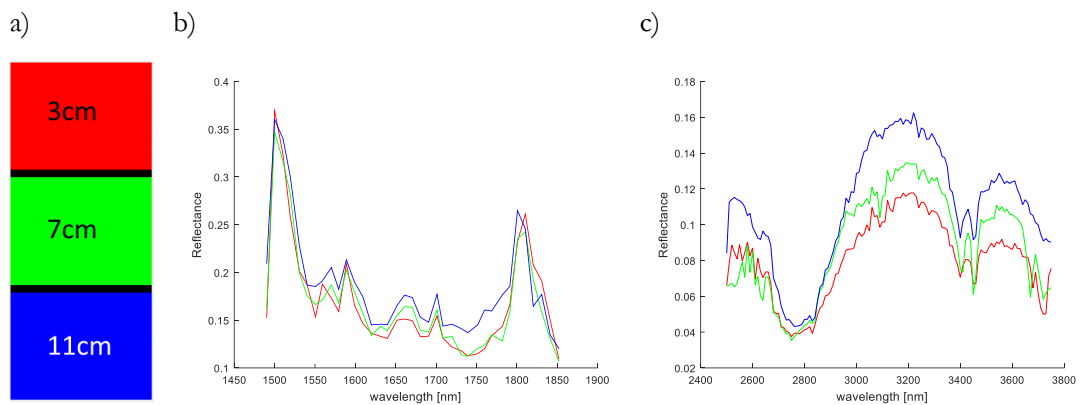
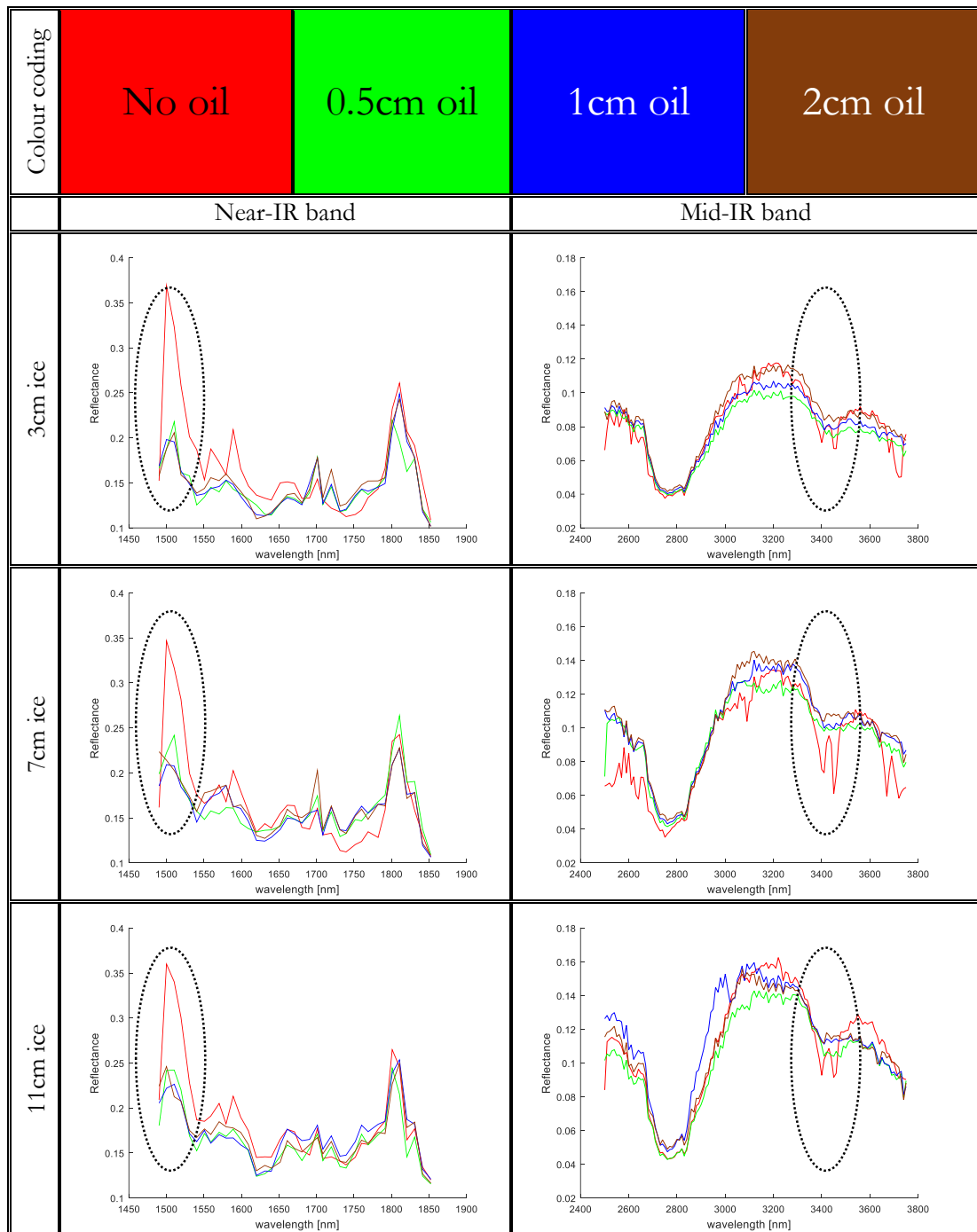


Figure 4.19. Colour coding (a) and averaged spectral response of 3cm, 7cm and 11cm pure ice layers, in Near-IR (b) and Mid-IR (c) spectral region, extracted from the data acquired with active system.

There was no significant change observed in spectral signature of pure ice in Near-IR region, regardless of the ice thickness. The spectral response in the Mid-IR range was similar to the one observed with the NIR passive system. The intensity of the spectral signature, at selected bands, increased as the ice layer thickness increased (see Figure 4.19). For the results from the passive system this behaviour was understandable, as light on shorter wavelengths penetrates ice to some extent and its thickness could potentially increase the amount of specular reflections. During the course of the project the same occurrence was observed, however from the perspective of the completed study it was found that the radiation did not penetrate analysed ice completely and the results for longer wavelengths could not be explained by the same principle. It is considered that different ice surface roughness was affecting the level of reflected signal and its increasing trend with the greater ice thickness was a coincidence. However, since this phenomenon was not taking place in the Near-IR range, no unequivocal explanation was found for this observation.

Table 4.5. Colour coding and averaged spectral response of 3cm, 7cm and 11cm ice layers without and with oil injections underneath, in Near-IR and Mid-IR spectral region, extracted from the data acquired with active system. Dotted ellipses highlight spectral features of interest for oil under ice identification.



A comparison of pure ice spectra with the one containing oil underneath, acquired during this imaging run, revealed two bands (one in Near-IR region and one in Mid-IR region) with significant spectral changes appearing when oil was introduced beneath ice. Within these bands it

is possible to identify specific features presented in the pure ice case that disappeared upon injection of oil – see dotted ellipses in Table 4.5. Apart from the features, there is no significant difference between the spectra of pure ice and the case with oil underneath. These results did not reproduce any of the previous measurements. During the project it was believed that it might be related to changes made in experimental conditions, since these tests were the first done with properly prepared and maintained ice structure. Based on obtained results, showing that tangible variations came from the presence of oil underneath ice and no obvious differences between spectra from varying oil thicknesses were observed, it was assumed that with this technique only the presence of oil can be identified underneath ice, but no information about its thickness could be extracted.

4.6.1.6. Automatic detection of oil beneath ice

Features demonstrated in Section 4.6.1.5 allow attempting the automatic classification between pure ice and the scenarios with oil presence underneath. As hyperspectral imaging is very powerful in detection and identification of spectral features, the whole spectrum is not always required for the classification. Occasionally, as illustrated in Table 4.5, only a narrow band is essential in order to present characteristic features. This observation leads to the simplification of a potential detection system, where the whole spectral range is not necessary. Consequently, the complexity of hardware, data storage and processing can be significantly reduced. To demonstrate the feasibility of automatic classification, a subset of only 4 bands was chosen from the whole Near-IR region (see Figure 4.20) and the classification was performed on the data set from 3cm ice thickness case (see Table 4.6).

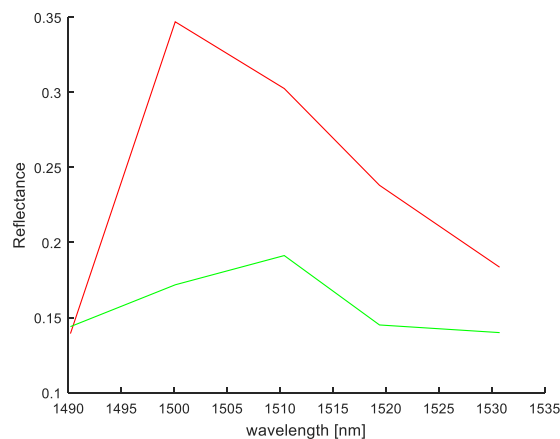




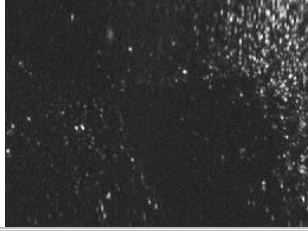
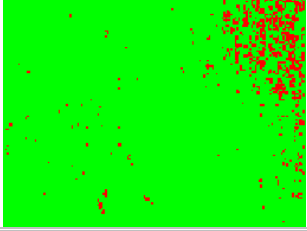

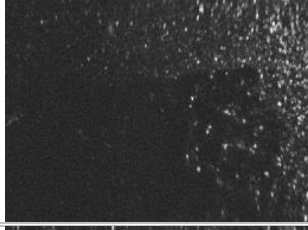
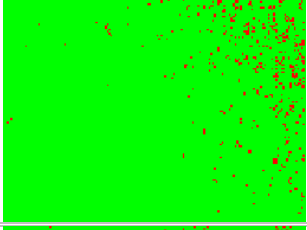
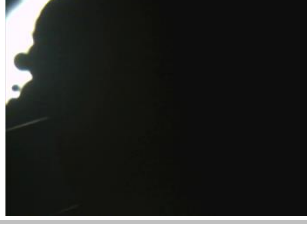
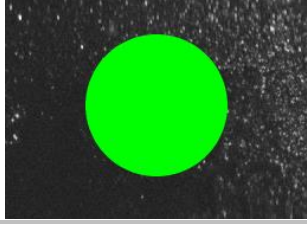
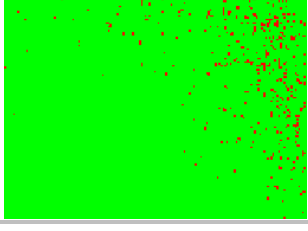


Figure 4.20. Plot of the average reflected signal, reduced to first four bands, as used for training of the classifier. These average spectra are computed based on the data extracted from no-oil (red) and 2cm oil (green) cases of 3cm ice thickness. The training area is illustrated by the circles on the intensity images in Table 4.6 (b).

The example of data from the 3cm ice thickness was chosen for this analysis due to the complicated layout of oil beneath ice. As indicated in Section 4.3.3, oil did not spread evenly beneath the ice layer upon the injection. In this case, the oil sample injected under the ice block was distributed in a form of scattered regions – see 0.5cm oil case in column (a) of Table 4.6.

This example was used to check whether the oil contamination can be distinguished from pure ice in one image. Table 4.6 (b) illustrates intensity images (at 1500nm) of all the oil cases from the 3cm ice thickness and colour circles indicate the regions where the data was extracted for training of the algorithm (average spectra from these areas are presented in Figure 4.20). For the purpose of this project, the classification algorithm was built based on the Support Vector Machine (SVM), a very robust machine learning technique for solving classification problems [17, 18, 19]. The algorithm used for this classification is contained in the LIBSVM package [20], which uses a Classification SVM Type 1 (C-SVM) and its implementation was described in Section 3.4.2.

Table 4.6. Data acquired from the 3cm ice layer test for all the oil injection conditions: (a) the underwater images of the oil distribution, (b) single band intensity images (at 1500nm) of all the test cases with indication of the regions used for training data, (c) graphical representation of the SVM based classification results.

	(a)	(b)	(c)
No oil			
0.5cm oil			
1cm oil			
2cm oil			

As demonstrated earlier in Section 4.6.1.5, there is no significant difference between the spectral responses of various oil layer thicknesses, therefore a training set of the case with oil being present was made on the 2cm oil layer data. This decision was made to ensure that there is full coverage of oil beneath ice (see 2cm oil example showed in column (a) of Table 4.6). The colours used to mark the training data represent the pixel-by-pixel classification results of all the test cases (column (c) of Table 4.6).

As mentioned in Section 4.5, the results could be affected by the strong specular nature of the dataset. A similar classification was therefore done based on spectral signatures averaged over the neighbourhood of 4x4 and 8x8 pixels. In both these cases, the results were similar to these obtained in a pixel-by-pixel basis presented in column (c) of Table 4.6.

As can be observed in column (c) of Table 4.6, the classification results of the 3cm thick ice with 0.5cm oil case did not reproduce the sparse distribution of oil spots under ice. The whole data set of this case was analysed but the spectral diversity was not observed. Following the lack of spectral repeatability between to-date performed experiments, these analyses showed an uncertainty in the validity of the results. After this observation, for the first time during the project execution, a hypothesis was made that the observed spectral changes are not caused by the presence of oil under ice, but by the process of the oil introduction performed during the experiments. The decision was made to execute a series of verification imaging runs to confirm the spectral response.

4.6.2. First small sample test - repeatability of the ice spectra

First tests of spectral response verification were done with the small ice samples allowing multiple repeats of rapid ice growth. The ice growth was performed in a laboratory freezer - Labcold Sparkfree Freezer 447L RLCF1520 (see Figure 4.21).




Figure 4.21. Experimental setup for the small sample runs of ice imaging. The two photographs depict the Firefly IR Imager next to the Labcold freezer imaging the ice sample located inside the freezer.

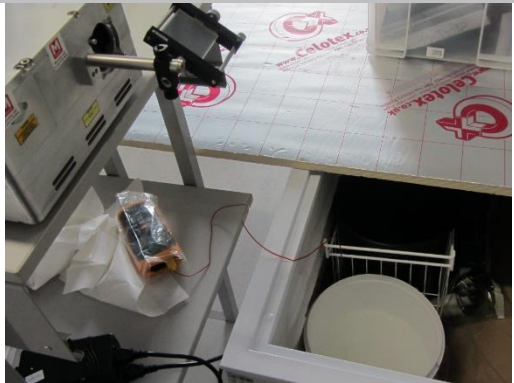
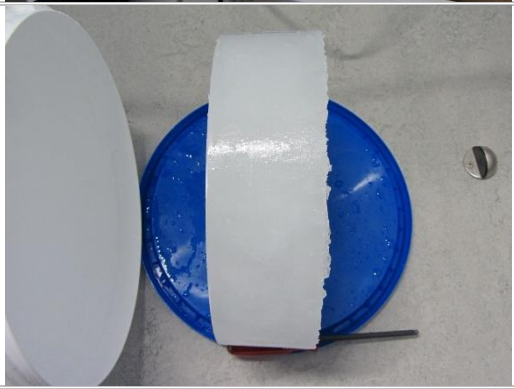

Use of this freezer provided a facility to grow ice in small cylindrical buckets (approximately 25cm base diameter, 25cm height), with operating temperature set to -20°C (actual temperature reading oscillates between -17°C and -23°C). The chest configuration of this freezer allowed not only the ice growth but also maintenance of sub-zero local ambient temperature for the duration of the imaging.

4.6.2.1. Experimental procedure

To verify the repeatability of the spectra, 5 ice samples were grown and subsequently imaged. Each time water in the bucket was changed (water was always from the same source – Scottish shore near Oban, salinity ~ 30 psu) and the growth of ice always started from water at room temperature. Additionally, to verify impact of ice handling on the reflectance spectra, the ice block was each time taken from the original bucket where it was growing, and placed in other bucket containing pre-cooled water, where it was subsequently imaged as floating ice. This approach enabled the collection of the information about spectral repeatability as well as spectral change upon modification in imaging conditions. The full procedure is presented in the Table 4.7.

Table 4.7. Experimental procedure of small sample test.

Step	Description	Photo
1	Prepare approximately 8cm of sea water in a bucket and place it in the freezer (the bucket not insulated - freezing of the whole water content).	
2	Wait until water is fully frozen (for practical reasons the freezing time was varying between each imaging - minimum freezing time of 20 hours and maximum time of 100 hours).	
3	Pour down any liquid water staying on the ice surface (it was observed that independent from the freezing time there was always few millilitres of not frozen water – it was poured away to prevent this water from absorbing the laser radiation).	
4	Using another bucket, place water in the freezer for the time of imaging of ice (approximately 30 min). Within this time water is pre-cooled to minimise the impact of warm water on ice melting during the imaging of the floating ice block. The water column height in the bucket was maintained at approximately 15cm.	

5	Image the ice specimen in the original bucket - as grown.	
6	Take the ice block from the bucket (in all cases the ice sample was extracted from the bucket in one piece – thickness of the block always maintained at approximately 8cm)	
7	Place the ice block on the surface of the pre-cooled water.	
8	Image the ice block floating on water. Due to low temperature of water and ice, the free floating ice was fixed to the bucket at the end of imaging (imaging time approximately 30 min).	

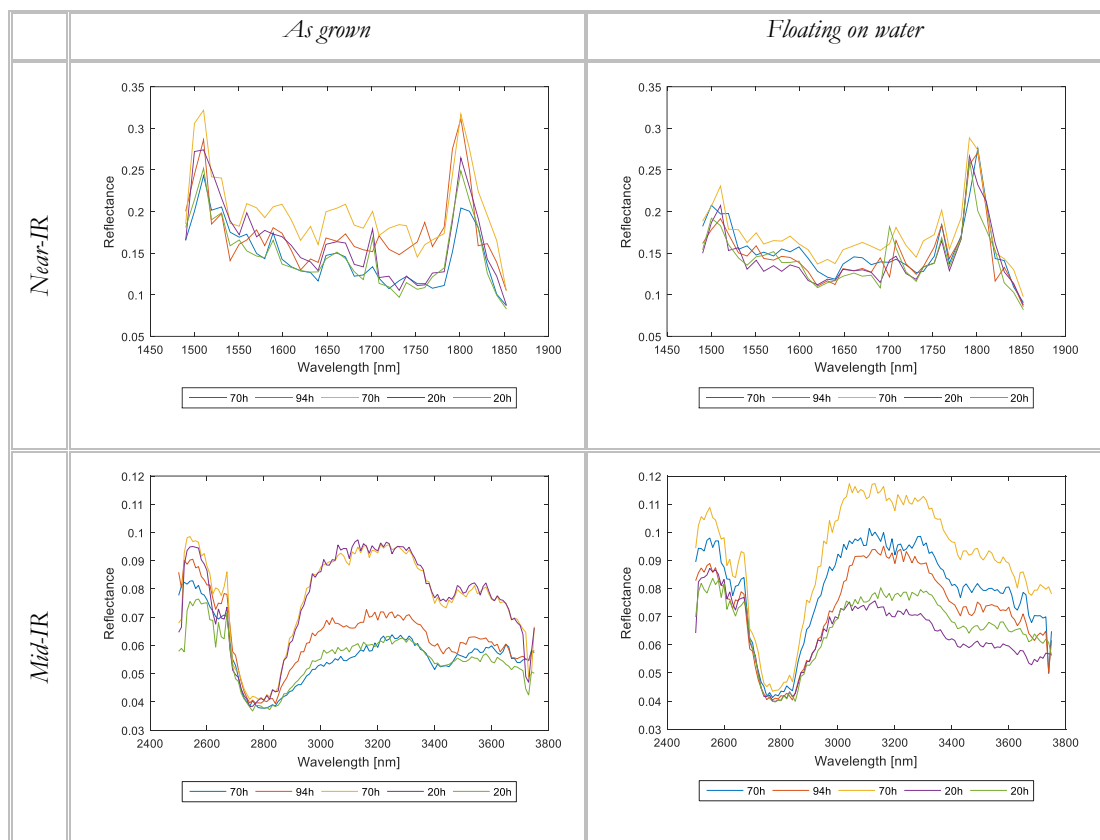
4.6.2.2. Ice spectra repeatability results

The spectral data were analysed in the same way as described in the Section 4.5 – the average spectra were extracted from the whole imaged surface of the ice samples. The Table 4.8 illustrates the data extracted from both imaging conditions: (I) as grown, fixed in the bucket and (II) floating on water) in both available spectral bands – Near-IR (1490nm – 1850nm) and Mid-IR (2500nm – 3750nm). Each spectrum corresponds to one imaged ice sample, with legend describing the freezing time of each specific ice block.

As shown in Table 4.8, there is a big variance in the intensity of the spectra between different ice growth cases. It is understood that it is caused by the structure of ice and therefore varying

amount of specular reflections, as was explained in the Section 4.5, they stand as the main carrier of the information back to the detector. This variance is much stronger in Mid-IR than in Near-IR. The ‘two-peak’ feature (at $\sim 3400\text{nm}$) observed in Mid-IR during the second session of the first full scale experiment (4.6.1.5) is not present in any repeat of the ice sample measurement. The Near-IR peak feature at 1500nm can be observed, however it is significant only on the “As grown” condition – when the ice sample was removed from the first bucket and placed on water, the peak was nearly gone. This resembles the behaviour of the spectral change observed upon the oil injection during the full scale experiment.

Table 4.8. Average spectra of the ice samples imaged in two conditions (as grown and floating on water) in both available spectral bands – Near-IR and Mid-IR. The legend of each graph demonstrates the relation between the colour coding and the freezing time of each ice block.



4.6.2.3. Impact of the ice surface condition

As presented in the section 4.6.2.1, this experiment required extracting the ice block from one container and placing it on the water surface in another one. The placement of the ice specimen on water required extra care in order to not to overflow the ice surface with water. Despite this care, in one case half of the ice block was overflowed (flooded) with water, which very quickly froze and changed the structure of the ice surface (see Figure 4.22).

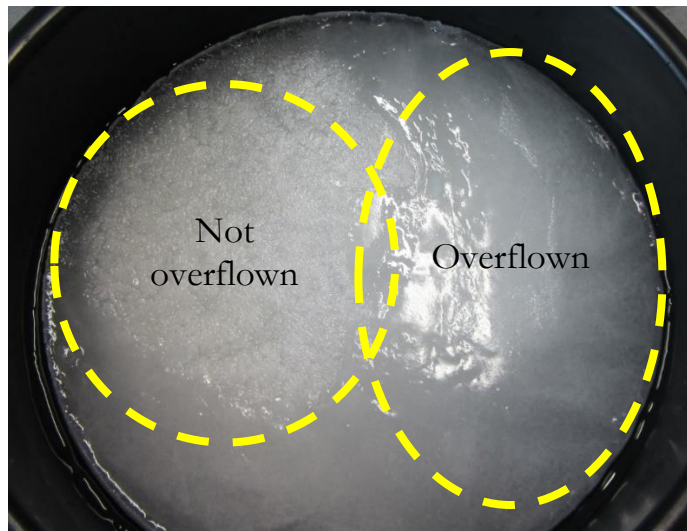
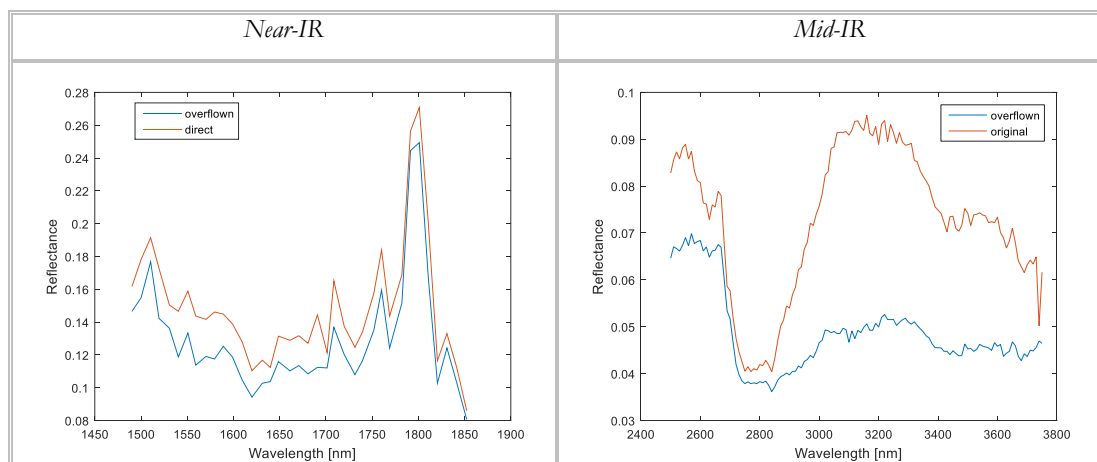


Figure 4.22. Photograph of the ice block partially overflown with water during placement for the floating ice condition. Water rapidly froze down changing the ice surface into a smooth, mirror-like structure.

For the purpose of the spectral repeatability monitoring, only the not overflown part of tested ice was included in analysis (data presented in Table 4.8), however the spectral response between the overflown and not overflown part of the analysed ice was also compared (Table 4.9).

Table 4.9. Average spectra of the ice sample floating on water with the data extracted from the original surface (red line) as well as the one changed upon overflown and freezing of water (blue line).



The ice layer created on the surface of the ice block from freezing of the overflown water is very smooth, mirror-like. The only detectable signal from this condition is the hardware baseline (for comparison see Table 4.3) which indicates that the detector could not read the signal since whole radiation was absorbed or reflected by this mirror-like surface in other direction. This example demonstrated not only the extent of the system susceptibility regarding the ice surface conditions, but also the fact that the amount of acquired signal depends fully on that. Moreover, due to this

observation, another fact was constituted suggesting that the detected signals in all the oil and ice studies came only from ice surface reflection.

4.6.2.4. Impact of the oil injection

Although this analysis was meant for testing of the ice spectra repeatability, the last ice block sample was contaminated with oil and respective spectra were acquired. In this single case an engine lubrication oil was used for the test instead of crude oil. This change was done for practical reasons only as the crude oil was stored at SAMS for all the full scale tests and the sample of lubrication oil was available after the HIDE experiment. Water surrounding the free-floating ice froze during the spectral measurements of the pure ice, fixing it in the bucket. Injection underneath this fixed ice was done by two bores prepared on two sides of the ice block (see Figure 4.23).

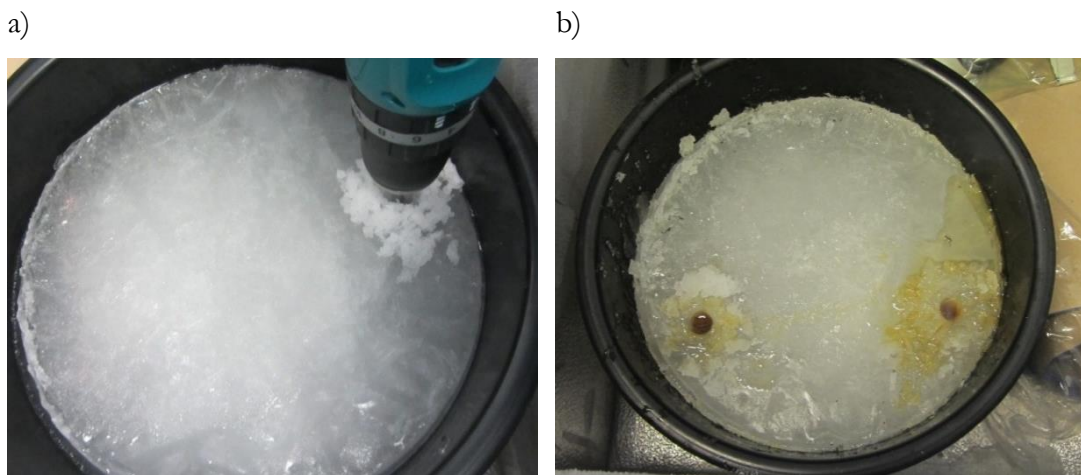


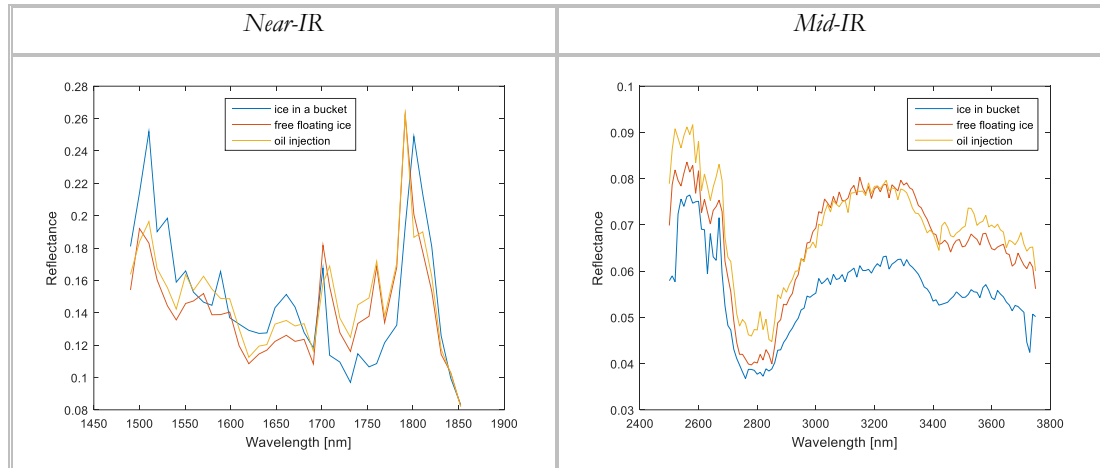
Figure 4.23. Photographs of the ice preparation for the oil introduction: a) drilling the bores b) ice block with oil introduced through the two bores, with oil spilled around the wholes during injection.

In this short experiment there was no underwater monitoring camera and the oil sample was introduced without verification of its distribution underneath the ice specimen. There was 100ml of oil introduced in total that assuming uniform distribution, would result in 2mm oil layer thickness. Providing unknown distribution of oil, the spectral profile was extracted only from the area near the two bores (but not containing any oil on the surface of the ice). Table 4.10 illustrates the average spectra of the pure ice from the last ice growth (marked with the green line on the graphs in Table 4.8) in “as grown” condition as well as the “floating on water” and compared with the spectra from the oil layer underneath the ice sample.

This test demonstrated that although there is a spectral difference in between the two measuring conditions of pure ice (“as grown” fixed in the bucket and free floating), the spectra

of the ice samples with oil underneath did not differ significantly from these acquired from pure, free-floating ice. These results point towards the same hypothesis drawn during first full scale test, that the observable spectral changes are not caused by the presence of the oil layer but instead, by the handling of ice during the experiment.

Table 4.10. Comparison of the Near-IR and Mid-IR average spectra of the ice block fixed in the bucket “as grown” (blue line), “floating on water” (red line) and the one after oil injection (yellow line).



4.6.2.5. Summary of the experiment

This test provided a set of significant results. It was observed that despite the consistency of the spectral response within one test group (as seen in Section 4.6.1.5), the data from ice measurements varied significantly in between different ice growths. Additionally, some significant spectral features observed during first full-scale experiment were not present in this data set. These results call into question the use of the obtained data for automatic detection and discrimination between different ice conditions. Furthermore, it was observed that the surface conditions have a major impact on the collected signal, casting doubt on the earlier assumption that the signal is acquired from across the whole ice thickness. At the end, the changes of the spectral response were observed as a results of the ice handling, but no further alterations were detected when the oil sample was injected underneath. These observations go in line with the hypothesis that the data were collected only from the surface of the ice samples and all the previous spectral changes could be caused by ice handling during the experimental execution.

At this stage, the next full scale imaging session in SAMS was already scheduled. Results of this test were meant to provide additional confirmation of previous observations with special attention to the impact of ice handling, as well as to check any potential influence of the ambient temperature on the spectral response.

4.6.3. Second full scale test

4.6.3.1. Experimental setup

The setup of the second full scale experiment taking place on the premises of SAMS was very similar to the one used during first approach, nevertheless a series of lessons learned before were implemented. As it was prepared previously, the cold room was equipped with a shelf supporting the hyperspectral imager and insulated ice tanks were located underneath. During this imaging session only the Firefly IR Imager was used for verification of the produced data. Having learned the pros and cons of the oil and ice management during the first full scale tests, this time only floating ice approach was used, as described in Section 4.3.2. The central part of the ice in the first tank was grown to a thickness of 10cm while for tanks 2 and 3 the thickness of 8cm was achieved at the time of imaging. The thin edge sections from the final ice growth stage were removed in between the imaging process to assure free floating ice before oil injections.

4.6.3.2. Test plan

The test was executed as demonstrated in Table 4.11 in order to accomplish its objectives: to verify (I) spectral stability of the ice with special attention on the mechanical handling of the ice and (II) the impact of the ambient temperature on the spectral response.

Table 4.11. Test plan of the second full scale imaging session. The numbers in the table indicate the sequence of data acquisition per each condition.

	Ambient temperature in the range -10°C to -7°C (tank 1)	Ambient temperature in the range -7°C to -4°C (tank 2)	Ambient temperature in the range -3°C to +1°C (tank 3)
Pure ice, as grown, attached to the ice tank – not cut	1	4	7
Pure ice, floating – the edge parts cut out	2	5	8
Ice with Oil injected beneath the floating ice (after cutting out the edges)	3	6	9

For this session three ice tanks were prepared and each of them was used to test different ambient temperatures. The reading of actual temperature in the cold room was monitored and for each test case the temperature was fluctuating in a range of 3-4 °C. First data acquisition (from

tank 1) was performed in the temperature range -10°C to -7°C , second in the range -7°C to -4°C (tank 2) and third in the temperature range -3°C to $+1^{\circ}\text{C}$ (tank 3). Each tank was scanned three times to acquire the data from ice in the growing condition – still attached to the container by the thin edge layer. Subsequently the edge parts were cut and removed and then the same pure ice was rescanned. Finally, oil was injected underneath the ice block and this condition was scanned once more.

The oil distribution was also monitored during this experiment with the underwater camera. In each case up to 200ml of oil was injected providing surface coverage sufficient to create the oil layer spread below the ice sample within the field of view of the Firefly IR Imager. Figure 4.24 illustrates the oil distribution for each tank.

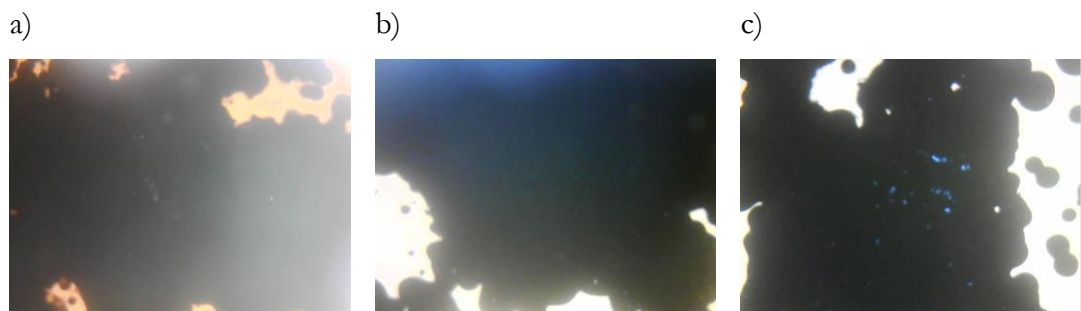


Figure 4.24. Oil distribution underneath the ice block viewed from below of ice in the tank 1 (a), tank 2 (b) and tank 3 (c).

4.6.3.3. Results

The average spectra extracted from the data acquired according to the plan are presented in Table 4.11. These were compared between each other from the perspective of both tests objectives - the ice handling and ambient temperature. The overviews of average spectra are presented in Table 4.12 and Table 4.13 respectively.

Table 4.12. Average spectra in the Near-IR and Mid-IR range comparing all the ice handling cases for each ambient temperature range. The spectra in red colour represent the pure ice in “as grown” condition, the spectra in green are extracted from free floating ice and the ones in blue represent oil under ice condition.

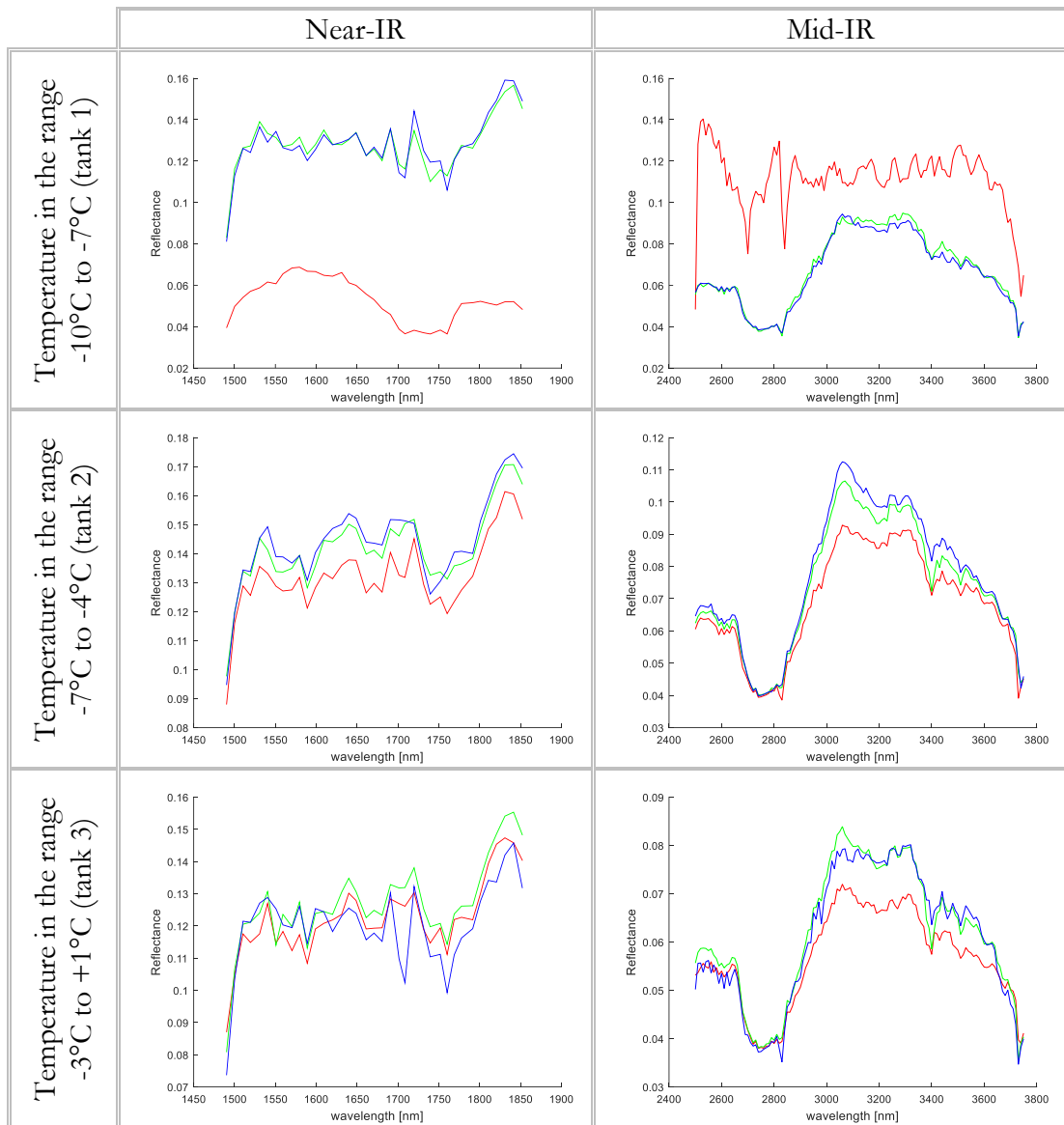
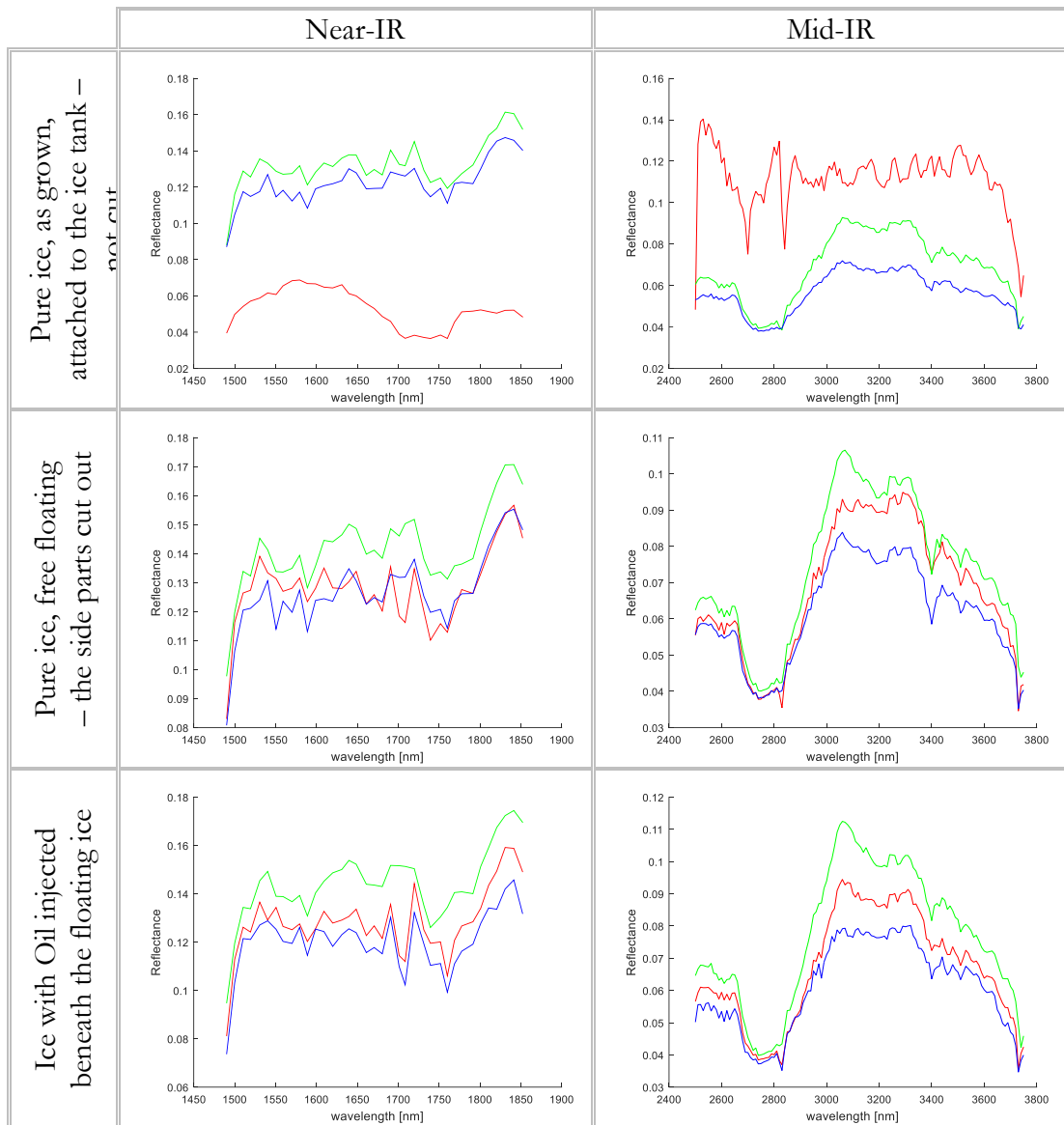


Table 4.13. Average spectra in the Near-IR and Mid-IR range comparing all the different ambient temperature variations for each ice condition. The spectra in red colour represent the -10°C to -7°C range, in green represent the -7°C to -4°C range and the ones in blue represent the -3°C to $+1^{\circ}\text{C}$ range.



Although the stabilisation of the Imager was performed before initiation of the data acquisition as well as checking all the points suggesting that the system was stable, it can be observed in both tables above that the first collected dataset (from pure, as growing ice at the lowest temperature range, with average spectra drawn with red line) is faulty. As it was not known during the data acquisition, the repeated dataset was not collected and therefore this spectral response was ignored from further analysis.

Based on the collected data the impact of the ambient temperature is difficult to observe. It is unknown if there is any dependency at all in the studied temperature range. Due to temperature inertia of the ice block it is possible that the change of the cold room setting had virtually no impact on the actual temperature of the ice. For each temperature condition there is variation in the intensity of the spectra, however no specific trend between intensity and temperature is present. Additionally, there is lack of spectra reproducibility between different ice growth runs. None of the acquired spectra shows the peak at 1500nm or double peak structure at ~3400nm as in earlier stages of the project. During the data collection, for the first time, the spectra from Near-IR region did not feature a peak at approximately 1800nm. As it was described in Section 4.4, the peak was present even in the hardware baseline, thus this observation could suggest that there had been some change within the hardware. However, since all the settings were maintained and no other potential root cause was found, in light of low significance of this outcome for the overall project, it was not further studied.

Throughout the first full scale imaging session the spectral change was observed during the oil injection that was the first experimental handling of the ice samples. From the perspective of current observations, it is expected that the spectral changes were also caused by the handling of ice but not the fact that oil was introduced underneath it. In this test, the first manipulation done on ice was the drilling of the initial opening to cut and remove edge of the ice block. As described here, the process affected the detected signal on the intensity level only, not any other specific features were observed – similar to small scale test as presented in Section 4.6.2.4. Basically, an introduction of oil beneath ice brings virtually no further changes in the measured spectra.

To further study the phenomenon of the spectral change upon the ice handling, the ice samples were monitored with the imager on a single band (set for 3200nm) during the first interaction with ice. Figure 4.25 illustrates selected images at the most significant stages explaining the increase of signal intensity.

As described in Section 4.5, the single band intensity image of the ice specimen acquired with the HSI camera was presenting very low signal levels, with majority of the points without any significant signal and with random high intensity pixels of radiation reflected towards the detector. During this monitoring it was observed that at the moment when the drill bit pressed the ice, the amount of points carrying some signal decreased but as soon as the bore was made the bright pixels appeared again, filling much more space on the image. After the ice was fully cut and stabilised in the free floating condition, many more pixels carrying information could be detected.

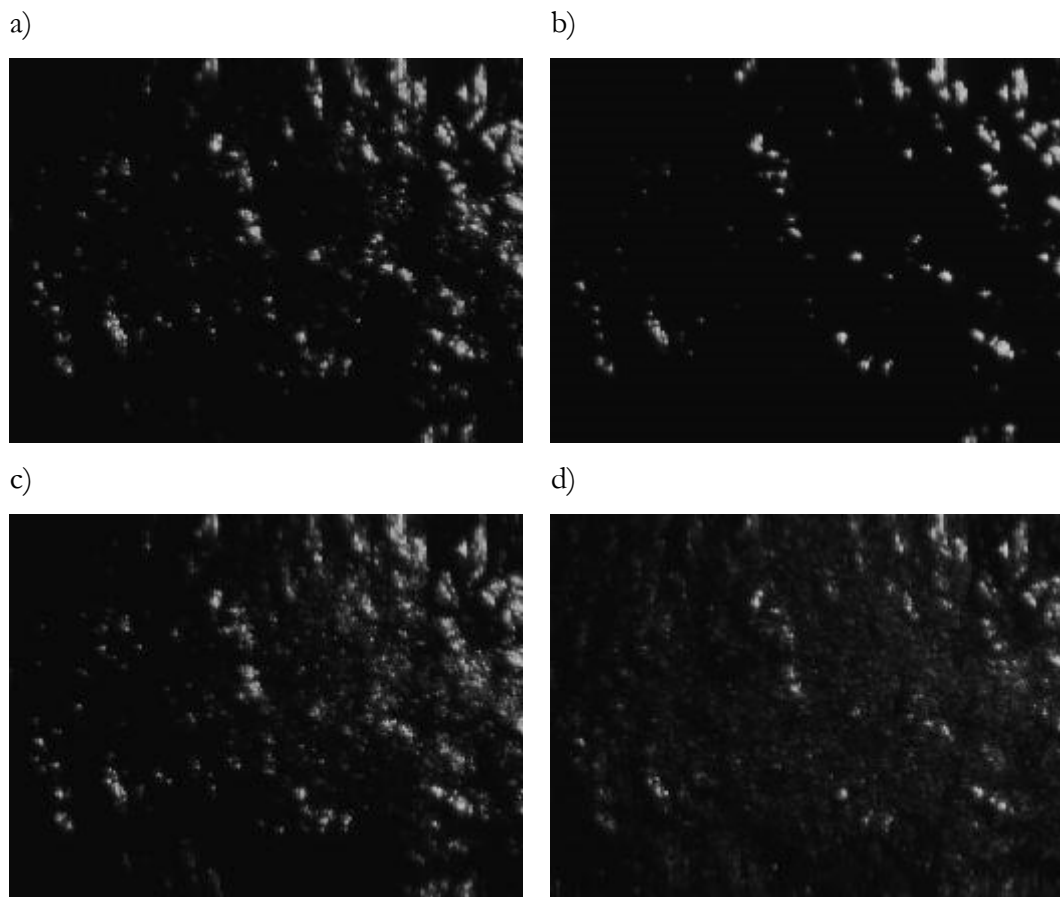


Figure 4.25. Intensity image at 3200nm of the pure ice sample in different moments of the its handling: uncut ice, stationary condition (a), pressure on ice from the drill bit, just before first drilling (b) situation just after the first hole was drilled (c), free floating ice, stationary condition (d).

Upon averaging the signal from the whole spatial domain of the image, the resulting signal had higher value. This observation clarified higher intensity of the average spectra graphs, however, the explanation why this phenomenon takes place was not found. During the project two hypotheses were developed, that (I) there is some pressure accumulated underneath ice which is released when the bore is made, what is changing the ice structure, or that (II) the impact of the drill is causing a change in crystalline structure of ice. Although, an attempt was made to study the second hypothesis (see Section 4.6.6), none of mentioned above could be confirmed during the course of this project.

4.6.3.4. Other oil and ice conditions

After all the conditions from the test plan being imaged, one more test was performed. To simulate more versatile settings of oil and ice, an oil stain was placed on top of the floating ice sample to sink into the ice structure from the top, the oil sample was mixed with water and slush

at the edge of the ice block (see Figure 4.26). Data obtained from imaging of both analysed liquids were compared with the spectrum of the ice sample with the oil layer underneath (see Table 4.14).

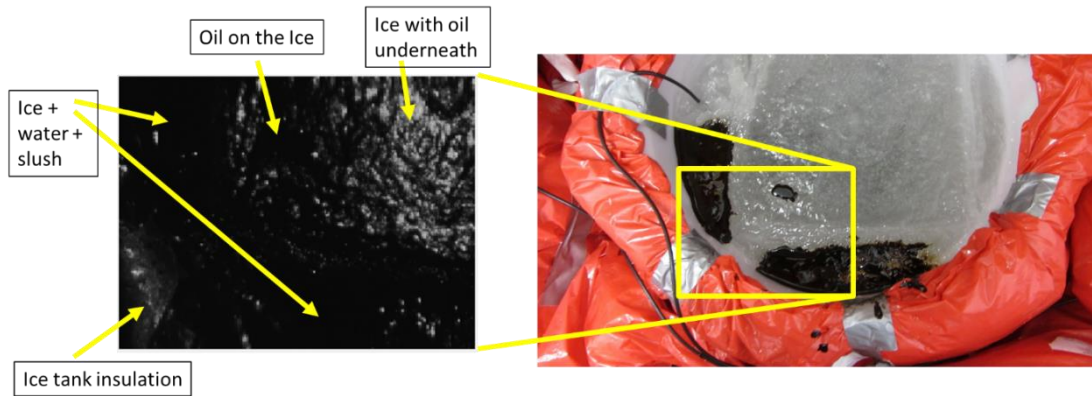
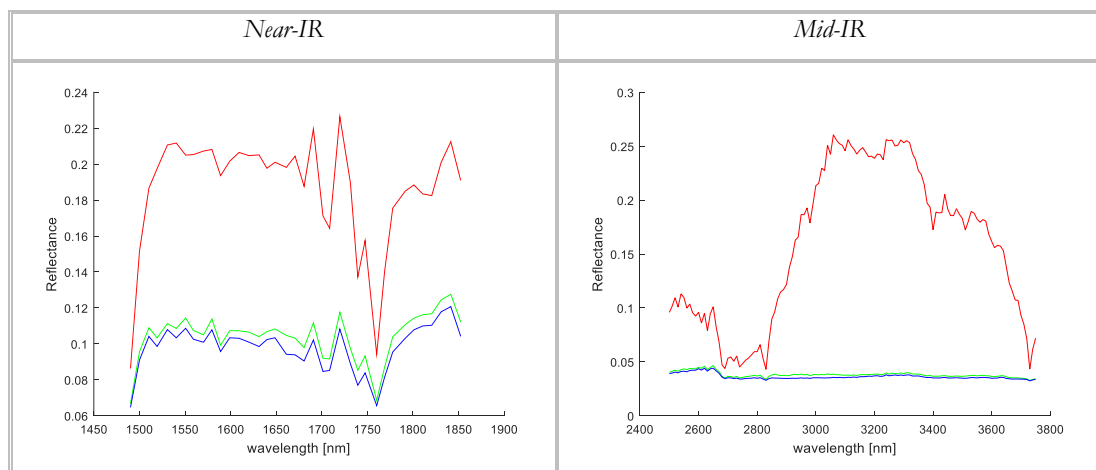


Figure 4.26. Top view of the ice tank with more versatile oil spill simulation: the oil stain on top of the floating ice block, the oil sample mixed with water and slush at the edge of ice with oil spilled underneath. The subset of this view captured by the Firefly IR Imager is presented and a single band intensity image (at 3200nm) of this test setup is also demonstrated, with all the different areas identified.

The spectrum of the ice block with oil underneath is similar to data from previous acquisitions (presented in Section 4.6.3.3), however for this case the area for averaging is different and this could explain any observed alterations. Spectra of the oil sample on top of the ice block and of the mixture of oil with water and slush did not represent any reflected signal and only hardware background was recorded by the detector (see Table 4.14). This is consistent with the result obtained during background characterisation described in Section 4.4, where it was identified that the radiation was fully absorbed by both crude oil as well as water in the whole available spectral range.

Table 4.14. Comparison of the Near-IR and Mid-IR average spectra of the three conditions: oil mixed with water and slush (blue line), oil on top of ice (green line) and oil underneath ice (red line).



4.6.3.5. The notion of the visible range illumination for the oil detection

The access of Firefly IR Imager into the mid-infrared region is based on the Optical Parametric Oscillation (see Chapter 2). As a side effect of this process, alongside the infrared radiation, there is also a very low power of visible radiation generated, at the wavelength (colour) changing with the position of the nonlinear crystal. During the operation of Firefly IR Imager this is usually used for the alignment of the camera and identification of its field of view. Installing the underwater camera in the ice tank, made possible to visualise and register visible range radiation passing through the ice block. The light was highly scattered while passing the ice sample and only very low light intensity (from originally low power beam) could be observed. Figure 4.27 illustrates two frames of the underwater camera footage, where an orange light line (Figure 4.27 (a)) and green (Figure 4.27 (b)) can be observed.

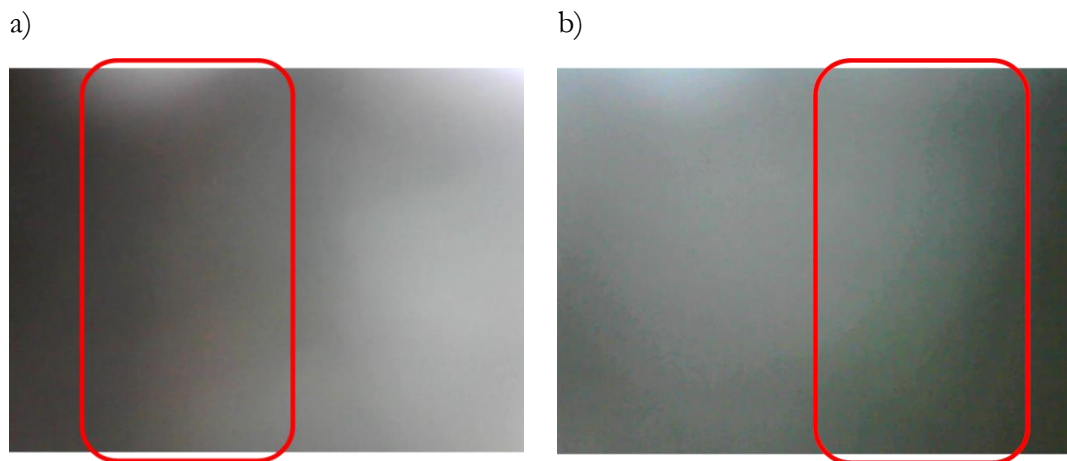


Figure 4.27. Frames of the underwater camera footage, where highly scattered visible laser radiation can be observed passing through 10cm of the ice specimen. Both the orange coloured radiation (a) and green radiation (b) are barely visible in the still form and can be better observed only when the scanning process moves this radiation with respect to background. The place where this highly broadened light line is present at these given images is marked by red rectangle.

This observation confirmed that some visible laser radiation can certainly pass through ice. Moreover, all the performed measurements were indicating that the systems operating in infrared region are not providing any repeatable results, therefore changing into the visible range was considered. Although during the project, an active laser-based hyperspectral camera was not available, a short test with visible laser diodes was performed and its results are presented in Section 4.6.5.

4.6.3.6. Summary of the experiment

The experiment described above proved to be a critical one for the whole project. Having mastered the ice control and whole experimental setup, the test provided a reliable set of spectra data. As such, the results demonstrate that the spectral response of ice, although repeatable within one ice growth run, is not reproducible in between different ice growths. Additionally, it was again observed that the spectral changes do not come from the presence of the oil layer underneath ice, but are merely artefacts of the experimental procedure. It is the large variability associated with physical conditions of ice, such as its temperature, surface roughness, growth procedure, an oil injection method etc. This strengthens the hypothesis that any acquired data were always coming from the surface of the ice block only and any impact of the oil presence was never monitored. The verification of ice transmission was subsequently scheduled and the results are demonstrated in Section 4.6.4. Due to the fact that some laser radiation in visible range was observed passing the ice sample, the measurement of the ice transmission in this range was also scheduled and results of the test are presented in Section 4.6.5. Observing that the changes in spectral response occur during mechanical handling of ice, a short test was scheduled to verify the influence of mechanical impact on the spectral response of ice (results presented in Section 4.6.6.).

4.6.4. Verification of the ice transmission in the infrared region

The ROSDAM project aimed in detecting a greatly absorbing object (oil) under highly scattering and absorbing medium (ice). Despite the knowledge of very high absorption coefficient and short penetration depth [10, 11] the initial results lead to the mistaken assertion that the active imager is able to detect the presence of oil underneath the ice layer. Since all the results collected at the later phase of the study as well as the developed theory – that all the to-date acquired data come only from the ice surface – a next experiment was executed where highly reflective objects were placed underneath the ice block, providing unequivocal confirmation of this hypothesis.

4.6.4.1. Design of the experiment

To test the transmission of ice at the wavelengths available for Firefly IR Imager, three aluminium blocks of different heights (105mm, 55mm and 30mm – see Figure 4.28 (a)) were used, creating together with the bottom of the plastic bucket, the target objects to be observed through the ice sample. Due to the fact that the aluminium is a broadband, highly reflective material in the infrared region and the plastic bucket is a great absorber (as demonstrated in the Section 4.4.1),

both provided the extreme conditions for this verification test. To achieve a highly diffuse reflection, the top surface of each ice block was roughened. Additionally, in order to create variations in the ice thickness between the surface and the target object, each of the aluminium blocks used in this test had different height. These subsequently were placed in the bucket and sea water was poured to cover all of them. The overall height of the water column was 120mm constituting after freezing the distance between the surface of the ice and the bottom of the bucket. The depth of ice between three aluminium blocks had then from the highest to the lowest respectively 15mm, 65mm and 90mm. The whole system was placed in the Labcold freezer (as described in Section 4.6.2) and water was frozen with all the aluminium blocks in it (Figure 4.28 (b)).

4.6.4.2. Results

The set of the three different heights of the aluminium targets, gave results for three different heights of the ice columns between the surface and the target. Providing that there would be sufficient penetration depth of the infrared radiation through the ice sample, the spectral response should be strongest for the highest aluminium block (the shortest ice layer to penetrate – 15 mm) and then gradually decrease for the next two blocks with the lowest response on the bottom of the plastic bucket. However, this result would be observable only if the radiation would actually penetrate the ice completely.

The ice block with all the encapsulated targets was imaged in similar setup as presented in Section 4.6.2 and the average spectra extracted from this data are presented in the Table 4.15. Figure 4.28 (a) demonstrates the image made with standard digital camera compared with the same field of view captured on the single band intensity image (at 3200nm) taken with Firefly IR Imager (Figure 4.28 (c)), illustrating that the image in the infrared does not contain any information from underneath the ice specimen.

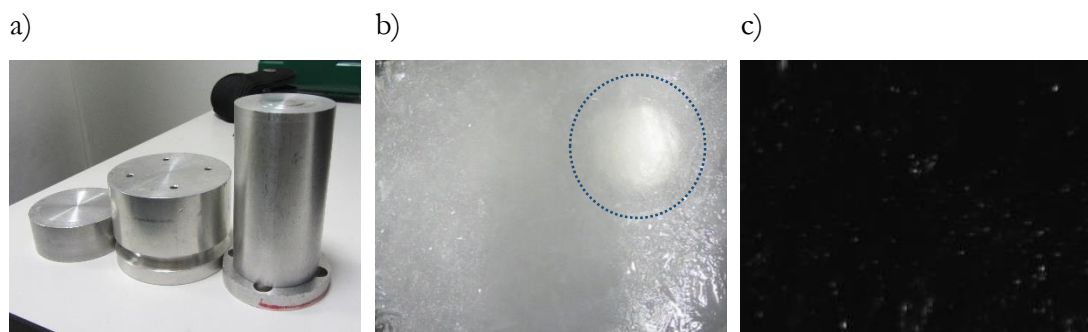
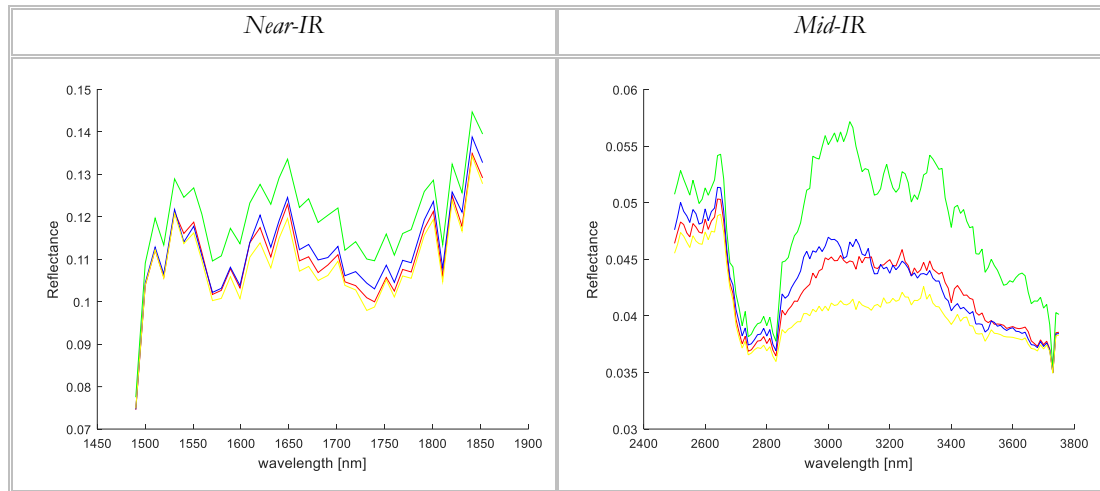


Figure 4.28. Photograph of the three aluminium blocks (before surface roughening) used in this experiment (a) and comparison of the top view on the ice sample with encapsulated aluminium targets made with standard digital camera (b) and with a single band image (at 3200nm) captured with Firefly IR Imager (c). The tallest block is visible through ice on the image (b).

Table 4.15. Comparison of the Near-IR and Mid-IR average spectra of the four targets located under the ice: the three aluminium blocks with the ice column between them and the surface being 15mm - represented by yellow line, 65mm - blue line, 90mm - red line and the bottom of the bucket with 120mm ice column - green line.



The spectra extracted from the areas where the targets would be expected are all very similar and all of them have very low intensity signal. The expected gradual decrease of the signal was not observed because none of the aluminium targets had any impact on the acquired data. The green lines show the highest intensity values of all these extracted from the image, while they represent the spectra of region above the highly absorbing bottom of the plastic bucket. It is observed only due to the higher amount of specular reflection in this area of the image, that usually has higher intensity signal (see Section 4.5) and it is known to be not related to the objects underneath the ice layer.

This experiment provides an unequivocal proof that the assumption about the Near-IR and Mid-IR laser penetrating ice to sufficient depth to detect oil was incorrect and none of the previous results was actually caused by the presence of oil beneath the ice layer.

4.6.5. Measurement of the ice transmission in the visible region

As it was mentioned in Section 4.6.3.5, during the full scale experiment in SAMS the visible radiation was observed passing through 10cm of ice. The transmitted radiation was highly scattered and the intensity of the light passing the ice sample was very low. To quantify this observation a short measurement in the visible range was performed. Due to the fact that a visible range, laser-based, active hyperspectral camera was not available, this test was executed by use of

single detector and three different off-the-shelf laser diodes of comparable optical power, operating in red, green and blue with their spectral central lines at 630nm, 532nm and 405nm respectively (for the purpose of this experiment the exact spectral signature and linewidth of these laser diodes was not characterised). The detector used for this test was a big surface (10mm x 10mm) silicon based photodiode helping to capture also a small level of scattered light (no focusing optics applied). The results of these measurements contain drop of the signal on the way through the ice block from both, absorption and scattering of the light. Because the latter effect is very strong, the distance between the photodiode and the ice specimen had big impact on the detected signal. For the purpose of this experiment, to unify the results, the detector was placed closely behind the ice block (in 3cm distance) of 25 x 50 x 130 mm size. Figure 4.29 illustrates the measurements setup with all the three laser diodes aligned along the longest dimension of the ice sample.

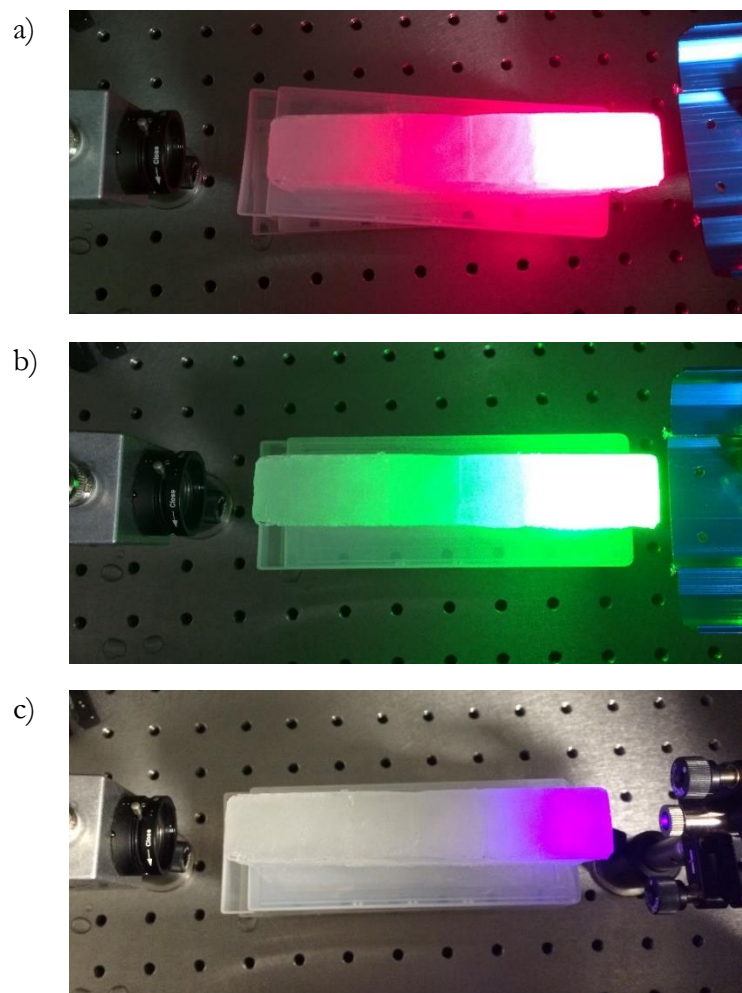


Figure 4.29. Setup of the ice transmission measurement in the visible spectral region with the selection of three laser diodes a) red (630nm) b) green (532nm) and c) blue (405nm).

The ice transmission was measured over all three dimensions, providing three path lengths affecting the light transmission that resulted with an indicative dataset presented in the Figure 4.30.

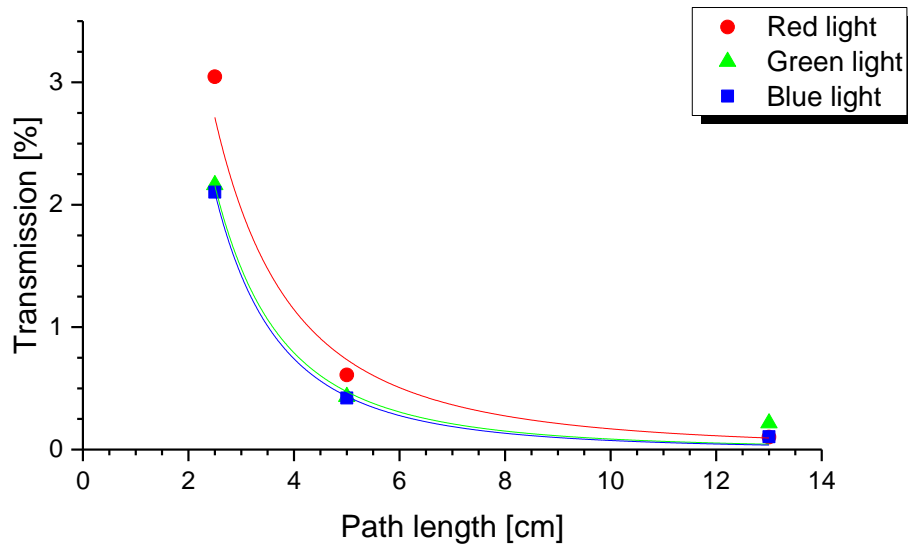


Figure 4.30. Graphical representation of the ice transmission data for the three laser diodes (red, green and blue) and three ice path lengths (2.5cm, 5.0cm and 13.0cm).

As it is presented in Figure 4.30, only very low levels of light are transmitted through the ice towards the detector, dropping to the lowest value of 0.1% at the 13cm ice path length. Additionally, this test simulates only transmission from one directional pass through the ice block. In case of Hyperspectral Imaging, the radiation would have to pass through ice, be reflected from the object of interest and transmitted back to the detector through the same thickness of the ice sample. This would result - at best - with similar attenuation ratio on the second pass through ice. However, in this application the object of interest (oil) is black/dark brown, indicating that in the visible range it will also highly absorb the radiation, providing only fractional reflection towards the detector. These test results indicate that even active, laser based HSI system in the visible spectral range would fail to provide any data allowing the oil under ice detection.

4.6.6. Verification of the influence of mechanical impact on the ice spectra

Resulting from the conclusions drawn after the experiments described in Sections 4.6.2 and 4.6.3, one of the potential reasons for the observed spectral changes of ice, was the mechanical effect onto the surface of the ice samples. It was assumed that the impact may be changing the

crystalline structure on the surface of the ice that could subsequently influence the amount of specular reflections detected by the imager. Although this phenomenon could explain the increase of the signal observed in the small sample verification test as well as the second full scale test, it would not explain the changes in specific spectral features, as observed in first full scale experiment. Within the course of this project, the explanation for this occurrence was not found.

4.6.6.1. Spectral measurements

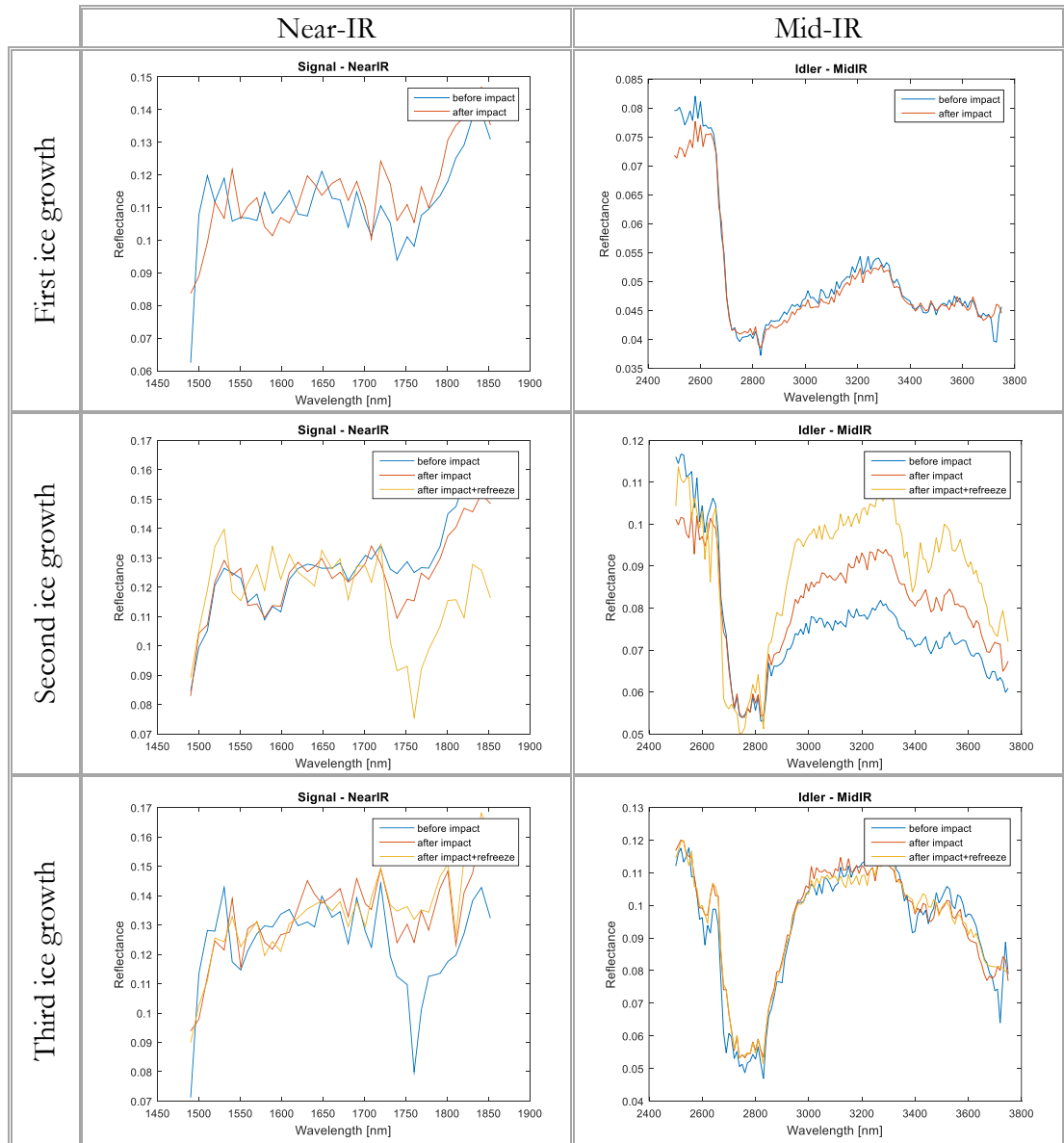
The test attempting to prove the influence of mechanical impact onto the ice surface was executed as a small sample test with use of the Labcold freezer. Three ice growths were completed and three imaging runs were made for each of them, taking the data from: (I) the ice samples not affected by impact – as growing in the bucket, (II) directly after the impact - made with a hammer on the surface of the ice, outside of the Imager field of view) and (III) in two out of these three cases (second and third ice growth) - after period of subsequent freezing (re-freezing - without any additional mechanical impact). The Table 4.16 represents the average spectra extracted from the acquired dataset.

The spectra acquired from the first ice growth featured only the hardware baseline. No signal was reflected back to the detector – nearly no specular reflections were observed from this ice sample. Due to the fact that this situation did not change even after the impact onto the ice surface, the refreezing part of the test was abandoned for this case.

The spectra acquired from the second ice growth did show an increase of the signal intensity in a similar manner as observed earlier in a full scale verification test (see Section 4.6.3). Scan after subsequent refreezing of the ice resulted in further increase of the signal, however this acquisition was performed after 24h of the next freezing and due to practical reasons of the labs space use, the Imager had to be moved out from the freezer space in the meantime. Due to the fact that the intensity of the signal relies only on the specular reflections from the ice surface, it is possible that the Imager was not exactly at the same position as during the previous tests and that could have an effect on the intensity of acquired signal.

The last imaging session resulted in average spectra that did not change under any of the conditions. To avoid moving of the Imager, the re-freezing lasted only 2 hours, however even with not changed position, no extra conclusions could be made, as the signal stayed unchanged.

Table 4.16. Average spectra in the Near-IR and Mid-IR range comparing all spectral responses of the three ice growths in three different conditions: ice before the impact, as grown (blue line), just after the impact (red line) and after re-freezing (yellow line). The re-freezing condition was not acquired for the first ice growth.



4.6.6.2. Visual inspection

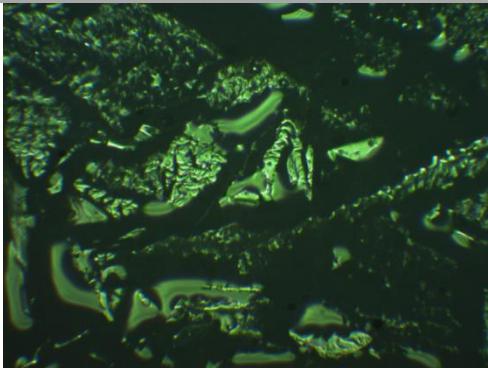
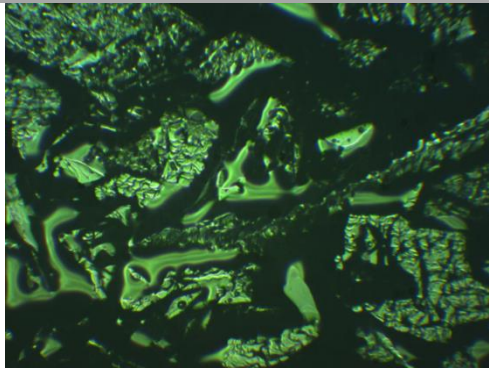
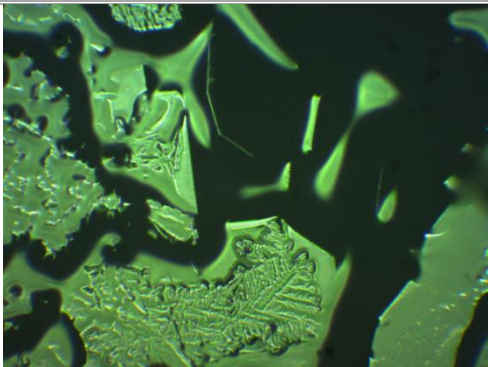
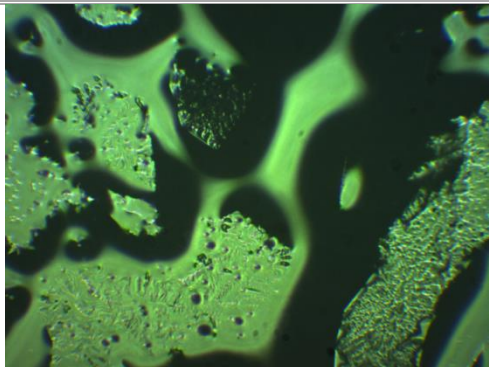
In addition to the spectral test, an ice growth was made in two small containers that could allow observation of the ice surface under the microscope. Assuming that the change in the spectra intensity and amount of specular reflections was caused by the change in the crystalline structure of the ice surface, the ice sample was examined under the microscope before and after the mechanical impact. To perform this inspection, the container with ice was fixed under the microscope objective, and its state was captured. Subsequently a mechanical impact was generated

and an image from post-impact ice surface condition was captured. For practical reasons this inspection could not be performed in the negative temperature so all the actions were executed rapidly to minimise the influence of the melting of the ice sample. Table 4.17 illustrates two observations of the ice surface from before and after the impact conditions.

Results of this study showed no significant changes in the crystalline structure of the ice surface upon the mechanical impact. Although the test was performed fast, some melting of the ice could be observed instantly after removing it from the freezer and the difference observed on the images in Table 4.17 are explained by the melting of microscopic structures, which took place even without application of any mechanical impact.

These tests did not provide any confirmation that the spectral changes were caused by mechanical impact on the surface of the ice. Although one experiment demonstrated behaviour similar to the one observed in the second full scale test, this phenomenon is hard to reproduce. Although the effort was taken to keep the conditions of all tests as similar as possible, there may be other factors causing spectral response changes. For instance, the confirmation test did not account for water underneath ice and therefore any potential influence of the freeboard (distance between the water line and the top ice surface) could not be verified.

Table 4.17. Microscopic images of the ice surface from two ice samples before and after the mechanical impact taken.

	Before Impact	After Impact
Observation 1		
Observation 2		

The observations under the microscope, demonstrated that no clear changes in the crystalline structure can be seen on the ice surface upon a mechanical impact. This helps to refute the hypothesis that the changes in the crystalline structure of ice generate the increase of specular reflections from the ice surface. As such, this phenomenon was also not explained in the context of the project.

4.7. Conclusions

Although a casual observer could say that the work conducted in this project was doomed to fail due to the physical and optical properties of ice, and indeed the final results confirmed this inapplicability of chosen techniques, the data observed during initial tests were misleadingly encouraging. The results achieved during the project can serve as an experimental confirmation that the passive and active hyperspectral imaging techniques, operating in near- and mid-infrared spectral regions, are not applicable for the oil under ice detection.

Over the course of the project, a set of observations was made. The first significant remark was that the data produced by the passive hyperspectral camera were lacking in consistency. It was decided to discontinue use of the passive system in this project already after the first full scale test. On the other hand, the data acquired with an active imager initially provided very coherent and promising results. Spectral features differentiating pure ice conditions from the one with oil underneath were observed regularly across different ice thicknesses. These features were believed to constitute the basis for an automatic identification of the oil affected regions. It was demonstrated that these different study cases could be distinguished through a set of classification algorithms. However, variations in the ice spectral response were observed during experiments. Therefore, further set of performed tests focused on the authentication of obtained values.

The results from the verification experiments demonstrated large variations in observed spectral responses between different ice growths, suggesting that the spectra measured by the available imaging systems could not provide sufficient information for the discrimination of various ice and oil conditions. The results also showed that the variability of the observed spectra was mainly due to the physical changes of the ice surface (not caused by the presence of the oil), sometimes modified by handling of ice during the experiments. These observations were followed by verification whether the laser radiation emitted by the active imager could penetrate through the ice structure. The results showed that this could not be done and indeed all previous measurements were coming from changing the ice surface conditions. Additional tests were also performed, attempting to explain the origin of observed spectral variations, however an unambiguous answer was not found.

In summary, despite considerable efforts by the researchers involved in the study, it must be concluded that the HSI devices used in this project are not suitable for the oil under ice detection and none of the performed experiments could demonstrate reliable application of the current technology for this purpose. Additionally, given the strong absorption and high level of similarity between water and oil spectra in the Mid-IR range, it can be concluded that using this spectral range, regardless of the specific instrumentation, HSI will not work.

Many challenges have been addressed during this project, including the development of reliable methodology in the ice growth and its maintenance, handling oil and HSI imaging in sub-zero temperature conditions as well as the analysis of the HSI data from the samples of ice and oil. The methodology and technology developed throughout this project could be used to study new emerging technologies for oil under ice detection. New imaging methods for underwater environment are being developed. Using time correlated single-photon counting [21] or quantum imaging [22, 23] demonstrate unprecedented capabilities for underwater imaging. With further development of above mentioned techniques and the commercialisation of the hardware driving them, an application of these in oil spills under ice could be considered.

4.8. Acknowledgments

This study was carried out within the framework of a ROSDAM project financed by the R&D Award from the International Tanker Owners Pollution Federation Limited (ITOPF). This project was also supported by the EPSRC Centre for Doctoral Training in Applied Photonics, funded by the UK Engineering and Physical Sciences Research Council (grant EP/G037523/1) and by an Industrial Fellowship from the Royal Commission for the Exhibition of 1851. Professor Bruce Rafert, from North Dakota State University (at the time of the discussion), contributed to the idea generation and initial planning of this work. The ice and oil handling was performed by Dr Phil Hwang and Bernard Hagan from Scottish Association for Marine Science.

References

- [1] I. Leifer, W. J. Lehr, D. Simecek-Beatty, E. Bradley, R. Clark, P. Dennison, Y. Hu, S. Matheson, C. E. Jones, B. Holt, M. Reif, D. A. Roberts, J. Svejksky, G. Swayze and J. Wozencraft, "State of the art satellite and airborne marine oil spill remote sensing: Application to the BP Deepwater Horizon oil spill," *Remote Sensing of Environment*, vol. 124, pp. 185-209, 2013.

- [2] C. Brekke and A. H. Solberg, "Oil spill detection by satellite remote sensing," *Remote Sensing of Environment*, vol. 95, pp. 1-13, 2005.
- [3] T. Puestow, L. Parsons, I. Zakharov, N. Cater, P. Bobby, M. Fuglem, G. Parr, A. Jayasiri, S. Warren and G. Warbanski, "Oil Spill Detection and Mapping in Low Visibility and Ice: Surface Remote Sensing," Arctic Oil Spill Response Technology Joint Industry Programme (JIP), 2013.
- [4] R. Goodman, "Oil under ice detection: What is the state-of-the-art?," in *Oil Spill Response: A Global Perspective*, Springer, 2006, pp. 7-19.
- [5] M. Fingas and C. E. Brown, "Detection of Oil in Ice and Snow," *Journal of Marine Science and Engineering*, no. 1, pp. 10-20, 2013.
- [6] J. Wilkinson, T. Maksym and H. Singh, "Capabilities for detection of oil spills under sea ice from autonomous underwater vehicles," Arctic Oil Spill Response Technology Joint Industry Programme (JIP), 2013.
- [7] M. Nischan, R. Joseph, J. Libby and J. Kerekes, "Active Spectral Imaging," *LINCOLN LABORATORY JOURNAL*, vol. 14, no. 1, pp. 131-144, 2003.
- [8] A. Polak, S. Marshall, J. Ren, B. Hwang, B. Hagan and D. J. M. Stothard, "Remote Oil Spill Detection and Monitoring Beneath Sea Ice," in *Living Planet Symposium 2016*, Prague, 2016.
- [9] M. W. Davidson, "ZEISS Microscopy Online Campus | Tungsten-Halogen Lamps," [Online]. Available: <http://zeiss-campus.magnet.fsu.edu/articles/lightsources/tungstenhalogen.html>. [Accessed 15 January 2016].
- [10] G. M. Hale and M. R. Querry, "Optical constants of water in the 200 nm to 200 μm wavelength region,," *Applied Optics*, vol. 12, pp. 555-563, 1973.
- [11] D. M. Wieliczka, S. Weng and M. R. Querry, "Wedge shaped cell for highly absorbent liquids: infrared optical constants of water," *Applied Optics*, vol. 28, pp. 1714-1719, 1989.
- [12] L. W. Tilton and J. K. Taylor, "Refractive index and dispersion of distilled water for visible radiation at temperatures 0 to 60 degC," *Journal of Research of the National Bureau of Standards*, vol. 20, pp. 419-477, 1938.
- [13] N. E. Dorsey, *Properties of Ordinary Water-Substance in all its phases: water-vapor, water, and all the ices.*, New York: Reinhold Publishing Corporation, 1940.
- [14] L. B. Maykut GA, "Refractive-index measurements in freezing sea-ice and sodium chloride brines," *Applied Optics*, vol. 34, no. 6, pp. 950-961, 1995.
- [15] A. K. George and R. N. Singh, "Correlation of Refractive Index and Density of Crude Oil and Liquid Hydrocarbon," *International Journal of Chemical, Environmental & Biological Sciences*, vol. 3, no. 5, pp. 420-422, 2015.
- [16] F. E. Nicodemus, "Directional Reflectance and Emissivity of an Opaque Surface," *Applied Optics*, vol. 4, no. 7, pp. 767-775, 1965.

- [17] C.-W. Hsu, C.-C. Chang and C.-J. Lin, "A Practical Guide to Support Vector Classification," National Taiwan University, Taiwan, 2010.
- [18] N. Cristianini and J. Shawe-Taylor, *An Introduction to Support Vector Machines and Other Kernel-based Learning Methods*, Cambridge: Cambridge University Press, 2000.
- [19] P. Du, G. Li, W. Zhang, X. Wang and H. Sun, "Consistency Measure of Multiple Classifiers for Land Cover Classification by Remote Sensing Image," in *Multiple Classifier Systems: 8th International Workshop, MCS 2009, Reykjavik, Iceland, June 10-12, 2009, Proceedings*, Reykjavik, 2009.
- [20] C.-C. Chang and C.-J. Lin, "LIBSVM : a library for support vector machines," *ACM Transactions on Intelligent Systems and Technology*, vol. 2, no. 3, pp. 27:1--27:27, 2011.
- [21] A. Maccarone, A. McCarthy, X. Ren, R. E. Warburton, A. M. Wallace, J. Moffat, Y. Petillot and G. S. Buller, "Underwater depth imaging using timecorrelated single-photon counting," *Optics Express*, vol. 23, no. 26, 2015.
- [22] M. Lanzagorta, "A Quantum Imaging System for Underwater Arctic". United States of America Patent 14/800,769, 16 July 2015.
- [23] M. Lanzagorta, J. Uhlmann and S. E. Venegas-Andraca, "Quantum sensing in the maritime environment," in *OCEANS 2015 - MTS/IEEE Washington*, Washington, 2015.

Chapter 5: IC-OPO-PAS

5.1. Project background

In recent years the use of explosives-based weapons by terrorist perpetrators has increased significantly. They come to be simple and easily deployable, however still capable of creating substantial damage [1, 2, 3]. Thus, detection of explosive materials is one of the major aspects of homeland security and counter-terrorism. Since explosives are usually manufactured from volatile organic compounds (VOCs), gas detection has become an important vehicle to identify a threat. This task is facing a series of challenges, such as concealment of the source material, mixed vapours, low vapour pressures of most VOCs and usually only traces of them in the ambient atmosphere. Various techniques were developed and applied for explosives detection, ranging from spectroscopic methods, through olfactory and chemical sensors to nanoscale and thin films sensing [4]. Within the family of spectroscopic methods there are varieties of tools and techniques that were applied for explosives detection. Between them: Ion Mobility Spectroscopy, Mass Spectrometry, Laser-Induced Breakdown Spectroscopy or Raman Spectroscopy are only a limited selection of methods employed for this critical task [4, 5, 6, 7, 8, 9]. Among many spectroscopic techniques, the Photoacoustic Spectroscopy (PAS), in its many configurations, has over the past decades established a considerable number of records in applications for gas trace detection [10, 11, 12, 13]. This chapter demonstrates the results of the project entitled “Ultrasensitive explosive detector using PAS & OPO”, funded in a competitive bid for the Innovative Research Call in Explosives and Weapons Detection 2016 sponsored by the UK and US governments.

Photoacoustic Spectroscopy belongs to the class of photothermal techniques where absorbed radiation changes the thermal state of the sample. It has been developed in 1880 by Alexander Graham Bell as a potential system for optical communication. However, Bell himself recognised the possibility of using photoacoustic effect for spectroscopic applications [14]. This discovery was not practically exploited until the development of lasers as the excitation source, low-noise electronics and high-sensitivity microphones [13, 15]. If the wavelength of the radiation incident on the target is chosen such that it is coincident with a molecular absorption, then a portion of this radiation is absorbed, which in turn leads to weak heating of surroundings and thus, a change in density of the targeted medium. Modulation of the incident wave causes an associated alteration in gas density, resulting in a periodic change in pressure. This periodically

varied pressure produces a sound wave that can subsequently be detected with a microphone-type arrangement [16, 17], eliminating the need for optical detection. It is especially important for explosive detection since many of the peak rotational and vibrational absorption features, exhibited by complex molecules such as VOCs, occur at mid- and deep-infrared wavelengths [18, 19], where detectors require cooling and exhibit poor detectivity. A secondary advantage of the photoacoustic approach is that the sound detection can take place in an acoustically resonant ‘organ-pipe’ type arrangement, thereby improving the acoustic signal by allowing it integrate over multiple modulation cycles [17, 20]. A simplified illustration of such an arrangement is presented in Figure 5.1.

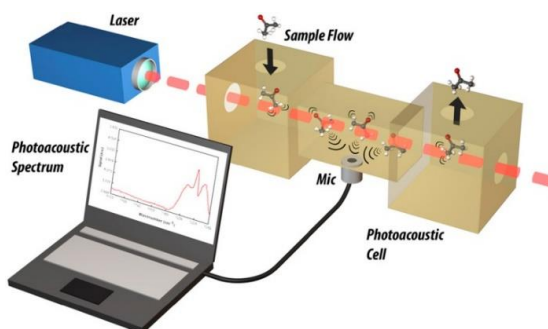


Figure 5.1. An illustration of a photoacoustic setup [21].

An extension of this is the quartz-enhanced spectrophone, where a quartz-tuning fork (as commonly used in electronic timing applications) replaces the microphone. Here, the enormous resonant quality factor Q exhibited by such tuning forks typically on the order of 10,000 can lead to unprecedented levels of sensitivity [20, 22]. The signal resulting from the PAS setup S (often expressed as the voltage reading on the Lock-in Amplifier) can be written as [20, 23]

$$S = CP\alpha \quad [5.1]$$

where C is the instrumental constant, P is the incident optical excitation power from the laser and α is the molecular absorption of the compound. The instrumental constant C depends on the geometry of the cell, the modulation frequency of the incident radiation, the efficiency of the transducer and the quality factor Q [20]. As with any transducer-type system, the ultimate limit on sensitivity is described by the level at which the signal produced by the device is indistinguishable from the noise floor. The signal S can therefore be maximised by selecting the excitation wavelength to coincide with the strongest peak absorption coefficient α and designing the spectrophone to maximise the Q factor. However, the viscosity of air and finite absorption indicate that these parameters cannot be endlessly maximised [13, 20]. Increasing the incident optical power P is an excellent route to realise enhanced sensitivity. Although very high-power lasers operating in the infrared (namely carbon dioxide [CO₂], carbon monoxide [CO], deuterium fluoride [DF] and hydrogen fluoride [HF] lasers) are commercially available, their fixed frequency

operation and large size make them impractical as explosives detection devices outside of a laboratory environment.

Optical Parametric Oscillators (OPOs) – introduced in Chapter 2 – stand as very potent tools used for producing widely tuneable mid-infrared radiation. In the past, OPOs (in their traditional extra-cavity configuration - ECOPO) also required large pump lasers to bring the weak parametric process to the threshold. However, in the intracavity setup (IC-OPO), where the OPO device is placed within the high circulating optical field of the laser (tens of watts), the threshold of the parametric effect is reached already with several hundred milliwatts of the primary diode pump power [24]. This facilitated miniaturisation of these devices and make them an attractive source of mid-infrared radiation.

The aim of this project was to demonstrate a proof-of-concept ultra-sensitive point-sample ‘sniffing’ technology for application in the detection of concealed explosives. The ultimate goal for this project was to realise a real-time technology that could exhibit few parts-per-quadrillion (ppq) levels of sensitivity, thereby bringing an unprecedented quality of measurement to operational environments, which are normally associated with off-line, laboratory-type techniques. In this proof-of-concept activity, the objective was to demonstrate detectivity of ammonia (NH_3), a simulant target molecule, down to the ppb level. The fundamental principle underpinning the innovation is the combination of photoacoustic spectroscopy with the Intracavity Optical Parametric Oscillators. More specifically, the very high circulating optical field of the resonant down-converted wave found within an intracavity OPO is exploited. This is achieved by placing the photoacoustic spectrophone inside, (intracavity to) the IC-OPO. Use of OPOs as the excitation source for PAS was already reported [25, 26, 27] as well as the idea of placing the photoacoustic spectrophone within a high finesse optical cavity [11, 28]. However, location of the photoacoustic spectrophone inside the intracavity OPO (IC-OPO-PAS) was never attempted before. Compared to the extra-cavity position of the spectrophone, its intracavity location offers orders of magnitude higher excitation field, which is available to induce a much stronger signal in the photoacoustic spectrophone. OPOs are usually used as tuneable sources of mid-infrared, output-coupled radiation. Figure 5.2 illustrates quartz-enhanced photoacoustic spectroscopy (QE-PAS) in such a configuration.

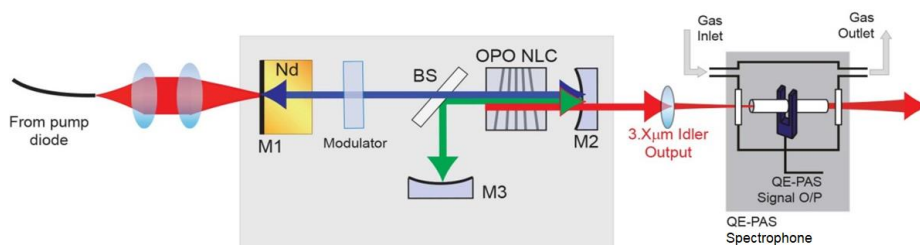


Figure 5.2. An intracavity OPO exciting an extra-cavity photoacoustic spectrophone.

Typically, this device would be pumped at the \sim few watts level (of primary diode pump power), with signal oscillating within the cavity, leading to \sim 150mW of non-resonant idler output to be used for photoacoustic excitation. However, the choice of signal or idler resonance is made simply by selecting the correct coatings on the mirrors (M2, M3), beam splitters (BS) and other optical parts. This innovation comes by recognising that the down converted signal wave, trapped within its cavity (M2-BS-M3 in Figure 5.2), builds up to very high optical power levels – in the above example, possibly 20W. By changing the coatings of the device to make the idler wave resonant (and in consequence, trapped in the cavity) and placing the spectrophone intracavity, as shown in Figure 5.3, the enormous enhancement in optical excitation field at mid-infrared wavelengths can be exploited. It is the development of the key sub-modules – the excitation OPO and the PAS spectrophone – which was the crucial activity in this project. Some aspects of it were described in a technical report and presented to the funding body as well as published in [29].

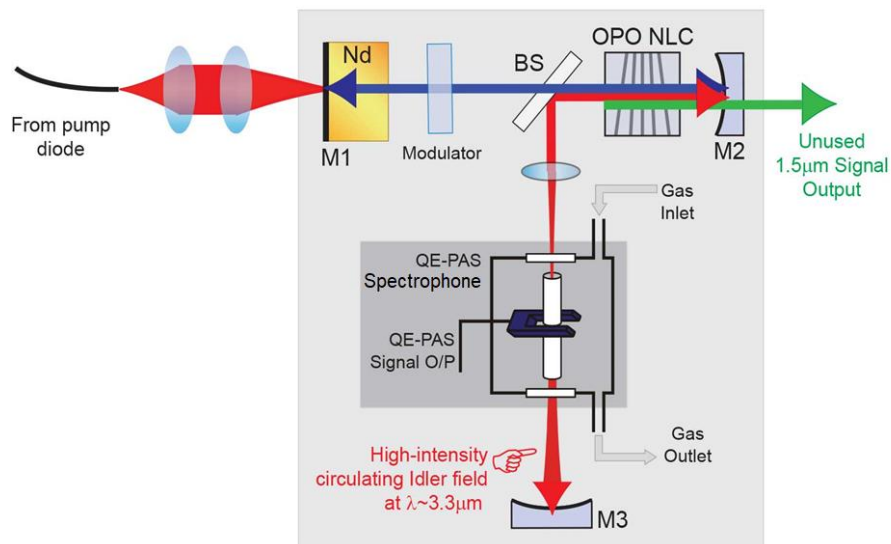


Figure 5.3. Intracavity OPO with intracavity quartz enhanced photoacoustic spectrophone.

5.2. Optical Parametric Oscillator

5.2.1. Design

During this project a standing wave cavity design was chosen for the intracavity OPO. With aforementioned selection of ammonia as a simulant molecule in this project, a signal resonant configuration of the OPO was selected to explore the absorption lines in near-infrared region. The schematic diagram of the IC-OPO-PAS (with microphone based spectrophone) is shown in Figure 5.4

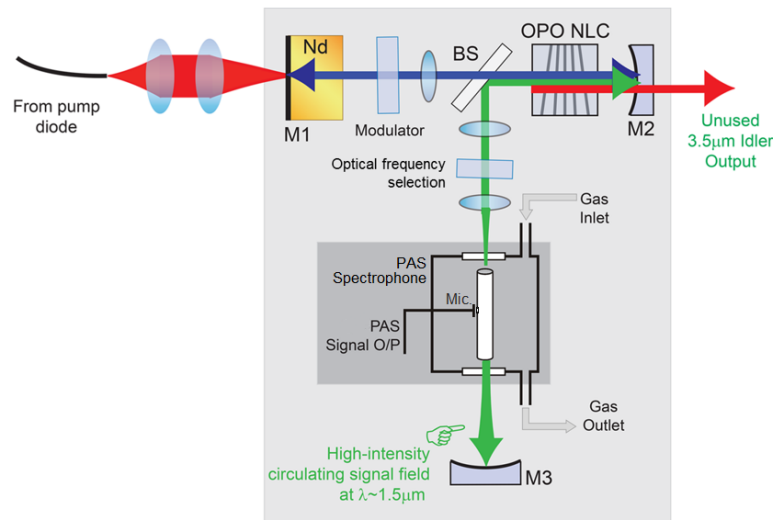


Figure 5.4. Schematic representation of the signal resonant IC-OPO as developed during this project.

The parent laser cavity, oscillating a pump wave at 1064nm, is determined by mirrors M1, (a highly-reflecting (HR) dielectric coating applied to the outer surface of a 3x3x1mm³ a-cut 2% doped Nd:YVO₄ laser gain crystal), and M2 with similar coating. All components in between the mirrors were anti-reflection (AR) coated at this pump wavelength. The M1 coating was additionally AR coated for 808nm diode pump light supplied by a 4W, 200µm core size fibre-coupled laser diode (Sheaumann Laser, Part No: HF-808-010W-25C). An acousto-optic modulator (AOM) (Gooch & Housego, Part No: I-QS080-1C10G-4-OS13) was placed in the pump cavity to influence amplitude modulation on the circulating field. This could have been done by controlling the primary diode pump power but a modulator in the cavity eliminates the need for high frequency current switching and parasitic relaxation oscillation effects, that result from the finite (~120µs) upper state lifetime exhibited by the neodymium ions in the YVO₄ host.

The nonlinear gain material was a periodically-poled 30x15x1mm³ MgO doped LiNbO₃ crystal (in this thesis referred to simply as PPLN) which featured a fanned-shape quasi-phase matching grating. The crystal was sourced from HCP Photonics, Taiwan and coatings were made by LaserOptik, Germany. The grating period ranged from 27-32µm over the 15mm axis of the crystal resulting in phase matching range of 1380 - 1780nm ($\Delta\lambda_s \approx 400\text{nm}$) for signal and 2645 - 4645nm ($\Delta\lambda_i \approx 2000\text{nm}$) for idler. In the developed arrangement, the temperature of the crystal was not controlled as the presence of an etalon in the signal cavity (to be discussed below) stabilised the operation wavelength well within the phase matching bandwidth of the nonlinear process. Despite the fact, that stronger and more characteristic absorption lines are present at the deeper-IR idler wavelengths, for this proof-of-concept experiment, a signal-resonant device was chosen as it was a better match to the diagnostics and optical component inventory accessible at the time of the project. The signal cavity was defined by mirror M2 (HR at the signal as well as

the pump wavelength), dichroic beam splitter BS (AR coated on both sides for the pump wave; HR on the inner surface for the signal) and M3 (HR at the signal wave). The common end-mirror M2 was fabricated from a CaF₂ substrate to ensure high transmission at deeper IR wavelengths; it was also coated for good transmission at the idler bandwidth which exited through this mirror after being generated in the nonlinear material. It should be noted that the parametric process (see Chapter 2) does not exhibit spatial hole burning or its analogue. This is due to the fact that parametric gain arises from perturbation in electronic orbits in the nonlinear material, rather than to electron level population changes that take a place in the laser. Thus, if only the incident pump radiation corresponds to the phase matching acceptance bandwidth of the parametric process, it can be in multi-longitudinal mode (i.e. multi-frequency) and even so, generate a single-frequency signal wave. As a result, no frequency selective components (e.g. etalons) were necessary in the pump cavity that typically oscillated on three longitudinal modes spaced by ~ 60 GHz. However, as will be introduced later in this chapter, etalons were introduced in the signal cavity to allow for its control and fine tuning. The phase-matching bandwidth (the gain bandwidth accessible to the down-converted wave) of the PPLN crystal lies between 250 and 750GHz (8 - 25 cm⁻¹), depending on the grating period. At the frequency of the selected ammonia absorption lines the gain bandwidth is approximately 300GHz (~ 10 cm⁻¹), as illustrated in Figure 5.5. Due to this fact, some form of frequency selectivity was required in the signal arm of the cavity. This was primarily applied to eliminate erratic mode hopping, rather than to lessen the instantaneous linewidth, which was single-frequency.

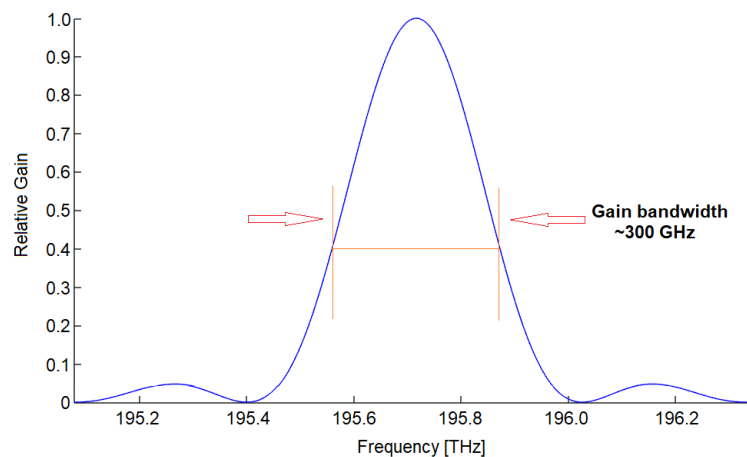


Figure 5.5. Parametric gain lineshape simulated for the PPLN crystal with full-width at half-maximum gain bandwidth centred around 6529 cm⁻¹.

During this project two forms of frequency selective devices were implemented: a 333GHz free spectral range (FSR), 20% reflectivity (R) at the signal wavelengths range air spaced etalon (ASE) and a 4.155mm long uncoated solid silicon etalon (~ 10 GHz FSR) whose surfaces exhibit a Fresnel-reflectivity of 30%, caused by the high refractive index of silicon. Both etalons

were supplied by LightMachinery Inc., Canada. The modelled transmission properties of these two components are shown in Figure 5.6. The free spectral range of the ASE was well correlated to that of the phase matching bandwidth, enabling $\sim 10\text{cm}^{-1}$ tuning over the spectral feature of interest, however the finesse was relatively low caused by the use of low reflectivity coatings. The piezo actuation of the ASE allowed very large tuning to be obtained with the etalon near its optimal ‘flash’ position, where walk-off losses were minimised. In contrast, the solid etalon could only be tuned with angle (using a precision galvanometer for this purpose) and due to its thickness, was prone to walk-off losses. Its higher per-surface reflectivity ($\sim 30\%$, because of the high Fresnel reflection) and significantly smaller FSR provided over ten times better selectivity when compared to the ASE, but causing the loss of tuning range, which was reduced by equal amount. With a complete permissible actuation potential of 100V on the ASE piezo, it was found that one total free-spectral range (of 333GHz) was achieved for 5V actuation. This indicates that if the tuning of the etalon were synchronised to that of the phase-matching condition (by simultaneously varying the PPLN crystal position and ASE piezo voltage), a continuous tuning range of 6.6THz (220cm^{-1}) would be reached. Such an activity was beyond the scope of this project. However, it signifies the tuning effectiveness of air spaced etalons, compared to their walk-off loss limited solid etalon alternatives.

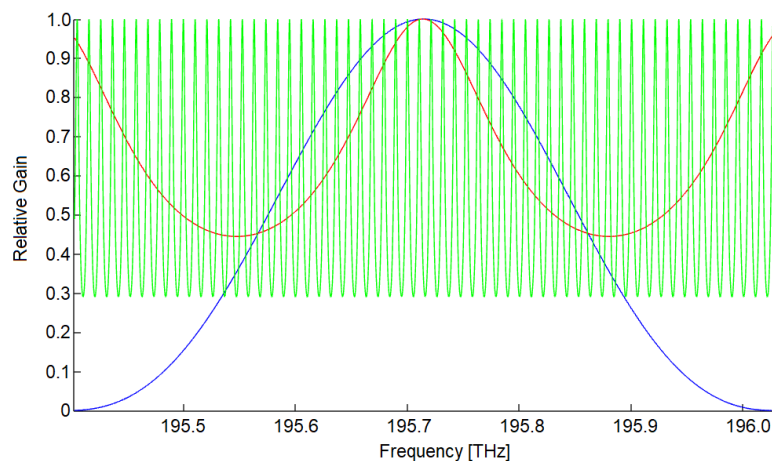


Figure 5.6. Frequency selectivity of the air-spaced (red) and solid silicon (green) etalons used in this study, projected onto the parametric gain lineshape of the PPLN crystal (as will be described below, the FSR of the corresponding OPO cavity is $\sim 430\text{MHz}$).

In order to increase etalon selectivity and reduce walk-off and mode-matching loss (present when there is discrepancy between the incident optical wave-front curvature and the plane surface of the etalon), a large beam waist collimated arm was constructed in the signal cavity. This was accomplished by placing a telescope in the area of the etalon region of the cavity. This also formed a waist in between the telescope and the end of the cavity (M3 in Figure 5.4) creating the space for the spectrophone to be placed later. Optical cavity designs of the pump and signal

cavities – created in the Psst! (Photonics Simulation Software for Teaching) – a software package developed at the University of St Andrews – are presented in Table 5.1 and a photo of the resulting system is shown in Figure 5.7.

Table 5.1. Designs of the pump (upper) and signal (lower) cavities. In the latter, the waist between lens L2 and the end mirror M2 is to place the spectrophone. The collimated area in between L1 and L2 is evident. Main parameters of used components are indicated in the description, where: λ – resonant wavelength; M1, M2, M3 - end mirrors of created cavities; QS – Q-Switch (Acousto-optic modulator); IC-L, L1, L2 – intracavity lenses; BS – beam splitter; PPLN – nonlinear PPLN crystal.

Pump cavity design	Description
	<ul style="list-style-type: none"> - $\lambda = 1064\text{nm}$ - M1: plane on 2% doped Nd:YVO4 - QS: $n=1.55$ (quartz crystal) - IC-L: $f=50\text{mm}$ - BS: $n=1.46$ (infrasil) - PPLN: $n=2.2$ - M2: $r=30\text{mm}$
Signal cavity design	Description
	<ul style="list-style-type: none"> - $\lambda = 1531\text{nm}$ - M2: $r=30\text{mm}$ - PPLN: $n=2.2$ - L1: $f=100\text{mm}$ - L2: $f=75\text{mm}$ - M3: $r= 50$ - 2nd waist radius $r=0.06\text{mm}$ - ASE: FSR=333GHz

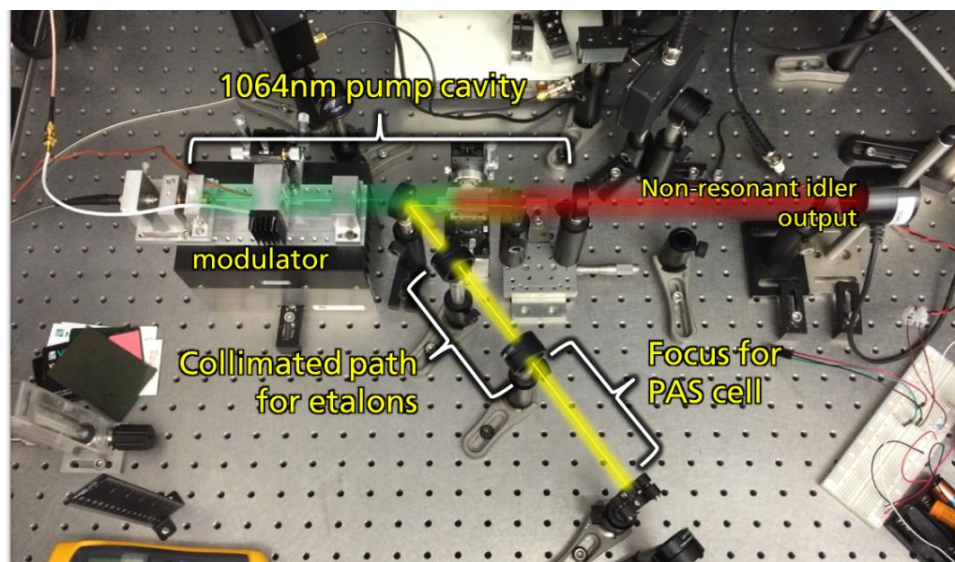


Figure 5.7. Intracavity OPO with extended signal arm to accommodate etalons and spectrophone (not shown).

The knowledge of the cavity length (based on the carefully replicated design from Figure 5.6) in the signal arm of the OPO, allows to derive free spectral range based on the formula [5.2].

$$FSR = \frac{c}{2 \sum n l} \quad [5.2]$$

where c is the speed of light, n the refractive index of the medium and l is the length of the cavity. For this design the FSR of the signal cavity is approximately 430MHz.

5.2.2. Power performance

Upon building and alignment of the IC-OPO, its power performance was characterised. In Figure 5.8 the extracted idler power is shown as a function of incident diode pump power. During these measurements neither etalons nor the spectrophone were present inside the cavity. It can be seen that at maximum incident 4W of diode pump power, 220mW of idler power at a wavelength of 3.3 μ m is obtained through M2. Considering the quantum defect between the idler and signal (that can be understood adequately as the ratio between their wavelengths) and the fact that the signal and idler are produced in both directions, it is possible to derive the total down-converted power. This allows to determine how much power is being converted from the circulating pump to signal and idler power during the parametric process. Down-conversion is the effective output coupling mechanism that the laser with IC-OPO experiences. However, it is an output coupling through the parametric process as opposed to linear one through a partial high reflector (as in a 'normal' laser). The calculated down-converted power is also overlaid in the figure. It can be seen that ~1.45W of power was down-converted from the circulating 1064nm pump to the signal and idler fields. Taking into account the round-trip linear loss of the pump (approximately 5%) and an optimal output coupled pump power (1.7W), a down-conversion efficiency amounts to 85%.

By estimating the round-trip loss of the signal cavity, the total optical field contained therein can be calculated using the expression 5.3.

$$P_s = \left(\frac{\lambda_i}{\lambda_s} \cdot 2 \cdot P_{idler_ex} \right) \frac{1}{\beta_s} \quad [5.3]$$

where λ_i and λ_s are the respective wavelengths of the idler and signal, P_{idler_ex} is the extracted idler power (also, bearing in mind extraction loss) and β_s is the signal cavity round-trip loss. Anticipating 5% round trip loss of the pump (that is approximation and is most likely less than that), an extracted idler power of 220mW corresponds to 19.2W circulating signal power of excitation to act on the photoacoustic spectrophone.

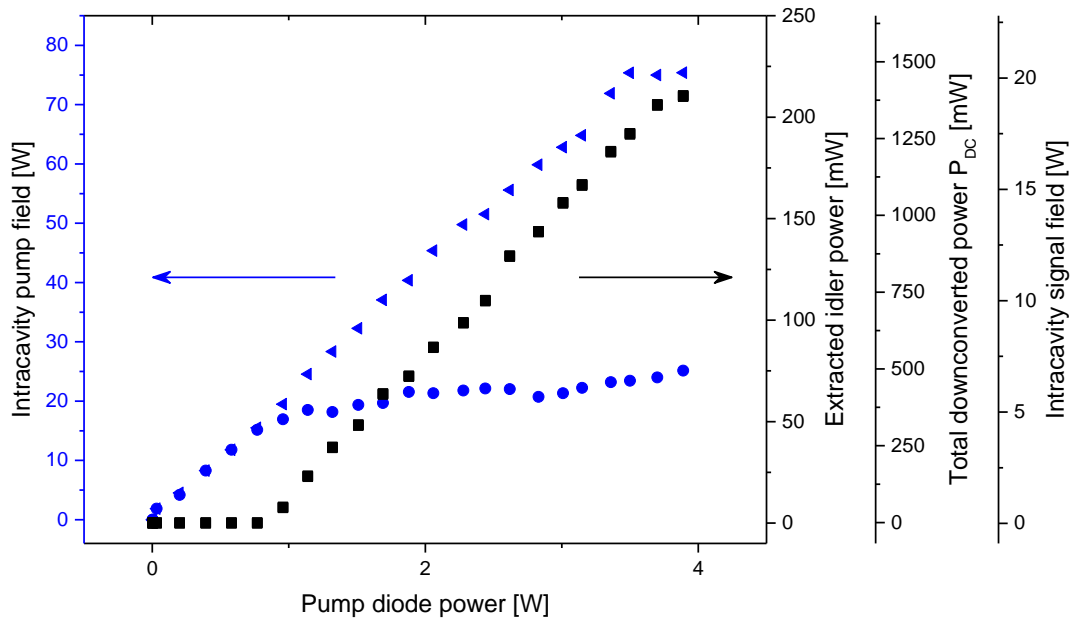


Figure 5.8. Power characteristics of constructed OPO where blue triangles represent intracavity pump field with OPO not working, blue circles depict the same with OPO working and black squares represent extracted idler power, total down-converted power and intracavity signal field on their respective axes.

To produce a signal in the AC-coupled photoacoustic process, the signal field amplitude has to be periodically modified. This was accomplished by varying the round-trip loss in the pump cavity by using the AOM. To get the maximum amplitude modulation in the signal field whilst maintaining the circulating pump field, the induced modulation depth needs to be carefully controlled. Three different amplitude modulations are presented in Figure 5.9. In zone (a), the modulation level is too low. Although some measure of modulation (green trace) is imprinted on the signal wave (yellow), the modulation depth is weak, thereby effectively wasting the DC offset that sits below it. In zone (b), the modulation drive signal has been increased to bring almost 100% modulation depth in the signal, but leaving the pump wave (purple) untouched. Initially this scheme was perceived as the best modulation regime. In the last place, zone (c), the result of modulation signal being increased too far can be seen. The duty cycle of the signal wave falls off and the modulation is so deep that it influences the circulating pump wave, which consequently can trigger relaxation oscillations and as such is detrimental. However, it was observed that the instantaneous PAS signal increases when amplitude modulation is raised to this level and the results presented below were achieved when the modulation was increased just beyond the zone (b). The relaxation oscillations affect the lineshape of the oscillating waves (both pump and signal), by introducing a high frequency noise across the line of the laser (see Figure 5.10). This is expected to be the source of low long term wavelength stability of the system. The fact that the pump wave is only affected at very high levels of modulation is an example of the ‘optical Zener’ effect of the

intracavity OPO clamping the field of the pump at the OPO threshold value (clearly demonstrated in Figure 5.8 and introduced in chapter 2.3.3.1).

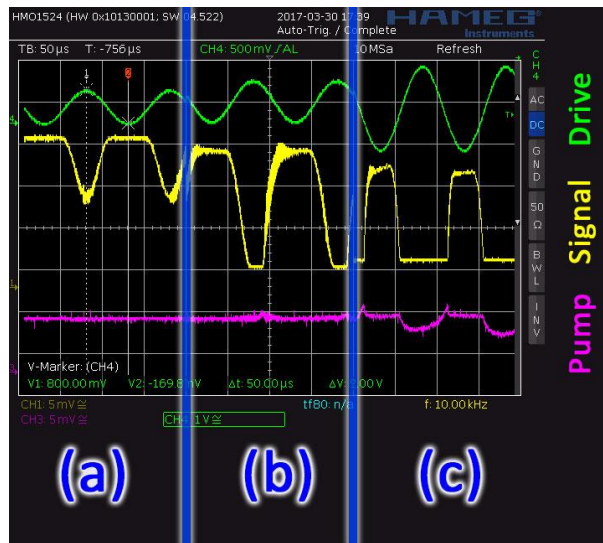


Figure 5.9. Impact of three different AOM modulation levels on the pump and signal fields. Green trace: modulation drive signal; yellow trace: circulating signal power; purple trace: circulating pump field. The three regions are described in the text.

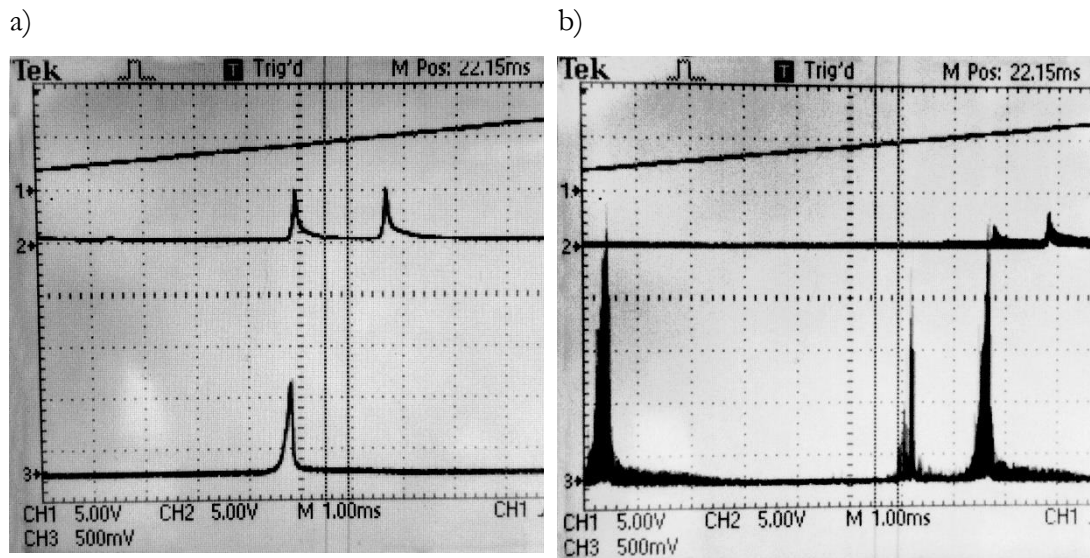


Figure 5.10. Oscilloscope traces of the scanning Fabry-Perot Interferometers for a) the modulation working zones (a) and (b) (see Figure 5.9) where pump wave is not affected and b) the modulation working zone (c) where the loss created by the AOM affects the pump wave, which subsequently induces the relaxation oscillations and high frequency noise in the pump and signal lineshapes. Trace 1 is the ramp signal of the interferometer; trace 2 is the lineshape of the oscillating pump wave and trace 3 that of the oscillating signal wave.

5.2.3. Wavelength, linewidth and tuning properties of the IC-OPO

The coarse tuning of the OPO is specified by its phase matching condition and therefore consecutively, for a defined temperature, is set by the lateral position of the PPLN crystal within the pump beam (see Chapter 2). As a result, the tuning of the OPO can be done by translating the crystal through the beam, as shown in Figure 5.11. The signal and idler waves tune over the range $1.48\mu\text{m}$ - $1.63\mu\text{m}$ and $3.05\mu\text{m}$ - $3.82\mu\text{m}$, respectively and cover a spectroscopically large part of the mid-infrared spectrum.

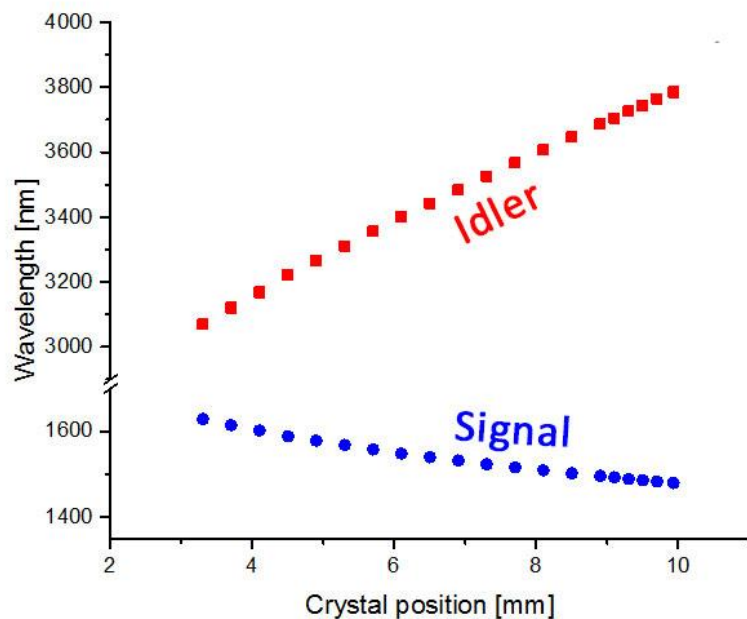


Figure 5.11. Coarse tuning of the OPO by varying the grating period.

The signal field operates on a single instantaneous longitudinal mode by reason of the mentioned above absence of spatial hole burning, gained throughout the parametric process. The specific cavity mode, with adjacent spacing $\sim 430\text{MHz}$ (as demonstrated in Section 5.2.1), at which point it functions, is just weakly selected by the very wide phase matching bandwidth ($\sim 300\text{GHz}$) of the parametric process. Therefore, to receive high precision control over the particular optical frequency by which the wave signal operates, etalons were introduced into the cavity. After synchronising the spacing of the ASE with the length of the signal cavity, it is possible to demonstrate mode-hop free tuning over many 10's or 100's GHz. Nevertheless, this was not executed in this study, since hopping on adjacent cavity modes every $\sim 430\text{MHz}$ was well within the pressure-broadened linewidth ($\sim 3\text{GHz}$ wide) of the characteristics of interest. As this setup was built in a standing wave configuration, the interfaces between the AR coated intracavity components and air, that is nodal effects at substrate borders, give rise to a weak but finite,

parasitic, frequency selective effect inside the cavity, which can interfere with the tuning performance of the etalon.

In Figure 5.12 the tuning behaviour of the signal field is presented, as controlled by the air-spaced etalon and measured using an optical wavemeter (Hewlett Packard, 86120B Multi-Wavelength meter, resolution: 100MHz). This result was obtained by altering the voltage on the ASE piezo and recording the optical frequency of the signal wave at each time when a mode hop was generated. The pattern shown in Figure 5.12 is repetitive every time the free spectral range of the etalon is exceeded. Thus, the saw-tooth pattern displayed in this figure would continue up to a maximum piezo voltage of 100V. The shaded area of the figure highlights that the frequency tuning span of the signal is very well controlled over the free spectral range tuning extent of the ASE (333GHz) and provides an excellent span for a spectroscopic measurement.

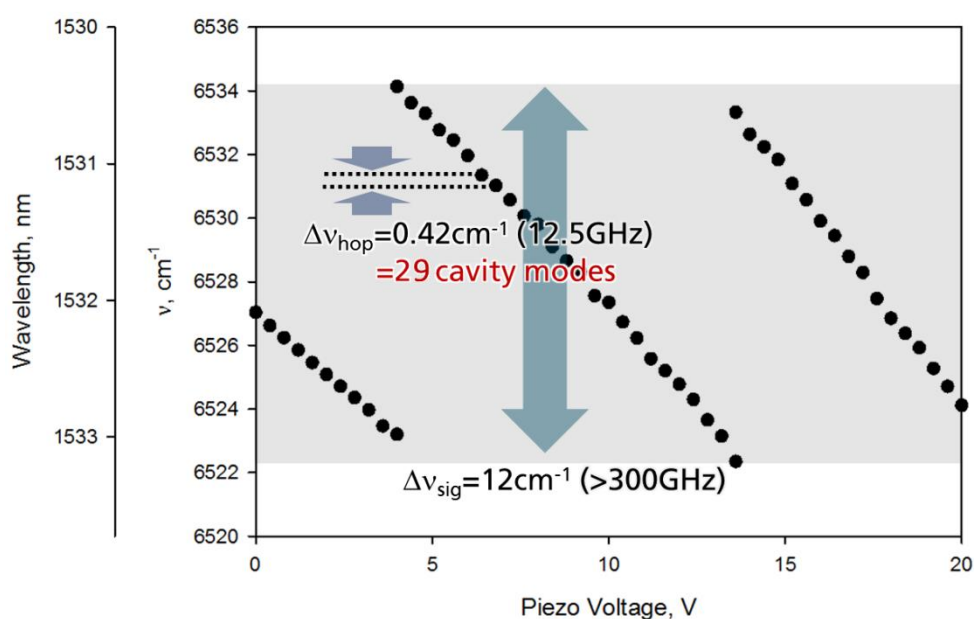


Figure 5.12. High precision tuning of the signal wave with air-spaced etalon.

Due to the nodal problem mentioned above, combined with the low finesse of the etalon, there is an obstacle data manifesting itself in this result. Rather than on adjacent $\sim 430 \text{ MHz}$ cavity modes, the signal field hops multiple cavity modes each time. In this case, the average jump was $\sim 12.5 \text{ GHz}$ which corresponds to ~ 29 cavity modes. This in itself does not exclude photoacoustic spectroscopy but significantly decreases the spectral resolution of the system. Moreover, it makes the tuning into the absorption line of selected molecule challenging. To ameliorate the system, an additional, solid silicon etalon was incorporated into the collimated section of the signal arm. However, to accommodate this etalon the signal arm of the OPO had to be redesigned (see Table 5.2), and it was rebuilt as shown in Figure 5.13. It is worth pointing out that an extra fold was built into the signal arm to achieve a more compact geometry.

Table 5.2. Changed design of the signal cavity allowing sufficient space in the collimated section for multiple etalons.

Signal cavity design	Description
	<ul style="list-style-type: none"> - $\lambda = 1531\text{nm}$ - M2: $r=30\text{mm}$ - PPLN: $n=2.2$ - L1: $f=150\text{mm}$ - L2: $f=100\text{mm}$ - M3: $r= 50$ - 2nd waist radius $r=0.052\text{ mm}$ - SE, FSR=10GHz - ASE, FSR=333GHz

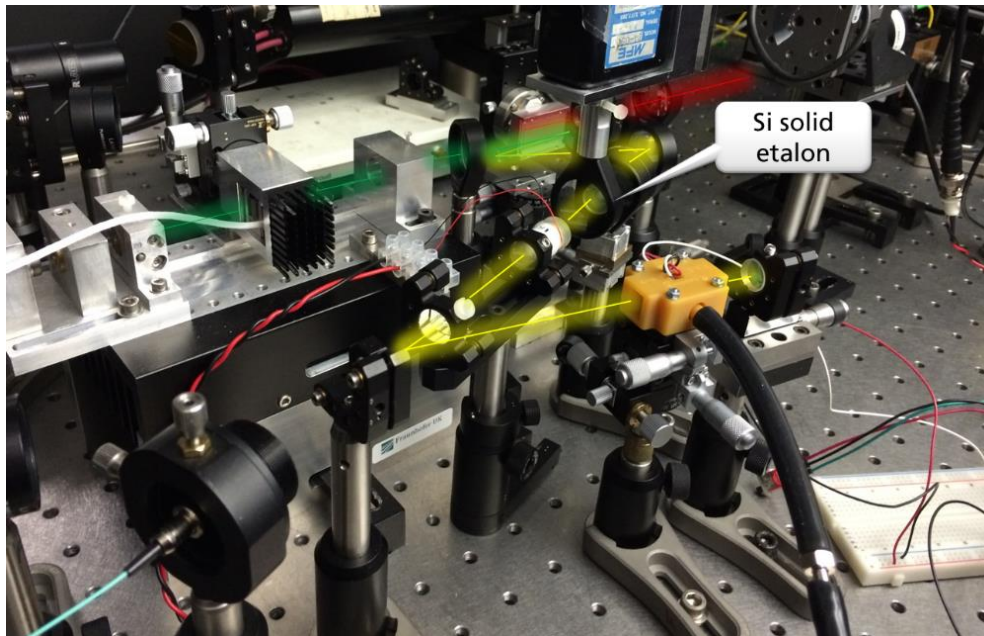


Figure 5.13. Folded signal cavity containing both air-spaced and solid silicon etalons. Note, the silicon etalon is mounted on a galvanometer for precise angular control and the PAS cell is located at the second focal point.

Furthermore, a spectrophone was placed in the focus of the signal field. This new design resulted in the physical length of the cavity extended to 509mm which, based on the formula [5.2], rendering the free spectral range in the signal arm to $\sim 293\text{MHz}$. Both etalons were used simultaneously: the ASE to suppress adjacent free-spectral ranges of the silicon etalon by effectively narrowing the phase-matching gain. The fine selectivity was granted by the silicon etalon. The resulting tuning behaviour is presented in Figure 5.14.

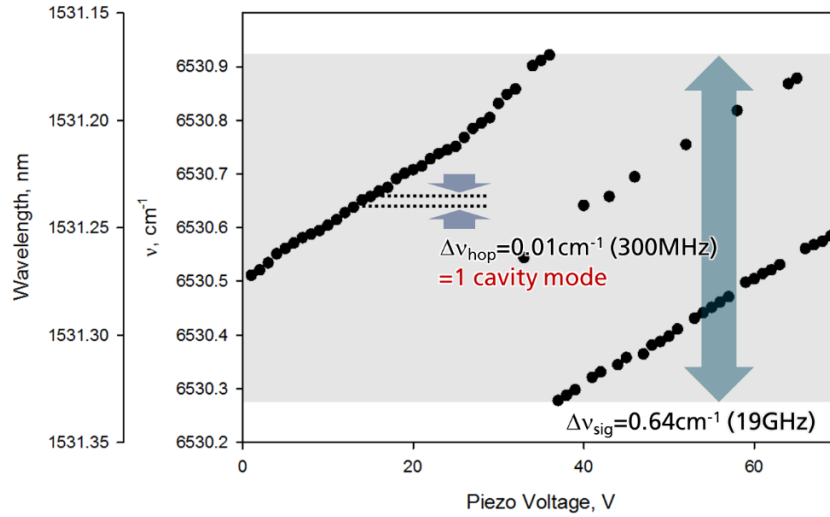


Figure 5.14. High precision signal tuning with both ASE and solid silicon etalon.

As shown in Figure 5.14, the benefit of the improved selectivity conferred by the solid silicon etalon incorporated into the system is clear. The signal field hops on adjacent modes of the cavity in which it is resonant. Therefore, the spectroscopic features can be resolved down to the free spectral range of the signal cavity, which is a width of $\sim 300\text{MHz}$, – well within the pressure-broadened linewidth that the molecular features of interest would exhibit. Unusually for this type of tuning, the plot presented in Figure 5.14 demonstrates jump of approximately 2 free spectral ranges of the solid etalon, with only sparse data points on the 1 FSR distant mode. It is expected that this phenomenon is caused by the nodal effects of standing wave cavity and many other frequency selective losses caused by the cavity design, superimposed with the phase matching bandwidth and etalons, favouring the modes 2 FSR away.

The penalty paid by the free spectral range exhibited by this etalon (approximately 10GHz) manifests itself in greatly reduced overall tuning range - in this case 19GHz . However, it will be revealed in Section 5.4.1.1 that it is still sufficient to tune across the peak of the absorption features of interest, even if this range is over an order of magnitude lower than that of the ASE. The main focus of this proof-of-concept experiment was to show the sensitivity enhancements conveyed by the intracavity approach, as opposed to broad spectral resolution (even though this is still greatly desirable). Including the second etalon facilitated precise and stable control over the signal field optical frequency. This arrangement allows to demonstrate proof-of-concept results, but a more optimal solution would be accomplished through a single ASE with more sophisticated coatings, in addition to the application of a ring-type signal cavity that would not exhibit the parasitic nodal frequency-selective effects. This is discussed thoroughly in the Section 5.6.2 of this document. The introduction of the two etalons increased the round-trip loss of the signal cavity which had an adverse impact on the signal field power available for the photoacoustic excitation.

Optical power of $\sim 19\text{W}$ circulating without any etalons present in the cavity was reduced to $\sim 12\text{W}$ with just the ASE inserted and 10W with both etalons. Comparing this to 220mW of output-coupled idler, (or approximately 450mW of signal, assuming only impact of quantum defect and comparable losses for both waves) represents significant, $\sim 20\text{x}$ excitation power increase. This, set side by side with only 4W of primary pump power, demonstrates the potency of this configuration.

5.3. Photoacoustic spectrophone

5.3.1. Microphone-based spectrophone

5.3.1.1. Design

In order to achieve a functioning photoacoustic system operating as quickly as possible, the adopted design was inspired by a 3D-printed spectrophone reported in the literature [30] – see Figure 5.15. The choice of this particular spectrophone was based on a number of attractive features: it was miniature in nature, could be 3D printed and had an expected resonance Q of ~ 20 . Additionally, it exhibited a resonant frequency of the same order as that of the quartz-enhanced spectrophone that we hoped to use later in the project. More than that, the buffered output stage of the capacitive electret-type microphone had reasonably low impedance, making easy interfacing possible and subsequent lock-in signal recovery.

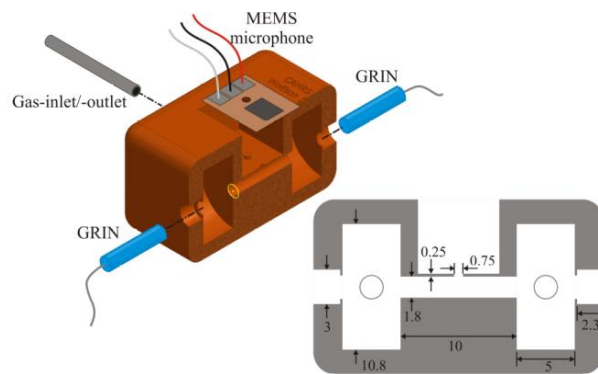


Figure 5.15. 3D printed spectrophone (basis of adopted design) in cross section [30].

A cross section of the spectrophone, as detailed in the cited paper, appears in Figure 5.15. The total length of the cavity, that is the section in which the photo-induced acoustic wave is resonant, is only 10mm , revealing the small nature of the module. The large buffer area at each end forms a sharp drop in pressure, such that the incident sound wave is reflected back into the cell. Therefore, solid windows are not obligatory to be present in order to contain the acoustic wave. This setting is advantageous since windows can introduce optical loss into the signal cavity. In the

quoted paper, light was coupled into the cavity via optical fibres and graded-index (GRIN) lenses. There is no need for these in the current configuration because of the excellent Gaussian beam quality of the circulating mode with waist diameter approximately $120\mu\text{m}$. The modified design, stimulated by the above, is demonstrated in cut away and completed form in Figure 5.16 (a) and (b) respectively.

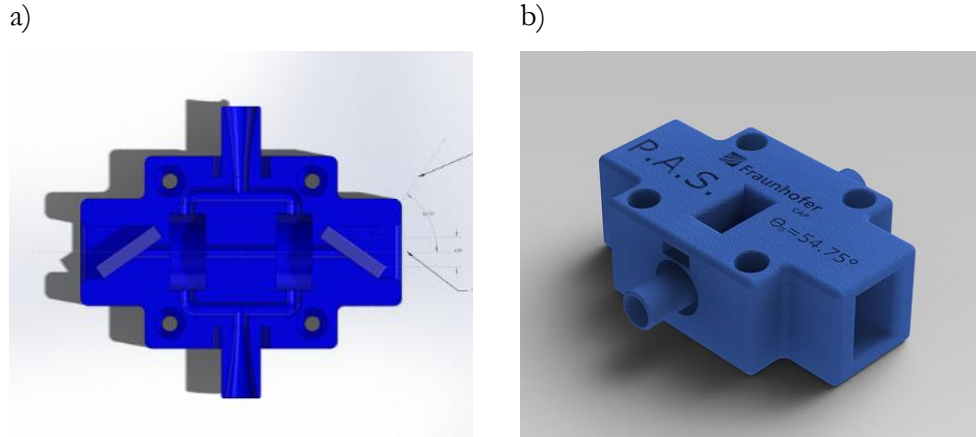


Figure 5.16. PAS spectrophone designed for this project.

As shown in Figure 5.16(a), the acoustic cavity is bounded by the two plenum areas at either end. The sampled gas enters by the spigot to the top of the figure and flows into the acoustic chamber via these plenum areas. This reduces noise instigated by the influx of gas. Optional Brewster windows are clear in presented cross-section, which provides a mechanism to seal the chamber if necessary, while introducing minimal loss to the incident signal field. Due to very high transmission at the desired wavelength range, Calcium Fluoride (CaF_2) was selected as the material used for the windows. To optimise the resonating idler configuration, the holders were designed with an angle of 54.75° , which is the Brewster angle at $3.3\mu\text{m}$ wavelength for this material. The angle for resonating signal at $1.5\mu\text{m}$ is 54.95° as shown in Figure 5.17.

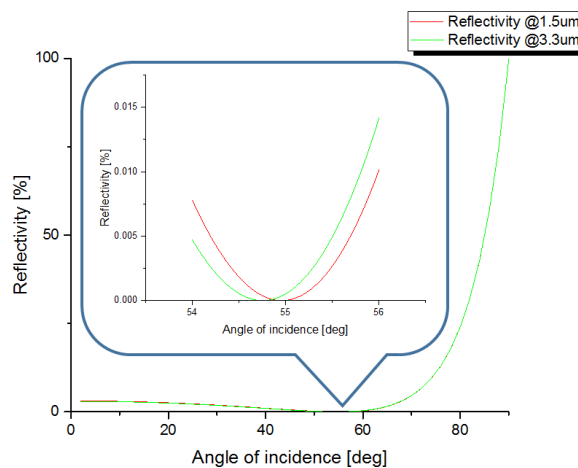


Figure 5.17. Reflectivity curves for Calcium Fluoride at $1.5\mu\text{m}$ and $3.3\mu\text{m}$ radiation wavelength with an insert plot showing an offset between the two respective Brewster angles.

Next to the abovementioned changes in the design of the cell, the length of the acoustic cavity was kept at 10mm. The resonant frequency f_c of the spectrophone is given by formula [5.4] for the resonance frequency of open-end pipes.

$$f_c = \frac{c}{2l} \quad [5.4]$$

where c is the speed of sound in given medium, and l is the length of the resonator. The quality factor of the resonator can be calculated based on the formula [5.5].

$$Q = \frac{r \cdot \sqrt{\rho \pi c}}{(\gamma_h - 1) \cdot \left[\frac{2\kappa}{c_p} + \sqrt{2\mu} \right] \cdot \sqrt{l}} \quad [5.5]$$

where r is the radius of the resonator and l is its length, ρ is the gas density, κ is the thermal conductivity, C_p is the heat capacity, γ_h is the specific heat ratio of the target gas and μ is the dynamic viscosity. Based on geometrical design of the spectrophone and choice of the nitrogen as the gas medium, both these parameters can be derived resulting with resonance condition of $f_c = 17.6\text{kHz}$ and $Q = 21$.

The rectangular dip in the top of the casing exhibited in Figure 5.16(b) is designed for placement of the microphone. To assure that the frequency response of the microphone will overlap with the resonance condition of the cell, an Invensense INMP504 ultra-miniature Micro-Electrical-Mechanical Systems (MEMS) capacitive-type electret transducer was used, whose relative acoustic response is shown in Figure 5.18.

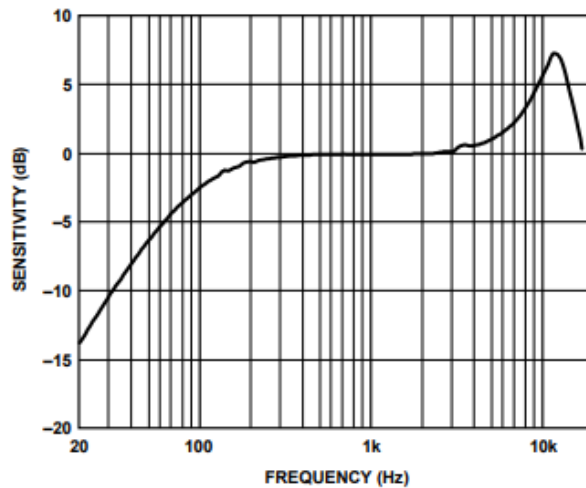


Figure 5.18. Typical (measured) frequency response of the INMP504 microphone [31].

The cell was 3D printed using the UV-cured liquid resin technique, to ensure good surface finish of the inner bore. This is significant, as roughness facilitates obstruction of the resonant acoustic

wave and thus a reduction in Q . The resulting cell is shown in Figure 5.19: fully fabricated in (a) and installed in the laser in (b).

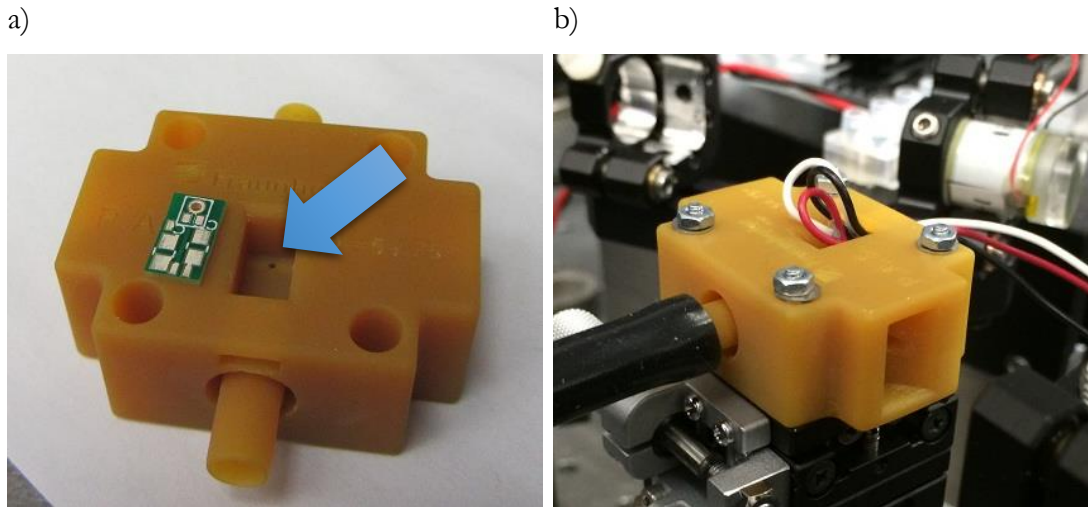


Figure 5.19. 3D-printed spectrophones as used in this project: (a) before integration with microphone, featuring the PCB for microphone connection and (b) fully integrated and installed in the optical setup.

To maximise the coupling of the acoustic wave, the microphone is assembled on an especially thin printed circuit board (PCB) – 0.8 mm. As shown in Figure 5.19(a), there is the small hole (indicated with the arrow) though which a small portion of the anti-nodal standing acoustic wave exits.

5.3.1.2. Characterisation

The characterisation of the spectrophone was done in two different locations, extra- and intracavity to the OPO and with use of two different gas mixtures: butane-air in unknown ratio in extra-cavity configuration and with 100ppm of ammonia mixture with nitrogen (balance) in the intracavity case.

In the extra-cavity arrangement pure butane was used to ensure a strong photoacoustic response in the idler range. The spectrophone was filled with this gas, however since this was not in a form of continuous flow but rather a single injection, pure butane was certainly diluted with air. The OPO was tuned to the 3365nm in the non-resonant idler that was coincident with the absorption feature of butane. During this test the pump laser was operating in pulsed regime, by Q-Switching technique with the frequency of approximately 220kHz. This is the only test done in this project with OPO pumped by pulsed laser and all the other tests were performed with laser in continuous wave (CW) regime. The average idler power of 150mW was additionally amplitude-modulated by gating the AOM operating at Q-Switch frequency. The modulation (gating)

frequency was linearly varied between 5kHz and 25kHz. The response from the spectrophone was measured in a form of the Lock-in Amplifier (LIA) voltage as the function of changing modulation frequency. This characteristic is presented in Figure 5.20.

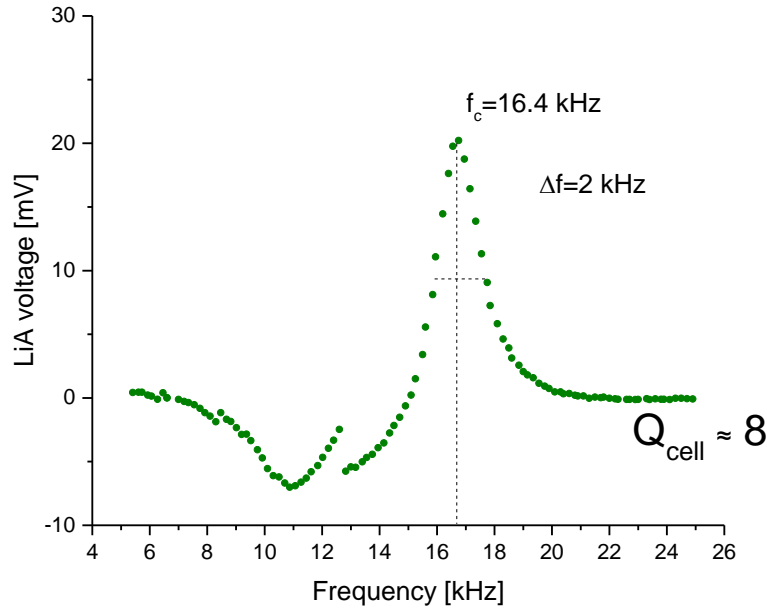


Figure 5.20. Characteristic of the PAS spectrophone in the extra-cavity position as a function of the modulation frequency.

Due to the unknown ratio of the butane-air mixture it is impossible to calculate the exact speed of sound of that medium, however it can be estimated as between 348 m/s (for pure air) and 194 m/s (for pure butane) at the temperature of 300K (26.85°C) [32]. Based on these values and the formula [5.4] the resonance frequency was expected to lie in the range between 17.4kHz and 9.7kHz. As can be seen in Figure 5.20, the resonance condition was met at the 16.4kHz frequency, which would suggest that there was an air-rich mixture in the spectrophone. The quality factor can be calculated based on the formula [5.5], however knowing the frequency characteristic of the resonator, it also can be derived based on the formula [5.6].

$$Q = \frac{f_c}{\Delta f} \quad [5.6]$$

where Δf is the full width at half maximum (FWHM) bandwidth of the damped resonator. Based on the measured characteristic, the bandwidth was 2kHz resulting in the Q factor of approximately 8. The measured Q factor is about 3 times smaller than the theoretical value. This can be associated with effects of the aforementioned surface roughness of the inner bore altering the resonance of the reciprocating wave. Nonetheless, the resonance of the spectrophone still gives an approximate order of magnitude improvement over simply placing the microphone in proximity of the excitation beam. It also offers a suitable mechanism to deliver the sample gas to the test area in a controlled and reproducible manner. The operating frequency of $f_c = 16.4\text{kHz}$ is advantageous

since it is far above the majority of the background acoustic spectral noise density. The discontinuities of the characteristic observable in Figure 5.20 are artefacts associated with the gated-pulsed operation of the laser and each time when amount of pulses per gate decreased, average power of the laser was changed resulting in a discontinuity in the acquired plot.

Upon successful characterisation of the spectrophone in the extra-cavity configuration with output-coupled idler as the excitation radiation, a similar profile was recorder for the intracavity position. The PAS cell was placed at the waist of the circulating signal wave of the OPO tuned to operate on 1531nm (to coincide with the 6528.8cm^{-1} absorption line of ammonia). In this case, as for all the subsequent tests, the pulsed operation was replaced by the CW regime and the amplitude modulation was performed at a fixed depth using the AOM, as previously described in Section 5.2.2. Similar to the extra-cavity characterisation, the modulation frequency was tuned between 5kHz and 25kHz. The gas used in this test (100ppm of ammonia in N_2) was connected to the PAS cell from the pressurised cylinder containing this mixture. The gas flow was controlled and it was delivered to the cell at the rate of 130ml/min. This mixture was continuously flowing through the cell, therefore it can be assumed that there was no ambient atmosphere in the resonator and only this mixture was monitored by the device. The resulting characteristic is presented in the Figure 5.21.

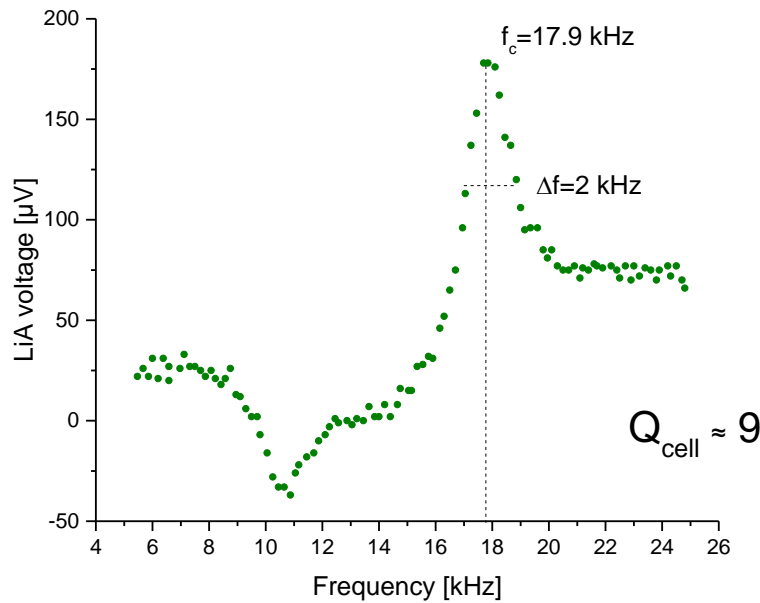


Figure 5.21. Characteristic of the PAS spectrophone in the intracavity position as a function of the modulation frequency.

Due to the fact that the gas mixture used during this test had only trace levels of ammonia in nitrogen, for the characterisation purpose approximation can be made that the balance gas was used as the only medium in the cell. The speed of sound in nitrogen at 300K is 352m/s therefore, as described in Section 5.3.1, the resonance condition of the cell with this medium is

$f_c = 17.6\text{kHz}$. The test result illustrated in Figure 5.21 indicates a resonance frequency at $f_c = 17.9\text{kHz}$ which is in good agreement with the theoretical calculation. The higher resonance frequency observed in practice could be caused by the presence of 100ppm of ammonia in the gas mixture, which with its higher speed of sound (440m/s at 30°C (303.15K) [33]) would increase the overall resonance condition for that mixture. The FWHM bandwidth was the same as for the extra cavity test and therefore empirically obtained Q factor based on formula [5.6] is approximately 9. This value is in line with the extra cavity result and it suggests that indeed the difference between real and theoretical Q factor for this spectrophone is created rather by the cell finish quality than gaseous medium or excitation source.

5.3.2. Quartz tuning fork-based spectrophone

The detection of sound waves may be done using an entirely different method called quartz-enhanced photoacoustic spectroscopy (QE-PAS) [34]. The microphone is not used in the usual sense but the piezo-electric effect in a quartz tuning fork is exploited to create a sinusoidal signal at the incident modulation frequency. There are two crucial advantages of QE-PAS: (i) the only piezo-active vibrational mode in such a tuning fork arrangement is in the opposing vibrational mode (i.e. where the prongs oscillate in opposite directions) and (ii) the fact that the resonance in vacuum has an enormous Q of 100,000, dropping to $\sim 10,000$ in air (due to viscous drag) [20, 34]. The former gives excellent immunity to background acoustic noise, even if this happens at a frequency coincident with the resonance. The latter offers a route to exceptional sensitivity.

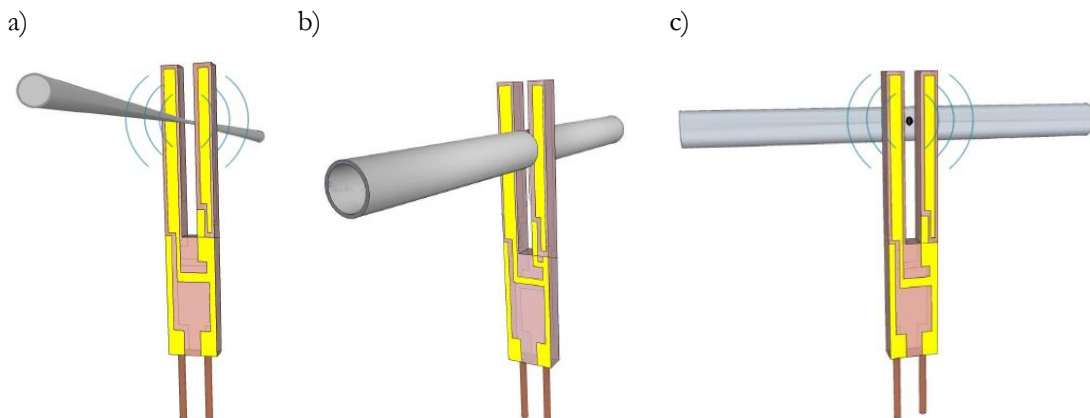


Figure 5.22. QE-PAS spectrophone geometries. (a) bare QTF, (b) in-line, and (c) off-axis (adapted from [20]).

The quartz tuning fork (QTF) described above, and how it is used in its simplest embodiment is presented in Figure 5.22(a). The incident excitation beam is simply focused down within its two prongs to generate a vibrational mode through the photo-thermal effect. The

spacing in between the prongs is only 300 μ m and it is crucial that beam does not interact with the prong arms directly since it can create a very large background signal that severely decreases the SNR. To improve the SNR even more, the QTF can be placed within an acoustically resonant tube, by using the same methodology as the standard PAS cell above, as indicated in Figure 5.22(b) and (c). A QTF equipped with the resonator tubes is called acoustic detection module (ADM). An enhancement factor of ~ 30 can be obtained by placing a resonance tube on either side of the QTF, but getting alignment and integration in the beam is more difficult than in the bare QTF alone [20, 35]. The off-axis strategy can be used as a compromise solution, where the resonant acoustic wave is coupled into the QTF through a flute-like aperture in the side of the tube. This diminishes the enhancement by a factor of ~ 1.7 when compared to the in-line method, but alignment becomes considerably easier [20, 36].

5.3.2.1. Commercial spectrophone from CDP Systems

This investigation was based on making the best use of the considerable advantages offered by QE-PAS spectrophones. However, this time without having to spend significant time in the design and construction cycle that includes: (i) extraction QTF crystals from their packaging, (ii) design and fabrication of micro-scale resonance tubes then (iii) aligning them to the QTFs and (iv) signal recovery of the resulting $\sim \mu$ V signals. To accomplish this, a commercial QTF spectrophone system from CDP Systems was acquired. This approach allowed the project to have quick access to a QTF pre-aligned with an in-line resonance tube as demonstrated in Figure 5.22(b), along with mature instrumentation enclosing automated resonance frequency detection, low-noise trans-impedance amplifier, Q-calculator and digital lock-in signal recovery. A photo of the purchased system is displayed in Figure 5.23.



Figure 5.23. Commercial CDP Systems QE-PAS system purchased for use in this project.

This device does not come with dedicated software and only commands for the remote control are provided. To facilitate the project, the graphical interface-based control software was written

in Matlab environment, controlling all main settings and allowing data acquisition. The screenshot is presented in Figure 5.24.

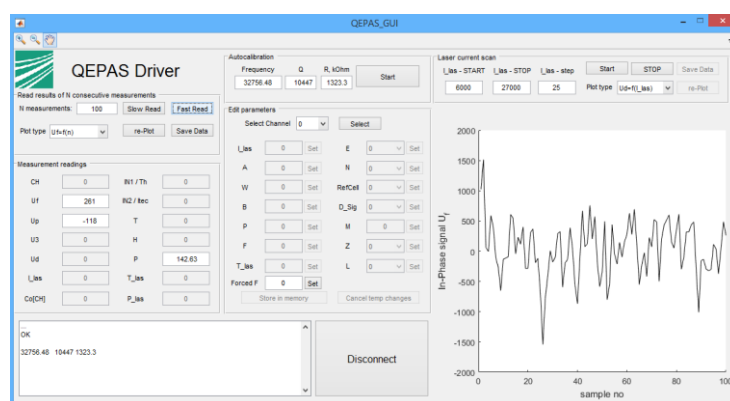


Figure 5.24. Graphical interface of the software controlling the CDP Systems QE-PAS system.

Due to the fact that ammonia was chosen as a target molecule in this project, this instrument was equipped with an internal distributed feedback (DFB) laser tuned into an absorption feature of ammonia at 6528.8cm^{-1} (1531.68nm). The control unit allowed frequency modulation of the laser diode and its output was fibre coupled into a QE-PAS cell in a standard, extra-cavity setup. This feature was useful as it facilitated the possibility of calibration and cross-checking our proposed device once operational.

The purchased spectrophone was not developed to a high level of refinement since QE-PAS is a relatively low-volume market so far, dominated by the Research and Development (R&D) sector. The instrumentation supplied with the device was adequate, however, the quality of the spectrophone needed significant improvement. A photo in Figure 5.25 indicates the build quality of the device. The fabrication strategy was to put the resonance tube in place within a slot of housing. This is a creditable approach, as it gives some freedom to optimise the tube position around the prongs while the resin solidifies. However, the original slot in which the tube resides appears to have been cut with a hacksaw.



Figure 5.25. Acoustic detection module received from CDP Systems.

Figure 5.26(a) indicates the precision with which this must be aligned. A bridge between the two tubes passing in between the forks is noticeable. Its function is to maximise containment of the circulating acoustic wave as well as guarantee that an anti-node in the standing wave exactly corresponds with the centre of the tube [37, 38]. The design or the manufacturing approach was not the main problem with the delivered device but the quality of its finish, as indicated in Figure 5.26(b). A severe burr is evident on the end of the tube that in practice made it impossible to mount the spectrophone inside the OPO cavity of the signal wave without introducing so much loss that the OPO did not reach threshold. It was still impossible to get the OPO to operate while the QE-PAS cell was in place even after cleaning the end of the tube, as shown in Figure 5.26 (c). Presumably this was due to additional structures such as burrs within the tube that were impossible to be seen or accessed.

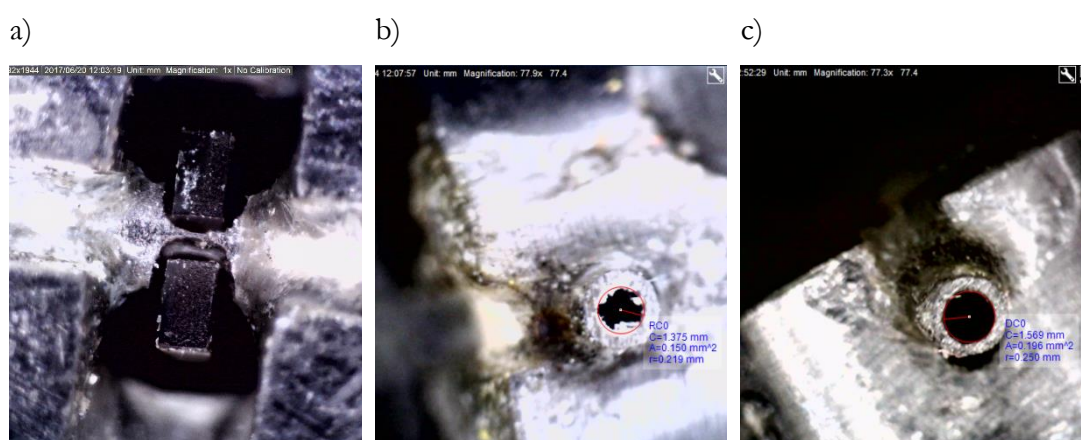


Figure 5.26. Close up of the CDP Systems ADM. (a) resonance tube surrounding QTF, (b) poor finish on tube end, (c) tube end after de-burr.

5.3.2.2. In-house fabricated spectrophone

The lack of success with the commercial spectrophone initiated an attempt at an in-house fabrication of a QE-PAS spectrophone. Photographs of two early attempts are shown in Figure 5.27 where two materials – Polyether ether ketone (PEEK) and brass – were evaluated. PEEK seemed to be an attractive choice since the exceptionally fine features had to be machined into the material (the bridge width was $\sim 150\mu\text{m}$). Nevertheless, the derived thin sections did not present sufficient mechanical strength that was necessary to avoid chatter under processing, leading to ragged features. On the contrary, the brass test piece machined well. These elements were test pieces only to assess which material would be most suitable to make a spectrophone. They were not intended to be integrated into the system, since the slot width of $\sim 2\text{mm}$ (limited by the cutter size available at the time) was far too wide for efficient coupling of the acoustic wave energy into the QTF. In effect, the air would ‘escape’ around the sides of the QTF.

As it will be described in Section 5.4.2, significant issues were experienced when focussing the signal excitation field down in between the prongs of the standard QTF with an adequately small waist to avoid clipping a prong. Therefore, it was decided to proceed with an off-axis design (Figure 5.22 (c)). This strategy was inspired by Liu et al [36], where micro-slots were cut into the side of a hypodermic needle as shown in Figure 5.28(a). The 50 μ m ridge on either side of the slot was present to reduce viscous drag on the oscillating QTF prongs.

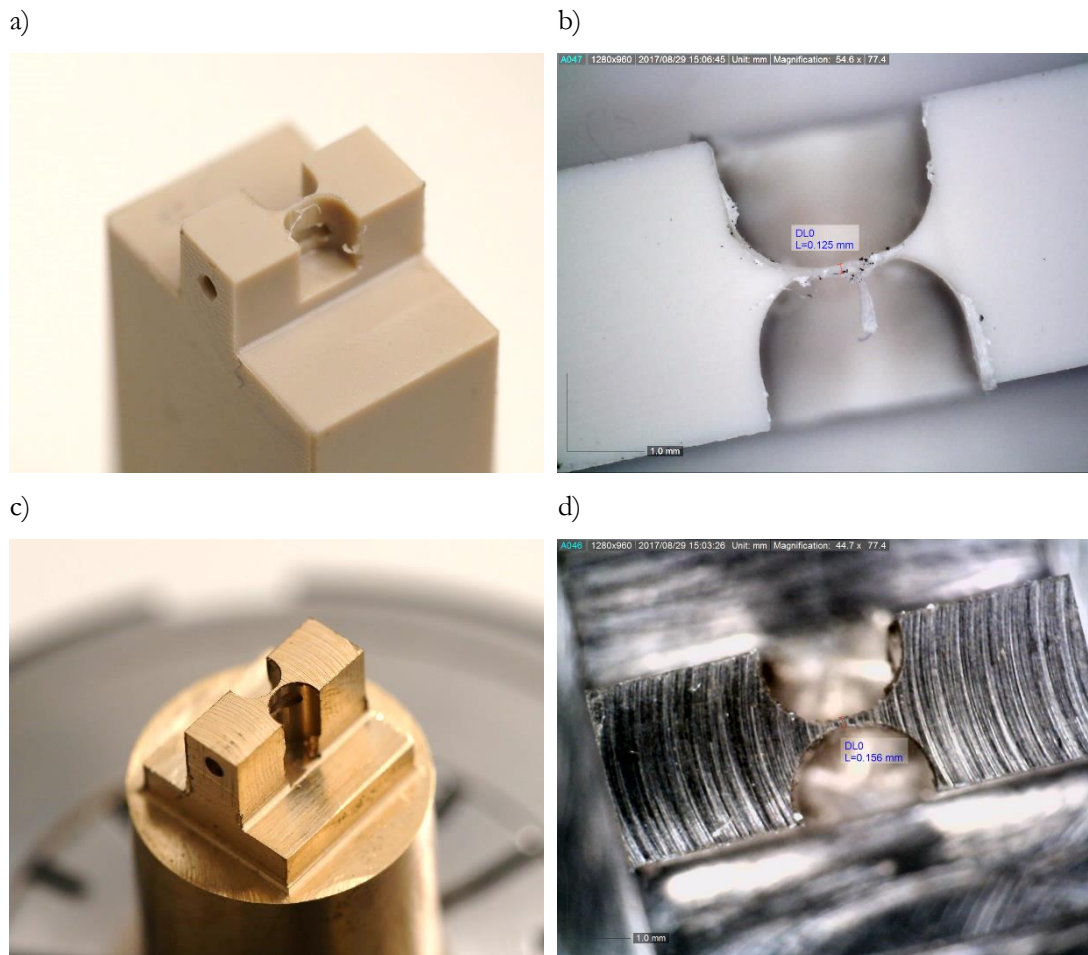


Figure 5.27. Preliminary material evaluation with PEEK [(a) & (b)] and brass [(c) & (d)].

The in-house adapted design module is shown in Figure 5.28(b), where the QTF will be held by an x-y-z- θ - ϕ stage and manoeuvred into position symmetrically above the exit slot. The fork prongs must be within $\sim 50\mu$ m for effective acoustic coupling, so alignment will use a microscope. While epoxied, the QTF will be held in place by the mount. Unfortunately, the work described here was not finalised during the duration of this project and so the efficacy of this approach and the performance of the resulting spectrophone, cannot be reported in this thesis. It will be pursued and completed in the subsequent projects following up this activity.

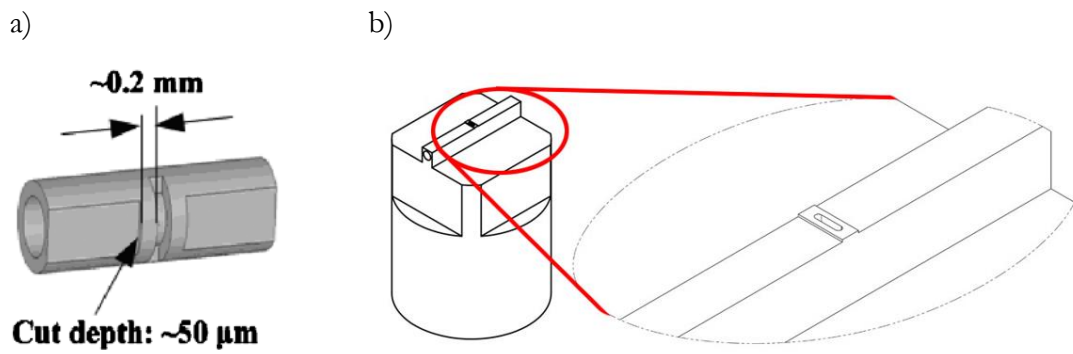


Figure 5.28. Off-axis QE-PAS spectrophones. (a) Literature design (8mm long, 150 μ m slot width) [36], (b) in-house design (dimensions same as in (a)).

5.3.2.3. Bare QTF spectrophone

In the absence of a viable resonant-enhanced spectrophone, the application of a bare QTF-based photoacoustic sensor was studied. For this task COTS 32,768Hz QTF elements were purchased and extracted from their containing cans. This was accomplished by reverse-mounting of each can in a pin chuck and cutting through its base with a sharp half-moon needle file. A photo of the extracted QTF, along with its measured dimensions, appears as Figure 5.29.

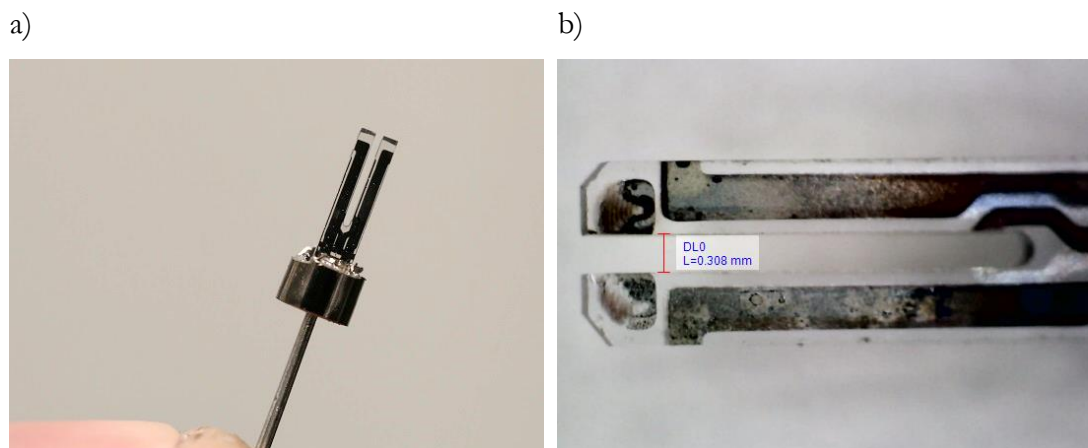


Figure 5.29. A QTF removed from its packaging (a) and a close-up with the measurement of the gap between the prongs (b).

The CDP Systems control unit was able to characterise the crystal attached to it in terms of resonant frequency and Q. Monitoring the resonance frequency of the crystal ‘on the fly’ is a very advantageous feature as the modulation of the excitation beam can be slaved to it and thus, ensure that the peak QTF resonance is consistently excited. Removing the QTF from its can exposes it to the viscosity of air, which acts as a significant damping mechanism that in turn, impacts upon Q. Figure 5.30 shows the comparison of the Q of the exposed QTF: the one supplied by CDP and another, still within the vacuum of its casing.

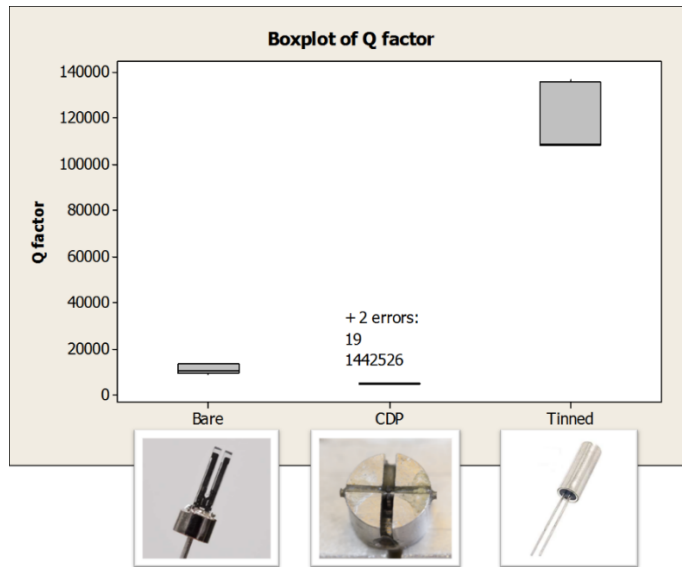


Figure 5.30. Comparison of QTF performance under different conditions.

Removing the QTF from its packaging resulted in a significant drop in Q, but still the bare QTF exhibited a very respectable Q in excess of 13,000. Next, the bare QTF crystal was mounted on a circuit board for permanent attachment to the CDP preamplifier, which subsequently was mounted on a high precision multi-axis adjuster for installation inside the signal cavity, as shown in Figure 5.31.

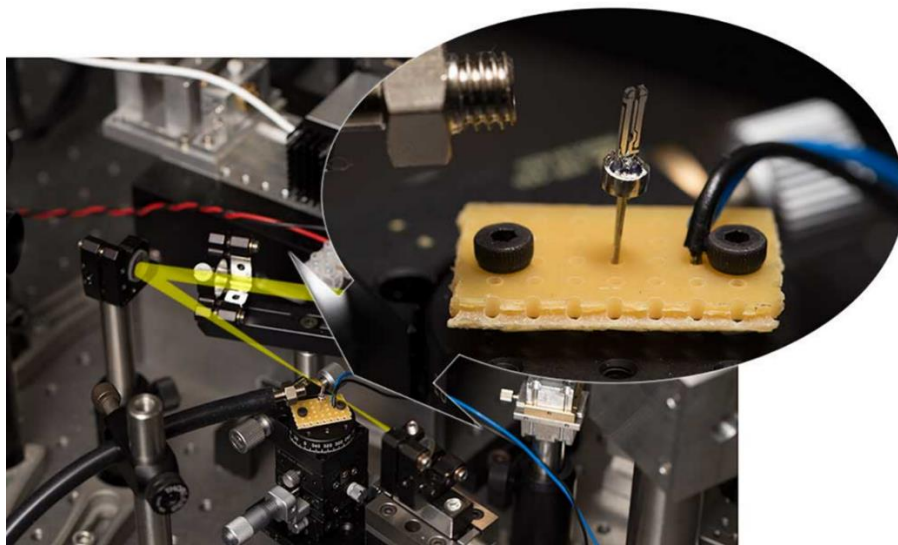


Figure 5.31. Bare QTF spectrophone mounted in the signal cavity. The yellow tracer indicated the path and waist positions of the signal excitation mode.

A nozzle supplying the flow of ammonia was placed in close proximity to the QTF to overflow the area with tested sample gas. Initially many signalling precautions were not exercised when handling the supply from the QTF to the preamplifier as indicated in the Figure 5.31 above.

Simple multi-strand conductors were utilised to connect the fork however, twisted or coaxial screened cable should have been used to suppress the noise. This issue revealed itself in substantial spurious noise pickup from the QTF and its leads, even when the laser system and most of the instrumentation were switched off. It is worth mentioning that there was a significant increase in detected ‘signal’ when the function generator controlling the AOM modulator was switched on (but the modulator and laser driver were off). Obviously, the very high impedance of the QTF and the input stage of the preamplifier, coupled with its enormous Q factor, were leading to significant pickup. Moreover, it was unsatisfactory to just ‘blow’ sample gas over the QTF. For these reasons, a plenum-type sample cell was constructed (see Figure 5.32), where an upper chamber held the QTF prongs and had an inlet barb for the incoming sample gas. Two holes in the chamber wall allowed the optical field to pass through the cell and provided a route for the sample gas to exit. The lower chamber was provided for connection of two screened leads, terminated to earth at both ends. A cover (not shown) guaranteed that the QTF was essentially sealed within a Faraday-cage type arrangement to minimise electrical noise pickup. A photograph of the cell appears in Figure 5.32.

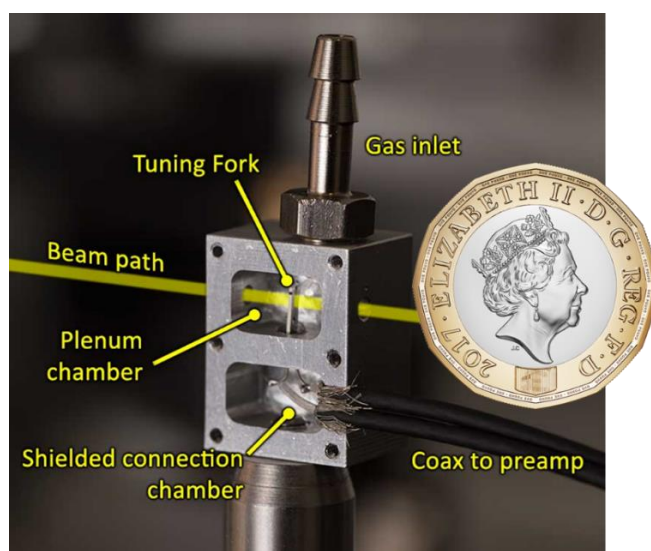


Figure 5.32. QTF within its plenum cell. Note here the cover has been removed. The pound coin is provided for scale.

This approach reduced the noise up to two orders of magnitude. Figure 5.33 presents the noise spectral density measured at the output of the preamplifier with a dynamic signal analyser (Stanford Research Systems, Model SR785). The measurement was carried out under three different conditions: (i) with no QTF attached to its input; (ii) with the exposed and poorly terminated QTF connected (as shown in Figure 5.31) and (iii) the chambered QTF.

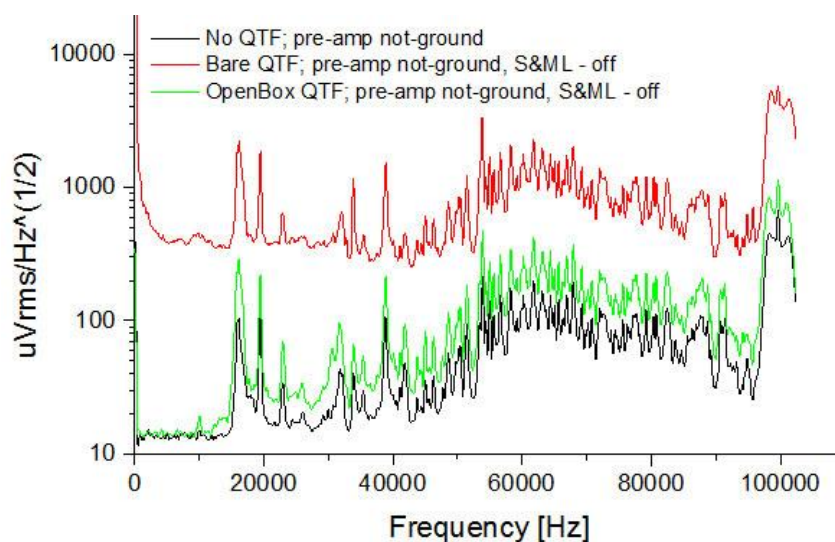


Figure 5.33. Noise spectral density at the output of the preamplifier under various conditions.

The black trace indicates the output of the pre-amplifier with no QTF (or lead) attached, therefore it is effectively a measure of the preamplifier noise. The noise floor is lifted significantly once the unshielded QTF is attached, as specified by the red trace. The efficacy of the plenum chamber as well as properly shielded and terminated leads is marked by the green line that returns the signal to near QTF-free levels of noise. It should be mentioned that this latter measurement was taken with the box lid removed. Whether it was in place or not, it did not make a difference to the noise characteristics due to the long wavelengths involved in the \sim kHz regime, when compared to the dimensions of the crystal and conductors in the cell. With the background noise suppressed, the system was ready for photoacoustic experimentation as described in the Section 5.4.2.

5.4. Results

5.4.1. Microphone-based PAS cell results

5.4.1.1. Spectroscopy and sensitivity

Ammonia was chosen as the molecular test medium for system evaluation since it exhibits several specific absorption features over the signal tuning range in which the OPO operated. Among these, one (at 6528.8cm^{-1}) coincided with the DFB laser installed within the CDP Systems instrument. A cylinder of NH_3 diluted with nitrogen to a level of 100ppm was acquired, that was further diluted with air using a large-bore syringe to obtain lower final concentrations of tested gas in the chamber.

The initial photoacoustic experiments used the ‘standard’, 3D printed spectrophone with integrated MEMS-microphone. The OPO was amplitude modulated and a function generator was tuned to the acoustic resonant frequency of the cell. The signal from the microphone was recovered by use of a Lock-in Amplifier (Stanford Research Systems, Model: SR830 DSP) without further time averaging. Originally, no pre-amplification was used. The signal wave operational optical frequency was measured using an optical wavemeter (Hewlett Packard, Model: 86120B).

A spectrum of NH_3 in the region of interest simulated at air pressure based on library data [39] is presented in Figure 5.34. The shaded region signifies the tuning range available from the system for stable phase matching condition, simply tuned with the air-spaced etalon. This range corresponding to 333GHz as shown in Figure 5.12.

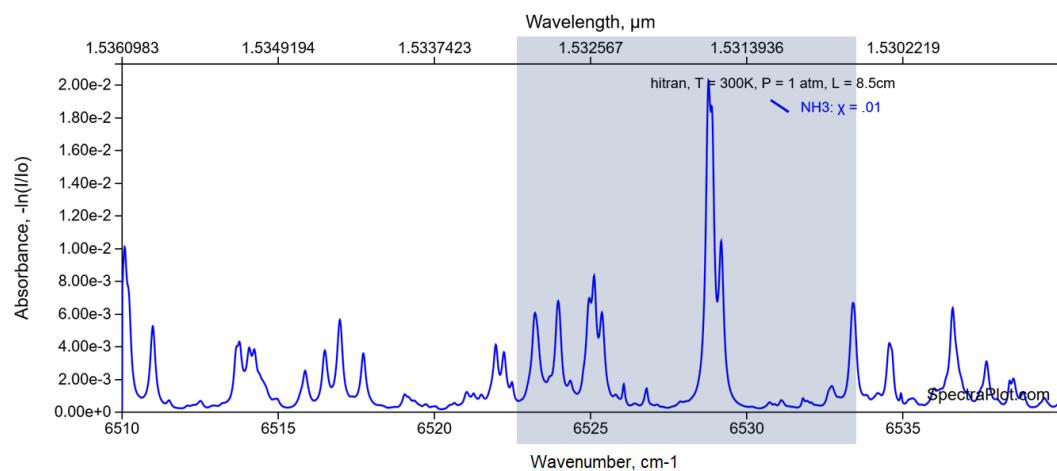


Figure 5.34. Absorption spectrum of NH_3 . Shaded area shows tuning range of OPO under ASE control [39].

To guarantee good photoacoustic response and tuning of the system by the single air-spaced etalon, initial spectroscopic measurements were executed at a relatively high NH_3 concentration of 100ppm. Figure 5.35 displays the measurement result in conjunction with the corresponding library spectrum for comparison. Note that, as demonstrated in Section 5.2.3, when using the single ASE element, the signal wave on each jump hopped ~ 29 cavity modes (corresponding to 12.5GHz or just under half a wavenumber). This signifies that whilst the linewidth of the signal is narrow (less than 1MHz), the spectrum could only be sampled every 12.5GHz. Even so, Figure 5.35 shows that despite under sampling in optical frequency, measured results correspond very well with the principle features evident in the library spectrum, both in the frequency at which absorption occurs and relative strength of the measured absorption features.

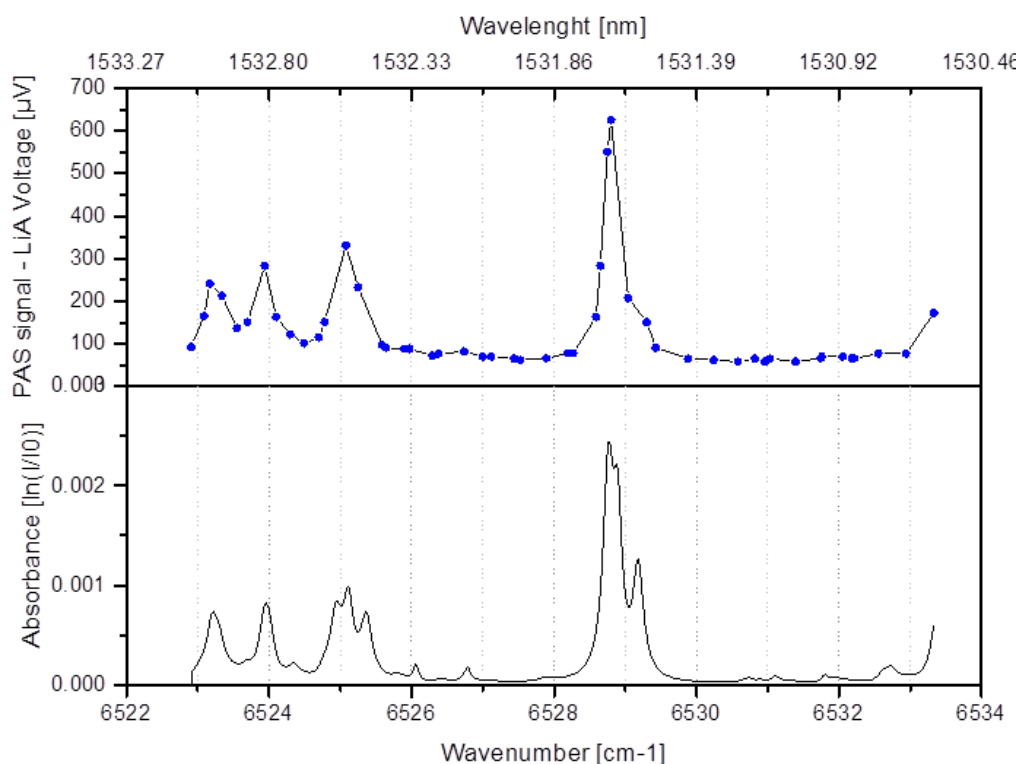


Figure 5.35. First intracavity PAS result. Upper trace: measured; lower trace: library.

The problem with under sampling is clear when looking at the most prominent feature centred on $\sim 6529\text{cm}^{-1}$. While the library trace indicates a clear doublet (or even a weak triplet, as the peak exhibits a barely resolved double feature), the measured result shows little evidence of this characteristic with the peak merely exhibiting a minor asymmetry with a ‘hump’ on the higher frequency side. The second solid silicon etalon was employed to address this issue. The result of spectrum measurement taken over the peak feature at $\sim 6528.8\text{cm}^{-1}$ is demonstrated in Figure 5.36. The higher spectral resolution and the significantly reduced span of the measurement are noticeable. The slightly irregular signal is caused by the parasitic nodal frequency effects in the signal cavity ‘fighting’ with the selectivity of the silicon etalon, along with the small loss this induces that results in a lowering of excitation power. Normalising the photoacoustic signal against the power in the excitation field would diminish it, although this was not done during this work.

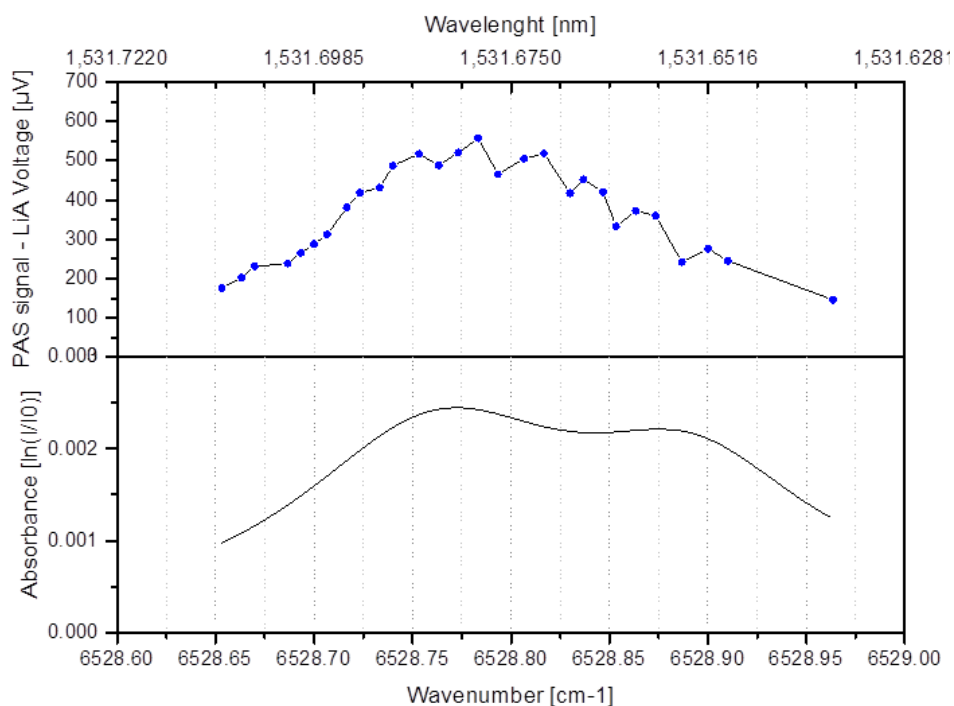


Figure 5.36. Higher resolution spectrum enabled by silicon etalon. Upper trace: measured; lower trace: library.

The induced photoacoustic signal was measured as a function of NH_3 concentration to achieve the sensitivity of the device. It was done with the signal frequency set to the peak absorption at 6528.78cm^{-1} and is presented in Figure 5.37. Clearly, the sensitivity is limited by the substantial level of background signal, whose origin will be discussed in this section.

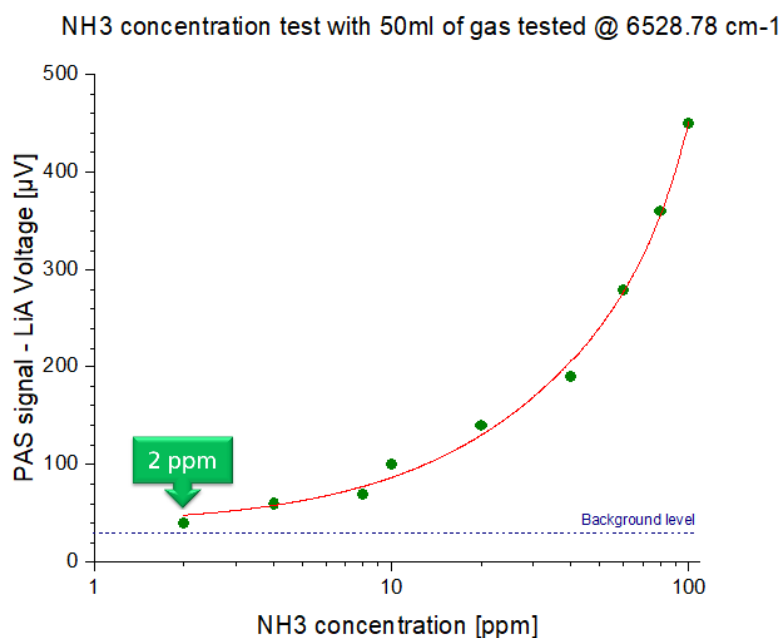


Figure 5.37. Initial sensitivity measurement.

By recognising an alternative and significantly stronger ammonia absorption feature at a frequency of 6605cm^{-1} (as shown in Figure 5.38), the initial sensitivity was improved. Tuning to this frequency was accomplished through translation of the PPLN crystal, keeping it well within the phase matching range of used crystal.

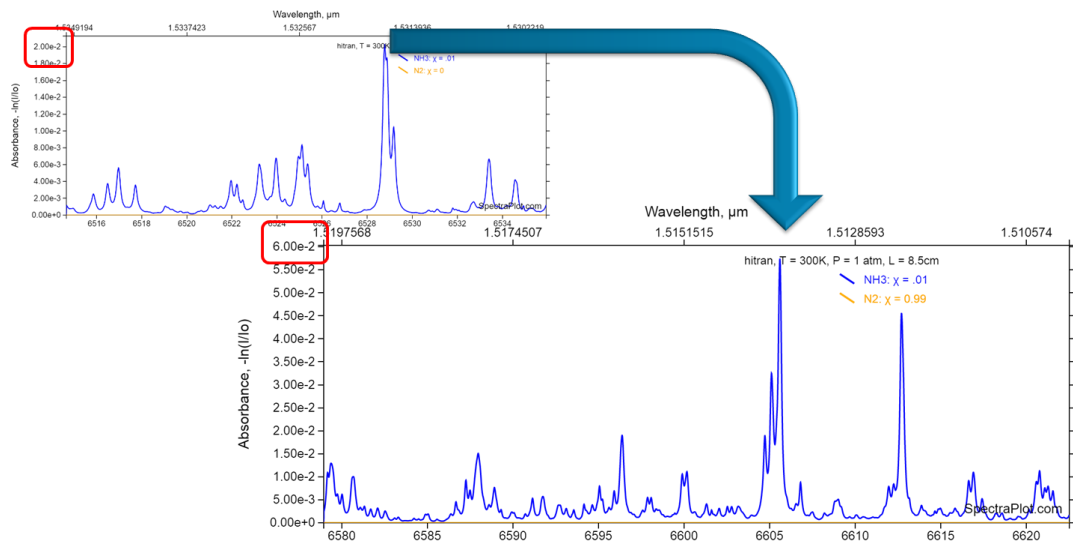


Figure 5.38. Identification of alternative, stronger absorption feature in the ammonia spectrum.

The resulting photoacoustic spectra for both the coarse (ASE only) and fine (ASE & silicon etalon) tuning modalities are shown in Figure 5.39.

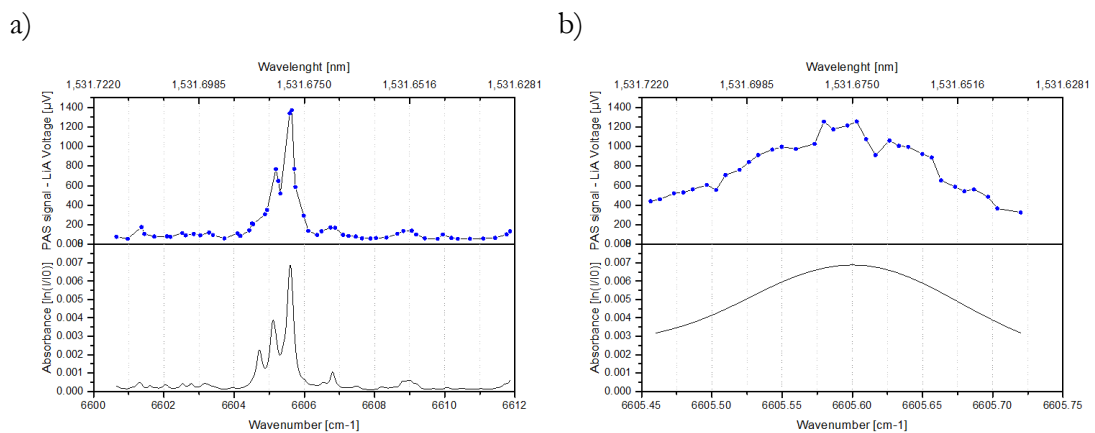


Figure 5.39. Photoacoustic response centered at the 6605.6cm^{-1} line with coarse (a) and fine (b) etalon tuning.

The resulting spectra again correspond very well to the library results, with one of the triplet peaks at 6605.2cm^{-1} now being resolved in the coarsely tuned profile. With the system tuned to the peak feature at 6605.6cm^{-1} , its response was measured once again as a concentration function and the resulting figure is shown in Figure 5.40.

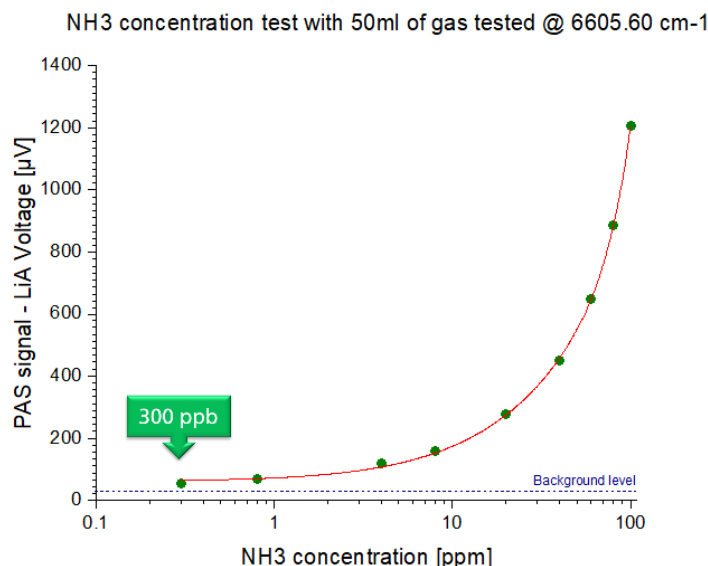


Figure 5.40. Sensitivity of the system when tuned to 6605.6cm⁻¹.

As expected, an improvement in sensitivity proportional to the enhanced absorption coefficient was experienced, however it was still limited by the relatively high background signal.

In order to ensure that the background was not caused by a genuine photoacoustic signal produced by another molecular species present within the sample gas, a ‘spectrum’ of the background was measured by tuning the excitation field without introducing any NH₃. The resulting spectrum is shown in Figure 5.41(a). The characteristic acquired from PAS signal matched well with the library spectrum of the water vapour. The relative humidity next to the experimental setup was measured at the time of the experiment resulting in 37%, at temperature T = 22°C and pressure p = 1019mbar, which corresponds to the water concentration of 9700ppm. Comparing this with the 100ppm NH₃ measured at the same bandwidth, very good agreement can be observed between the PAS measured and library spectra as displayed in Figure 5.41(b).

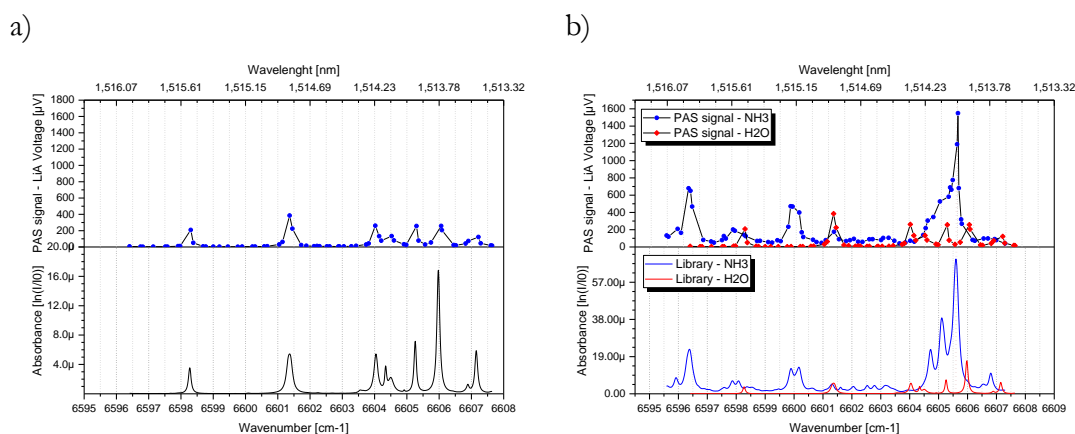


Figure 5.41. Photoacoustic and library spectra of water vapour alone (a) and compared with 100ppm of NH₃ (b).

The water line (6605.97 cm^{-1}) does not overlap with the ammonia line (6605.6 cm^{-1}), however due to limited selectivity of PAS cell, the water vapour signal certainly contributes to the background on the ammonia absorption line. It is recognised that this is not the only factor contributing to background level, however it is expected that in dry gas environment the impact of the water vapour on the background reading could be reduced. For that reason, sensitivity was limited to $\sim 300\text{ppb}$ as this was just above the background reading. Eliminating it was the main route to further decrease detectable concentration. Although the dry gas environment could not be introduced, the system was supplemented in two other improvements: (i) Increase the photoacoustic signal strength, but at the same time do not intensify the background signal and (ii) Decrease spurious background from actual ammonia residues remaining in the PAS cell. The former of these upgrades was achieved through pre-amplification of the microphone. Although the photoacoustic signal was analysed by a Lock-in Amplifier, the signal levels from the microphone were on the $\sim\mu\text{V}$ level. Given that the CDP Systems QE-PAS came supplied with a pre-amplifier for placement in close proximity to the QTF, a similar methodology was followed and a bespoke pre-amplifier was fabricated. It was anticipated that a certain amount of the 'background' noise was instrumental within the LIA, and whilst amplifying the microphone acoustic background noise would be increased, the 'contrast' between the photoacoustically induced signal and latent instrumentation background noise could be improved. The input impedance of the produced amplifier was matched into that of the microphone, and exhibited a gain of 4. This already helped to get the signal during flow of 100ppm NH_3 of ~ 1500 to $\sim 7000\ \mu\text{V}$ (4.6x), whereas the background only increased from 50 to $\sim 150\ \mu\text{V}$ (3x). This is explained through the microphone-produced noise being significantly less than that within the LIA. Since the pre-amplifier appears in the chain before the LIA, the very low levels of noise generated by microphone only manifest themselves once amplified above the LIA noise floor. However, the photoacoustic signal is already above this, so benefiting from the SNR being linear with amplification lower levels of detectability are enabled.

Another issue bearing upon experimental technique is the very large dynamic range of molecular concentration flowing through the cell (from 100ppm to single ppb or less – i.e. nearly six orders of magnitude) leading to a strong possibility of contamination. It was noticed that the background level of $\sim 150\ \mu\text{V}$ could easily be increased to $\sim 200 - 300\ \mu\text{V}$ by the residues of ammonia left in the PAS cell after previous tests. The small capillary nature of the bore within the spectrophone made high-throughput flushing of the cell with the utilised manual pump very difficult in a timely manner. This is particularly true for the cell not endowed with Brewster windows. In this case, rather than flow through and flush the internal bores, air simply entered or exited through the large aperture at either end, where the optical field propagated. Therefore, an automated pump was installed, which offered continuous flow of air through the system to improve flushing.

In addition to these two major improvements, further refinements to the setup were also implemented:

- New design of signal arm in the OPO. There is much tighter focus ($1/e^2$ diameter at the focus $2\omega = 52\mu\text{m}$, which is half of the previous size), potentially inducing stronger molecular vibration in proximity to the focus. This is discussed in the following Section 5.4.2.
- Improved galvanometer for control of the solid etalon using a closed loop, temperature stabilised module with enhanced etalon. This granted angular selection (and therefore also the selection of the optical frequency) to a far higher level of precision. As a result, the excitation frequency did not ‘wander off’ during an experimental run. The solid silicon etalon was also substituted with a 30%R (for the signal wave), 100GHz FSR solid etalon. This allowed stable single frequency to be maintained without the need for the ASE and consequently, increased the circulating field power
- Amplitude and offset settings on the AOM driving function generator were re-optimised in order to maximise induced photo-thermal signal
- Re-optimised LIA phase shift
- Modestly increasing power of the laser from 3.5 to 4.2W primary diode pump.

The combined results of these improvements are shown in Figure 5.42.

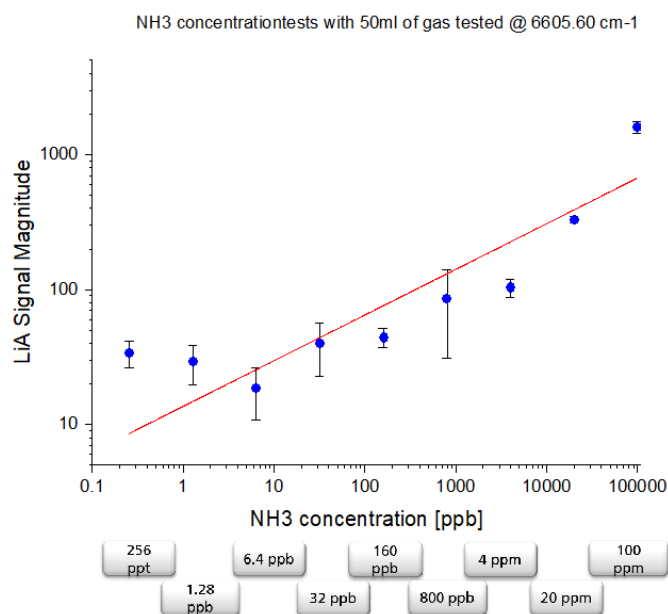


Figure 5.42. System response with its improvements implemented.

It can be seen that the system after improvements was able to exhibit levels of sensitivity on the parts per-billion scale. When one accounts for the enormous improvement the intracavity

excitation field confers, presented result commensurate with the detectability levels reported by Bauer et.al. [30], upon whose evaluated design our spectrophone was based. In their experiment Bauer's group found the sensor they were using to be limited to 2.5ppm for 22mW excitation power and no averaging. Given the similar absorption coefficients of the C₂H₂ sample gas they used and the NH₃ used in this test, also assuming a circulating signal-wave power of ~10W, a sensitivity improvement of ~450 would be expected, placing the sensitivity limit in the region of a 1 ppb. This was indeed the observed result.

It was hoped to take advantage of the considerable benefits that may be given by lock-in averaging, where the phase-sensitive output from the device is averaged, potentially over seconds, to improve sensitivity. Other researchers have demonstrated up to three orders of magnitude improvement with this simple technique. However, it was not possible to maintain the amplitude stability of the laser over the required timescale to achieve desired effect, as indicated in Figure 5.43. The time series plot shows the ~50% amplitude instability that manifests itself in only a modest (~10x) level of sensitivity improvement though averaging, as specified on the Allan variance plot [40] in Figure 5.43(b). Significant benefits associated with moderate time averaging would occur upon stabilisation of the OPO by enclosing the beam paths, improving the mounting of frequency selective components and eventually implementing a mono-block type technique for laser design.

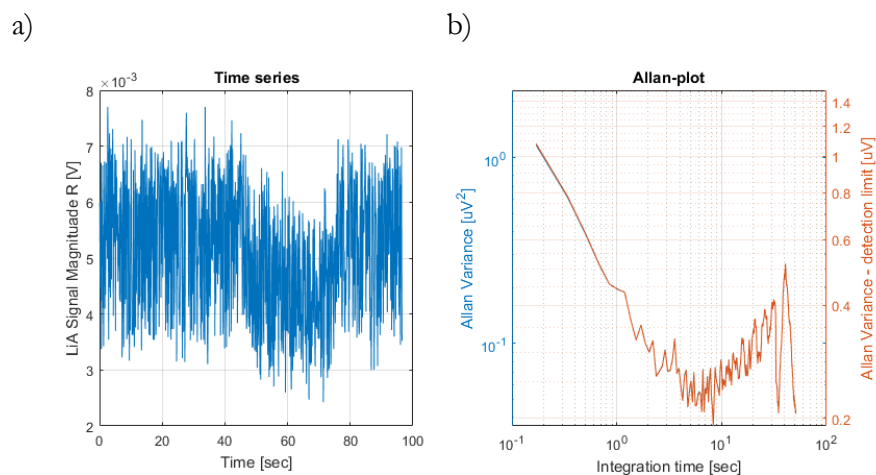


Figure 5.43. Amplitude stability of the system: time series (a) and Allan variance plot based on this data (b).

5.4.1.2. Comparison with extra-cavity photoacoustic configuration

An extra cavity system was set-up to test the spectrophone and compare its performance in this configuration with the intracavity approach. The DFB semiconductor laser installed within

the CDP Systems control unit was utilised. This laser provided an excitation power of 32mW at 1531nm wavelength and could be frequency-modulated to induce a photoacoustic response. The radiation from the laser was fibre coupled and focussed into the photoacoustic cell using the anti-reflection coated, collimating, microscope objective lens shown in Figure 5.44.

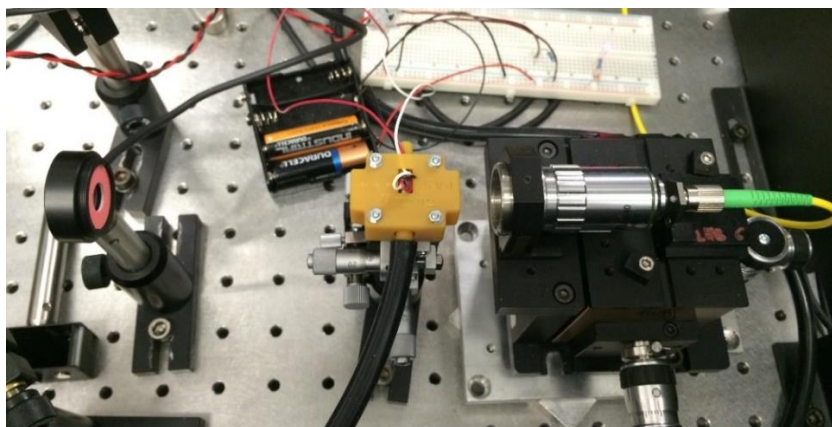


Figure 5.44. Extra-cavity photoacoustic spectroscopy configuration.

The results and like-for-like comparison between the responses from the PAS cell were possible to obtain since the OPO and DFB laser could be tuned into the same NH_3 feature at 6528.8cm^{-1} . As expected, the response of the spectrophone system as a function of DFB modulation frequency, is very similar to that measured in the intracavity setup, as presented in Figure 5.45. Once offset was removed, the Q factor was measured at 10.8.

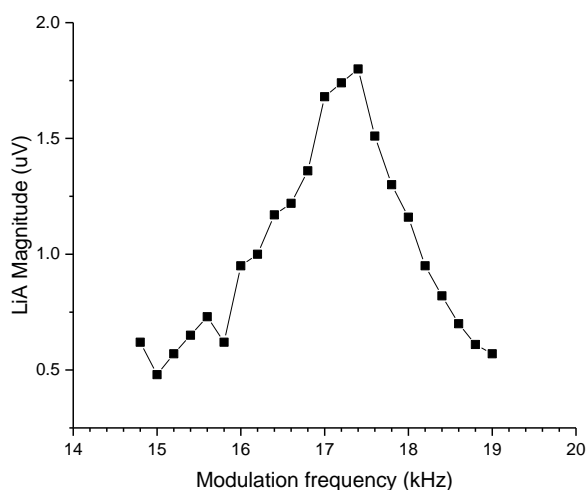


Figure 5.45. Resonance response of the spectrophone with the excitation from the DFB laser.

A direct comparison between the two excitation schemes was undertaken with the LIA parameters and NH_3 concentration unchanged. For the DFB laser system, with excitation power of 32.4mW, the flow of 100ppm NH_3 mixture with N_2 (balance) within the spectrophone induced a signal of $1.8\mu\text{V}$. Under the same conditions, $428\mu\text{V}$ was obtained when operated intracavity to the OPO.

The OPO was not operating under optimal conditions while this measurement was taken. Both the ASE and silicon etalons were installed within the cavity and other factors such as particular cavity geometry (to make experimentation easier) had an impact on performance, with the extracted idler power down to 58mW (compare to the 220mW in Figure 5.8). Nevertheless, based on obtained results the intracavity approach provided an increase in SNR of $\sim 240x$ over that of the DFB laser. This is a highly significant result as it indicates that the presented technique brings about a substantial improvement in sensitivity. This value can be used to measure the excitation field within the OPO signal cavity as it is simply 240x more than that of the DFB power. Consequently, the circulating field was measured to be 7.7W. As shown in Figure 5.8, circulating fields $\sim 2.5x$ greater than this were demonstrated which, if used on a photoacoustic context, would represent a signal $\sim 560x$ stronger than that of the DFB laser. Frequency-controlled fields approaching this power could be realised through the use of optimised etalons.

5.4.2. QE-PAS results

It is clear that even with the relatively poor Q exhibited by the fabricated miniature PAS cell, the system displayed very encouraging levels of sensitivity due to the high circulating field present within the down-converted wave cavity. Although several routes to improve the sensitivity will be discussed in the Section 5.5, the most significant of these will be considered here. It is taking advantage of the substantial gains that can be attained in improving SNR through the exploitation of the enormous Q of quartz tuning forks. Given the excessively poor quality of the procured commercial CDP QE-PAS spectrophone, implementing QE-PAS turned out to be more problematic than anticipated. In this section the difficulties faced in the system implementation will be assessed.

The single most significant issue encountered when attempting QE-PAS approach was clipping of the circulating signal field by the prongs of the QTF. Although it is relatively straight forward to develop a cavity with a beam waist diameter substantially smaller than the width in between the prongs of 300 μm , it can be misleading to assume that the system will work once the established waist size is smaller than this value. It happens because of the Gaussian intensity profile effectively extends well beyond that of the $1/e^2$ waist size which is typically quoted. Improving passage of the field in between the prongs can be done by focusing down even tighter, to tens of microns, in the beam waist, but this in turn results in a significantly larger divergence which would strike on the resonant tubes. Over the extent of the QE-PAS spectrophone the beam must be designed for minimum modal volume and this converts to matching the Rayleigh range of the focused beam to that of the micro-resonator tube.

A diagram of the signal cavity into which the QTF was initially placed, including calculated mode diameter, is shown in Figure 5.46. The position of the QTF is clearly marked. At this point, the modelled $1/e^2$ diameter was $\sim 100\mu\text{m}$. A rough rule of thumb is that 99.9% of the energy contained within the mode is within three times this $1/e^2$ diameter. It should be noted that the simulation assumes beam quality with $M^2=1$ however the real value was not measured during this project. Evidently, given the prong spacing exactly $300\mu\text{m}$, the alignment was critical. The QTF was placed into the signal cavity and alignment was adjusted the way that no reduction in non-resonant idler power was observed.

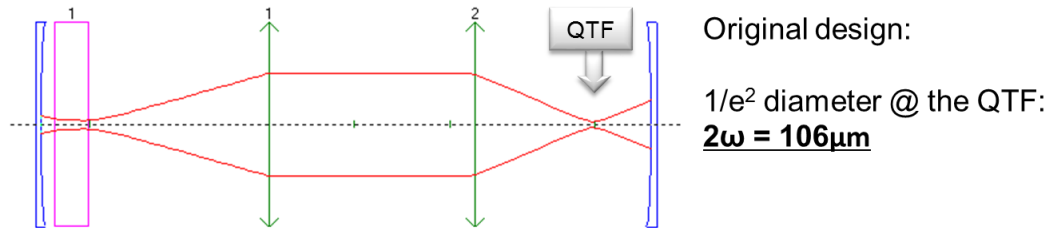


Figure 5.46. Signal cavity model with approximately $100\mu\text{m}$ waist diameter at QTF position.

The laser modulation frequency was set to 32751.88Hz (corresponding to the resonance frequency of selected tuning fork) and the corresponding signal obtained from the spectrophone is displayed in Figure 5.47. The graph in Figure 5.47(a) shows the signal resulting at all scanned frequencies.

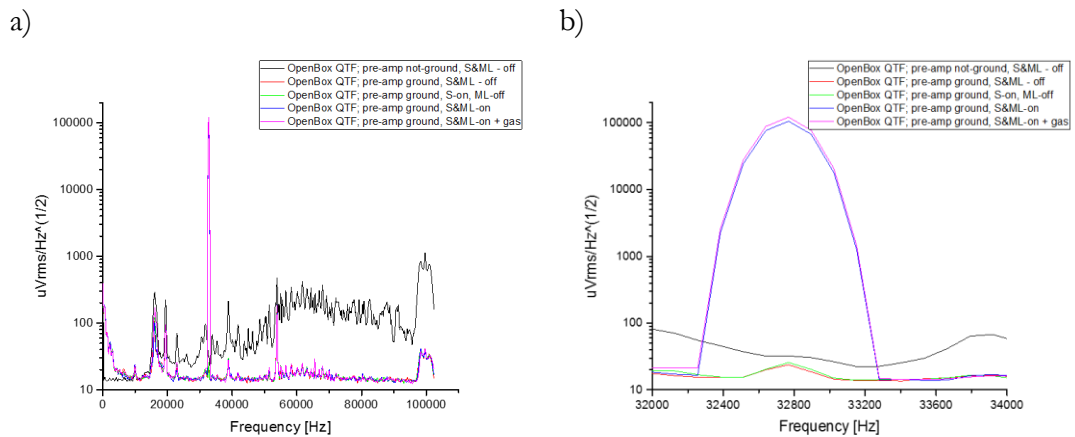


Figure 5.47. Spectrum of signal produced by QTF (and preamplifier): full frequency sweep (a) and a close up in the region of the QTF resonance (b); In the legend S stands for Signal generator and ML for Modulated laser; note the logarithmic y-axis.

There are only two traces clearly visible in this figure – the black and purple one. There are also other traces present, which were taken under various test conditions (amplifier grounded, cell lid on/off, etc.), but these produced very similar results that in consequence the traces are overlaid. The black trace corresponds to the response from the spectrophone (and pre-amplifier) with the

laser switched off, but without connection to ground. The purple line indicates the response after the noise suppression techniques outlined in section 5.3.2.3, and with the laser switched on. Although during acquisition of this trace the gas sample was present, the blue profile, covered by the purple one, demonstrates nearly identical signal recorded without the presence of the gas. Significantly reduced noise at all frequencies can be seen (thanks to noise suppression) but a very large signal is appearing at the modulation, and QTF resonance frequency. A close up of the obtained data in the region around the QTF resonance of $\sim 32.7\text{kHz}$ is shown in the Figure 5.47(b) where other traces are visible. The black line still demonstrates the response with no grounding and the instrumentation switched off. The green and red traces indicate the response from the system with the QTF pre-amplifier grounded, but the laser still switched off. The blue and purple lines again specifies the signal generated when the laser was activated (respectively without and with the gas flow through the cell). It is clear that the laser is inducing a signal which is about four orders of magnitude greater than the background noise. In order to ensure that this was not a proper reading of some background atmospheric absorption, the laser was tuned to the 6605.6cm^{-1} absorption line of ammonia and the cell was flushed with the ammonia/nitrogen mixture, which did not change the response of the system. This strongly indicated that the incident beam was influencing the prongs of the QTF.

Whereas the above measurements were undertaken with the QTF placed within the absorption cell shown in Figure 5.32, it was replaced with the exposed QTF to detect any possible effects of clipping. Unfortunately, the clipping effect could not be directly observed because of lacking a camera with spectral response at the signal wavelength. The etalons (which block the visible and near infrared waves) were removed to detect any of the parasitic sum-frequency (red) or second harmonic (green) light (which traces the path of the signal). The result of this test is presented in Figure 5.48.



Figure 5.48. Bare QTF with laser on. The green light visible on the prongs of the QTF results from the parasitic doubling of the 1064nm pump.

This photograph shows that there is at least some direct interaction between the optical field and the QTF, however it may be far less significant at the resonant signal wave than observed in Figure 5.48 with green light. It stands that way due to the non-resonant nature of the green second harmonic generated (SHG) light that is less confined, i.e. its spatial profile is significantly ‘flabbier’ than the resonant waves of pump or signal. It should be noted that the signal wave passes through two etalons within the cavity, and these can cause a fanning effect of the beam as shown in Figure 5.49(a). This phenomenon could be observed by monitoring the QTF signal while translating the fork position through the excitation beam.

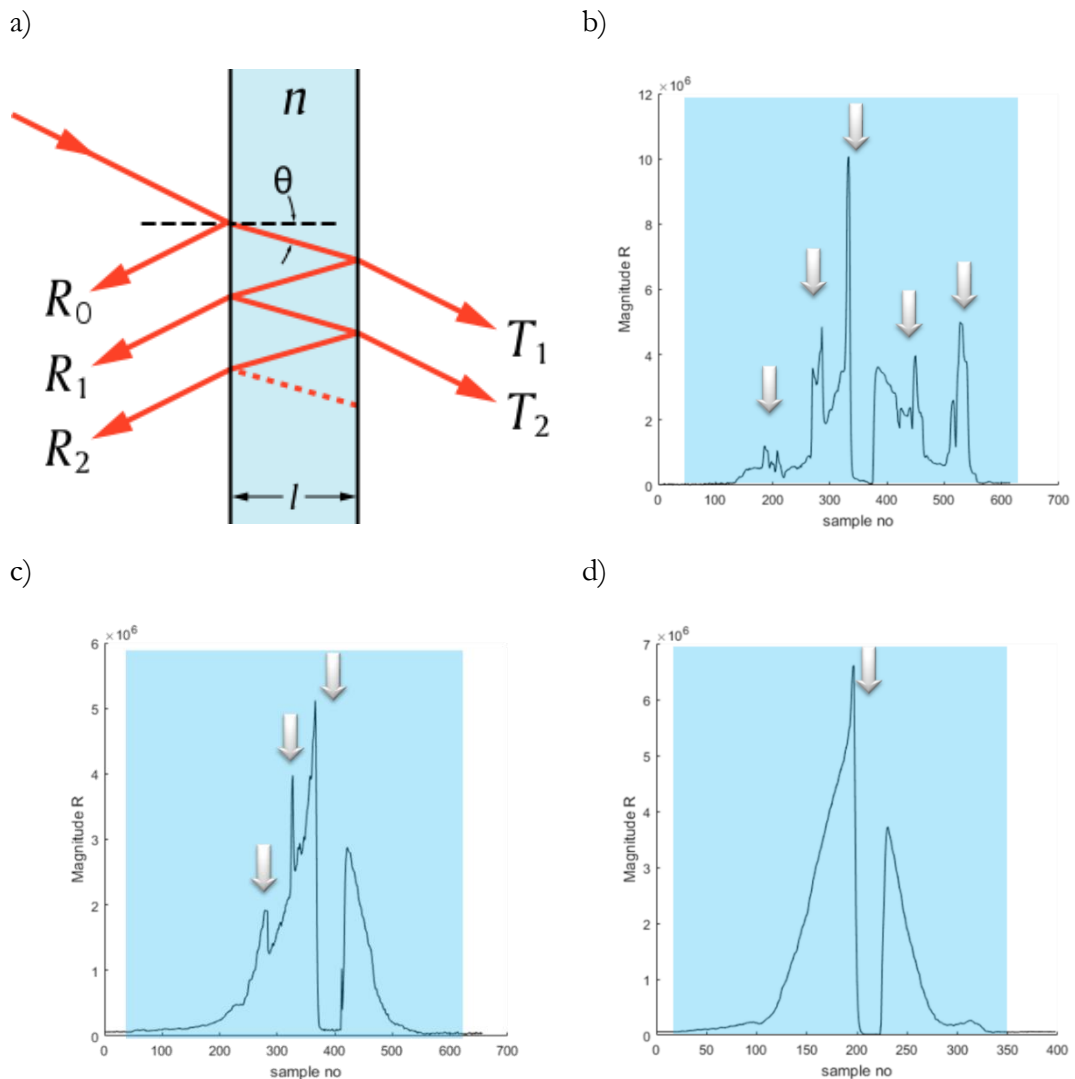


Figure 5.49. Multiple beam paths upon radiation transmission through the etalon (a) (Image source: https://en.wikipedia.org/wiki/Fabry-Perot_interferometer); Magnitude of the QTF signal as a function of acquired samples during translation of the fork across the laser beam with solid etalon and ASE included in the cavity (b), with only solid etalon tilted off-axis (c) and with only solid etalon in near perpendicular alignment (d); Shaded area shows 8mm travel range of the translation and the arrows indicate where the clipping of the beams (main and satellite) occurred; note that there is a dip in the centre of each graph, as obscuring the main beam with the QTF switches off the OPO

In Figure 5.49 the photoacoustic signal is shown from QTF translated 8mm across the beam with ASE included in the cavity (b), without ASE but with tilted solid etalon (c) and with solid etalon in near perpendicular alignment (d). In the Figure 5.49(b) and (c) it can be clearly seen (also indicated by arrows) that the increased PAS signal at the points where the side beams clip on the fork prongs, while in Figure 5.49 (d) only the main beam is present and detectable by QTF. The observable dips in these plots come from the places where fork blocks the laser beam, which switches off the OPO. In order to suppress any possible effective widening of the beam through this effect, apertures were introduced into the cavity to block the satellite modes. This however did not have any significant impact on the high background signal produced by the QTF when the laser was switched on.

The signal cavity was redesigned and aligned with mirror's focal lengths and component positioning such that a much tighter focus was formed at the beam waist, as shown in Figure 5.50. The fact that the mode size in extent of the Rayleigh range at either side of the waist was now substantially increased did not matter in the current context, as the spectrophone did not have the acoustic resonance tubes around it.

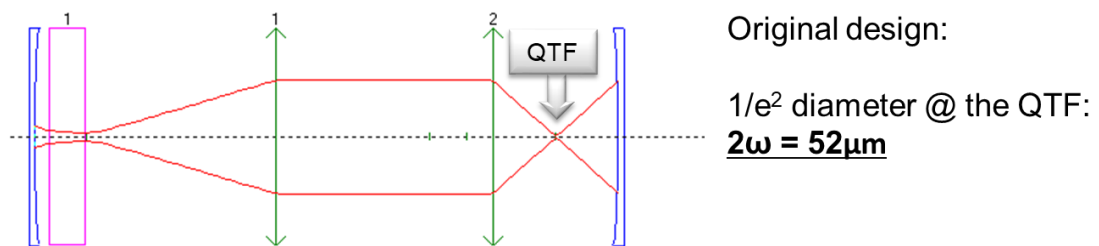


Figure 5.50. Modified signal cavity model with tighter focus - approximately $50\mu\text{m}$ waist diameter at QTF position

The resulting tighter focussing and inclusion of baffles within the signal cavity only led to a moderate decrease in clipping signal. It is understandable that further work is required to characterise the spatial mode of the signal field. There is no fundamental reason why the field cannot be focussed down through the forks as there are various reports in literature with successful demonstration of this (for example [34, 35, 37, 38]). Unfortunately, the time restrictions of the project did not allow for full investigation of this single issue standing in the way of implementation of QE-PAS. The problem of clipping was the reason to choose an off-axis resonance tube to be fabricated. Also, an assessment of this is one of the suggested actions for the follow up of this work as described in the following Section 5.6.1.

5.5. Conclusions

In this proof-of-concept project, a route towards an ultra-sensitive molecular detection system based on a novel embodiment of photoacoustic spectroscopy was demonstrated. With that goal, the primary aim, focused on the sensitivity improvements of photoacoustic techniques, was successfully accomplished by the implementation of the very high circulating field found within the cavity of an optical parametric oscillator.

In order to achieve this, a singly-resonant continuous-wave intracavity optical parametric oscillator was constructed which, for the purposes of this project, was resonant at the down-converted signal wave. The device could phase-match tune from 1.48 to 1.63 μm in the resonant signal wave by changing the lateral position of the MgO:PPLN nonlinear crystal. It could also produce up to 220mW of non-resonant idler power, corresponding to $\sim 19\text{W}$ of circulating signal excitation field. Fine frequency control and tuning was realised by placing various frequency-selective etalons into a suitably collimated section of the signal cavity. The standing wave nature of the cavity introduced parasitic frequency selective effects into the system. This interfered with the quality of tuning caused by the air spaced etalon due to its relatively low finesse. This effect meant that the signal wave stepped over ~ 29 cavity modes ($\sim 12.5\text{GHz}$) between mode hops, but the very high free-spectral range of 333GHz, offered by the etalon, resulted in an appropriately large tuning range. Using a higher finesse, uncoated solid silicon etalon solved the problem of this coarse tuning.

Two spectrophone modalities were investigated, where one was formed upon traditional microphone-based acoustically resonant cavities and the other upon quartz-enhanced transducers. The former employed a 3D printed micro-chamber and a miniature MEMS microphone. Its chamber contained plenum spaces at each end to form baffle areas to reduce acoustic noise caused by incoming sample gas as well as to serve as 'reflective' regions to form a standing acoustic wave. Brewster windows could optionally be installed on each end of the cell to seal it from the environment with minimal insertion loss into the signal cavity. The resulting cell had a resonant frequency of approximately 17.9kHz (with nitrogen as the gaseous medium) and a Q factor of ~ 9 .

A commercial QE-PAS spectrophone was purchased to expedite the actions through the considerable knowledge required to implement these transducers. It took the form of both QTF embedded within a pre-aligned resonance tube, in addition to control instrumentation which comprised analogue preamplifier, digital lock-in and an internal DFB excitation laser diode. Due to the poor build quality of the spectrophone module, it was unsuitable for use in this study and so alternative in-house designs were explored.

The photoacoustic spectroscopy with the spectrophone internal to the OPO signal cavity was successfully demonstrated. Even though the power circulating in this cavity was not optimised, it was shown that this approach improved the detection sensitivity by a factor of 240 when compared to established DFB-laser techniques. This corresponded to a circulating excitation field of 7.7W. Its value in the cavity was also shown being ~ 2.5 times higher than this. In that case a sensitivity improvement of well over two orders of magnitude would have been obtained in comparison to DFB laser setup.

A noise-limited sensitivity to NH_3 of 1ppb was demonstrated by optimising the acoustic signal originating in the spectrophone and subsequent instrumentation, when tuned into the 6605.6cm^{-1} absorption line. This sensitivity result was achieved without any averaging. Once the stability of the system is improved, the considerable averaging benefits can be expected on the measurement.

Considerable progress was made during the learning process of constructing the QTF-based spectrophones, but due to clipping of the circulating mode on the prongs of the QTF crystal, the QE-PAS technique could not be demonstrated within the given timeframe. This in result caused signal induced by direct interaction of the excitation radiation with the fork's prongs surpassing the one that originated from the photoacoustic effect. Full characterisation and solving of this problem, could not be fully pursued in the lifetime of this project and together with an off-axis spectrophone concept was not further carried on. Following Section 5.6 describes the activities – including the implementation of quartz enhanced transducers – that could lead to increased sensitivity of proposed device.

5.6. Improvements & future work

Whilst all the efforts during the project showed the efficacy of the intracavity PAS approach, they also indicated where significant improvements to the sensitivity and selectivity could be made for both, optical and instrumentation part. Moreover, it provided a base line from which the benefit of proposed improvements could be quantified. Clearly, a crucial driver for performance is sensitivity and improving this should form a fundamental part of the continuing development activities. Furthermore, the refinements in frequency tuning, selectivity and mechanical design were proposed in order to translate this technology from its current status as a laboratory demonstrator, into a robust and fully autonomous detector ready for operational use outside of the laboratory.

5.6.1. Sensitivity improvements

The current state-of-the-art detection limit of 1ppb (for ammonia with the 6605.6cm⁻¹ absorption line), as developed under this proof-of-concept programme, can be used to extrapolate the potential performance of the approach. These projections relate to optical spectroscopy in general and photoacoustic spectroscopy in particular.

Firstly, one can normalise the performance of the proposed detector in terms of circulating field and material absorption coefficient. As presented in Section 5.1, the photoacoustic signal S produced by the spectrophone is given by the Formula [5.1]. This provides three major strategies feasible to significantly improve in the detected signal S , that will translate directly into an improvement in SNR. As mentioned above, the current detection limit of 1ppb can be used to estimate the resulting sensitivity limit, once the improvements have been implemented. Each of the parameters in the Formula [5.1] can be considered as a potential route to improve the performance. It is assumed that improvements resulting from increasing the lock-in time constant (i.e. averaging) will result in improvements to the instrument constant C . The absorption coefficient is clearly a parameter set down by nature, but stronger lines can be accessed through moving to an idler-resonant system in the 3-4 μ m range. Standard spectrophones with Q-factor values exceeding 1000 have been reported [41, 42] but the values in the range between few tens and few hundred are typically expected for such a configuration [12, 42, 43]. Whereas these are significantly better Q-factors than what demonstrated in this study, proposed design employed miniaturised 3D printed cell that could affect this characteristic. As discussed, the enormous Q exhibited by QTFs in quartz-enhanced spectrophones is up to two orders of magnitude greater than this and then QE-PAS is an obvious route that could lead to further improvements in sensitivity.

Significant improvements in circulating optical power are not anticipated. The use of optimised, low-loss etalons of the appropriate finesse and position within the cavity may give rise to modest advancements, but a significant increase will only occur through an increase in primary diode pump power. Although this is feasible, it is not proposed as a practical route to enhanced sensitivity, since a significant increase in diode pump power will create problems of heat extraction and, in consequence, drive power that acts against the accomplishment of compact and efficient sensor modules. The circulating power may in fact decrease if the system is translated to an idler resonant design as the quantum nature of the OPO, coupled with the quantum defect between the signal and idler wavelengths (effectively the ratio of their wavelengths) resulting in an unavoidable drop in power [24, 44]. This is more than compensated for through access to higher and more characteristic absorption coefficients.

These improvements, along with a quantification of their magnitude are summarised in Table 5.3 below, where the current sensitivity level, as developed in this programme is used as a base line to give an indication of the anticipated noise-limited sensitivity that could be realised through implementation of the improvements outlined in this section.

Each one of these parameters shows some potential for improvement. The figures presented below are derived from established absorption spectra [39] or other literature sources [24, 30]. It can be seen that if all the amendments could be implemented simultaneously, the sensitivity of the system could approach canine-like levels [45].

Table 5.3. Summary of the predicted improvements, along with quantification of their magnitude; the sensitivity developed in this project is used as a base line to these projections (* - selected NH₃ absorption lines).

Parameter	Current (PAS spectrophone at signal wavelength)	Refinement (QE-PAS spectrophone at idler wavelength)	Improvement in SNR	Sensitivity limit (w.r.t current 1ppb)
a	Signal absorption coefficient*: 4.2e-2 cm-2/atm	Idler absorption coefficient*: 5.1e-1 cm-2/atm	10x	100ppt
Q	10 (Figure 5.21)	12,000 (Figure 5.30)	1200x	85ppq
P	7.7W	4W (power drop due to estimated signal idler quantum defect)	0.5x	170ppq
C	No time averaging implemented	Time averaging	100x	~2ppq

It is obvious that the single improvement, which presents the greatest benefit, is the implementation of QE-PAS and this has been a significant motivator throughout the project and justifies the significant investment to develop the in-house spectrophone technology. Whereas unable to implement this in the duration of the study, some of the technological building blocks necessary to realise this ability were developed in the time of the project. One is the brass off-axis spectrophone discussed in Section 5.3.2.2. The part was manufactured based on proposed design, presented earlier in Figure 5.28(b), and is revealed below in Figure 5.51.

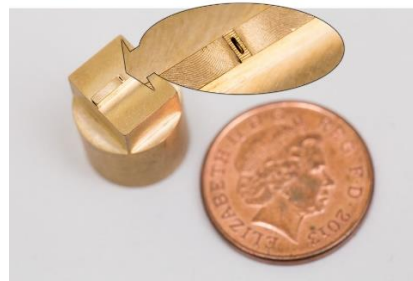


Figure 5.51. Off-axis QE-PAS spectrophone designed during this project. The slot (highlighted) is only 150µm wide

Another approach builds on an advanced microfabrication capability available in the Fraunhofer Centre of Applied Photonics (FCAP). With this technique it is possible to 'write' structures into dielectric materials, such as glass, through inscribing with very high peak power lasers. The system is essentially an optical milling machine but uses a pulsed laser instead of a mechanical cutter. The features are not formed through ablation but by the pulses changing the electronic structure of the glass which is then dissolved using standard clean-room etchants. This approach allows the fabrication of structures on the mm's scale with 10's nm precision. Although such fabrication techniques have been developed and have shown great utility in micro-integrated 'lab-on-a-chip' type systems, their exceptional flexibility and precision can to be exploited in the context of photoacoustic spectroscopy, where improved dimensional tolerance and inner bore smoothness should result in Q enhancement. An example of such an off-axis resonator is shown in Figure 5.52.

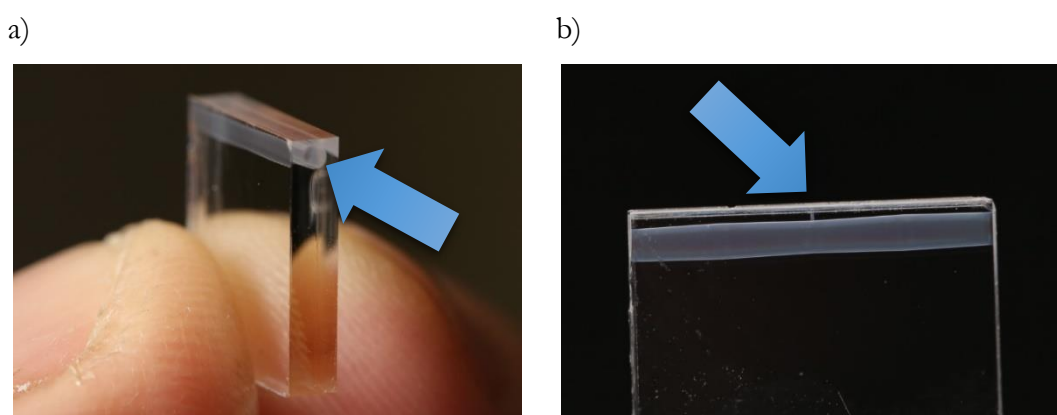


Figure 5.52. QE-PAS spectrophone based upon inscribed glass, as developed at FCAP. Here, the glass has been 'written' but not etched (indicated with an arrow); (a): acoustic bore; (b) anti-nodal pipe for QTF excitation

Both of these approaches should be assessed in follow up activities and each could be readily fabricated in volume once the technology is translated to commercial manufacture.

5.6.2. Tuning

The ease and finesse with which any spectroscopic system can tune, directly impacts on the selectivity it exhibits. Even though it was found that the linewidth of the developed single-frequency laser-based source was excellent, the multi-signal cavity mode hopping that it exhibited reduced the effective resolution of the technology. This aspect is important, as moving forward it is desirable to conduct photoacoustic measurements at reduced pressure. This is because, even if it leads to fewer molecules within the photoacoustic cell, the reduction in pressure broadening and the enhanced Q of QTF that results from reduced viscous drag, will lead to an enhanced

signal and selectivity. This is presented in Figure 5.53, where the absorption spectrum of ammonia was simulated [39] under two different pressure conditions: 1atm and 0.1atm. A tenfold decrease in pressure resulted in lower intensity spectral features, nevertheless their selectivity increased significantly. The benefits of this approach are limited to the point where the signal cavity can be hopped on adjacent cavity modes in predictable manner.

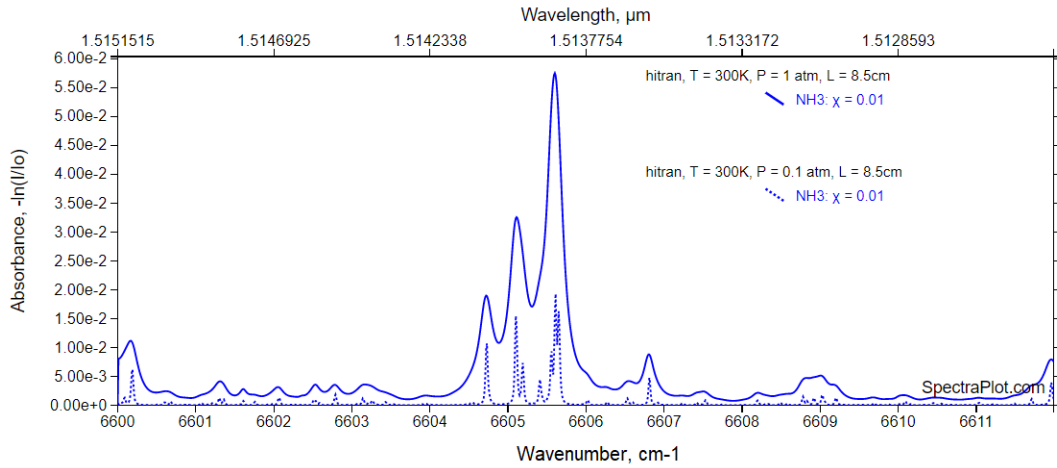


Figure 5.53. Simulated ammonia absorption spectrum at the selected spectral range with ambient pressure of 1 atm (continuous line) and with ambient pressure decreased ten times (dotted line); note the increased selectivity of the spectral features, with the dominating triplet peak at the centre of the plot now being resolved as actually 7 distinct peaks [39].

The optimised selection of the ASE coatings is the simplest route to realise improved tuning control. The module used in this project was a bequest part from the existing FCAP inventory. Therefore, the 20% reflectivity of its internal surfaces was not selected for this application, as the finesse it produced (1.8 with the resonance bandwidth of approximately 190GHz) was unable to overcome the parasitic nodal frequency selective effects, resulting from the standing wave geometry. Through numerical modelling [46], it was established that a 70%R coating (with net finesse of 8.7 at the resonance bandwidth of approximately 38GHz) can provide the same selectivity as the solid silicon etalon used in this study. As a result, it will deliver adjacent mode-hop tuning, but with the free-spectral range and consequently $\sim 11\text{cm}^{-1}$ tuning range of the ASE. The simulated transmission plots for both ASE are displayed in Figure 5.54. This new etalon can offer an optimal balance between selectivity and diffraction losses introduced by the low Fresnel number of the etalon.

A second and more elegant solution is moving to a travelling-wave, ring cavity configuration, where the amplitude of the wave is time averaged over the propagation axis of the cavity (i.e. the nodes and antinodes are moving) and subsequently, the nodal positions coinciding with dielectric interfaces are removed (see example diagram in Figure 5.55). This results in excellent single frequency behaviour for the pump-wave, because of spatial hole burning being

eliminated as well as remarkable tuning of the signal cavity. This would allow one to utilise etalons with lower finesse, exactly as the ASE used in the reported here study. The follow up actions should investigate both of ideas described above and implement these as required.

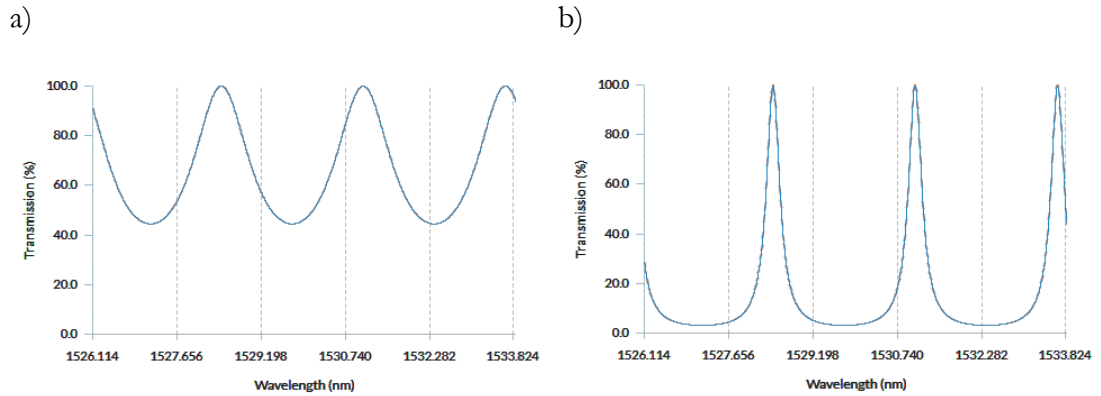


Figure 5.54. Simulated transmission plots for two 333GHz FSR etalons with 20%R (a) and 70%R (b). Both plots illustrate 3 FSR's of respective etalons, centred on 1530nm; adapted from [46].

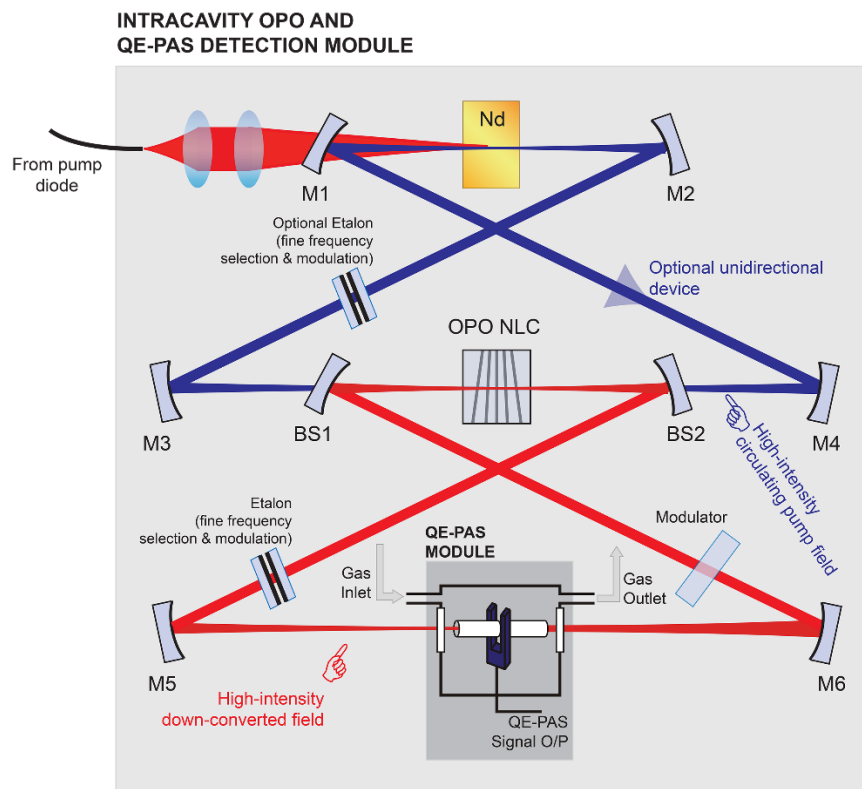


Figure 5.55. Example diagram of an IC-OPO in the ring configuration with QE-PAS module located intracavity to the ring with circulating down-converted field.

5.6.3. Modulation

In the work outlined in this report, amplitude modulation (AM) was used to induce a photoacoustic signal in the spectrophone. For single molecules or ones exhibiting unique spectral features, this route offers a simple and effective modulation scheme. However, as an alternative, maintaining constant optical amplitude and varying the optical frequency (Frequency Modulation [FM], also referred as Wavelength Modulation [WM]) of the excitation wave provides a superior modulation mechanism. This would allow fine spectral features of interest to be 'AC coupled' and therefore isolated from broader background features [20], such as water vapour. An approach like this becomes even more potent when the measurement occurs at reduced pressure, for the reasons outlined above in Section 5.6.2. Moving to FM could be achieved through AC drive of the etalon, with the amplitude of the signal driving the etalon dictating the frequency modulation depth imparted on the signal wave. It would also eliminate the need for an AOM and associated radio frequency (RF) drive circuitry.

5.6.4. Excitation in deeper IR

The efficacy of proposed approach was shown using the resonant down converted signal wave operating over the range $\sim 1.4\text{-}1.6\mu\text{m}$ in a PPLN-based optical parametric oscillator. As stated, this can readily be translated to the mid-infrared ($\sim 2.8\text{-}4.2\mu\text{m}$) idler wave through appropriate coating choice in order to resonate the idler wave. Such a refinement gives access to stronger, more characteristic absorption features. In the same manner, a move towards even longer wavelengths is even more desirable. This is indicated in Figure 5.56 where the absorption spectrum of an acetone is shown. For clarity, it is separated into near (i.e. signal wave), mid (idler) and deep infrared zones. It is clear that moving even deeper into the infrared, gives access to absorption features which are both stronger (therefore yielding higher sensitivity) and are more distinctive. The parametric process can phase-match well out into near microwave wavelengths [47, 48], but material transparency is often the limiting factor as in the case of the one used in this study - PPLN. The lithium niobate, material from which it is made, becomes opaque at $\sim 4.4\mu\text{m}$, which therefore sets its upper wavelength generation limit. Recently, nonlinear optical materials based upon semiconductor crystals have been developed, such as GaAs and GaP, and have become commercially available. Such crystals have the double benefit of exhibiting very high nonlinear gain coefficients and transparency over the spectrally rich 'fingerprint' region ($\sim 5\text{-}12\mu\text{m}$) [49].

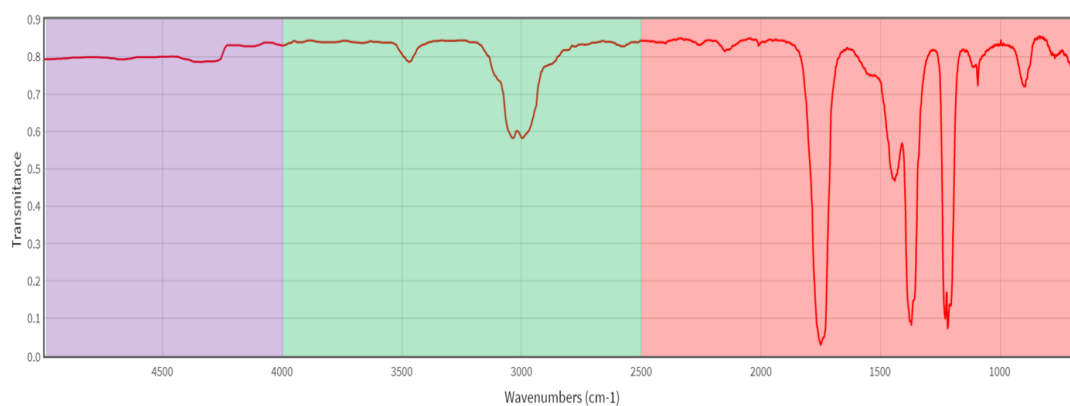


Figure 5.56. Infrared transmission spectrum of acetone. The purple, green and red zones roughly correspond to the near-, mid- and deep infrared regions. Note the strong and very characteristic features in the latter (adapted from <http://webbook.nist.gov>).

Successful translation of the intracavity OPO / intracavity PAS combination to this spectral range would therefore result in a detection technology with enhanced levels of sensitivity and selectivity in particular. It is also worth to emphasise again the additional benefit which photoacoustic spectroscopy brings to deep-infrared spectroscopy by removing the requirement for photodetectors. This is particularly compelling in the case of these very long wavelengths, where direct detection is severely hampered, as optical signals are easily lost in room temperature black-body radiation, which is at its peak precisely within the deep-infrared waveband. For that reason, detectors require cooling (often to cryogenic temperatures), that helps to mitigate the noise caused by thermally induced carriers.

Quantum-cascade lasers (QCL) represent another potential source of tunable light over the fingerprint spectral region. However, intracavity enhancement techniques cannot be translated to these laser sources due to the very high coupling loss which their waveguide-type gain materials introduce to external-cavity diode cavities, thus precluding significant intracavity powers.

5.6.5. Preparations for deployment

In order to extend the impact of the presented technology beyond the boundaries of the laboratory, significant refinement of its instrumentation is required. This translates to essentially unifying all of the laboratory drivers, amplifiers and diagnostic tools into a single and autonomous device under embedded processor control. High-resolution spectra are ineffective for the end-user without their robust conversion into quantitative declarations. This is particularly true in case of autonomous sensing devices which are required to provide a 'go/no-go' alarm.

In addition to instrumentation, the opto-mechanical embodiment of the technology clearly needs to be improved over that described here in the laboratory-based demonstrator, in order to realise its full potential. This encompasses not only the opto-mechanical design of the laser and OPO, but the gas sampling, conditioning and delivery. Upon successful development of the technology, these factors will need to be addressed separately.

5.7. Acknowledgments

This project was funded under the Innovative Research Call in Explosives and Weapons Detection 2016. This is a Cross-Government programme sponsored by a number of Departments and Agencies under the UK Government's CONTEST strategy in partnership with the US Department of Homeland Security, Science and Technology Directorate. This work was also supported by the EPSRC Centre for Doctoral Training in Applied Photonics, funded by the UK Engineering and Physical Sciences Research Council (grant EP/G037523/1) and by an Industrial Fellowship from the Royal Commission for the Exhibition of 1851.

References

- [1] R. J. Colton and J. N. R. Jr., "Making the World a Safer Place," *Science*, vol. 299, no. 5611, pp. 1324-1325, 2003.
- [2] S. Hallowell, "Screening people for illicit substances: a survey of current portal technology.," *Talanta*, vol. 54, no. 3, pp. 447-458, 2001.
- [3] L. Senesac and T. G. Thundat, "Nanosensors for trace explosive detection," *Materials Today*, vol. 11, no. 3, pp. 28-36, 2008.
- [4] J. S. Caygill, F. Davis and S. P. Higson, "Current trends in explosive detection techniques," *Talanta*, vol. 88, pp. 14-29, 2012.
- [5] C. Crawford and H. Hill, "Comparison of reactant and analyte ions for ⁶³Nickel, corona discharge, and secondary electrospray ionization sources with ion mobility-mass spectrometry," *Talanta*, vol. 107, pp. 225-232, 2013.
- [6] Y. Fleger, L. Nagli, M. Gaft and M. Rosenbluh, "Narrow gated Raman and luminescence of explosives," *Journal of Luminescence*, vol. 129, no. 9, pp. 979-983, 2009.
- [7] F. C. D. L. Jr., J. L. Gottfried, C. A. Munson and A. W. Miziolek, "Double pulse laser-induced breakdown spectroscopy of explosives: Initial study towards improved

- discrimination,” *Spectrochimica Acta Part B: Atomic Spectroscopy*, vol. 62, no. 12, pp. 1399-1404, 2007.
- [8] Y. Song and R. G. Cooks, “Atmospheric pressure ion/molecule reactions for the selective detection of nitroaromatic explosives using acetonitrile and air as reagents,” *Rapid Communications in Mass Spectrometry*, vol. 20, no. 20, p. 3130–3138, 2006.
- [9] J. Yinon, Ed., *Counterterrorist Detection Techniques of Explosives*, Elsevier Science, 2007.
- [10] C. Bauer, U. Willer, R. Lewicki, A. Pohlkötter, A. Kosterev, D. Kosynkin, F. K. Tittel and W. Schade, “A Mid-infrared QEPAS sensor device for TATP detection,” *Journal of Physics: Conference Series*, vol. 157, no. 1, pp. 1-6, 2009.
- [11] F. J. M. Harren, F. G. C. Bijnen, J. Reuss, L. A. C. J. Voesenek and C. W. P. M. Blom, “Sensitive Intracavity Photoacoustic Measurements with a CO₂ Waveguide Laser,” *Applied Physics B*, vol. 50, no. 2, p. 137–144, 1990.
- [12] A. Khalil, M. Gondal and N. Al-Suliman, “Resonant photo-acoustic detection of carbon monoxide with UV Laser at 213 nm,” *Applied Physics B*, vol. 103, no. 2, p. 441–450, 2011.
- [13] A. Miklós, P. Hess and Z. Bozóki, “Application of acoustic resonators in photoacoustic trace gas analysis and metrology,” *Review of Scientific Instruments*, vol. 72, no. 4, pp. 1937-1955, 2001.
- [14] A. G. Bell, “Upon the Production of Sound by radiant Energy.,” *Philosophical Magazine and Journal of Science*, vol. 11, pp. 510-528, 1881.
- [15] J. F. McClelland, S. J. Bajic, R. W. Jones and L. M. Seaverson, “Introduction to Photoacoustic Spectroscopy with Step Scan and Constant Velocity Scan FTIR Spectrometers,” in *Modern Techniques of Applied Molecular Spectroscopy*, John Wiley & Sons, Inc., 1998.
- [16] D. W. Ball, “Photoacoustic Spectroscopy,” *Spectroscopy*, vol. 21, no. 9, pp. 14-16, 2006.
- [17] D. V. Bageshwar, A. S. Pawar, V. V. Khanvilkar and V. J. Kadam, “Photoacoustic Spectroscopy and Its Applications – A Tutorial Review,” *Eurasian Journal of Analytical Chemistry*, vol. 5, no. 2, pp. 187-203, 2010.
- [18] J. Janni, B. D. Gilbert, R. Field and J. I. Steinfeld, “Infrared absorption of explosive molecule vapors,” *Spectrochimica Acta Part A: Molecular and Biomolecular Spectroscopy*, vol. 53, no. 9, p. 1375–1381, 1997.
- [19] M. E. Webber, M. Pushkarsky and C. K. N. Patel, “Optical detection of chemical warfare agents and toxic industrial chemicals: Simulation,” *Journal of Applied Physics*, vol. 97, no. 11, pp. 1-10, 2005.
- [20] P. Patimisco, G. Scamarcio, F. K. Tittel and V. Spagnolo, “Quartz-Enhanced Photoacoustic Spectroscopy: A Review,” *Sensors*, vol. 14, pp. 6165-6206, 2014.

- [21] COPAC - Copenhagen Photonic-Acoustic Corporation, "PHOTOACOUSTIC SPECTROSCOPY," COPAC, [Online]. Available: <https://www.copac.dk/photoacoustic-spectroscopy/>. [Accessed 20 January 2018].
- [22] A. Kosterev, P. Buerki, L. Dong, M. Reed, T. Day and F. Tittel, "QEPAS detector for rapid spectral measurements," *Applied Physics B: Lasers and Optics*, vol. 100, no. 1, p. 173–180, 2010.
- [23] A. Elia, P. M. Lugarà, C. D. Franco and V. Spagnolo, "Photoacoustic Techniques for Trace Gas Sensing Based on Semiconductor Laser Sources," *Sensors*, vol. 9, pp. 9616-9628, 2009.
- [24] D. J. M. Stothard, "Practical Continuous-Wave Intracavity Optical Parametric Oscillators," in *Advances in Optical and Photonic Devices*, K. Y. Kim, Ed., InTech, 2010, pp. 293-328.
- [25] M. M. J. W. v. Herpen, S. Li, S. E. Bisson and F. J. M. Harren, "Photoacoustic trace gas detection of ethane using a continuously tunable, continuous-wave optical parametric oscillator based on periodically poled lithium niobate," *APPLIED PHYSICS LETTERS*, vol. 81, no. 7, pp. 1157-1159, 2002.
- [26] M. v. Herpen, S. Bisson, A. Ngai and F. Harren, "Combined wide pump tuning and high power of a continuous-wave, singly resonant optical parametric oscillator," *Applied Physics B Lasers and Optics*, vol. 78, pp. 281-286, 2004.
- [27] A. Miklós, C.-H. Lim, W.-W. Hsiang, G.-C. Liang, A. H. Kung, A. Schmohl and P. Hess, "Photoacoustic measurement of methane concentrations with a compact pulsed optical parametric oscillator," *APPLIED OPTICS*, vol. 41, no. 15, pp. 2985-2993, 2002.
- [28] S. Borri, P. Patimisco, I. Galli, D. Mazzotti, G. Giusfredi, N. Akikusa, M. Yamanishi, G. Scamarcio, P. D. Natale and V. Spagnolo, "Intracavity quartz-enhanced photoacoustic sensor," *APPLIED PHYSICS LETTERS*, vol. 104, no. 9, pp. 1-4, 2014.
- [29] A. Polak and D. J. M. Stothard, "Enhanced photoacoustic spectroscopy sensitivity through intra-cavity OPO excitation," in *SPIE Defense + Commercial Sensing Conference*, Orlando, 2018.
- [30] R. Bauer, G. Stewart, W. Johnstone, E. Boyd and M. Lengden, "3D-printed miniature gas cell for photoacoustic spectroscopy of trace gases," *OPTICS LETTERS*, vol. 39, no. 16, pp. 4796-4799, 2014.
- [31] InvenSense Inc, "INMP504 - Ultra-Low Noise Microphone with Bottom Port and Analog Output," 14 May 2014. [Online]. Available: <https://www.invensense.com/wp-content/uploads/2015/02/INMP504.pdf>. [Accessed 26 January 2018].
- [32] Begell House, "Thermopedia," 2 February 2011. [Online]. Available: <http://www.thermopedia.com/content/1240/>. [Accessed 29 January 2018].
- [33] The Engineering Toolbox, "Gases - Speed of Sound," [Online]. Available: https://www.engineeringtoolbox.com/speed-sound-gases-d_1160.html. [Accessed 7 February 2018].
- [34] A. A. Kosterev, Y. A. Bakhirkin, R. F. Curl and F. K. Tittel, "Quartz-enhanced photoacoustic spectroscopy," *OPTICS LETTERS*, vol. 27, no. 21, pp. 1902-1904, 2002.

- [35] L. Dong, A. Kosterev, D. Thomazy and F. Tittel, “QEPAS spectrophones: design, optimization, and performance,” *Applied Physics B, Lasers and Optics*, vol. 100, pp. 627-635, 2010.
- [36] K. Liu, H. Yi, A. Kosterev, W. Chen, L. Dong, L. Wang, T. Tan, W. Zhang, F. Tittel and X. Gao, “Trace gas detection based on off-beam quartz enhanced photoacoustic spectroscopy: Optimization and performance evaluation,” *Review of Scientific Instruments*, vol. 81, p. 103103:1–103103:6., 2010.
- [37] D. Serebryakov, I. Morozov, A. Kosterev and V. Letokhov, “Laser microphotoacoustic sensor of ammonia traces in the atmosphere,” *Quantum Electronics*, vol. 40, no. 2, pp. 167-172, 2010.
- [38] H. Zheng, L. Dong, A. Sampaolo, H. Wu, P. Patimisco, X. Yin, W. Ma, L. Zhang, W. Yin, V. Spagnolo, S. Jia and F. K. Tittel, “Single-tube on-beam quartz-enhanced photoacoustic spectroscopy,” *Optics Letters*, vol. 41, no. 5, pp. 978-981, 2016.
- [39] SpectraPlot Ltd., “SpectraPlot - the wavelengths search engine,” SpectraPlot Ltd., 2017. [Online]. Available: <http://spectraplot.com/>. [Accessed 23 February 2018].
- [40] P. Werle, R. Mucke and F. Slemr, “The Limits of Signal Averaging in Atmospheric Trace-Gas Monitoring by Tunable Diode-Laser Absorption Spectroscopy (IDLAS),” *Applied Physics B*, vol. 57, pp. 131-139, 1993.
- [41] E. Nodov, “Optimization of resonant cell design for optoacoustic gas spectroscopy (H-type),” *Applied Optics*, vol. 17, no. 7, pp. 1110-1119, 1978.
- [42] L. J. T. III, M. J. Kelly and N. M. Amer, “The role of buffer gases in optoacoustic spectroscopy,” *Applied Physics Letters*, vol. 32, no. 11, pp. 736-738, 1978.
- [43] G. A. West, J. J. Barrett, D. R. Siebert and K. V. Reddy, “Photoacoustic spectroscopy,” *Review of Scientific Instruments*, vol. 54, no. 7, pp. 797-817, 1983.
- [44] D. J. M. Stothard, *Continuous-wave, singly-resonant optical parametric oscillators pumped internal to Nd:YVO4 lasers*, St Andrews: University of St Andrews, 2001.
- [45] C. Angle, L. P. Waggoner, A. Ferrando, P. Haney and T. Passler, “Canine Detection of the Volatilome: A Review of Implications for Pathogen and Disease Detection,” *Frontiers in Veterinary Science*, vol. 3, no. 47, 2016.
- [46] Lightmachinery Inc., “Etalon Designer,” Lightmachinery Inc., [Online]. Available: <https://lightmachinery.com/optical-design-center/etalon-designer/>. [Accessed 2 March 2018].
- [47] Z. H. Wang, C. P. Sun and Y. Li, “Microwave degenerate parametric down-conversion with a single cyclic three-level system in a circuit-QED setup,” *Physical Review A*, vol. 91, no. 4, pp. 1-7, 2015.
- [48] C. F. Ockeloen-Korppi, E. Damskäg, J.-M. Pirkkalainen, T. T. Heikkilä, F. Massel and M. A. Sillanpää, “Low-Noise Amplification and Frequency Conversion with a Multiport Microwave Optomechanical Device,” *Physical Review X*, vol. 6, pp. 1-7, 2016.

- [49] L. Maidment, P. G. Schunemann and D. T. Reid, “Molecular fingerprint-region spectroscopy from 5 to 12 μm using an orientation-patterned gallium phosphide optical parametric oscillator,” *Optics Letters*, vol. 41, no. 18, pp. 4261-4264, 2016.

Chapter 6: Conclusions

6.1. Introduction

In the final chapter of this thesis, the results achieved and conclusions drawn during all the projects of the demonstrated portfolio will be reviewed, and the potential avenues for future research in these fields will be considered.

6.2. Summary of the portfolio and conclusions

In the introductory chapters, the background for all the work done during this programme was described. The importance of spectroscopy, and imaging spectroscopy in particular, represented by hyperspectral imaging, was demonstrated. Although, a vast number of spectroscopic tools operating in the visible and near-infrared regime exist, devices operating in mid-infrared region are rarely implemented outside of the research laboratories. A wide deployment of these devices is restricted due to the limited access to illumination sources in this range. Tuneable lasers have been identified as very powerful tools for spectroscopic applications. Optical parametric oscillators, especially in their intracavity configuration, were discussed in more depth, as these devices constitute the basis of all the spectroscopic hardware presented in the thesis.

However, even the most sophisticated spectrometer applied to a specific task, gives only a set of data that must be analysed in order to extract the required information. Due to the fact that reflectance spectra are like a fingerprint for different substances, these devices have the potential to provide very precise information. In order to extract it from the sensor output data and simplify the analysis, numerous signal processing techniques can be employed. In this dissertation, various classification techniques were presented as tools of very high importance in examination of spectral data. The generic process for successful application of these tools was displayed as well as a survey of different types of classification algorithms, showing abundant variety of signal processing techniques available for given applications. Two techniques, namely Support Vector Machine and Partial Least Square regression, were described in detail, illustrating approaches for analysis of classification results.

This theoretical background set solid foundations for the three projects presented in Chapters 3 to 5. Although, all these projects were interlinked by use of the IC-OPO, the first two

– INHERIt and Rosdam – had more common points. During both these projects new applications have been explored, intended for a laser-based, active hyperspectral imager that thanks to the use of an OPO as the illumination source, operates in near-IR and mid-IR regimes (with use of signal and idler waves respectively). A big part of the research was done with the use of a commercialised system – Firefly IR Imager. Although, this piece of equipment has undeniable unique capability, allowing spectral imaging in the spectral region otherwise hard to access, it has a set of characteristics that may restrict use of this technology for certain applications. As a laser-based imaging device, it has a number of features, typical for this category of imagers, which affect the image quality. The main aspects impacting the image quality are: the pulse-by-pulse intensity jitter, collection efficiency variation in the spatial domain caused by the beam deflection as well as susceptibility to specular reflections and speckle effect. In Chapter 3, the results of the experimental studies, where laboratory-based setup was used to reproduce basic capabilities of the commercial imager were demonstrated along with a set of potential mitigation mechanisms for presented issues. In addition to these artefacts of coherent illumination and scanning mechanism, the recording time for high resolution hyperspectral data set may also cause problems in some uses of this system. Although, this equipment offers video framerate on single wavelength, the acquisition of data across hundreds of accessible wavelengths results in long lasting process requiring static and unchanging object. All these characteristics may not cause any problems for some detection applications, where presence of an object or substance can be identified in contrast to the background scene. However, when sophisticated statistical analysis of the image is expected, the quality of the image may restrict the performance of signal processing tools applied for specific task. During the INHERIt project, described in Chapter 3, the applicability of this technology for the authentication of the artwork by identification and classification of pigments was studied. For this task, a set of algorithms for image analysis and labelling of paints used in studied artwork was developed. The labelling was based on the specially developed spectral library of pigments relevant for this work. The data from the mid-infrared imager was compared to the one produced by conventional hyperspectral camera operating in the near-infrared region. The performance of the system was tested on bespoke paintings and the moderate-high rate of correct classification was shown, where among all analysed paints properly labelled were: 67% based on the Firefly IR Imager's data and 78% based on the data from conventional near-IR camera. Additionally, it was demonstrated that these systems were able to identify an anachronistic paint – Titanium white – in both, the bespoke test painting made for this project as well as analysed real world forgeries [1, 2]. These results showed that even during this initial, proof of concept study, hyperspectral imaging in the infrared regime, complemented by signal processing algorithms, is a very useful tool for authentication of the painted artwork.

During the work presented in Chapter 4 a completely different application for the same technology was studied. In this part of the dissertation, the short study ‘Hyperspectral Ice/Oil Detection Experiment’ (HIDE) and the project ‘Remote Oil Spill Detection And Monitoring on ice-covered waters’ (Rosdam) are described, both focused on assessing if the available hyperspectral devices are applicable for the detection of oil in ice-affected waters. These were laboratory-based studies, with the experimental work done in the cold room, and for some tests with the use of a freezer, to grow and maintain the ice structures. During short, proof of principle experiment (HIDE) slight difference in the spectral response between the pure ice and oil under ice samples was observed, which was sufficient for classification algorithm to distinguish various samples. However, a lot of aspects of this test were not optimal. It was based on a single sample only and the imager was not ready to operate in sub-zero ambient temperatures, forcing the data acquisition to be done in room temperature, what over the time of the scan lead to melting of the ice sample. Although, the penetration depth of water in the infrared regime is very short [3] and it was expected that the available hardware may not be optimal for this task, the initial, promising results facilitated the decision to perform the full-scale study of this topic – the Rosdam project. During this work a very extensive set of tests was executed, including two large scale imaging runs in the cold room. The first tests ended with the lack of any consistency within the data acquired by the passive, near-IR system. However, the results from Firefly IR Imager showed very strong features, which were originally perceived as the unique characteristics for the ice samples with and without oil underneath. Even though, these observations varied from the initial ones, made during the HIDE experiment, these were done in fully controlled environment and primarily it was assumed that this was the reason for the noted differences. Despite of very explicit features observed in the majority of individual samples, some of them did not reproduce these spectral variances and that was the reason for devoting the following tests to verify these observations. The results showed very big variations in acquired spectra, disproving the unique characteristics for given test conditions. It was also noticed, while running the tests, that all the spectral features and alterations resulted rather from the sample handling than from actual physical response of the scene. These observations were verified and confirmed by additional tests, and, even though during this project it was not possible to verify what process was manifesting itself in the spectral profile change, it was proved that all the observed positive results were only artefacts of experimental procedure and indeed, actual presence of oil under ice was not demonstrated in any of the test cases. Based on above description of the project one could question the chances of success at the outset of the project. Yet, even if with extremely short penetration depth in the infrared, a very high surface reflectivity and specular reflections from its crystalline structure, it was still worth to try to challenge these difficult conditions and fully verify the technology, especially after the successful classification of test samples based on data from the first

experiments that fortified this idea. Although, finally it was shown that the tested devices are not applicable for oil under ice detection, several experimental techniques were developed during this project, such as methods for safe operation of Firefly imager in sub-zero temperatures, repeatable growth and maintenance of ice samples and oil injection techniques. These may enable new applications for this imager and robust testing conditions for potential new technologies undertaking the challenge of oil under ice detection.

In Chapter 5 of this dissertation, the final project is described. In contrast to the previous two studies, this one was not focused on the exploration of a new application for the mid-IR imaging spectroscopy or signal processing techniques, but on the development of a new, ultra-sensitive spectroscopic technique. In this proof-of-concept study, the sensitivity improvement of the photoacoustic spectroscopy was successfully demonstrated by a novel combination of this method with an optical parametric oscillator and use of high optical field circulating within its cavity as an excitation source. The base platform for this development was an intracavity OPO pumped by Nd:YVO₄ laser and PPLN based SRO configuration with oscillating signal wave. This system could produce 220mW of extracted idler power, what is equivalent to approximately 19W of circulating signal field. The frequency control of the system was achieved by the use of etalons in the signal arm of an OPO: an air-spaced etalon of 333GHz FSR for coarse tuning, in addition to 10GHz solid silicon etalon providing means for fine tuning of the system's frequency and its precise coincidence with absorption features of sought molecules. To observe photoacoustic effect, two spectrophone modalities were investigated: traditional, microphone based and quartz enhanced, based on quartz tuning fork. The former one was fabricated in a form of a miniature, 3D printed chamber with built-in MEMS microphone. This arrangement was characterised by resonance frequency of 17.9kHz (for nitrogen) and quality factor Q value of approximately 9. Investigations of quartz enhanced technique were initially based on commercial QE-PAS spectrophone with tuning fork together with resonator arrangement pre-aligned and matched with amplification and read-out electronics. Unfortunately, due to the poor finish of resonance tube, it was unsuitable for the intracavity excitation method. Attempts to attain other QE-PAS configurations were initiated, but they were not finished within the framework of this project. Over the course of this study, sensitivity improvement of the photoacoustic spectroscopy was presented when the intracavity, oscillating field was used as an excitation source. When compared to a typical, external-cavity arrangement, where DFB laser was used for induction of photoacoustic effect, the demonstrated technique showed 240x higher sensitivity. Moreover, additional 2.5x improvement is expected after the power optimisation of the utilised laser system. These experiments were performed with the ammonia as the target molecule and the noise-limited sensitivity of 1ppb was shown when tuned to the 6605.6cm⁻¹ absorption line. Due to erratic

instability of the system, these results are based on instantaneous data only. After improved stabilisation of the laser setup, that averaging would bring additional rise of sensitivity.

6.3. Future work

Any future work based on the results achieved during this programme, should be considered individually for each studied subject, however general future endeavours could also be identified.

Artwork identification is a difficult and often inconclusive process. Even if various art scientists rely on a number of techniques to support their investigation, the hyperspectral imaging is certainly useful tool for rapid and non-destructive examination of an object. Although HSI alone often would not identify if a painting is genuine or forged, it could further enhance sophisticated toolkit of available analysis procedures. Additionally, the use of classification algorithms and bespoke software, designed for artwork authentication would certainly help to deal with multidimensional and potentially also multimodal data. This combination could accelerate the inspection process and limit the number of destructive tests required for the final validation of a piece, what could simplify the authentication procedure and make it much more cost effective. The mid-IR, active system, studied during the INHERIt project has the potency to be used in this application. Although in its current form, it has provided useful data for the proof-of-concept study, it is not ready to be applied commercially for this task. All the identified imaging artefacts should be addressed to offer a user-friendly device, producing high quality data. The mitigation techniques presented in this work would need to be translated from a laboratory system into an engineered solution. Although easily accessible passive HSI systems operating in visible and near-infrared regions, which do not struggle with these image quality issues, may satisfy major part of examination needs. The complementary nature of the results provided by mid-infrared active imager could help to find answers that are otherwise difficult to obtain.

In modern society, where significant portion of energy is still created from combustible fuels, the ships transporting vast volumes of oil are daily crossing Polar Regions. Although, these carriers are prepared to minimise any chances of spills, these still occasionally happen, and when it takes a place, it often brings a big environmental catastrophe for this region. Ecological organisations, coastal guards as well as generally understood oil industry would certainly benefit from new, stand-off techniques for detection and monitoring of oil spills. While, the Rosdam project proved that proposed mid-IR hyperspectral imaging is not a tool for this purpose, other optical imaging methods may be still applicable for this task. The testing methodology and techniques developed throughout this project could be used to study new emerging technologies for oil under ice detection. Multiple studies of quantum technologies in recent years, lead to the development of single photon detectors that could be suitable for operation in such a difficult

environment as water and ice. The literature already shows that time-correlated single-photon counting [4] and quantum imaging [5, 6] show unprecedented capabilities for underwater imaging. Further work of these techniques and their verification for imaging through ice could bring a new hardware for application in oil spills detection and monitoring.

While the two application exploration projects, presented in Chapters 3 and 4, within their timescale reached conclusive results, the last project of this thesis, before its formal end, has merely shown the potency of proposed concept and allowed to draw a base line for further improvements. To fully exploit this novel approach for photoacoustic spectroscopy, series of improvements in sensitivity, selectivity, frequency tuning and stability of the system are required. Sensitivity can be enhanced by a number of ways. In this project, near-infrared circulating signal field of the OPO was utilised. This wavelength regime contains only modest absorption lines of ammonia and the use of deeper infrared region would benefit from significantly higher absorption coefficient. To do so, a modification of the SRO configuration from the oscillating signal to the idler wave would enable higher intensity field in mid-infrared, accessible for excitation of photoacoustic effect. Although, in this case, with fixed primary pump power, the power of circulating field would drop due to the quantum defect between the signal and idler fields, this is expected to be compensated by much stronger absorption coefficient. A change of the oscillating field within the same configuration of the OPO (based on PPLN crystal) could bring the excitation to 3 - 4 μm . However, applying other nonlinear gain medium could potentially move this technique to the fingerprint region – around 10 μm . Another significant refinement in sensitivity is the use of a spectrophone with significantly higher quality factor Q . The one employed in presented work resulted in very low Q (<10) and had significant impact on the limitation of achieved results. Although, the traditional, microphone-based spectrophones may reach Q factor exceeding 1000 [7, 8], the state-of-art for Q factor improvement is the use of quartz enhanced photoacoustic spectroscopy which utilises quartz tuning fork with Q factor of 10,000 [9]. Lastly, an improvement of the system's stability will enable the averaging of instantaneous signal, leading to further sensitivity increase. The Table 6.1 summarises all these techniques and anticipated magnitude of the enhancement achieved by their implementation, as compared to the current performance level.

Next to sensitivity, improvement of the frequency stability and selection (tuning) is of paramount importance. Despite of knowledge that IC-OPO is prone to relaxation oscillations, the system used in this initial study had no suppression mechanism implemented. This lead to erratic frequency jumps. This effect was mitigated by the application of an etalon in the signal cavity, but this one was not optimised for this application. Using methods for suppression of relaxation oscillation [10] and dedicated etalon would help to stabilise and accurately tune the OPO to selected wavelength. This new etalon and stabilised system would also enable frequency

modulation of the excitation source, as opposed to the amplitude modulation employed during this work. This technique isolates the system from any broader features of the background. Finally, all this work was performed on a lab-based system and before demonstrating its operation in a field, the full opto-mechanical arrangement would need to be engineered to a robust and ruggedised device. All these improvements have been described in the last section of Chapter 5.

Table 6.1. Summary of the predicted improvements, along with quantification of their magnitude; the sensitivity demonstrated during described project is used as a base line to these projections (- selected NH₃ absorption lines).*

Parameter	Current (PAS spectrophone at signal wavelength)	Refinement (QE-PAS spectrophone at idler wavelength)	Improvement in SNR	Sensitivity limit (w.r.t current 1ppb)
a	Signal absorption coefficient*: 4.2e-2 cm-2/atm	Idler absorption coefficient*: 5.1e-1 cm-2/atm	10x	100ppt
Q	10 (Figure 5.21)	12,000 (Figure 5.30)	1200x	85ppq
P	7.7W	4W (power drop due to estimated signal idler quantum defect)	0.5x	170ppq
C	No time averaging implemented	Time averaging	100x	~2ppq

6.4. Summary

All the projects presented in this thesis demonstrate the strength of OPOs and, in particular, the intracavity configuration of these devices for the spectroscopic measurements. Both, an imaging configuration for direct absorption spectroscopy as well as an excitation source for the photoacoustic effect, prove to be very versatile and potent devices. The other pillar of this thesis – signal processing – was also omnipresent in these studies to various extents. The first two application-oriented projects showed enhancement of the results achieved by utilisation of signal processing techniques to the acquired data. Although, in Rosdam project the technology was identified as unsuitable for selected task, the applied algorithms helped to analyse captured data and provide strong conclusions. While the last project presented in this dissertation was strongly focused on the hardware development, classification algorithms were not required at this point. However, in this early stage of development, basic signal processing tools (such as averaging or background removal) were already enriching the demonstrated results.

This thesis showed a successful combination of seemingly two independent fields of science which, when utilised together, can provide superior results. Moreover, it demonstrated the need for broadly tuneable laser sources operating in infrared spectral region. Although OPOs

are very versatile, they are relatively big, what often hampers their deployment in the field. Yet, the Quantum Cascade and Interband Cascade Lasers cover the same very broad range of infrared regime as OPOs and they are comparatively light and compact. It is apparent that the future of active infrared spectroscopy will be served by these lasers. Even though currently the unit cost for such lasers is very high, there is no technological reason why this could not be changed. These are semiconductor devices and as such they are open to the economy of scale. With mass market demand (for example: QCL in every smartphone) the cost of these sources would diminish significantly.

Novel signal processing algorithms assist development of new intelligent solutions, yet it is the availability of small, powerful and low cost computers that endows their deployment. Single board computers, microcontroller kits and FPGA boards are readily available and many of these credit-card-footprint machines have now more computing power than the most powerful desktop machines only couple years ago. This really enables implementation of these algorithms directly next to the hardware and production of truly intelligent devices.

The symbiosis of compact broadly tuneable sources and embedded data analysis has the potency to revolutionise current perception of spectroscopic devices and their applications. The work presented in this dissertation is to a great degree preparation for the time when signal processing-enhanced mid-infrared spectroscopy is omnipresent in peoples' everyday-lives, without them even realising this.

References

- [1] C. Finn, "The Devil in the Detail," *Apollo: The international art magazine*, vol. CLXXIX, no. 616, p. 50 – 54, January 2014.
- [2] H. Keazor and T. Öcal, Eds., *Der Fall Beltracchi und die Folgen. Interdisziplinäre Fälschungsforschung heute.*, Berlin: De Gruyter, 2014.
- [3] D. M. Wieliczka, S. Weng and M. R. Querry, "Wedge shaped cell for highly absorbent liquids: infrared optical constants of water," *Applied Optics*, vol. 28, pp. 1714-1719, 1989.
- [4] A. Maccarone, A. McCarthy, X. Ren, R. E. Warburton, A. M. Wallace, J. Moffat, Y. Petillot and G. S. Buller, "Underwater depth imaging using timecorrelated single-photon counting," *Optics Express*, vol. 23, no. 26, 2015.
- [5] M. Lanzagorta, "A Quantum Imaging System for Underwater Arctic". United States of America Patent 14/800,769, 16 July 2015.

- [6] M. Lanzagorta, J. Uhlmann and S. E. Venegas-Andraca, "Quantum sensing in the maritime environment," in *OCEANS 2015 - MTS/IEEE Washington*, Washington, 2015.
- [7] L. J. T. III, M. J. Kelly and N. M. Amer, "The role of buffer gases in optoacoustic spectroscopy," *Applied Physics Letters*, vol. 32, no. 11, pp. 736-738, 1978.
- [8] E. Nodov, "Optimization of resonant cell design for optoacoustic gas spectroscopy (H-type)," *Applied Optics*, vol. 17, no. 7, pp. 1110-1119, 1978.
- [9] P. Patimisco, G. Scamarcio, F. K. Tittel and V. Spagnolo, "Quartz-Enhanced Photoacoustic Spectroscopy: A Review," *Sensors*, vol. 14, pp. 6165-6206, 2014.
- [10] D. J. M. Stothard, "Practical Continuous-Wave Intracavity Optical Parametric Oscillators," in *Advances in Optical and Photonic Devices*, K. Y. Kim, Ed., InTech, 2010, pp. 293-328.

Appendix A

I. The full description of all paints contained by the ‘grid canvas’.

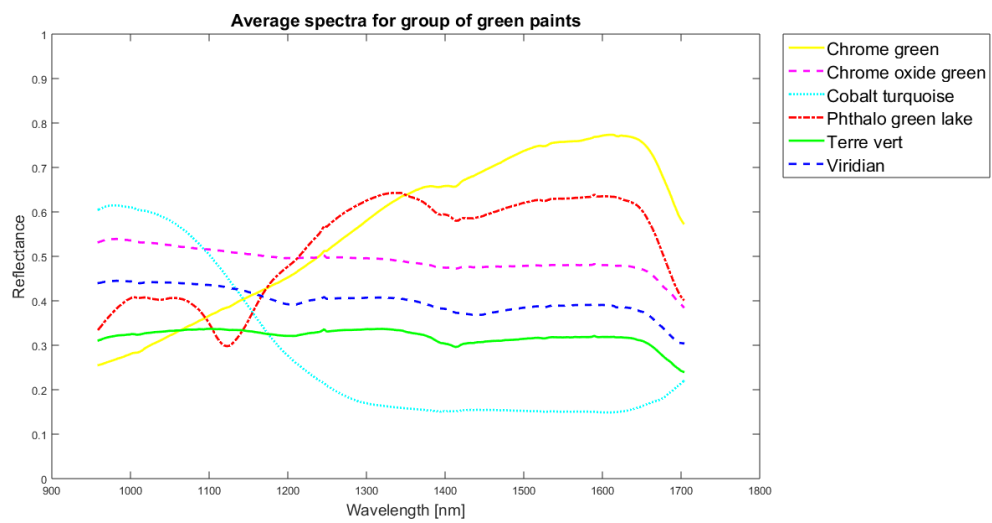
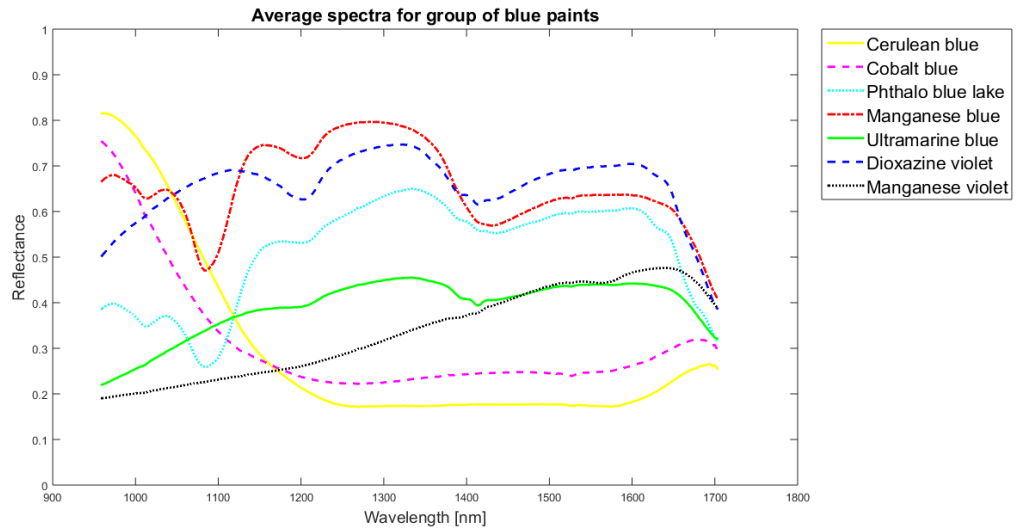
#	Colour	Supplier description	Confirmed composition
A1	Cerulean blue	MICHAEL HARDING Cerulean Blue, No.603 Series 6 PB 35 Cobalt Stannate and Oxides of Tin in linseed oil	Chromium cobalt aluminium oxide Barium sulfate
B1	Cobalt blue	MICHAEL HARDING Cobalt Blue, No.506 Series 5 PB 28 Oxides of Cobalt & Aluminium in Linseed Oil	Cobalt aluminium oxide
C1	Phthalo blue lake	MICHAEL HARDING Phthalocyanine Blue Lake, No.209 Series 2 PB 15.3 Chlorinated Copper in Linseed Oil	Phthalocyanine blue (CI Pigment Blue 15:3) Titanium dioxide
D1	Manganese blue	BLOCKX Manganese Blue PW4 + PB15:3	Phthalocyanine blue (CI Pigment Blue 15:3) Zinc oxide
E1	Ultramarine blue	MICHAEL HARDING Ultramarine Blue, No.113 Series 1 PB 29 Silicate of Sodium, Aluminium and Sulphur in Linseed Oil	Ultramarine, synthetic
F1	Dioxazine violet	BLOCKX Dioxazine Mauve PV 23 - Dioxazine	CI Pigment Violet 23 Titanium dioxide Calcium carbonate
G1	Manganese violet	MICHAEL HARDING Manganese Violet, No.304 Series 3 PV 16 Manganese Ammonium Pyrophosphate in Linseed Oil	Manganese phosphate
A2	Terre vert	MICHAEL HARDING Terre Verte, No.115 Series 1 PG 23 Natural Earth in Linseed Oil	CI Pigment Green 7 (phthalocyanine green) Calcium sulfate dihydrate, gypsum type
B2	Chrome oxide green	MICHAEL HARDING Oxide of Chromium, No.305 Series 3 PG 17 Oxides of Chromium in Linseed Oil	Chromium oxide

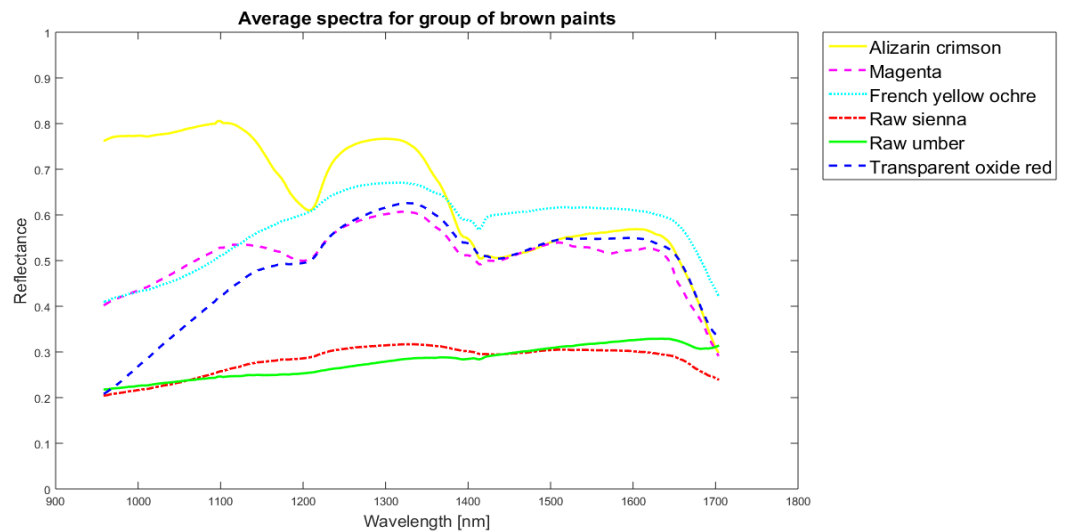
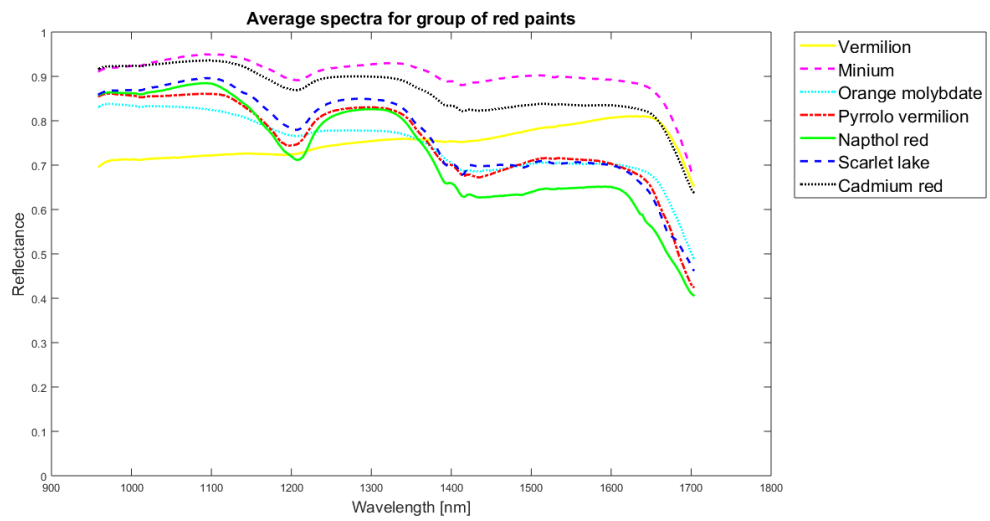
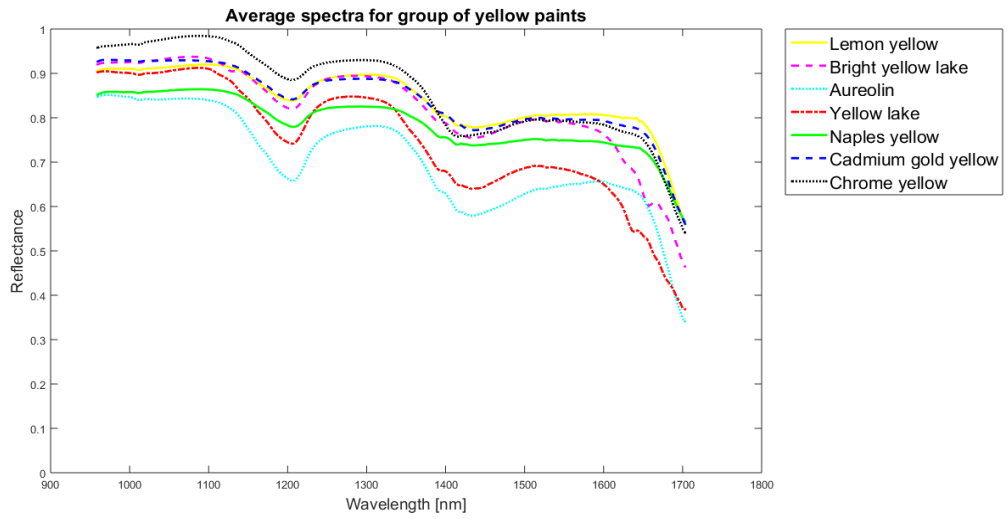
C2	Cobalt turquoise	MICHAEL HARDING Cobalt Turquoise Deep, No.507 Series 5 PB 36 Oxides of Cobalt & Aluminium in Linseed Oil	Cobalt chromium oxide Titanium dioxide, rutile type
D2	Phthalo green lake	MICHAEL HARDING Phthalo Green Lake, No.213 Series 2 PG 7 Chlorinated Copper Ground in Linseed Oil	CI Pigment Green 7 (phthalocyanine green)
E2	Viridian	BLOCKX Viridian PG 18 Ox. de Cr hydrate	Chromium oxide hydrate
F2	Chrome green	RUBLEV COLOURS Chrome Green, Series 5 Pigment Yellow 34 + Pigment Blue 27 Lead Sulfochromate and Ferric Ferrocyanide in Linseed Oil	Iron hexacyanoferrate(II) Lead chromate
A3	Lemon yellow	MICHAEL HARDING Lemon Yellow, No.108 Series 1 PY 31 Barium Chromate Ground in Linseed Oil	Barium chromate
B3	Bright yellow lake	MICHAEL HARDING Bright Yellow Lake, No.109 Series 1 PY 3 Diarylimide in Linseed Oil	CI Pigment Yellow 3 Calcium carbonate
C3	Aureolin	MICHAEL HARDING Aureolin, No.501 Series 5 PY 40 Cobalt Potassium Nitrate Ground in Linseed Oil	Potassium cobalt nitrite
D3	Yellow lake	MICHAEL HARDING Yellow Lake, No.110 Series 1 PY 74 Diarylimide Ground in Linseed Oil	CI Pigment Yellow 74
E3	Naples yellow	MICHAEL HARDING Genuine Naples Yellow Dark, No.606 Series 6 PY 41 Lead antimoniate in Linseed Oil	Lead antimony tin oxide Barium sulfate
F3	Cadmium gold yellow	MICHAEL HARDING Cadmium Golden Yellow, No. 403 Series 4 PY 35 Cadmium Sulphide in Linseed Oil	Cadmium sulfide
G3	Chrome yellow	RUBLEV COLOURS Chrome Yellow Medium, Series 4 Pigment Yellow 34 (Lead Chromate) in Linseed Oil	Lead chromate Barium sulfate

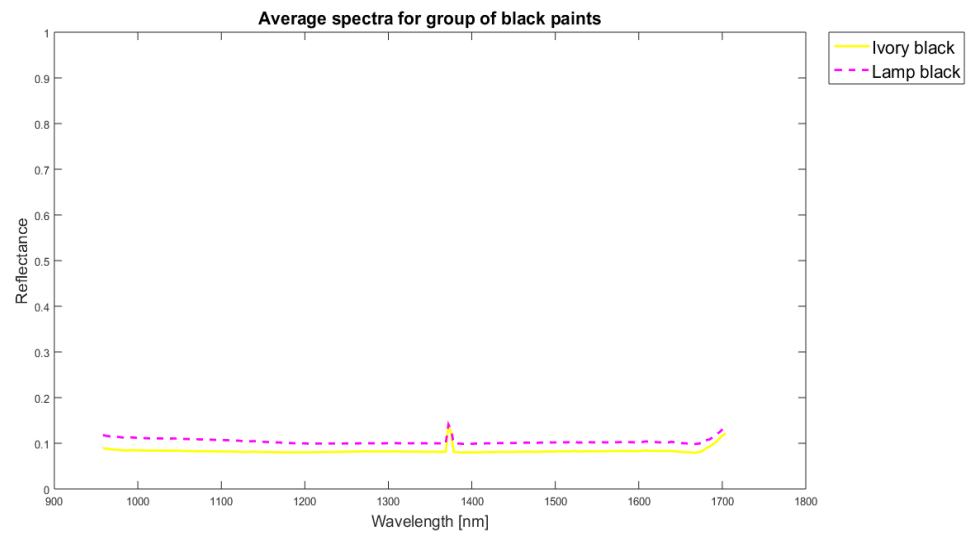
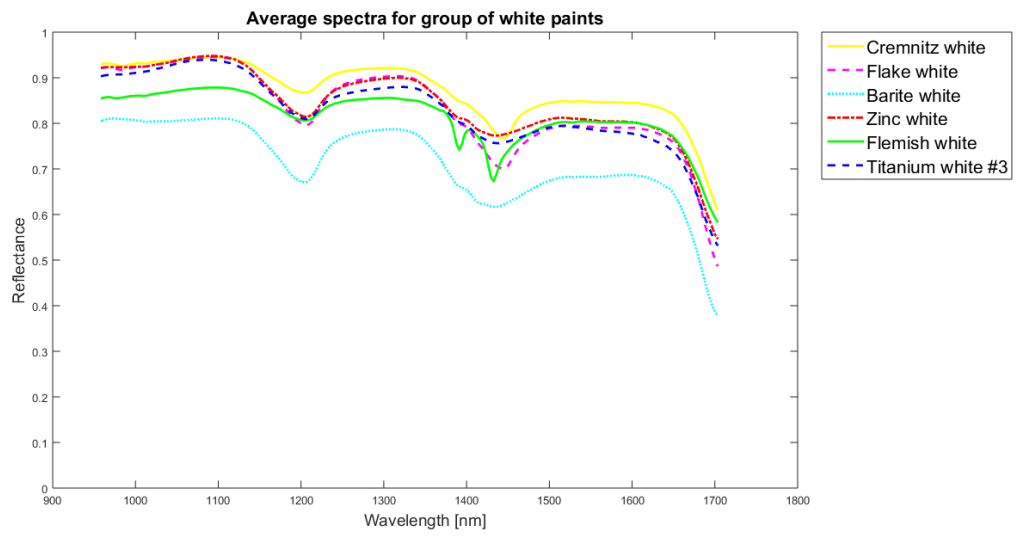
A4	Vermilion	RUBLEV COLOURS Genuine Vermilion, Series 10 Pigment Red 106 (Red Mercuric Sulfide) in Linseed Oil	Mercury sulphide
B4	Minium	RUBLEV COLOURS Minium (Red Lead), Series 5 CI Pigment Red 105 (Red Lead Trioxide) in Linseed Oil	Lead(II,IV) oxide
C4	Orange molybdate	RUBLEV COLOURS Orange Molybdate, Series 4 CI Pigment Red 104 (Lead Chromate Molybdate) in Linseed Oil	Lead chromate molybdate Barium sulfate
D4	Pyrrulo vermilion	BLOCKX Pyrrulo Vermilion PO 73 Diceto Pyrrulo Pyrrole	CI Pigment Orange 73 Calcium carbonate, calcite type
E4	Naphthol red	MICHAEL HARDING Naphthol Red, No.301 Series 3 PR 188 Naphthol Azo in Linseed Oil	PR 188
F4	Scarlet lake	MICHAEL HARDING Scarlet Lake, No.205 Series 2 PR 170 Naphthol Azo in Linseed Oil	CI Pigment Red 170
G4	Cadmium red	MICHAEL HARDING ARTISTS OIL COLOURS Cadmium Red, No.504 Series 5 PR 108 Cadmium Sulphoselenide in Linseed Oil	Cadmium selenide sulfide
A5	Alizarin crimson	MICHAEL HARDING ARTISTS OIL COLOURS Alizarin Crimson, No.302 Series 3 PR 83 Dihydroxyanthraquinone in Linseed Oil	CI Pigment Red 83:1
B5	Magenta	MICHAEL HARDING Magenta, No.303 Series 3 PR 122 Quinacridone in Linseed Oil	CI Pigment Red 122
C5	French yellow ochre	MICHAEL HARDING French Yellow Ochre, No.133 Series 1 PY 43 in Linseed Oil	Natural earth containing goethite
D5	Raw sienna	MICHAEL HARDING Raw Sienna, No.120 PBr 7 Natural Earth Ground in Linseed Oil	Natural earth containing goethite and hematite
E5	Raw umber	MICHAEL HARDING Raw Umber, No.121 Series 1 PBr 6 Synthetic Iron Oxide in Linseed Oil	Natural earth containing manganese

F5	Transparent oxide red	MICHAEL HARDING Transparent Oxide Red, No.220 Series 2 PR 101 Synthetic Iron Oxide Ground in Linseed Oil	Hematite
A6	Cremona white	MICHAEL HARDING Cremona White, Series 1 PW 1 Pure Lead Carbonate Ground in Refined Linseed Oil	Lead carbonate hydroxide
B6	Flake white	MICHAEL HARDING Flake White, Series 1 PW 1 Lead Carbonate & PW 4 Zinc White Ground in Refined Linseed Oil	Lead carbonate hydroxide Zinc oxide
C6	Barite white	RUBLEV COLOURS Artists Oil Colour Barite White, Series 2 Pigment White 22 Natural Barium Sulfate Vehicle: Walnut Oil	Barium sulfate Calcium carbonate, calcite type
D6	Zinc white	MICHAEL HARDING Zinc White, No.103 Series 1 PW 4 Zinc Oxide Ground in Linseed Oil	Zinc oxide
E6	Flemish white	RUBLEV COLOURS Artists Oil Colour Flemish White, Series 3 Pigment White 3 + Pigment White 1 Basic Lead Sulfate + Basic Lead Carbonate Vehicle: Linseed Oil	Lead sulfate, monobasic Lead sulfate, tetrabasic Lead carbonate
F6	Titanium white #3	MICHAEL HARDING Titanium White No.3, No.130 Series 1 PW 6 Titanium Dioxide & PW 4 Zinc Oxide Ground in Linseed Oil	Titanium dioxide, rutile type
A7	Ivory black	MICHAEL HARDING Ivory Black, No.129 Series 1 PBk 9 Amorphous Carbon Ground in Linseed Oil	Carbon-based black as bone coke
B7	Lamp black	MICHAEL HARDING Lamp Black, No.128 Series 1 PBk 6 Carbon Ground in Linseed Oil	Carbon-based black

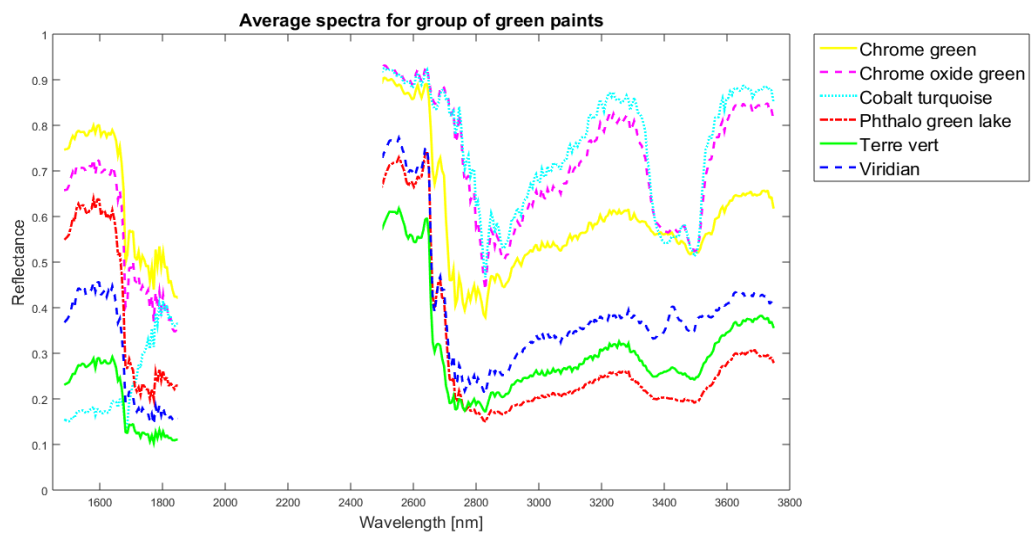
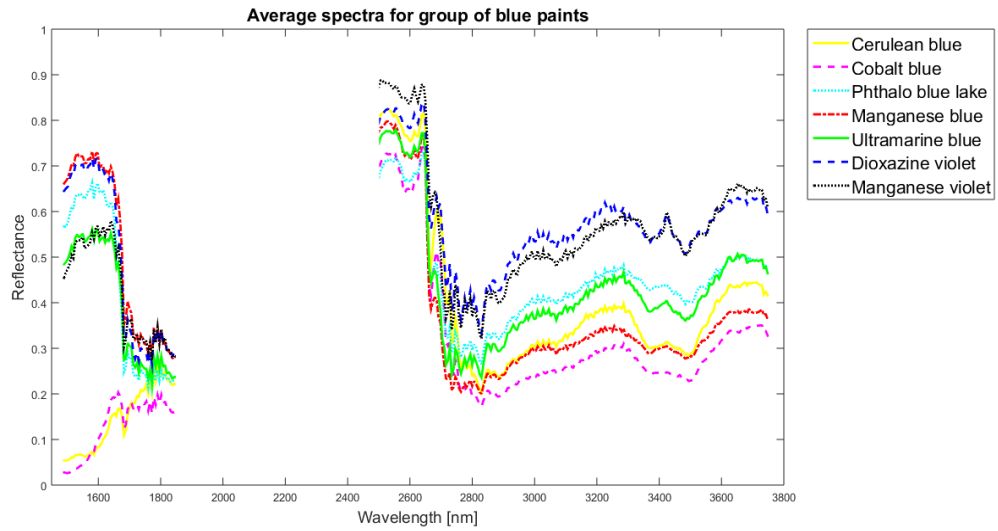
II. The average spectra from all paints contained by the 'grid canvas', imaged by the passive system.

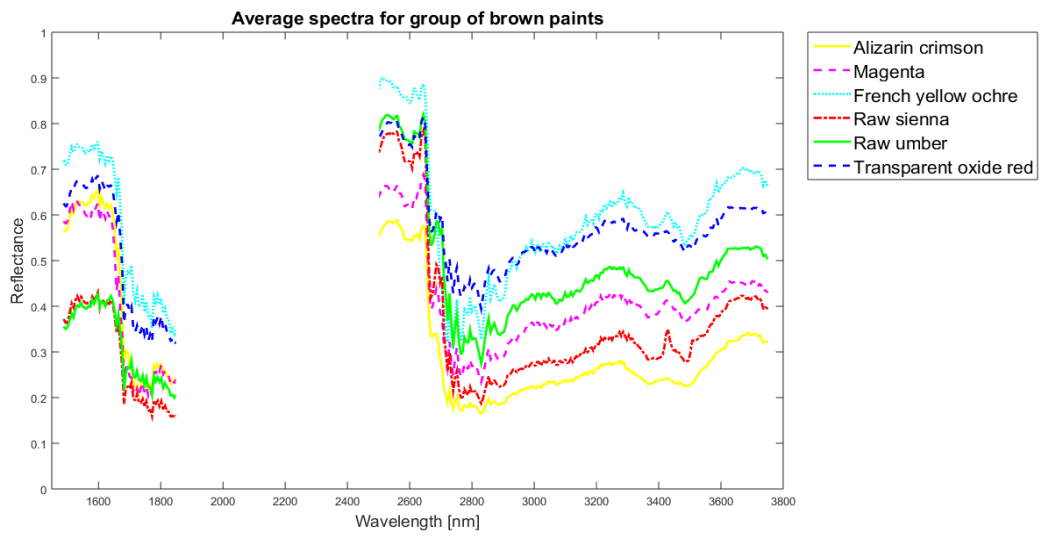
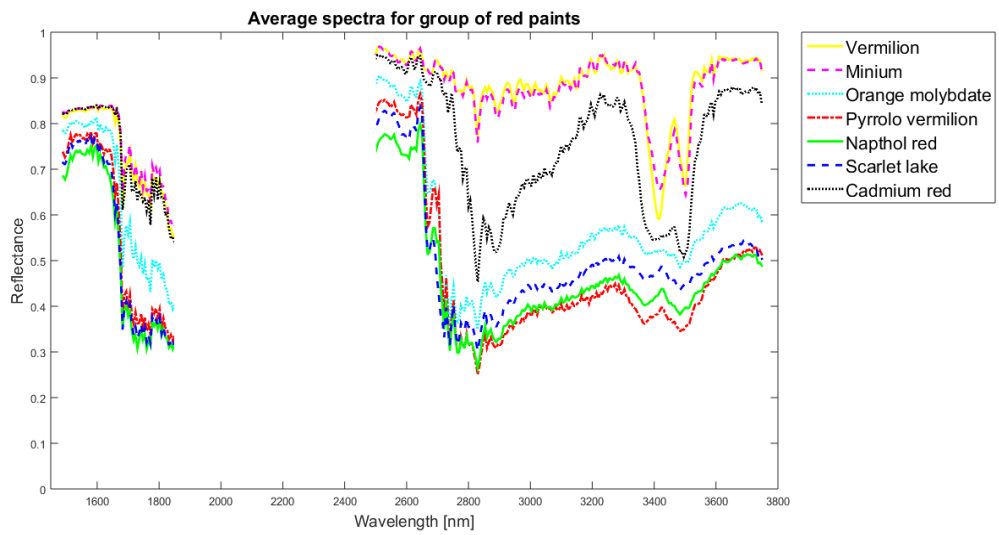
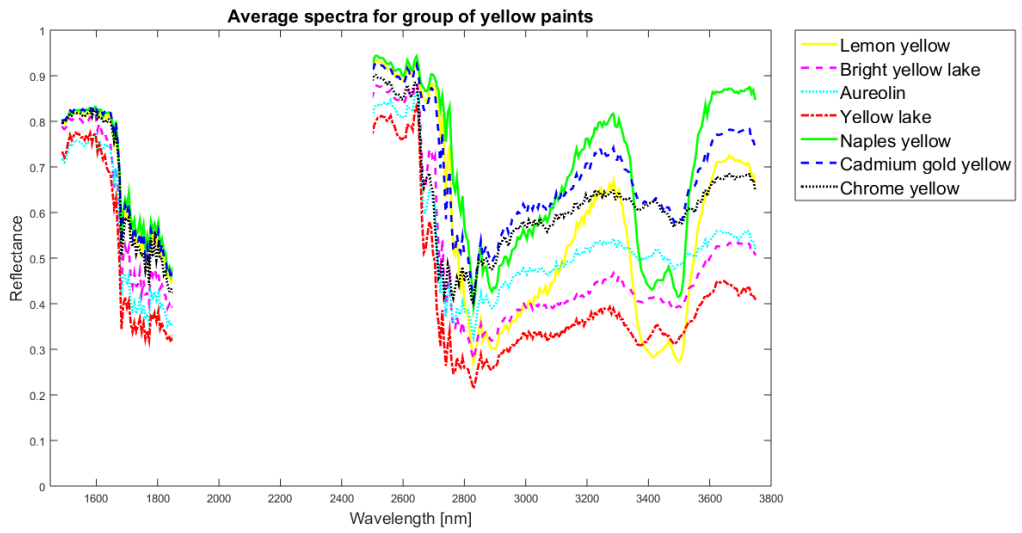


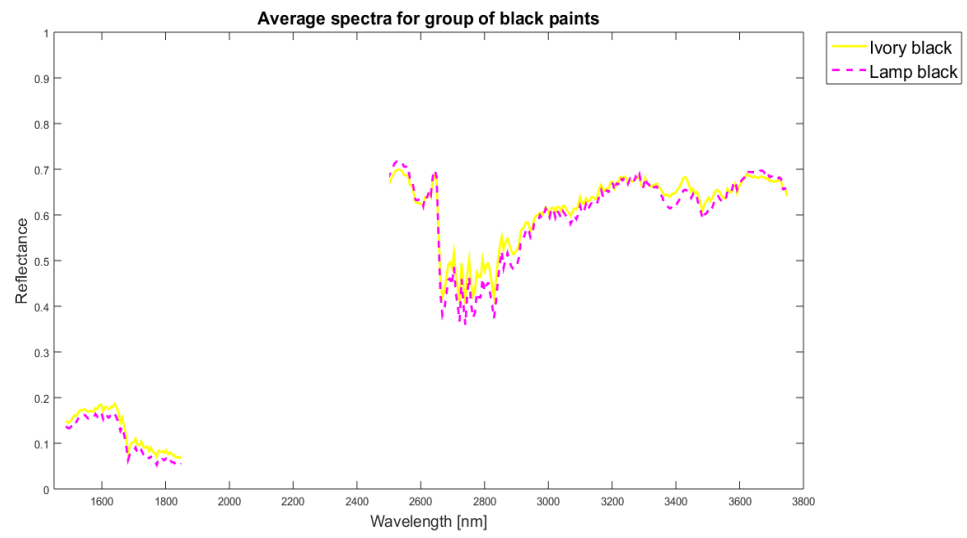
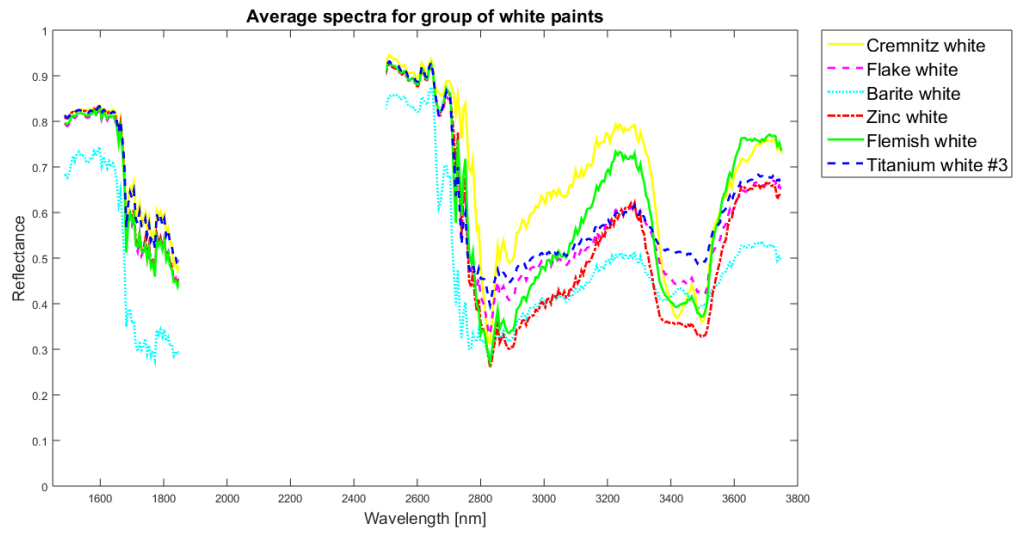




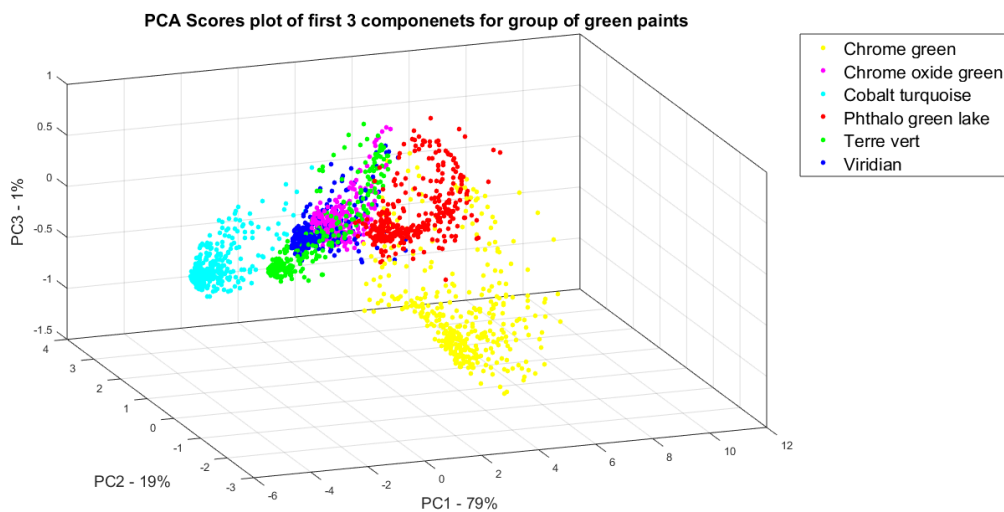
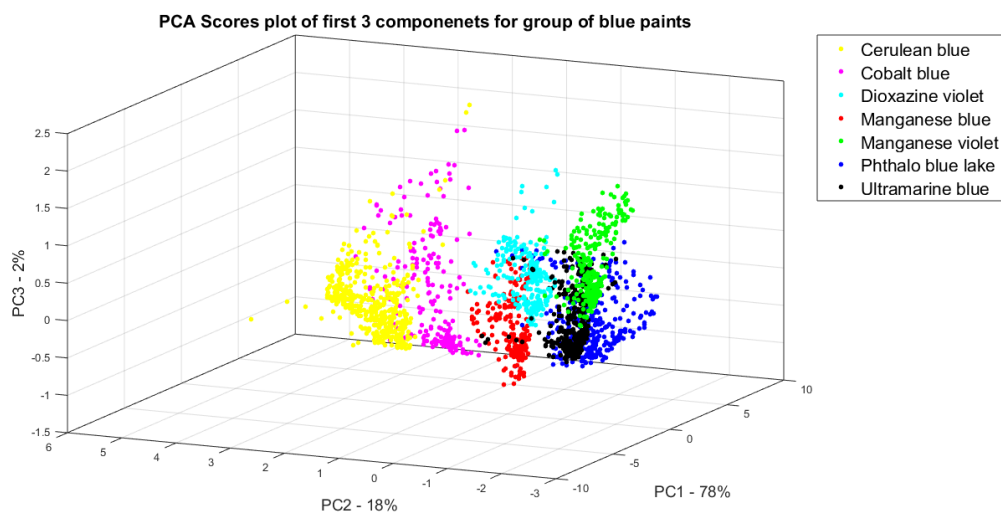
III. The average spectra from all paints contained by the 'grid canvas', imaged by the active system.



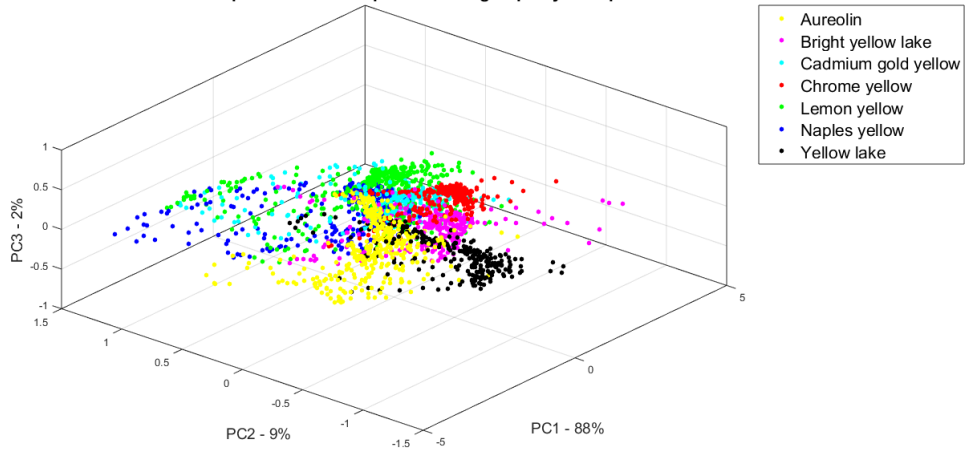




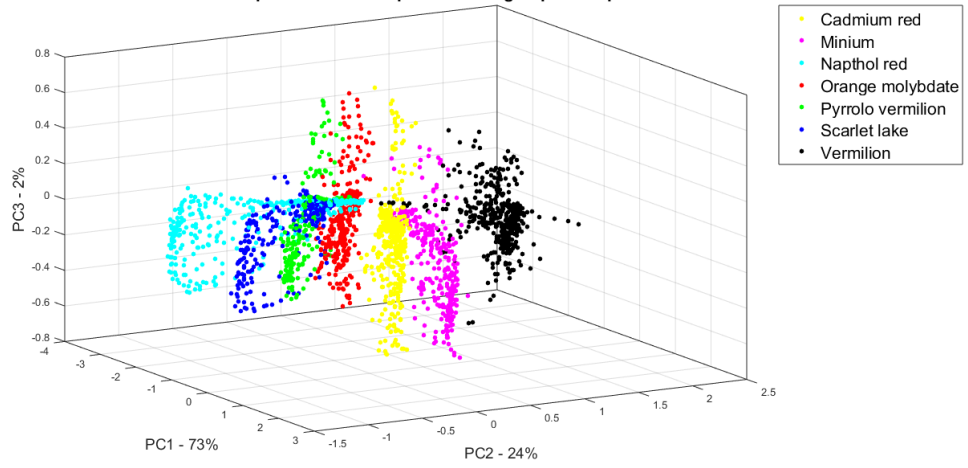
IV. The PCA scores plots for first three principal components obtained from all paints contained by the 'grid canvas', imaged by the passive system.



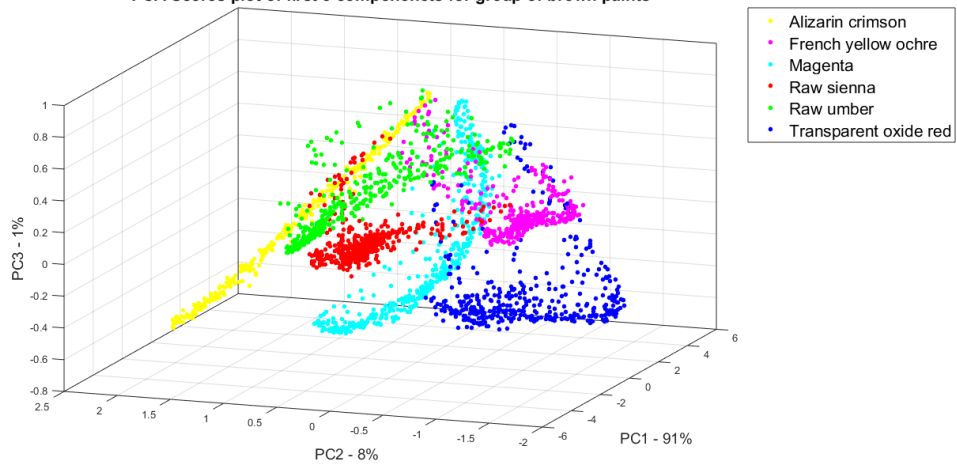
PCA Scores plot of first 3 componenets for group of yellow paints

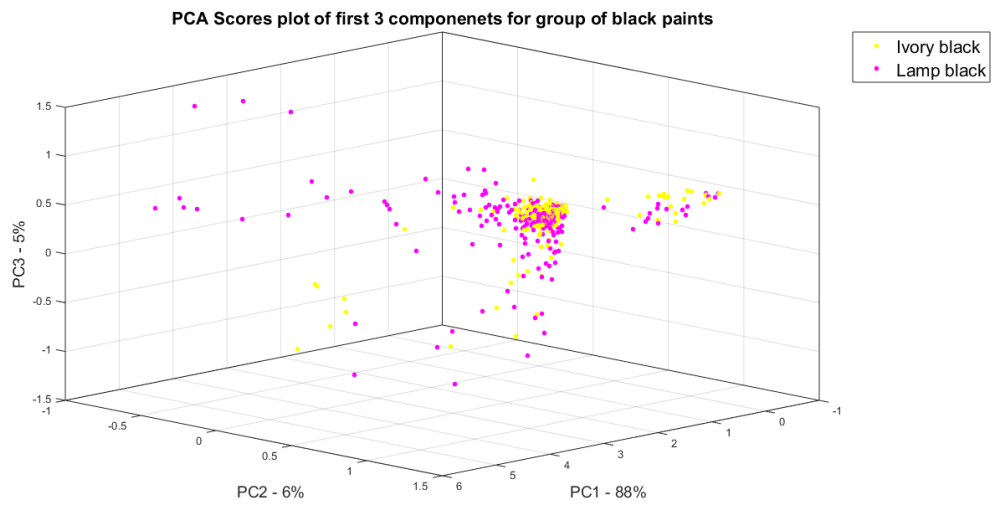
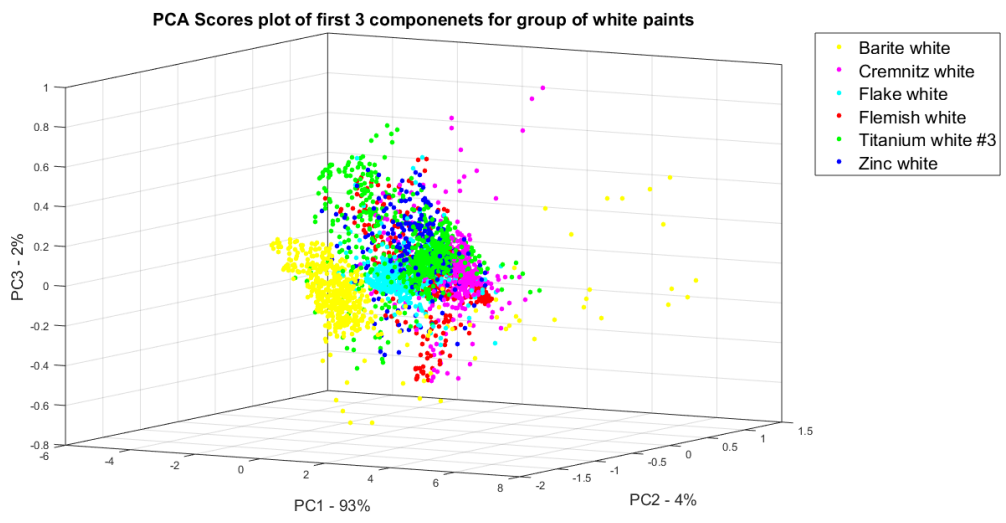


PCA Scores plot of first 3 componenets for group of red paints

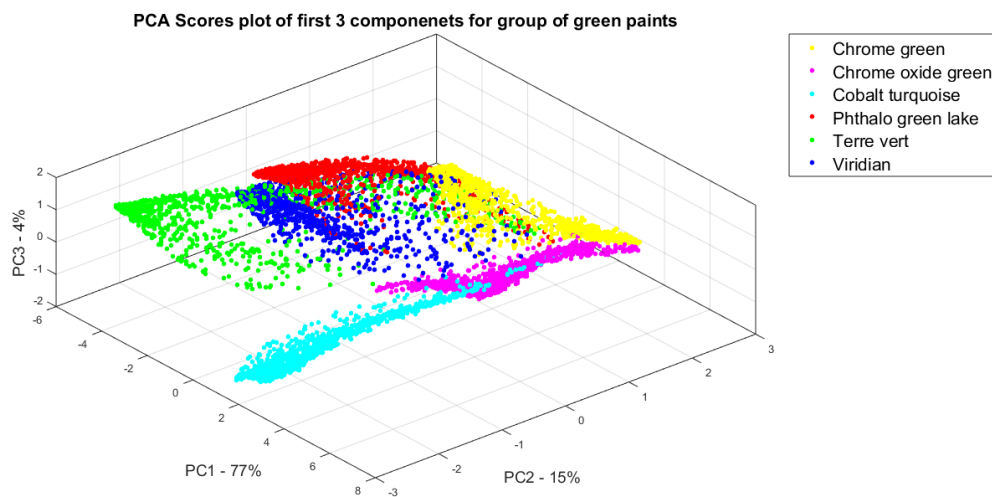
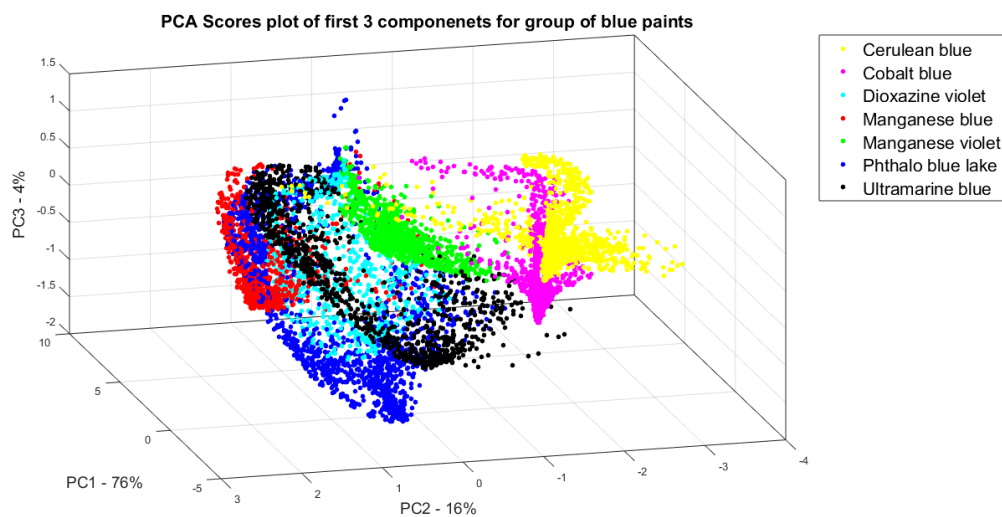


PCA Scores plot of first 3 componenets for group of brown paints

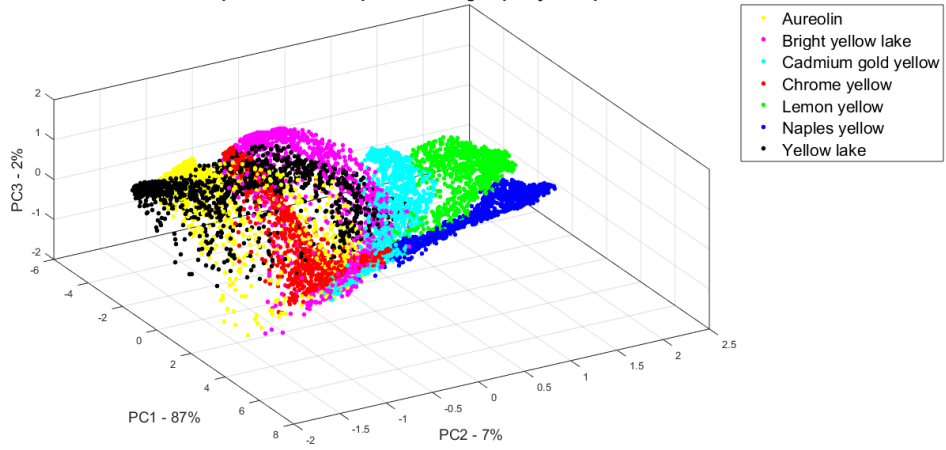




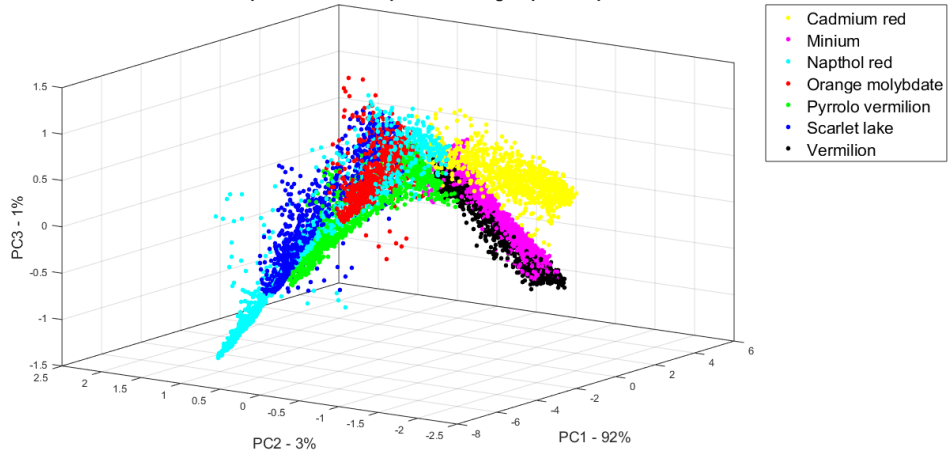
V. The PCA scores plots for first three principal components obtained from all paints contained by the 'grid canvas', imaged by the active system.



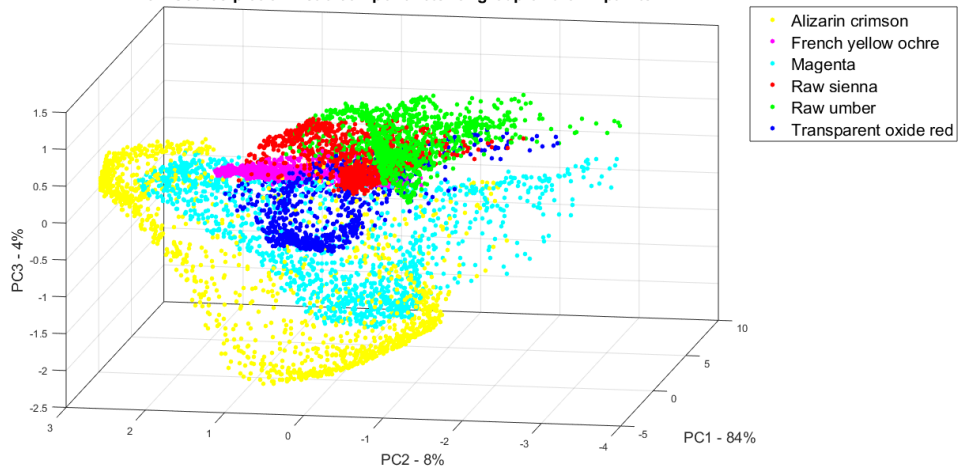
PCA Scores plot of first 3 componenets for group of yellow paints



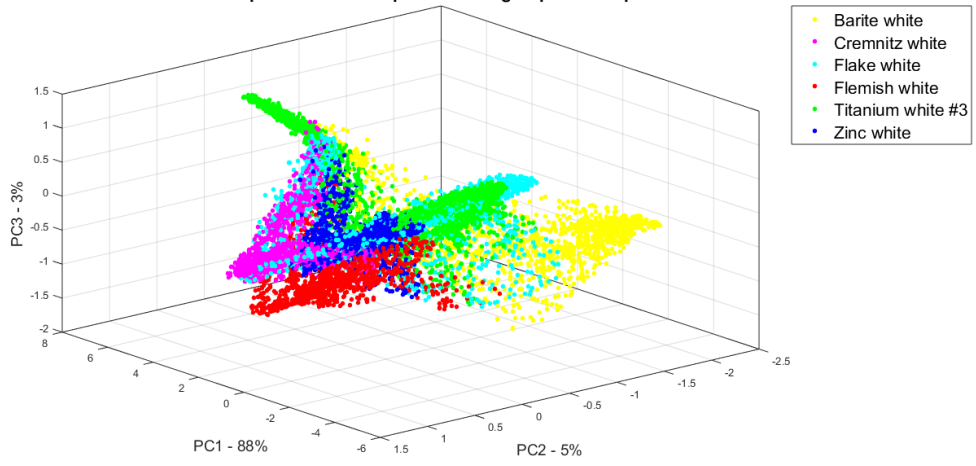
PCA Scores plot of first 3 componenets for group of red paints



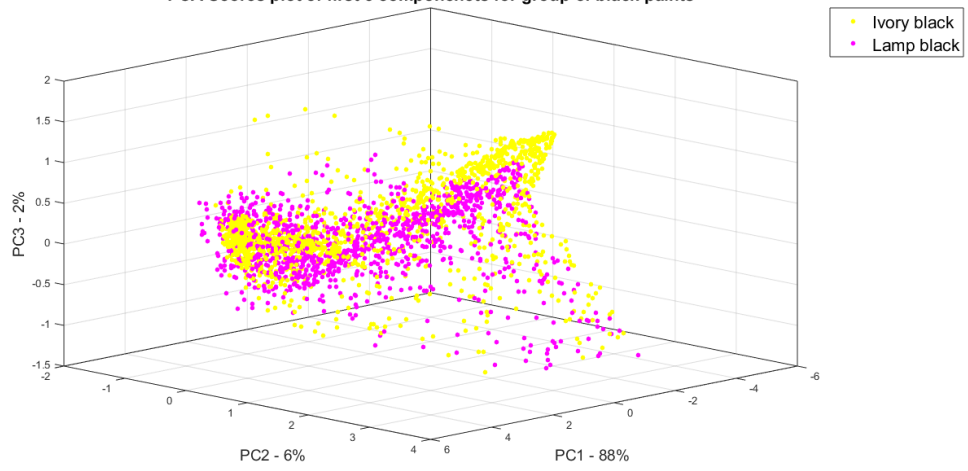
PCA Scores plot of first 3 componenets for group of brown paints



PCA Scores plot of first 3 componenets for group of white paints



PCA Scores plot of first 3 componenets for group of black paints



Appendix B

I. Journal Publications

1. A. Polak, T. Kelman, P. Murray, S. Marshall, D. Stothard, N. Eastaugh and F. Eastaugh, "Use of infrared hyperspectral imaging as an aid for paint identification," *Journal of Spectral Imaging*, vol. 5, no. 1, pp. 1-10, 2016, doi: 10.1255/jsi.2016.a2.
2. A. Polak, T. Kelman, P. Murray, S. Marshall, D. J. M. Stothard, N. Eastaugh and F. Eastaugh, "Hyperspectral imaging combined with data classification techniques as an aid for artwork authentication," *Journal of Cultural Heritage*, vol. 26, pp. 1-11, 2017, doi: 10.1016/j.culher.2017.01.013

II. Conference Proceedings

1. A. Polak, "Classification for Hyperspectral Imaging" presented at CDT Applied Photonics Annual Conference 2014, Edinburgh, UK
2. A. Polak, S. Marshall and D. J. M. Stothard, "Use of hyperspectral imaging for artwork evaluation" presented at CDT Applied Photonics Annual Conference 2015, Edinburgh, UK
3. A. Polak, S. Marshall, J. Ren, B. Hwang, B. Hagan and D. J. M. Stothard, "Remote oil spill detection and monitoring beneath sea ice", presented at ESA's Living Planet Symposium, Prague, Czech Republic, 9-13 May 2016.
4. A. Polak, T. Kelman, P. Murray, S. Marshall, D. J. M. Stothard, N. Eastaugh and F. Eastaugh, "Use of hyperspectral imaging for artwork authentication", presented at CDT Applied Photonics Annual Conference 2016, St Andrews, UK
5. A. Polak, T. Kelman, P. Murray, S. Marshall, D. J. M. Stothard, N. Eastaugh and F. Eastaugh, "Use of hyperspectral imaging for artwork authentication", presented at IASIM2016 - 6th Conference in spectral imaging, Chamonix-Mont-Blanc, France, 3-6 July 2016
6. A. Polak, S. Marshall, J. Ren, B. Hwang, B. Hagan and D. J. M. Stothard, "Remote oil spill detection and monitoring on ice-covered waters", presented at HSI2016 – Hyperspectral Imaging & Applications Conference, Coventry, UK, 12-13 October 2016.

7. A. Polak, D. J. M. Stothard, T. Kelman, P. Murray and S. Marshall, "Use of near- and mid-IR hyperspectral imaging for paint identification, as an aid for artwork authentication", presented at 43rd Freiburg Infrared Colloquium, Freiburg, Germany, 14 – 15 March 2017
8. A. Polak, F. Coutts, P. Murray, D. J. M. Stothard and S. Marshall, "The Use of Hyperspectral Imaging for cake moisture prediction", presented at CDT Applied Photonics Annual Conference 2017, Edinburgh, UK
9. L. Maidment, A. Polak, S. Marshall, and D. T. Reid, "Compressive sampling for spectral imaging," in Conference on Lasers and Electro-Optics, OSA Technical Digest (online) (Optical Society of America, 2017), paper JW2A.81.
10. A. Polak and D. J. M. Stothard, "Enhanced photoacoustic spectroscopy sensitivity through intra-cavity OPO excitation" presented at SPIE Defense + Commercial Sensing Conference 2018, Orlando, USA
11. J. Thomas, A. Polak, G. Bonner, S. Enderle, M. Dunn, D. J. M. Stothard, "Optical parametric oscillator-based trace detection of gases in the mid-infrared region using phase-fluctuation optical heterodyne spectroscopy" presented at SPIE Defense + Commercial Sensing Conference 2018, Orlando, USA
12. J. Thomas, D. Mahler, A. Polak, G. M. Bonner, P. Black, S. Rivers, J. Matthews and D. J. M. Stothard, "Squeezed Light in Photo-thermal Trace Detection" presented at 9th Annual SU2P Symposium: 21st – 22nd May 2018, Glasgow, UK